

# THERMODIFFUSION IN LIQUID BINARY AND TERNARY ALLOYS

DISSERTATION

for the degree of  
Doctor of Natural Sciences

at the  
Faculty of Physics and Astronomy  
Ruhr University Bochum

prepared at the  
Institute for Materials Physics in Space  
German Aerospace Center (DLR), Cologne

By  
Asbjørn Torsvik Krüger  
from  
Tønsberg, Norway

Cologne, Germany  
2024

1<sup>st</sup> assessor: Prof. Dr. Andreas Meyer

2<sup>nd</sup> assessor: Prof. Dr. Daniel Hägele

Date of thesis defence: 19<sup>th</sup> November 2024

# Contents

<b>1</b>	<b>Introduction</b>	<b>1</b>
1.1	History . . . . .	1
1.2	Alloys . . . . .	4
1.2.1	Ag–Al . . . . .	5
1.2.2	Ag–Cu . . . . .	6
1.2.3	Al–Cu . . . . .	6
1.2.4	Ag–Al–Cu . . . . .	7
1.2.5	Al–In . . . . .	7
<b>2</b>	<b>Theory</b>	<b>9</b>
2.1	Thermodynamics . . . . .	9
2.1.1	Gibbs energy . . . . .	9
2.1.2	Chemical potential . . . . .	12
2.1.3	Thermodynamic factor . . . . .	14
2.1.4	Phase diagrams . . . . .	15
2.2	Thermodiffusion . . . . .	18
2.2.1	Fundamental theory . . . . .	18
2.2.2	Transient thermodiffusion . . . . .	23
2.2.3	Different coefficients used for thermodiffusion in binary mixtures . . . . .	26
2.3	Predictive models of thermodiffusion . . . . .	27
2.3.1	The case for binary gases . . . . .	27
2.3.2	The case for binary liquids . . . . .	28
<b>3</b>	<b>Methods</b>	<b>35</b>
3.1	Selection of concentrations for alloys . . . . .	35
3.1.1	Ag–Al . . . . .	35
3.1.2	Ag–Cu . . . . .	36
3.1.3	Ag–Al–Cu . . . . .	37
3.1.4	Al–In . . . . .	39
3.2	Sample cell . . . . .	40
3.2.1	Furnace cell . . . . .	40
3.2.2	Shear cell . . . . .	42
3.2.3	Temperature distribution . . . . .	43
3.3	Sample preparation . . . . .	45
3.4	X-ray imagery . . . . .	47
3.4.1	Image noise . . . . .	48
3.5	Energy-dispersive X-ray spectroscopy . . . . .	51

3.6	Temperature measurement and control . . . . .	52
3.7	Data analysis . . . . .	57
3.7.1	Digitally tracking the sample . . . . .	57
3.7.2	Assigning grey values along the samples . . . . .	58
3.7.3	Calculating concentration from grey value . . . . .	60
3.7.4	XRR image scale calibration . . . . .	63
3.7.5	Calculating the Soret coefficient . . . . .	64
3.7.6	Calculating the interdiffusion coefficient . . . . .	66
<b>4</b>	<b>Results</b>	<b>73</b>
4.1	Ag–Al . . . . .	73
4.2	Ag–Cu . . . . .	79
4.3	Ag–Al–Cu . . . . .	83
4.4	Al–In . . . . .	85
<b>5</b>	<b>Discussion</b>	<b>91</b>
5.1	Comparison to previous measurements . . . . .	91
5.1.1	Ag–Al . . . . .	91
5.1.2	Ag–Cu . . . . .	94
5.1.3	Ag–Al–Cu . . . . .	96
5.1.4	Al–In . . . . .	101
5.2	Connecting the results with theory . . . . .	103
5.2.1	Predictive models for thermodiffusion . . . . .	103
5.2.2	Possible theory behind thermodiffusion contributions . . .	112
5.2.3	Hints to possible theory of thermodiffusion based on the results . . . . .	118
5.3	Selecting values for the excess Gibbs energy . . . . .	119
5.3.1	The case of Ag–Al . . . . .	120
5.3.2	The case of Al–In . . . . .	122
5.3.3	Summary . . . . .	122
<b>6</b>	<b>Conclusions</b>	<b>125</b>
<b>A</b>	<b>Small calculations</b>	<b>129</b>
A.1	The derivation of the heat of transport $Q^*$ . . . . .	129
A.2	Soret coefficient calculation using mass ratio . . . . .	130
A.3	X-ray absorption related to concentration . . . . .	132
A.4	The link between results on time-dependence . . . . .	133
<b>B</b>	<b>Data tables</b>	<b>137</b>
B.1	Ag–Al . . . . .	137
B.1.1	Figure 4.5 . . . . .	137
B.1.2	Figure 4.6 . . . . .	137
B.2	Ag–Cu . . . . .	138
B.2.1	Figure 4.12 . . . . .	138
B.3	Ag–Al–Cu . . . . .	138
B.3.1	Figure 4.14 . . . . .	138
B.4	Al–In . . . . .	140
B.4.1	Figure 4.19 . . . . .	140
	<b>Bibliography</b>	<b>143</b>



*CONTENTS*

v

<b>Publications</b>	<b>157</b>
<b>Acknowledgements</b>	<b>159</b>
<b>CV</b>	<b>161</b>
<b>Declaration of authorship</b>	<b>163</b>



# List of Figures

1.1	Portraits of the two pioneers of thermodiffusion. . . . .	2
2.1	The relation between the Gibbs energy and chemical potential. . .	13
2.2	Graphical explanation of the derivation of a phase diagram. . . .	16
2.3	Geometric explanation of eq. (2.35). . . . .	16
2.4	The Gibbs energy for a mixture with a miscibility gap. . . . .	17
2.5	Plot of eq. (2.74) as a function of $z$ and $t$ . . . . .	25
3.1	Calculated phase diagram of Ag–Al. . . . .	36
3.2	Calculated phase diagram of Ag–Cu. . . . .	37
3.3	Calculated liquidus surface of ternary Ag–Al–Cu. . . . .	38
3.4	Calculated phase diagram of Al–In. . . . .	39
3.5	Digital render of the compact sample cell. . . . .	40
3.6	Digital render of the sample cell in an exploded and cut view. . .	41
3.7	XRR images from a shear cell experiment. . . . .	43
3.8	X-ray image of the sample cell used for measuring the temperature distribution. . . . .	44
3.9	Plots of the temperature distribution in the sample cell. . . . .	45
3.10	Two poorly annealed Al–In due to the liquid miscibility gap. . . .	46
3.11	Before heating and shortly after melting of a new Al–In sample cell.	47
3.12	Schematic of the X-ray setup. . . . .	48
3.13	Raw XRR image straight from the detector. . . . .	49
3.14	Reference image used for flat-field correction. . . . .	50
3.15	Histograms of grey values in fig. 3.14. . . . .	50
3.16	Grey value along the samples in fig. 3.20 with and without filtering.	51
3.17	Light microscopy imaging of a sample of $\text{Ag}_{43.1}\text{Al}_{43.1}\text{Cu}_{13.8}$ later analysed with EDXS. . . . .	52
3.18	Indirect measurements of phase transitions during melting and solidification. . . . .	54
3.19	Comparison between the sets of PID coefficients in eqs. (3.6) and (3.7). . . . .	56
3.20	Tracking of the samples in an XRR image. . . . .	57
3.21	Grey values at one of the sample ends in fig. 3.20. . . . .	58
3.22	Fit of eq. (3.9) onto the orange line in fig. 3.21. . . . .	59
3.23	Calculated concentrations along the samples in fig. 3.20. . . . .	60
3.24	Ratio between grey value change from thermal expansion and Soret effect. . . . .	63
3.25	Plot of eq. (3.21). . . . .	66

3.26	Concentration for different times with result from linear fit of eq. (2.74).	68
3.27	Relative error for different amounts of terms in eq. (3.24).	69
3.28	Fitting the interdiffusion coefficient to calculated data from eq. (2.74).	70
4.1	Concentration along a sample of $\text{Ag}_{25}\text{Al}_{75}$ at the steady state.	74
4.2	Concentration difference $\Delta c(t)$ along a sample of $\text{Ag}_{25}\text{Al}_{75}$ .	74
4.3	The slope of the concentration fit from the centre of a $\text{Ag}_{25}\text{Al}_{75}$ sample.	75
4.4	Concentration data for a sample of $\text{Ag}_{25}\text{Al}_{75}$ with the fit of eq. (2.74).	76
4.5	Soret coefficients for the measured concentrations of liquid Ag–Al at a mean temperature of 1017 K, accumulated from all experiments.	77
4.6	Interdiffusion coefficients for the measured concentrations of liquid Ag–Al at a mean temperature of 1017 K, accumulated from all experiments.	78
4.7	Soret and interdiffusion coefficients for liquid Ag–Al using different methods for analysing the measured data.	78
4.8	Thermoeffusion coefficients $D_T$ for liquid Ag–Al at 1017 K.	79
4.9	Indicated concentration along a sample of $\text{Ag}_{60}\text{Cu}_{40}$ at the steady state.	80
4.10	Indicated concentration difference $\Delta c(t)$ along a sample of $\text{Ag}_{60}\text{Cu}_{40}$ .	80
4.11	XRR image from the thermoeffusion experiment of liquid $\text{Ag}_{60}\text{Cu}_{40}$ , revealing that sample B was not properly compressed.	81
4.12	Concentration along two sheared samples of $\text{Ag}_{60}\text{Cu}_{40}$ .	82
4.13	The slope of the concentration fit from the centre of a sample of liquid $\text{Ag}_{43.1}\text{Al}_{43.1}\text{Cu}_{13.8}$ .	84
4.14	Concentration along two sheared samples of $\text{Ag}_{43.1}\text{Al}_{43.1}\text{Cu}_{13.8}$ .	85
4.15	Concentration along a sample of $\text{Al}_{85}\text{In}_{15}$ at the isothermal and at the end of the experiment.	86
4.16	Concentration difference $\Delta c(t)$ along a sample of liquid $\text{Al}_{85}\text{In}_{15}$ .	87
4.17	The slope of the concentration fit from the centre of a sample of $\text{Al}_{85}\text{In}_{15}$ .	87
4.18	Concentration data for a sample of $\text{Al}_{85}\text{In}_{15}$ with the fit of eq. (2.74).	88
4.19	Soret, interdiffusion and thermoeffusion coefficients for liquid Al–In at a mean temperature of 1110 K using different methods for analysing the measurement data.	89
5.1	Cut-out of the phase diagram of Ag–Al, with temperatures from McKee and Stark indicated.	92
5.2	Concentration across the two sheared samples of $\text{Ag}_{17.6}\text{Al}_{68.6}\text{Cu}_{13.8}$ from Sondermann et al. [141].	97
5.3	Measured $\frac{\nabla c_i}{\nabla T}$ for Ag–Al–Cu and its binary constituents.	99
5.4	Concentration across the samples of $\text{Al}_{85}\text{In}_{15}$ and $\text{Al}_{78}\text{In}_{22}$ at the end of the experiment.	102
5.5	Concentrations of the investigated Al–In samples and the temperature subjected along them.	103
5.6	Calculated Soret coefficients for liquid Ag–Al with different models at a mean temperature of 1017 K.	105
5.7	Calculated Soret coefficients for liquid Ag–Cu with different models at a mean temperature of 1099 K.	106

5.8	Calculated Soret coefficients for liquid Al–In with different models at a mean temperature of 1110 K. . . . .	107
5.9	Calculated TDF from the approximation of eq. (2.97) and the actual eq. (2.31). . . . .	108
5.10	Calculated Soret coefficients for liquid Ag–Al with deviated parameters at a mean temperature of 1017 K. . . . .	109
5.11	Deviations in parameters for the two accurate predictions in fig. 5.10. . . . .	110
5.12	Calculated Soret coefficients for liquid Ag–Al with deviated parameters where within 100 % of the measurements at 1017 K. . . . .	111
5.13	Deviations in parameters used for predictions in fig. 5.12. . . . .	112
5.14	The derivative of the excess volume of the liquid Ag–Al system from Brillo et al., plotted over the Soret coefficients measured at 1017 K. . . . .	114
5.15	The measured Soret coefficients for Ag–Al, Ag–Cu, and Al–In plotted over their respective TDF. . . . .	115
5.16	Ternary TDF $\phi_{ij}$ for liquid Ag–Al–Cu at 1089 K. . . . .	117
5.17	Excess Gibbs energy $G_E$ for liquid Ag–Al, its two first concentration-derivatives, and TDF, all calculated for a temperature of 1017 K. . . . .	121
5.18	Excess Gibbs energy $G_E$ for liquid Al–In, its two first concentration-derivatives, and TDF, all calculated for a temperature of 1110 K. . . . .	123
5.19	Different calculated phase diagrams for the Al–In system, shown in the region where the measurements on $\text{Al}_{85}\text{In}_{15}$ and $\text{Al}_{78}\text{In}_{22}$ were performed. . . . .	124
A.1	Comparison between the equations for time-dependent concentration from Bierlein and Costesèque et al. . . . .	135



# List of Tables

3.1	List of metals used. . . . .	45
3.2	Sample lengths measured with different methods. . . . .	64
4.1	Fitted concentration gradient $\frac{\Delta c_{\text{Ag}}}{\Delta T}$ and Soret coefficient $S_T$ to the concentration data from the thermodiffusion experiment on $\text{Ag}_{60}\text{Cu}_{40}$ . . . . .	82
4.2	Fitted $\frac{\Delta c_i}{\Delta T}$ to the concentration data from the thermodiffusion experiment on $\text{Ag}_{43.1}\text{Al}_{43.1}\text{Cu}_{13.8}$ . . . . .	84
4.3	Frame-invariant ternary Soret coefficients for $\text{Ag}_{43.1}\text{Al}_{43.1}\text{Cu}_{13.8}$ as calculated with eq. (2.68) with the concentration gradients from table 4.2. . . . .	85
5.1	Liquidus and solidus temperatures for $\text{Ag}_2\text{Al}_{98}$ from different thermodynamic evaluations. . . . .	92
5.2	Fitted $\frac{\Delta c_i}{\Delta T}$ to the concentration data from the thermodiffusion experiment on near-eutectic $\text{Ag}_{17.6}\text{Al}_{68.6}\text{Cu}_{13.8}$ as conducted by Sondermann et al. [141]. . . . .	97
5.3	Frame-invariant ternary Soret coefficients for samples of near-eutectic $\text{Ag}_{17.6}\text{Al}_{68.6}\text{Cu}_{13.8}$ as calculated with eq. (2.68) with the concentration gradients from table 5.2. . . . .	98
B.1	Soret coefficients for the measured concentrations at a mean temperature of 1017 K. . . . .	137
B.2	Interdiffusion coefficients for the measured concentrations at a mean temperature of 1017 K. . . . .	137
B.3	Concentrations for $\text{Ag}_{60}\text{Cu}_{40}$ . . . . .	138
B.4	Concentrations in sample A of $\text{Ag}_{43.1}\text{Al}_{43.1}\text{Cu}_{13.8}$ . . . . .	139
B.5	Concentrations in sample B of $\text{Ag}_{43.1}\text{Al}_{43.1}\text{Cu}_{13.8}$ . . . . .	139
B.6	Soret coefficients for the measured concentrations at a mean temperature of 1110 K. . . . .	140
B.7	Interdiffusion coefficients for the measured concentrations at a mean temperature of 1110 K. . . . .	141





# Acronyms

**BCC** body-centred cubic.

**BN** boron nitride.

**DCMIX** Diffusion Coefficients in MIXtures.

**EDXS** energy-dispersive X-ray spectroscopy.

**FCC** face-centred cubic.

**GUI** graphical user interface.

**HCP** hexagonal close-packed.

**ISS** International Space Station.

**LJ** Lennard-Jones.

**MD** molecular dynamics.

**NEMD** non-equilibrium molecular dynamics.

**NEUF-DIX** Non-EqUilibrium Fluctuations occurring during Diffusion processes in multi-component complex fluids.

**NRTL** non-random two-liquid.

**ODI** optical digital interferometry.

**PID** proportional–integral–derivative.

**RK** Redlich-Kister.

**SAC** Sn–Ag–Cu.

**SEM** scanning electron microscope.

**TC1** thermocouple 1.

**TC2** thermocouple 2.

**TDF** thermodynamic factor.

**XRR** X-ray radiography.



# Chapter 1

## Introduction

### 1.1 History

**T**HERMODIFFUSION, or the *Diffusion between unequally heated locations of equally composed solutions*, as its discoverer first titled it,<sup>1</sup> was discovered by C. Ludwig (see fig. 1.1a) in 1856 [1]. He published a short, one-page report of his findings in the *Sitzungsberichte der Kaiserlichen Akademie der Wissenschaften*. Therein, he described how he had filled an inverted U-shaped glass tube with salt water, dipped one leg into boiling water, the other into melting ice, and left it like that for 7 days. While the salt crystallised in the tube, reducing the mean salinity of the water over time, he also measured a concentration difference between the hot and cold sides, with 4.31 % and 4.75 % at each side respectively. Some of the salt had in other words migrated from the hot to the cold side. He did not investigate the observation further, and never again published anything on the topic.

Twenty years after Ludwig’s first discovery, and without being aware of the work of Ludwig, C. Soret (see fig. 1.1b) performed the first systematic experiments on thermodiffusion, publishing several reports of experiments on the concentration distribution of salt solutions, the first of which he published in 1879, under the title ‘*On the state of equilibrium which an initially homogeneous saline solution, two parts of which are brought to different temperatures, assumes in terms of its concentration*’ [2, 3].<sup>2</sup>

With the mentioned scientific contributions, the field of thermodiffusion was established, and today also bears, among other names,<sup>3</sup> the name “Ludwig–Soret effect”. Over time, and perhaps acknowledging the systematic approach of Soret, or simply for nationalistic reasons, the name has been reduced to the “Soret effect”.

Today, we define thermodiffusion as

---

<sup>1</sup>Originally published in German with the title ‘*Diffusion zwischen ungleich erwärmten Orten gleich zusammengesetzter Lösungen*’.

<sup>2</sup>Originally published in French with the title ‘*Sur l’état d’équilibre que prend au point de vue de sa concentration une dissolution saline primitivement homogène dont deux parties sont portées à des températures différentes*’.

<sup>3</sup>Today, the effect is often labelled under less personalised names, like “thermodiffusion” (especially in liquids, and the term that will be used in this work), “thermomigration” (in solids) and “thermophoresis”/“thermotransport” (for individual particles, like colloids).



(A) Lithography of Carl Ludwig from 1856, the very year he reported his discovery of thermodiffusion. Courtesy of the Wellcome Collection [4] (public domain).



(B) Photography of Charles Soret, dated 'around 1880'. Courtesy of Bibliothèque de Genève [5] (public domain).

FIGURE 1.1: Portraits of the two pioneers of thermodiffusion.

the separation of the components of a mixture toward the hot/cold regions of a domain that is characterized by a nonuniform temperature distribution. [6]

After reading Soret's findings (unaware of Ludwig's publication), the Dutch scientist J. H. van't Hoff in 1885 explained the effect as a natural cause of the osmotic pressure in the mixture with the temperature gradient [7]. The first new experiments on thermodiffusion, other than the ones by Ludwig and Soret, were published in 1890, where P. van Berchem, citing the original publications of both Ludwig and Soret, described experiments on thermodiffusion in mixtures of hydrochloric acid and ammonia in water, using a similar apparatus to the one used by Soret, keeping the hot side at 50 °C and the cold side at 15 °C, letting the experiment diffuse for up to 42 days [8]. In 1894, S. Arrhenius made his own experiments on nine different diluted acids, being able to rebuke Hoff's theory by measuring different separations for the same temperature difference, but with different mixtures. [9]. The total interest in thermodiffusion was still low, however, and even in the obituary for Soret in *Nature* after his death in 1904, thermodiffusion was not even mentioned, focusing instead on his work in the field of crystallography [10].

During the first decades of the 20<sup>th</sup> century, thermodiffusion was again rediscovered, this time for gaseous systems, where using Maxwell-Boltzmann theory, D. Enskog and S. Chapman independently discovered thermodiffusion for a gas of hard-spheres, and found analytical descriptions for these separation factors [11–13]. This was in itself a rediscovery, as J. Tyndall in 1870 had observed that dust in a room would migrate away from a hot tube, although without any knowledge of the result by Ludwig or without any further investigation on the effect [14].

The focus on thermodiffusion had a large increase after the invention of the

so-called Clusius-Dickel-column in 1938, where Clusius and Dickel discovered that if combining thermodiffusion and sedimentation in a vertical column, one could purify gas mixtures, enabling them to enrich isotopes of neon and chlorine [15, 16]. This would prove useful during the Second World War, when this method was used to enrich uranium isotopes in gaseous form for the Manhattan Project [17].

During and after the war, the science on thermodiffusion matured, with more focus on the theoretical background of the effect, as well as equations describing the transient behaviour [13, 18–20]. Experiments have since been performed on aqueous salt solutions, molten salt systems, liquid metals, solid metals, gases, liquid organic systems, and glassy liquids, all of which observe the effect and influence of thermodiffusion [21–28]. It has been proposed that the effect of thermodiffusion has played a role in some of the most fundamental processes of the universe, such as the origin of life, and the convection in stars, the ionosphere, and in the Earth’s mantle [29–32].

Today, the biggest portion of scientific output on thermodiffusion is focused on organic systems, with several campaigns on the International Space Station (ISS) having been conducted to date, the most recent of which being the Diffusion Coefficients in MIXtures (DCMIX) project [33]. After establishing experiments with dodecane–isobutylbenzene–tetralin, later DCMIX campaigns investigated a system with a miscibility gap. Whereas thermodiffusion in most mixtures lead to a concentration separation of up to an atom-percent per kelvin of temperature difference, ground experiments on thermodiffusion in organic systems with miscibility gaps have shown how the concentration separation diverges towards the critical limit [26, 34–37]. For the coming round of experiments in space, the focus is centred on such critical mixtures, in addition to glass-forming systems [33, 38]. For a glass-forming system, when it gets cooled down to the glass transition, the viscosity by definition increases [28]. As estimated by the Stokes-Einstein relation, the diffusion in a liquid is approximately inversely proportional to the viscosity [39–41], so conversely the interdiffusion reciprocally decreases. Measurements of polystyrene in toluene at the glass transition by Rauch and Köhler showed that the thermodiffusion coefficient decreased at the same rate as the interdiffusion coefficient, and the Soret coefficient was thus insensitive to the glass transition [28]. Non-equilibrium molecular dynamics (NEMD) simulations on a glass-forming binary Lennard-Jones (LJ) mixture by Vaibhav et al. showed however that the interdiffusion slowed down quicker than the thermodiffusion, resulting in larger Soret coefficients [42]. For these reasons, investigations of thermodiffusion in glassy liquids is one of the topics of interest in the upcoming microgravity experiments of the Non-Equilibrium Fluctuations occurring during Diffusion processes in multi-component complex fluids (NEUF-DIX) project [38].<sup>4</sup>

Through the decades, several models have been proposed in attempts to explain and predict the concentration separation from thermodiffusion [6, 43]. These models are however rarely applied to the organic mixtures extensively investigated for the DCMIX project, and then only in fundamental simulations predicting only the qualitative properties of thermodiffusion, like direction of migration for the different components [44]. The comparison of models to experimental data may be easier for simpler systems that more resemble modelled liquids, like liquid binary alloys.

---

<sup>4</sup>The project is also known under the name *Giant Fluctuations*.

## 1.2 Alloys

Thermodiffusion is especially relevant in liquid alloys, as their high melting points involve high temperatures and large temperature gradients [45]. In metals, thermodiffusion can affect solders and the manufacturing of integrated circuits, it has been employed for crystal growth, and has recently been shown to be of use in creating metallic nanowires [46–50].

The measurement of thermodiffusion in liquid alloys is difficult, due to the high melting temperatures requiring thermal insulation that makes direct observation difficult. In previous experimental works on binary alloys, closed containers with columns of the liquid were submitted to a thermal gradient for a certain amount of time, then quickly cooled, and finally analysed in the solid state [51–53]. To avoid changes of the concentration gradient during solidification, some experiments instead used a shear cell technique, where the sample is split up into segments after the annealing time while still in the liquid state [54, 55]. A drawback of both these methods is that possible bubbles in the melt cannot be detected. The presence of bubbles may lead to Marangoni convection, which can disturb diffusion measurements [56, 57]. In interdiffusion measurements on liquid alloys, such bubbles have been shown to increase the apparent interdiffusion coefficient by a factor of two [58]. Also without bubbles, Marangoni convection can be induced from the temperature gradient of the interfacial tension between the liquid alloy and the furnace [59]. Recently, *in situ* X-ray radiography (XRR) has been shown to allow time- and space-resolved measurements of thermodiffusion in liquid alloys, where bubbles or free surfaces can be directly detected during the experiment [60]. Using this time-resolved method it is also possible to determine the coefficients for interdiffusion and thermodiffusion simultaneously. This method is however dependent on using only two components, and the contrast is dependent on the ratio between the atomic numbers of the components, making the analysis of mixtures of similar-mass components impossible. For the same reason, mixtures with high mass ratio between the components are especially suited for XRR, due to the high contrast between the two components in the X-ray spectrum [61–63].

Aluminium alloys are of great importance in the industry, with a huge number of alloys of various amounts of components being in use [64, 65]. With its low atomic number, it is one of the lightest naturally occurring metals. Combined with the abundance of the element on Earth and its low reactivity, these aspects underscore its significance in various industrial contexts.

With this industrial popularity, aluminium, and alloys containing it, have been subject to a lot of research [64]. This makes aluminium alloys a good basis for investigating the thermodiffusion in liquid alloys, as many thermophysical properties are already measured for the different alloys [66]. This makes it possible to analyse the results from thermodiffusion measurements in the context of the models for it, and to compare the interdiffusion coefficient attained from the transient concentration across the sample cell with previously reported values.

For this thesis, thermodiffusion in the liquid binary alloys Ag–Al and Ag–Cu will be investigated, as well as the ternary Ag–Al–Cu. The interdiffusion coefficients for the constituent binaries of Ag–Al–Cu (i.e., Ag–Al, Ag–Cu, and Al–Cu), as well as the eutectic composition of the ternary itself, have been investigated in detail in the PhD thesis of Engelhardt [62]. Furthermore, the thermodynamic evaluation for the ternary with reassessments of its constituent

binaries were performed by Witusiewicz et al. [67, 68]. This gives the opportunity to calculate the enthalpy, chemical potential, and thermodynamic factor (TDF) of the alloys. Finally, the density has been investigated over the entire binary composition range for all the binaries by Brillo et al. in various publications [69, 70].

In addition, selected alloys of the binary Al–In system will be investigated in this thesis. This system is particularly interesting from a scientific viewpoint, as it contains a large miscibility gap in the liquid range [71]. A miscibility gap means that the TDF approaches zero, which due to the Darken equation then implies that the interdiffusion approaches zero [72]. The coefficient for the concentration separation from thermodiffusion, the Soret coefficient, is defined as  $S_T \equiv \frac{D_T}{D}$ , where  $D_T$  is the thermodiffusion coefficient, and  $D$  the interdiffusion coefficient [6]. For a non-diverging, non-zero thermodiffusion coefficient, this would imply a diverging Soret coefficient when approaching the miscibility gap. This has previously been shown to be the case in organic critical mixtures [26, 34, 35], but has so far not been investigated for liquid alloys.

### 1.2.1 Ag–Al

For the first set of thermodiffusion experiments on liquid alloys in this thesis, the Ag–Al system was selected. The addition of silver to several aluminium alloys heightens the strength and hardenability [64].

The system has a high X-ray contrast, in part due to the different atomic numbers and mass densities between the two components, silver and aluminium, with densities of the pure liquids of approximately  $9.3 \text{ g cm}^{-3}$  and  $2.4 \text{ g cm}^{-3}$  respectively, slightly decreasing with increasing temperature [73–75].

With molar masses of  $107.87 \text{ g mol}^{-1}$  and  $26.982 \text{ g mol}^{-1}$ , the ratio between the molar masses of 4.00 is very high [76]. Almost all previous publications on liquid alloys are on binary systems where the atomic mass ratio of the two components is around two or less, such as Bi–Pb, Al–Cu, and Ag–Te [23, 53, 77]. The only exceptions so far are measurements on carbon<sup>5</sup> and trace amounts in a solvent [52, 78, 79]. The experimental data until now indicate that the Soret coefficient is generally dependent on the relative molecular weights of the species in the mixture [6]. Measuring the thermodiffusion in liquid Ag–Al for different concentrations therefore provides a new insight into the dynamics of thermodiffusion in an atomic fluid with a high mass ratio.

Also compared to previous measurements on thermodiffusion in organic systems, the atomic mass ratio of Ag–Al is exceptionally high. In the extensive measurements of Hartmann et al. on thermodiffusion in binary mixtures composed of 23 different pure organic components, where the measurements of 77 different binary combinations were reported, the highest atomic mass ratio was at 2.93 for the dodecane–acetone system [80].

The interdiffusion coefficient of liquid Ag–Al has previously been investigated by Engelhardt et al. over a broad concentration range [81], making it possible to compare the observed transient concentration separation from thermodiffusion

---

<sup>5</sup>The measurements of thermodiffusion in Fe–C (atomic mass ratio 4.65) by Brenan and Bennett didn’t return any measurable separation of the two components, making the Soret effect undetectable although the temperature difference across the sample was as much as 255 K [78].

with the previously published interdiffusion coefficient. This makes liquid Ag–Al a fitting system to investigate the concentration dependence of the Soret coefficient as well. Furthermore, a potential mismatch in the transient behaviour can then highlight disturbances in the newly developed experimental setup.

### 1.2.2 Ag–Cu

Silver and copper are the elements with the highest electrical conductivity at room temperature [82]. The two components are used together with tin in ternary Sn–Ag–Cu (SAC) alloys for soldering, leading the movement to replace the toxic lead based solders [83]. The Ag–Cu liquid alloy is therefore an interesting subject in the analysis of thermodiffusion, as the Soret effect has been shown to be of importance in solders, where the hot liquid solder is in contact with the cold substrate [46].

Liquid Ag–Cu was found by Brillo et al. to have negligibly small excess volume [69], meaning that the total density  $\rho_{\text{Ag–Cu}}$  of the liquid alloy can be described by the densities of the two pure elements alone. In other words, the liquid Ag–Cu, at least when it comes to the volume of the mix, behaves ideally.

Compared to Ag–Al, the molar mass of copper being  $63.546 \text{ g mol}^{-1}$  [76], the atomic mass ratio of 1.70 is the lowest of all the binary alloys investigated in this thesis. The zero excess volume and the low atomic mass ratio makes this system interesting to compare to the other systems, to investigate how these factors may influence the Soret coefficient of the system.

With the density of copper being  $8.0 \text{ g cm}^{-3}$ , combined with the previously stated density of liquid silver of  $9.3 \text{ g cm}^{-3}$ , the Ag–Cu mixture is much denser than Ag–Al, and thus darker under X-ray irradiation [84]. With the densities of the two components being much more similar than those for Ag–Al, analysing the Ag–Cu system gives insight into the dynamics of thermodiffusion in alloys with comparable densities.

### 1.2.3 Al–Cu

Since the beginning of the industrial use of aluminium, copper has been the most common alloying element, as the addition of copper to aluminium increases the strength of the metal [64].

The phase diagram of Al–Cu shows many intermetallic phases, in addition to regions of face-centred cubic (FCC) and body-centred cubic (BCC) phases, as reported by Witusiewicz et al. [67]. The eutectic point is from the Gibbs energies reported by Witusiewicz et al. calculated to be for  $\text{Al}_{82.5}\text{Cu}_{17.5}$ , with a melting point of 820.6 K.

Thermodiffusion in Al–Cu has already been investigated, as reported in publications by Bhat [51, 77]. The experiments were reported to be conducted at around 950 K, with temperature differences ranging from 120 K to 250 K across the liquid samples. They measured the thermodiffusion in binary alloys on the aluminium rich side, with copper concentrations ranging from trace amounts to 33 wt.% (17 at.%), where the eutectic point of the binary Al–Cu system lies. This is a relatively low amount of copper for the binary, but as the ternary concentrations measured here also had low copper concentration, in addition to Bhat reporting that the Soret coefficient levelled off at 25 wt.% (12 at.%), this



was seen as sufficiently investigated, and no further investigation of the Al–Cu system was made for this thesis.

### 1.2.4 Ag–Al–Cu

As previously mentioned, binary Al–Cu alloys are particularly prevalent in industry, due to the increased strength relative to pure aluminium and its light weight. The addition of silver slightly increases the strength and hardenability further [64]. The alloy is also relevant as silver is added to industrial Al–Cu–Mg alloys for increased strength [64, 85].

The eutectic point of this alloy,  $\text{Ag}_{18.1}\text{Al}_{69.1}\text{Cu}_{12.8}$ , has a relatively low melting point of 773.6 K, compared to the melting points of the pure components Ag, Al, and Cu, of 1234.94 K, 933.47 K, and 1357.77 K, respectively [68, 86].

The density has been investigated by Brillo et al., albeit only for a few selected compositions [87]. From their data, with constant 10 at.% silver and varying the two other components, the density of the liquid ternary system could be described from the densities of its binary constituents, and with a negative excess volume in total [66, 87].

So far, to the best of my knowledge, there has only been one reported measurement on thermodiffusion in liquid ternary alloys, with a quick investigation of liquid Bi–Pb–Sn by Winter and Drickamer, with fixed 50 at.% tin together with varying fractions of lead and bismuth [23]. They reported in a graphical description only a decreasing effect of thermodiffusion with respect to increasing bismuth concentration, with no information about the temperature or duration of the experiment. An investigation of thermodiffusion in liquid Ag–Al–Cu will therefore be the first detailed investigation into the thermodiffusion of a liquid ternary alloy, and the movement of its components.

### 1.2.5 Al–In

The binary Al–In system is scientifically interesting due to having a miscibility gap in the liquid state between indium concentrations from 4.8 at.% to 87.2 at.% [71]. Also in the solid state, aluminium and indium do not dissolve into the other component. If the alloy is mixed in the miscible liquid state (e.g., above the miscibility gap), cooling it down will make it separate again, and it is therefore practically impossible to get a homogenous sample of the solid Al–In alloy. This inhomogeneity makes liquid immiscible alloys of industrial interest, making it possible to utilise the different properties of the two phases of the solid alloy, such as for electrical switches and for self-lubricating bearings [88].

Indium, and alloys containing it, are especially interesting in the liquid state, as indium and generally alloys thereof have low melting points, making them applicable as agents for liquid metal cooling purposes, such as in nuclear reactors or electronic devices [89–91]. Especially in cases where the liquid metal is used as a cooling agent due to the very high heat conductivity of metals, thermodiffusion may play a significant role, as the heating circuit by definition introduces regions of high and low temperature in the liquid, where especially in immiscible systems a high concentration gradient can be expected.

Until now, thermodiffusion in immiscible liquid alloys has not been investigated, although the slowing down of the interdiffusion coefficient itself has been previously observed in other liquid alloys [92, 93].



# Chapter 2

## Theory

### 2.1 Thermodynamics

#### 2.1.1 Gibbs energy

##### Background<sup>1</sup>

A system that undergoes a change, from an initial to a final steady state, does so because the initial state is unstable relative to the final state [94]. The stability of a system is determined by its Gibbs energy,  $G$ , defined as

$$G = U + pV - TS, \quad (2.1)$$

where  $U$  is the internal energy of the system,  $p$  is the pressure,  $V$  is the volume,  $T$  is the absolute temperature, and  $S$  is the entropy.

The internal energy  $U$  term describes the energy from the particles in the system: the movements, vibrations, rotations, interactions, and bonds between the particles. The  $pV$  term describes the work required to place the system in space, by the energy needed to displace the volume  $V$  under pressure  $p$  to place our system there in the first place. The  $TS$  term describes the energy associated with the randomness of the system. The product represents the amount of energy that is unavailable as mechanical work, but only as heat. In a thermodynamic process, the system tends to increase the entropy, or disorder. Therefore, the energy associated to this disorder ( $TS$ ) increases, and is subtracted from the other energy terms ( $U + pV$ ) in the Gibbs energy to account for the “unusable” energy, giving the net amount of energy available to do work. This is why the Gibbs energy before often was called the “Gibbs free energy” [94].

Often,  $U + pV$  is collected into the term *enthalpy*,  $H$ , or the *heat content* of the system:

$$H = U + pV. \quad (2.2)$$

For liquids, for which this work is focused on, the internal energy is much greater than the  $pV$  term, so an often used approximation is [95]

$$H \approx U. \quad (2.3)$$

---

<sup>1</sup>Parts of this subsection are based on the book *Phase transformations in metals and alloys* by Porter et al. [94].

Our system is at equilibrium when the system stops changing, the previously mentioned *steady state*. For this system, the Gibbs energy is minimised, and it has no impetus to do any further change, as no more energy can be released. At this state,

$$dG = 0. \quad (2.4)$$

### The description of the Gibbs energy in mixtures

In mixtures, the total Gibbs energy is represented as the sum of three parts,

1. the pure part,  $G_0$ , which is the contribution from the pure components in the mix, weighted for their relative molar concentration  $c_i = \frac{N_i}{\sum_i N_i}$ , with  $N_i$  being the amount of particles of component  $i$ . This contribution is temperature dependent, and different for different phases of the component, like the liquid, face-centred cubic (FCC), and body-centred cubic (BCC) phases. In a mixture of multiple components with index  $i$ , the total pure Gibbs energy is

$$G_0 = \sum_i c_i G_{0i}, \quad (2.5)$$

where the Gibbs energy for the pure component  $i$ ,  $G_{0i}$ , is given as a function of the absolute temperature  $T$ ,

$$G_{0i} = a + bT + cT \ln T + \sum_n d_n T^n, \quad (2.6)$$

where the parameters  $a$ ,  $b$ ,  $c$ , and any higher order parameters  $d_n$  which may be described are numerical values fitted to experimental data, and as many parameters as is needed are defined to fit the data accurately. These parameters are standard values, and readily available for all natural elements [86].

2. the ideal part,  $G_i$ , which is the contribution from the ideal mixing of the components. “Ideal” here means that the enthalpy does not change ( $\Delta H = 0$ ), meaning that there is no interaction between the components, and therefore all the change in Gibbs energy comes from the  $-T\Delta S$  term:

$$G_i = -T\Delta S = RT \sum_i c_i \ln c_i, \quad (2.7)$$

where  $R$  is the molar gas constant.

3. the excess part,  $G_E$ , which describes the deviation from the ideal behaviour (no interaction between the atoms), which would simply have been  $G_0 + G_i$ . Each mix behaves a bit differently, and this deviation from an ideal mix is described in the excess Gibbs energy. As it describes some experimental, non-idealistic behaviour, it has no universal closed form, but is often modelled as a polynomial function. No matter the representation, it is important that the excess Gibbs energy goes to zero for when the concentration approaches the limits ( $c = 0$  or  $c = 1$  for the binary case), where the mixture goes to being wholly pure of one single component, and a pure mixture by definition is ideal. In other words, for a binary mixture:

$$G_E(c = 0) = G_E(c = 1) = 0. \quad (2.8)$$

The excess Gibbs energy  $G_E$  will be treated in more detail later.

The total Gibbs energy for a mixture,  $G$ , is thus given as

$$G = G_0 + G_i + G_E. \quad (2.9)$$

The Gibbs energy is of great importance in thermodynamics, as it is used to calculate the thermodynamic factor (TDF), the phase diagram, the chemical potential, the activity coefficient, the enthalpy, and more [94].

### The different descriptions for the excess Gibbs energy

As the excess Gibbs energy describes some experimentally observed behaviour, it has no universal closed form, but is often modelled for binary mixtures as a Redlich-Kister (RK) polynomial [96], given by

$$G_E = c_A c_B \sum_v (c_A - c_B)^v L_v(T) \quad (2.10)$$

for a binary mix of  $A$  and  $B$ , and where  $L_v(T)$  is a temperature dependent factor, often given as  $L_v(T) = A_v + B_v T$ , but sometimes with higher order parameters, analogue to eq. (2.6). For ternary mixtures, the description is expanded to the sums of the parts from all combinations of binaries, plus a new excess part for the ternary mix,

$$\begin{aligned} G_E = & c_A c_B \sum_v (c_A - c_B)^v L_{vAB}(T) \\ & + c_A c_C \sum_v (c_A - c_C)^v L_{vAC}(T) \\ & + c_B c_C \sum_v (c_B - c_C)^v L_{vBC}(T) \\ & + c_A c_B c_C (c_A L_{0ABC} + c_B L_{1ABC} + c_C L_{2ABC}). \end{aligned} \quad (2.11)$$

The RK polynomial is a fitted power series, where any deviation from the experimental data is mitigated by adding more and more terms of increasing order. This is arguably not physical, and the number of terms should be reduced to a minimum needed to adequately describe the thermodynamic behaviour, so that higher-order oscillations are not introduced, which get magnified for higher-order derivatives [97].

In an attempt to represent the excess Gibbs energy as a closed-form expression in liquid mixtures, the so-called Wilson model was developed [98]. Based on Flory-Huggins-theory, it models a binary solution of components  $A$  and  $B$ , and describes the excess Gibbs energy for the binary mixture as

$$G_E = RT(-c_A \ln[1 - \lambda_{BA} c_B] - c_B \ln[1 - \lambda_{AB} c_A]), \quad (2.12)$$

where the values  $\lambda_{AB}$  and  $\lambda_{BA}$  are temperature-dependent parameters fitted to the experimental data.

The Wilson equation is not able to model liquids with miscibility gaps, which is where liquids will refuse to mix due to the Gibbs energy having a

local minimum.<sup>2</sup> For this case, the non-random two-liquid (NRTL) model was developed, which gives the excess Gibbs energy for a binary mixture as [99]

$$G_E = RTc_Ac_B \left( \frac{\tau_{BA}\Lambda_{BA}}{c_A + c_B\Lambda_{BA}} + \frac{\tau_{AB}\Lambda_{AB}}{c_B + c_A\Lambda_{AB}} \right), \quad (2.13)$$

with

$$\tau_{AB} = \frac{g_{AB} - g_{BB}}{RT} \quad (2.14)$$

$$\tau_{BA} = \frac{g_{BA} - g_{BB}}{RT} \quad (2.15)$$

$$\Lambda_{AB} = e^{-\alpha\tau_{AB}} \quad (2.16)$$

$$\Lambda_{BA} = e^{-\alpha\tau_{BA}}, \quad (2.17)$$

where  $g_{AB} - g_{BB}$  and  $g_{BA} - g_{BB}$  are linear functions of temperature, and  $\alpha$  is a constant, giving three variables to fit for a specific temperature, compared to two for the Wilson model. The NRTL model is derived from a theory of each molecule of each component  $A$  and  $B$  being surrounded by other molecules of both type  $A$  and  $B$ , where  $g_{AB}$  is the Gibbs energy in the interaction between a type  $A$  molecule with type  $B$  molecule,  $g_{BB}$  the interaction energy between molecule  $B$  and  $B$ , and so on.

### 2.1.2 Chemical potential

The chemical potential  $\mu$  is the Gibbs energy change of a mix due to a change in concentration [100]. Mathematically it is expressed as the derivative of the Gibbs energy with respect to the molar fraction  $c$ :

$$\mu = \frac{\partial G}{\partial c}. \quad (2.18)$$

It being a potential, it is a relative measure, so it is always relative to another Gibbs energy, typically the Gibbs energy of the pure material, i.e.,  $c = 1$ . We are often interested in the chemical potential of one of the components of the mixture, so if we have a binary mix of  $A$  and  $B$ , the partial chemical potential  $\mu_A$  is related to the total chemical potential by

$$\mu = c_A\mu_A + c_B\mu_B = c_A\mu_A + (1 - c_A)\mu_B. \quad (2.19)$$

From the two relations eqs. (2.18) and (2.19), it follows that the chemical potential and its partial properties can be graphically illustrated as the tangent of the Gibbs energy function at the concentration that the mixture is currently at, as shown in fig. 2.1. From this, it can be shown that the chemical potential for component  $A$  in a binary mixture of  $A$  and  $B$ , is equal to the result of the tangent where it crosses the vertical axis of  $c_A = 1$ :

$$\mu_A(c_A) = G(c_A) + (1 - c_A) \frac{\partial G}{\partial c_A}. \quad (2.20)$$

---

<sup>2</sup>See section 2.1.4 for more on miscibility gaps.

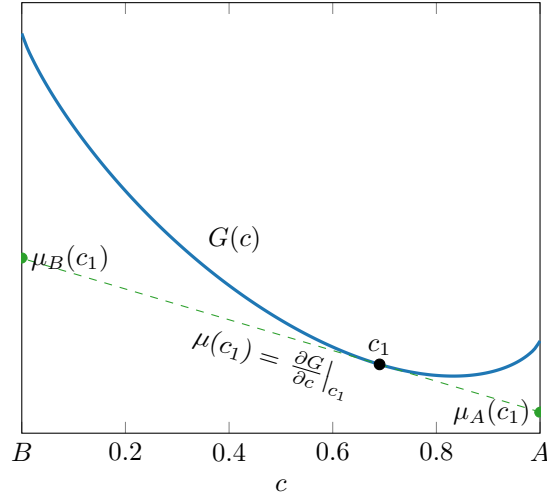


FIGURE 2.1: The relation between the Gibbs energy and chemical potential.

With the description of the Gibbs energy from its ideal, pure, and excess parts in eq. (2.9), eq. (2.20) can be separated for the different Gibbs energy contributions, into

$$\begin{aligned}
 \mu_A = & c_A G_{0A} + (1 - c_A) G_{0B} \\
 & + RT(c_A \ln c_A + [1 - c_A] \ln[1 - c_A]) \\
 & + G_E \\
 & + (1 - c_A) \left( G_{0A} - G_{0B} \right. \\
 & \quad \left. + RT[\ln c_A - \ln\{1 - c_A\}] \right. \\
 & \quad \left. + \frac{\partial G_E}{\partial c_A} \right), \tag{2.21}
 \end{aligned}$$

which reduces to the expression

$$\mu_A = G_{0A} + RT \ln c_A + G_E + (1 - c_A) \frac{\partial G_E}{\partial c_A}. \tag{2.22}$$

The part  $G_{0A}$  is the constant term which sets the chemical potential of the component in the mixture relative to that of the pure component. This term is often ignored, and will also be so here from now on, especially since we often will work with the *derivative* of the chemical potential, where the constant term will fall away anyway.

If the excess Gibbs energy is zero, the chemical potential of component A reduces to

$$\mu_A = RT \ln c_A, \tag{2.23}$$

which is the chemical potential of an ideal mixture (as  $G_E = 0$  means we have an ideal system). The alloys analysed in this thesis do not behave ideally, so  $G_E \neq 0$ , and thus the chemical potential is described as

$$\mu_A = RT(\ln c_A + \ln \gamma_A), \tag{2.24}$$

where  $\gamma_A$  is the activity coefficient of component  $A$ , and then with eqs. (2.22) and (2.24) given as

$$RT \ln \gamma_A = G_E + (1 - c_A) \frac{\partial G_E}{\partial c_A}. \quad (2.25)$$

The activity coefficient  $\gamma_A$  describes how non-ideal the mixture is behaving.

The same development as in eqs. (2.20) to (2.25) for component  $A$  can be done for component  $B$ , resulting in the following relation for the activity coefficient  $\gamma_B$  for component  $B$ :

$$RT \ln \gamma_B = G_E - c_A \frac{\partial G_E}{\partial c_A}. \quad (2.26)$$

Combining eqs. (2.25) and (2.26), we end up with the relation

$$G_E = RT(c_A \ln \gamma_A + c_B \ln \gamma_B) \quad (2.27)$$

for a binary mixture. This brings us back to the beginning, when we get that the Gibbs energy is given by

$$\begin{aligned} G &= c_A G_{0A} + c_B G_{0A} \\ &\quad + RT(c_A \ln c_A + c_B \ln c_B) \\ &\quad + G_E, \end{aligned} \quad (2.28)$$

and therefore due to eq. (2.27)

$$\begin{aligned} G &= c_A G_{0A} + c_B G_{0B} \\ &\quad + c_A RT \ln c_A + c_A RT \ln \gamma_A \\ &\quad + c_B RT \ln c_B + c_B RT \ln \gamma_B, \end{aligned} \quad (2.29)$$

which when using eq. (2.24) simply gives

$$G = c_A G_{0A} + c_B G_{0B} + c_A \mu_A + c_B \mu_B. \quad (2.30)$$

This result shows what we already defined in the beginning of this section, where the chemical potential of component  $i$  was defined as the change in the Gibbs energy when changing the concentration. So the total Gibbs energy of the mixture is the energy from the pure components, plus the energy added by mixing the components together.

### 2.1.3 Thermodynamic factor

An important value related to the chemical potential and thus the Gibbs energy is the thermodynamic factor (TDF). For a binary system it is defined as

$$\phi = \frac{c_i(1 - c_i)}{RT} \frac{\partial^2 G}{\partial c_i^2}, \quad (2.31)$$

where  $G$  is the Gibbs energy and  $R$  is the molar gas constant, and it is invariant to which component  $i$  is used.



It is a value that appears in many different publications, and consequently also in many different forms, like<sup>3</sup>

$$\phi = 1 + \frac{\partial \ln \gamma_i}{\partial \ln c_i}, \quad (2.32)$$

$$\phi = 1 + \frac{c_i(1 - c_i)}{RT} \frac{\partial^2 G_E}{\partial c_i^2}, \quad (2.33)$$

and

$$\phi = \frac{c_i}{RT} \frac{\partial \mu_i}{\partial c_i}. \quad (2.34)$$

All these expressions are equal, and equally valid.

From especially eq. (2.33) it is apparent that in an ideally behaving mixture ( $G_E = 0$ ), the TDF is equal to 1 over the entire concentration range. Furthermore, also in a non-ideal mixture, the TDF is equal to 1 in the dilute limit ( $c_i = 0$  or  $c_i = 1$ ).

Some publications replace the molar gas constant  $R$  by the Boltzmann constant  $k_B$ , and therefore also use an atomic Gibbs energy [101, 102]. But as long as the Gibbs energy is given in  $\text{J mol}^{-1}$ , the molar gas constant should be used. Typically,  $R$  is used in the fields of chemistry and experimental physics, while  $k_B$  is used in theoretical physics.

### 2.1.4 Phase diagrams

As mentioned in section 2.1.1, the Gibbs energy of a system and its phases can be used to calculate the phase diagram. In fig. 2.2, adapted from Porter et al. [94], the Gibbs energies in the solid and liquid states of a model fully miscible binary mixture is shown, with its resulting phase diagram. The sub-figures show the Gibbs energy as a function of molar fraction for the solid (S, blue line) and liquid (L, orange line) phases for the arbitrary temperatures  $T_1$ ,  $T_2$ , and  $T_3$ , plus for the melting points for the two materials  $A$  and  $B$ ,  $T_m(A)$  and  $T_m(B)$  respectively. The molar fraction goes from  $c_A = 0$  (pure  $B$ ) to  $c_A = 1$  (pure  $A$ ). The last sub-figure is the resulting phase diagram, which is calculated by finding the common tangent between the Gibbs energies of the two phases, and has the different temperatures from the previous sub-figures indicated.

As the liquidus and solidus curves in the phase diagram are solved by finding the common tangent of the two Gibbs energy curves for the two phases, they are the solution to the set of equations

$$\begin{cases} \frac{\partial G_L(c_1, T)}{\partial c} = \frac{\partial G_S(c_2, T)}{\partial c} \\ G_S(c_2, T) - G_L(c_1, T) = \frac{\partial G_L(c_1, T)}{\partial c} \times (c_2 - c_1) \end{cases} \quad (2.35)$$

This comes from that the common tangent is the point where the slope is the same (first part of eq. (2.35)), and the difference in value is equal to the slope times displacement (second part of eq. (2.35)), shown graphically in fig. 2.3. Note that by the first part of eq. (2.35) and the definition of the chemical potential

<sup>3</sup>Equation (2.32) is sometimes written as  $\phi = 1 + c_i \frac{\partial \ln \gamma_i}{\partial c_i}$ , which is equivalent.

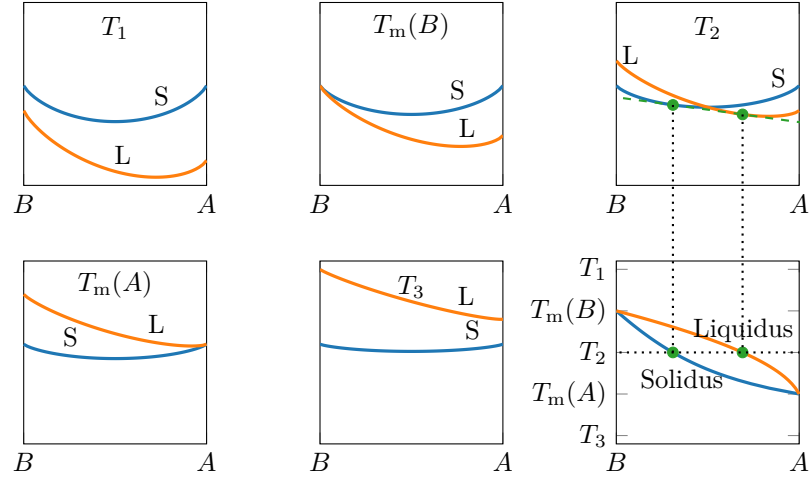


FIGURE 2.2: Graphical explanation of the derivation of a phase diagram.

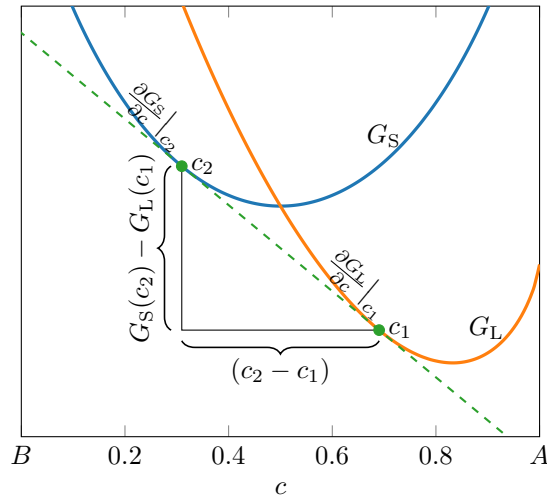


FIGURE 2.3: Geometric explanation of eq. (2.35).

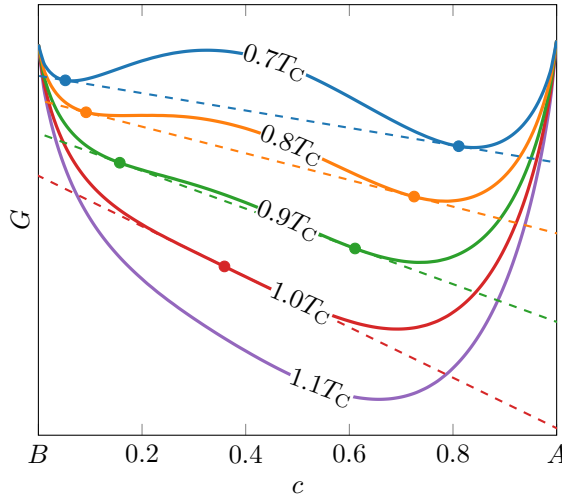


FIGURE 2.4: The Gibbs energy for a mixture with a miscibility gap.

in eq. (2.18), it follows that when two phases are in equilibrium, the chemical potentials of the two phases are equal.

A metal can have several different solid phases (FCC, BCC, etc.), and it is the state with the lowest Gibbs energy which is the stable state. So for a more complicated system than the one modelled in fig. 2.2 (where there were only two possible states, liquid and solid), there will be a Gibbs energy equation for each of the several states. Then the state with the lowest Gibbs energy is the stable one. If the Gibbs energy equation for another phase is crossing the reference phase Gibbs energy equation for some given temperature, there is an equilibrium of coexistence, and the liquidus and solidus concentrations at that temperature are found by finding the concentrations where the common tangent intersects the equations.

### Miscibility gap

Some mixtures will not mix if the temperature is not high enough, or the amount of added component is too high, and thus get saturated. This is called a miscibility gap, and is represented in the Gibbs energy function by it having an inflection point (a point where  $\frac{\partial^2 G}{\partial c^2} = 0$ ). This means that for a mixture with a miscibility gap, the Gibbs energy as a function of  $c$  has a common tangent with itself, instead of forming a common tangent with another phase, which was the case in fig. 2.3 [100]. The Gibbs energy at different temperatures is shown for a hypothetical mixture with a miscibility gap in fig. 2.4.

The top temperature where the miscibility gap still exists is called the critical point. Mathematically, it is the maximum temperature  $T_C$  where the inflection point in the Gibbs energy still exists, i.e., where the double-derivative of the Gibbs energy with respect to  $c$  still equates zero for some  $c_C$ , and therefore the

solution to the set of equations

$$\begin{cases} \frac{\partial^2 G(c_C, T_C)}{\partial c^2} = 0 \\ \frac{\partial^3 G(c_C, T_C)}{\partial c^3} = 0 \end{cases}, \quad (2.36)$$

solved for both  $c$  and  $T$ . Above the critical temperature  $T_C$ , the ideal contribution of the Gibbs energy is so large that the mixture doesn't have any common tangent with itself, and the mixture is fully miscible [94, 100].

## 2.2 Thermodiffusion

### 2.2.1 Fundamental theory

As described by Brownian motion, the particles in a system will move if the absolute temperature is non-zero. This movement is temperature dependent, as described by the Maxwell-Boltzmann distribution for statistical mechanics. When a temperature gradient appears over a system, the different temperature at different places will lead to different movement of the particles, and thus macroscopically lead to a concentration gradient. This mass flux is in a binary mixture described as

$$\mathbf{J}_{\text{th}} = -\rho c_0 c_1 D_T \nabla T, \quad (2.37)$$

the subscript “th” indicating “thermodiffusion”, where  $\rho$  is the density,  $D_T$  is the thermodiffusion coefficient, and  $c_0$  and  $c_1$  the concentrations of the two components. The thermodiffusion coefficient can depend on, and even change sign for different concentration and/or temperature [52, 80, 103].

In a binary mixture, the two concentrations by definition add up to unity:

$$c_0 + c_1 = 1, \quad (2.38)$$

so the factor  $c_0 c_1$  is often rather written as  $c_0(1 - c_0)$ . The factor is introduced so that  $\mathbf{J}_{\text{th}}$  is zero when the mixture is pure (either  $c_0 = 1$  and  $c_1 = 1 - c_0 = 0$ , or  $c_0 = 0$  and  $c_1 = 1$ ), as there can't be any de-mixing of components if there *is* no other component. This also allows the thermodiffusion coefficient to be non-zero at these endpoints, so that it does not need to vanish at  $c_0 = 0$  and  $c_0 = 1$ .

The induced concentration gradient will itself lead to interdiffusion, i.e., mixing in the system, described by Fick's 1<sup>st</sup> law as

$$\mathbf{J}_{\text{in}} = -\rho D \nabla c, \quad (2.39)$$

the subscript “in” indicating “interdiffusion”, where  $D$  is the interdiffusion coefficient. The interdiffusion coefficient also can depend on concentration, while its temperature dependence approximately follows an Arrhenius relation:

$$D(T) = D_0 e^{\frac{-E_A}{k_B T}}, \quad (2.40)$$

where  $D_0$  is a constant prefactor indicating the interdiffusion coefficient at infinite temperature,  $E_A$  the activation energy for interdiffusion, and  $k_B$  the Boltzmann constant. Still, the interdiffusion coefficient is always positive, as a negative coefficient from eq. (2.39) would imply spontaneous separation of the system,

which for a mixing process means reducing the entropy of the system, breaking the second law of thermodynamics.

The de-mixing and mixing are working against each other, with the total mass flux if no other mass-transport is present being the sum of the parts in eqs. (2.37) and (2.39):

$$\mathbf{J} = \mathbf{J}_{\text{th}} + \mathbf{J}_{\text{in}}. \quad (2.41)$$

For a system of two species, i.e., a binary mixture, the above situation is described mathematically as

$$\mathbf{J} = -\rho D \nabla c - \rho c_0 (1 - c_0) D_T \nabla T. \quad (2.42)$$

If the temperature gradient is sustained, the system will reach an equilibrium, where the de-mixing from thermodiffusion and mixing from interdiffusion is happening at the same rate, and is stable in its steady state. Then, no macroscopic mass flux is happening, i.e.,  $\mathbf{J} = 0$ , and the interdiffusion and thermodiffusion processes have reached an equilibrium, expressed as

$$D \nabla c = -D_T c_0 (1 - c_0) \nabla T. \quad (2.43)$$

This can then be rearranged to the following expression:

$$\nabla c = -\frac{D_T}{D} c_0 (1 - c_0) \nabla T, \quad (2.44)$$

where the ratio between the thermodiffusion and interdiffusion coefficients is called the Soret coefficient,

$$S_T \equiv \frac{D_T}{D} = -\frac{\nabla c}{\nabla T} \frac{1}{c_0 (1 - c_0)}. \quad (2.45)$$

For a one-dimensional binary sample in a linear temperature gradient, the total concentration difference across the sample from the total temperature difference  $\Delta T$  becomes

$$\Delta c_\infty = -S_T c_0 (1 - c_0) \Delta T \quad (2.46)$$

after reaching equilibrium. As can be seen from this, a positive Soret coefficient means that the reference component concentrates at the cold side, while the other component concentrates at the hot side. A reversal in  $S_T$  leads to a reversal of the concentration profile  $\Delta c$ . This also means that the Soret coefficient for the component with index 0 in the mixture is equal to the Soret coefficient with opposite sign for the component with index 1 in the same mixture. This follows from that the Soret effect gives a reduction of  $c_0$  in one end and therefore an equal and opposite increase in  $c_1$  in the same end, i.e., the same total concentration difference with opposite sign.

It should be noted that the Soret coefficient in a *binary* mixture is invariant to whether using atomic ratio or mass ratio for the concentration, as is shown in appendix A.2. We will use the atomic concentration in the entirety of this work.

## A theoretical approach

The formulation for the mass flux in eq. (2.42) does not only come from empirical reasoning, but can also be derived from irreversible thermodynamics theory [104,

105]. There, a flux is described as a linear combination of thermodynamic forces, with phenomenological coefficients as prefactors [104, 106]:

$$\mathbf{J}_i = \sum_j L_{ij} \mathbf{F}_j, \quad (2.47)$$

where  $\mathbf{J}_i$  is an independent flux component,  $L_{ij}$  are the phenomenological coefficients, and  $\mathbf{F}_j$  are the thermodynamic forces acting onto the system. The phenomenological coefficients  $L_{ij}$  are also known as the Onsager coefficients, where the diagonal ( $i = j$ ) coefficients are positive, and the rest follow the relation

$$L_{ij} = L_{ji}, \quad (2.48)$$

known as the Onsager reciprocal relations, which gathered its namesake the Nobel prize [107].

Excluding chemical reactions, viscous flow, and external forces, the phenomenological equations for our system with  $n$  components become [104, 106]

$$\mathbf{J}_q = -L_{qq} \frac{\nabla T}{T^2} - \sum_{j=0}^{n-2} L_{qj} \frac{\nabla(\mu_j - \mu_{n-1})}{T} \quad (2.49)$$

and

$$\mathbf{J}_i = -L_{iq} \frac{\nabla T}{T^2} - \sum_{j=0}^{n-2} L_{ij} \frac{\nabla(\mu_j - \mu_{n-1})}{T}, \quad (2.50)$$

where  $\mathbf{J}_q$  is the heat flux and  $\mathbf{J}_i$  is the mass flux of component  $i$ . The values  $\mu_j - \mu_{n-1}$  indicate that the chemical potential is calculated relative to the last component in the mixture, i.e., the last component with index  $n - 1$  is set as the reference.

For a binary system, the equations take the form

$$\mathbf{J}_q = -L_{qq} \frac{\nabla T}{T^2} - L_{q0} \frac{\nabla(\mu_0 - \mu_1)}{T} \quad (2.51)$$

and

$$\mathbf{J}_i = -L_{iq} \frac{\nabla T}{T^2} - L_{i0} \frac{\nabla(\mu_0 - \mu_1)}{T}. \quad (2.52)$$

The Gibbs-Duhem relation [99, 108]

$$\sum_i c_i \nabla \mu_i = 0 \quad (2.53)$$

in a binary mixture gives the relation

$$\nabla(\mu_0 - \mu_1) = \frac{1}{c_1} \nabla \mu_0. \quad (2.54)$$

Thus, eqs. (2.51) and (2.52) become

$$\mathbf{J}_q = -L_{qq} \frac{\nabla T}{T^2} - L_{q0} \frac{\nabla \mu_0}{c_1 T} \quad (2.55)$$

and

$$\mathbf{J}_0 = -L_{0q} \frac{\nabla T}{T^2} - L_{00} \frac{\nabla \mu_0}{c_1 T} \quad (2.56)$$

respectively, where we now have focused on the mass flux of component 0 only.

If we define two coefficients

$$D = \frac{L_{00}}{\rho c_1 T} \frac{\partial \mu_0}{\partial c_0} \quad (2.57)$$

and

$$D_T = \frac{L_{0q}}{\rho c_0 c_1 T^2}, \quad (2.58)$$

use the chain rule  $\nabla \mu_i = \frac{\partial \mu_i}{\partial c_i} \nabla c_i$ , and use that  $c_1 = 1 - c_0$  in a binary mixture, we get the equation for mass flux of component 0 in a binary mixture to be

$$\mathbf{J}_0 = -\rho D \nabla c_0 - \rho c_0 (1 - c_0) D_T \nabla T. \quad (2.59)$$

We have here defined the interdiffusion and thermodiffusion coefficients in eqs. (2.57) and (2.58), and gotten exactly the same expression as in eq. (2.42), using a theoretical approach with irreversible thermodynamics. Note that following the earlier statement that the diagonal entries of the Onsager coefficients have to be positive, the definition of the interdiffusion coefficient in eq. (2.57) proves that the interdiffusion coefficient cannot be negative. The only possibility to get a negative value for  $D$  is if the derivative of the chemical potential is negative, which only can happen if the Gibbs energy has an inflection point, which again means that the liquid is within a miscibility gap,<sup>4</sup> and a phase separation is driving the de-mixing instead.

If we use the same steps for the heat flux  $\mathbf{J}_q$  as we did to the mass flux in eq. (2.59), and define the coefficients

$$\lambda = \frac{L_{qq}}{T^2} \quad (2.60)$$

and

$$D_F = \frac{L_{q0}}{\rho c_0 c_1 T^2}, \quad (2.61)$$

we get the equation for heat flux in a binary mixture to be

$$\mathbf{J}_q = -\lambda \nabla T - \rho c_0 D_F T \left( \frac{\partial \mu_0}{\partial c_0} \right) \nabla c_0. \quad (2.62)$$

This is then a heat flux given by a concentration gradient, where concentration differences result in a temperature difference. This is known as the Dufour effect, discovered in 1872 by L. Dufour, and is the reciprocal of the Soret effect [109]. The Dufour coefficient  $D_F$  is defined very similarly to the thermodiffusion coefficient in eq. (2.58), and due to the Onsager relations in eq. (2.48), where we had

---

<sup>4</sup>See section 2.1.4.

that  $L_{q0} = L_{0q}$ , we can actually see that the Dufour coefficient is equal to the thermodiffusion coefficient:  $D_F = D_T$ . The coefficient  $\lambda$  is the well known heat conductivity, and indeed, just as for setting  $\nabla T = 0$  in eq. (2.59) gives Fick's 1<sup>st</sup> law for mass diffusion, setting  $\nabla c = 0$  in eq. (2.62) gives Fourier's law for heat conduction.

From eq. (2.62), it shows that in an experiment where a temperature gradient is applied, a concentration gradient results from the Soret effect, which itself results in a temperature change from the Dufour effect, etc. But this extra heat from the concentration gradient due to the Soret effect is on the order of  $10^{-3}$  K in liquids, and can therefore be safely ignored, which it most often is [59].

### Ternary mixtures

While binary systems allow for relatively simple equations, the real world is generally not that simple. Most systems in nature have a large amount of components and impurities, all interacting with each other.

In a ternary mixture, we have three concentrations,  $c_0$ ,  $c_1$ , and  $c_2$ . These by definition add up to unity:

$$c_0 + c_1 + c_2 = 1, \quad (2.63)$$

so the third concentration is often rewritten as  $c_2 = 1 - c_0 - c_1$ .

Now that there are two independent concentrations, there also are two independent thermodiffusion coefficients:  $D_{T,0}$  and  $D_{T,1}$ . There are now two independent mass fluxes,  $\mathbf{J}_0$  and  $\mathbf{J}_1$ , the mass fluxes of the two independent components in the mixture, defined as [110]

$$\mathbf{J}_0 = -\rho(D_{00}\nabla c_0 + D_{01}\nabla c_1 + [c_0(1 - c_0)D_{T,0} - c_0c_1D_{T,1}]\nabla T), \quad (2.64)$$

and

$$\mathbf{J}_1 = -\rho(D_{10}\nabla c_0 + D_{11}\nabla c_1 + [c_1(1 - c_1)D_{T,1} - c_0c_1D_{T,0}]\nabla T), \quad (2.65)$$

or, using matrix notation:<sup>5</sup>

$$\begin{pmatrix} \mathbf{J}_0 \\ \mathbf{J}_1 \end{pmatrix} = -\rho \begin{bmatrix} D_{00} & D_{01} \\ D_{10} & D_{11} \end{bmatrix} \begin{pmatrix} \nabla c_0 \\ \nabla c_1 \end{pmatrix} - \rho \begin{bmatrix} c_0(1 - c_0) & -c_0c_1 \\ -c_0c_1 & c_1(1 - c_1) \end{bmatrix} \begin{pmatrix} D_{T,0} \\ D_{T,1} \end{pmatrix} \nabla T. \quad (2.66)$$

We can see that the binary scalar interdiffusion coefficient  $D$  from eq. (2.42) has been replaced by a  $2 \times 2$  matrix  $\mathbf{D} = \begin{bmatrix} D_{00} & D_{01} \\ D_{10} & D_{11} \end{bmatrix}$ , and the concentration factor  $c_0(1 - c_0)$  has been replaced by another  $2 \times 2$  matrix we call  $\mathbf{C}$ :

$$\mathbf{C} = \begin{bmatrix} c_0(1 - c_0) & -c_0c_1 \\ -c_0c_1 & c_1(1 - c_1) \end{bmatrix}. \quad (2.67)$$

From this, it follows that there are two Soret coefficients for a ternary system,

---

<sup>5</sup>The author of the theoretical description used here applied square brackets for linear operators acting on vectors, and parentheses for the vectors themselves. I have here decided to use that same notation.



defined as [110]

$$\begin{bmatrix} S_{T,0} \\ S_{T,1} \end{bmatrix} = \mathbf{D}^{-1} \begin{pmatrix} D_{T,0} \\ D_{T,1} \end{pmatrix} = -\mathbf{C}^{-1} \begin{pmatrix} \frac{\nabla c_0}{\nabla T} \\ \frac{\nabla c_1}{\nabla T} \end{pmatrix}, \quad (2.68)$$

or, written a little nicer:

$$\begin{bmatrix} c_0(1-c_0) & -c_0c_1 \\ -c_0c_1 & c_1(1-c_1) \end{bmatrix} \begin{bmatrix} S_{T,0} \\ S_{T,1} \end{bmatrix} \nabla T = - \begin{pmatrix} \nabla c_0 \\ \nabla c_1 \end{pmatrix}. \quad (2.69)$$

Note that with this notation, if  $c_2 = 0$ , i.e.,  $c_1 = 1 - c_0$ , the system of equations in eq. (2.68) leads to the binary result that  $\nabla c_0 = -\nabla c_1$ . Also, in that binary-approaching case, the ternary Soret coefficient  $S_{T,i}$  approaches the binary Soret coefficient. Furthermore, in the pure limits, e.g.,  $c_0 = 1$ ,  $c_1 = c_2 = 0$ , both concentration gradients become  $\nabla c_0 = \nabla c_1 = 0$ , as one would expect.

With all this, the Soret coefficients and thermodiffusion coefficients in the matrices are invariant to whether using mass or molar fraction for the concentrations, just as for the binary system. The interdiffusion coefficients in  $\mathbf{D}$ , however, are *not* invariant. But since this work is submitted in the world of thermodiffusion scientists, the importance of being able to compare thermodiffusion coefficients with research groups using other frames of reference is worth not being easily able to do so for interdiffusion coefficients, which for us only serve as verification of the experiments anyway. Also, in the world of scientists studying interdiffusion in liquid metals, the molar fraction is the de facto standard anyway, so we can easily compare our measurements with them without any conversion [62, 63, 81, 111].

### 2.2.2 Transient thermodiffusion

Equations describing the transient concentration difference in a binary mixture as a function of time have been developed, applying several simplifications and assumptions to retrieve an analytical solution [20, 112–114].<sup>6</sup>

The equations base themselves off the fundamental mass conservation equation:

$$\rho \frac{\partial c}{\partial t} = -\nabla \cdot \mathbf{J}, \quad (2.70)$$

with the mass density  $\rho$ , molar concentration  $c$  and mass flux  $\mathbf{J}$ . Following the work by Costesèque et al., using the expression of the mass flux from eq. (2.42), assuming constant density, constant thermodiffusion and interdiffusion coefficients, and a small effect of thermodiffusion compared to interdiffusion, the mass conservation equation turns into

$$\frac{\partial c}{\partial t} = D \nabla^2 c + c_0(1-c_0) D_T \nabla^2 T. \quad (2.71)$$

<sup>6</sup>Note that in the publication by Bierlein, figure 1 is incorrect, and that they in their equation 20 actually pass by the end result from Costesèque et al., but in a very complicated form. The link between the different works is shown in appendix A.4.

With a linear temperature gradient,  $\nabla^2 T = 0$ , and therefore the expression in a one-dimensional sample reduces to simply

$$\frac{\partial c}{\partial t} = D \frac{\partial^2 c}{\partial z^2}. \quad (2.72)$$

Equation (2.72) is analogous to the so-called heat equation, and the solution with respect to concentration is thus a Fourier series. With the initial condition  $c(z, t \leq 0) = c_0$ , i.e., an initially perfectly mixed sample, in addition to boundary conditions for rigid walls at the sample ends  $z = 0$  and  $z = L$ , so that  $\mathbf{J} = 0$  there:

$$\frac{\partial c}{\partial z} + \frac{D_T}{D} c_0 (1 - c_0) \frac{\Delta T}{L} = 0, \quad (2.73)$$

the solution to eq. (2.72) with respect to concentration as a function of position  $z \in [0, L]$  and time  $t \in [0, \infty)$  is [113]

$$c(z, t) = c_0 - \Delta c_\infty \left( \frac{1}{2} - \frac{z}{L} - \frac{4}{\pi^2} \sum_{n=0}^{\infty} \frac{1}{[2n+1]^2} \cos \left[ \frac{\{2n+1\}\pi z}{L} \right] e^{-[2n+1]^2 t / \theta} \right), \quad (2.74)$$

where

$$\theta = \frac{L^2}{\pi^2 D} \quad (2.75)$$

is the characteristic time, with  $L$  being the sample length and again  $D$  being the interdiffusion coefficient. The steady-state concentration  $\Delta c_\infty$  is defined in eq. (2.46).

Note that eq. (2.72) is simply Fick's 2<sup>nd</sup> law, which is why the solution in eq. (2.74) is similar to for example the expression for the tracer concentration in self-diffusion experiments [115, 116].

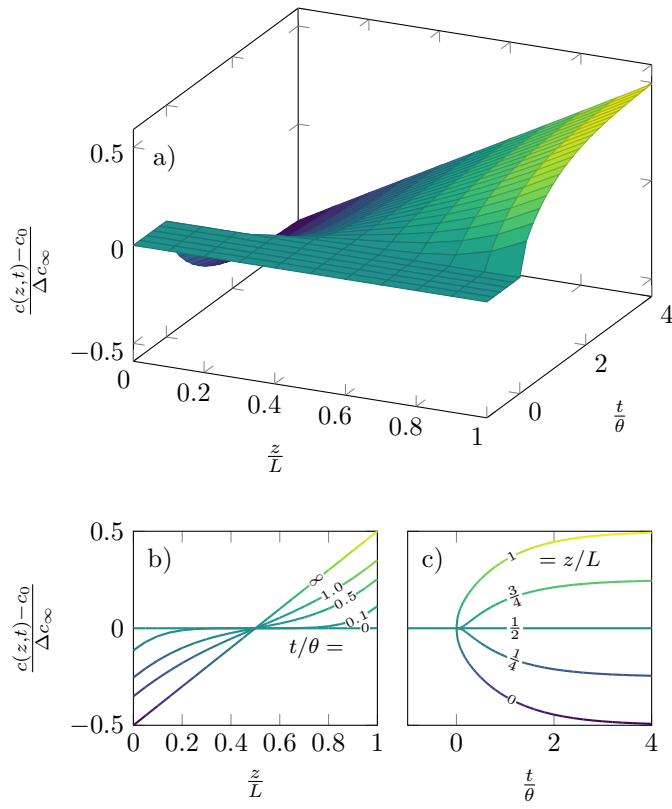
The derivation of eq. (2.74) assumed

- a one-dimensional sample cell,
- that the concentration across the sample at all times is similar to the initial homogeneous concentration:  $c(1 - c) \approx c_0(1 - c_0)$ , so that the Soret coefficient has to be small:  $S_T \ll 1$ ,
- that the density change with concentration, as well as any concentration dependent change in interdiffusion and thermodiffusion coefficient, is small for the concentration change at hand,
- that the temperature across the sample is linearly dependent, and
- that the temperature gradient is being instantaneously applied:

$$\Delta T(t) = \begin{cases} 0, & t < 0 \\ \Delta T_\infty, & t \geq 0 \end{cases}. \quad (2.76)$$

With all this, eq. (2.74) has still been shown to be in good agreement with experiments [117].

A three-dimensional plot of eq. (2.74) as a function of position  $z$  and time  $t$  is shown in fig. 2.5a, together with two-dimensional projections underneath, projected from the  $z$  axis (fig. 2.5b) and  $t$  axis (fig. 2.5c), respectively.

FIGURE 2.5: Plot of eq. (2.74) as a function of  $z$  and  $t$ .

### 2.2.3 Different coefficients used for thermodiffusion in binary mixtures

While the Soret coefficient ( $S_T \equiv \frac{D_T}{D}$ ) has been around for a century, and it is the dominant coefficient used in the field for binary mixtures, there are publications which use other coefficients for measuring the strength of the Soret effect in a system. To aid readers of the literature on thermodiffusion, the main coefficients will be presented, with equations to relate to the Soret coefficient.

#### Soret parameter, $S'_T$

In some experimental work, the Soret parameter has been used, which is much like the Soret coefficient, but without the division factor  $c_0(1 - c_0)$ . Thus, it is related to the Soret coefficient by the relationship

$$S_T = \frac{S'_T}{c_0(1 - c_0)}. \quad (2.77)$$

The definition is simpler than for the Soret coefficient, as it is simply

$$S'_T = -\frac{\Delta c_\infty}{\Delta T}, \quad (2.78)$$

but it has the drawback that it is not independent on whether using mass or atomic ratio for the concentration, which the  $S_T$  is. The Soret coefficient is therefore more robust than the Soret parameter.

#### Heat of transport, $Q^*$

Older publications tend to use the value  $Q^*$ , or the heat of transport, which in a binary mixture is defined as the ratio between the heat flux and the mass flux when a system is isothermal, or in other words: it describes the heat needed to keep a specific system isothermal during mass diffusion [104]. The heat of transport is therefore through the Dufour effect related to the Soret effect, given by the relationship<sup>7</sup>

$$S_T = \frac{Q^*}{\phi RT^2}, \quad (2.79)$$

where  $\phi$  is the thermodynamic factor (TDF)<sup>8</sup> and  $R$  is the molar gas constant. The units for the heat of transport thus is  $\text{J mol}^{-1}$ . For dilute mixtures, the approximation  $\phi \approx 1$  is useful. Some publications using  $Q^*$  use the crude approximation  $\phi \approx 1 - c_0$  for non-dilute mixtures [51, 118–121].

#### Thermodiffusion factor, $\alpha_T$

The last few decades, especially in theoretical works of the Soret effect, the thermodiffusion factor  $\alpha_T$  has been used. It is related to the Soret coefficient by the relationship

$$S_T = \frac{\alpha_T}{T}, \quad (2.80)$$

---

<sup>7</sup>For the derivation, see appendix A.1.

<sup>8</sup>See section 2.1.3.

where  $T$  is the mean temperature of the system, or  $T = \frac{T_c + T_h}{2}$ , where  $T_c$  and  $T_h$  indicate the temperatures at the cold and hot ends respectively. The factor is dimensionless, which possibly explains why it is used in theoretical treatments of the Soret effect and its models.

#### Thermodiffusion ratio, $k_T$

In mostly old theoretical works, even less used than  $\alpha_T$ , the thermodiffusion ratio  $k_T$ , or sometimes  $\kappa_T$ , has been used. It is related to the Soret coefficient by the relationship

$$S_T = \frac{k_T}{T c_0 (1 - c_0)}, \quad (2.81)$$

where again  $T$  is the mean temperature of the system. This means that the *thermodiffusion factor* and *thermodiffusion ratio* are related by the equation

$$k_T = \alpha_T c_0 (1 - c_0). \quad (2.82)$$

Consequently, also  $k_T$  is dimensionless. But as for the Soret parameter  $S'_T$ ,  $k_T$  is not independent on whether using mass or atomic ratio for the concentration.

## 2.3 Predictive models of thermodiffusion

Soon after the systematic works by Soret on the now-called Soret effect in 1879, there were attempts to describe the separation observed, and to predict the degree of separation before the experiment had been performed. This has turned out to be very difficult. A part of the problem lies in that thermodiffusion, as mentioned in the beginning of this thesis, occurs in all states of matter, from solids, through liquids, to gases. Finding a description for an effect occurring in so many different phases and circumstances has proven to be very tricky.

With the exception of the case for cold gasses, finding a description for the separation from thermodiffusion has until today been unsuccessful, as recently explained in a publication by Hoang and Galliero:

Regarding theory, kinetic approaches based on the solution of the Boltzmann equation have proven to be efficient to predict thermodiffusion in gas mixtures at ambient conditions. However, this is less clear in dense phases for which a comprehensive model able to predict thermodiffusion in atomic and molecular fluids seems to be still lacking despite numerous efforts. [122]

### 2.3.1 The case for binary gases

Expressions for the steady-state separation from thermodiffusion was discovered independently by Chapman<sup>9</sup> and Enskog, based on kinetic theory for simple gases [12, 123]. This theory is today called Chapman–Enskog theory [13]. For

---

<sup>9</sup>Note that the initial publication by Chapman contains algebraic errors, which were corrected in later publications by the author [18].

binary gasses, they found the expression [124, p. 271]<sup>10</sup>

$$S_T = \frac{5C}{T} \frac{c_0 S_0 - c_1 S_1}{c_0^2 Q_0 + c_1^2 Q_1 + c_0 c_1 Q_{01}}, \quad (2.83)$$

where  $c_i$  as usual is the concentration for component  $i$ ,  $T$  is the absolute temperature, and where all the other variables are functions of other functions again, depending on molecular masses, molecular characteristics of components, and temperature [122, 124].

The expression is very complicated, and has many various parameters, integrals, sub-functions, and reduced values, so the interested reader is directed to the literal textbook for the full expression [124, pp. 155, 159, 163, 165 and 271], or other derivative works which attempt to clarify the process [125–127]. The theory gives very good predictions for experiments with gasses, with experiments having been conducted for dozens of binary mixtures [124, p. 278].

### 2.3.2 The case for binary liquids

In the first decade after the publication of Soret on thermodiffusion in salt solutions, a first attempt of a model appeared. Hoff described the effect as differences in osmotic pressure, and based on the ideal gas law found an equation for the concentration ratio between the two ends at equilibrium given as [7]

$$\frac{c_c}{c_h} = \frac{T_h}{T_c}, \quad (2.84)$$

with the indices describing the cold (c) and the hot (h) end, for the concentration  $c$  and temperature  $T$ . This was quickly shown to be incorrect in measurements by Arrhenius [9].

In more modern history, with the results from irreversible thermodynamics,<sup>11</sup> it is clear that interdiffusion and thermodiffusion are dependent on changes in the chemical potential. If we calculate the Soret coefficient from the definitions of the interdiffusion and thermodiffusion coefficients in eqs. (2.57) and (2.58), we get the expression

$$S_T \equiv \frac{D_T}{D} = \frac{L_{0q}}{L_{00}} \frac{1}{c_0 T \frac{\partial \mu_0}{\partial c_0}} \left( = \frac{L_{0q}/L_{00}}{\phi R T^2} \right). \quad (2.85)$$

Because of this, most models share the factor  $c_0 T \frac{\partial \mu_0}{\partial c_0}$  in the divisor. As the derivative of the chemical potential can be calculated from the Gibbs energy, which can be measured and is integral in any thermodynamic evaluation, a model for predicting the Soret coefficient is really attempting to predict the ratio between the two phenomenological coefficients  $L_{0q}$  and  $L_{00}$ .

<sup>10</sup>They gave the expression for the thermodiffusion factor  $\alpha_T$ . I have here converted it to the Soret coefficient  $S_T$  (see section 2.2.3), as I have in all later models as well. Also, some models use the sign convention where positive Soret coefficient means enrichment at the *hot* side. This has also been converted, so that every model follows the modern convention of positive Soret coefficient meaning enrichment at the *cold* side.

<sup>11</sup>See section 2.2.1.

### Dougherty and Drickamer

The first model for thermodiffusion that is still cited today is the model of Dougherty and Drickamer from 1955, which is given as [128, eq. (23)]

$$S_T = \frac{M_0 \bar{V}_1 + M_1 \bar{V}_0}{2(M_0 c_0 + M_1 c_1) c_0 T \frac{\partial \mu_0}{\partial c_0}} \left( \frac{\Delta \bar{U}_0}{\bar{V}_0} - \frac{\Delta \bar{U}_1}{\bar{V}_1} \right), \quad (2.86)$$

where the component-specific parameters for component  $i$  are:  $M_i$  the molar mass,  $\bar{V}_i$  the partial molar volume, and  $\Delta \bar{U}_i$  a partial molar activation energy.

The partial molar volume describes the volume contribution of the component to the mixture, which for a pure fluid (or an ideal mixture) is simply then the volume per mole of the component, or

$$\bar{V}_i = \frac{M_i}{\rho_i(T)}, \quad (2.87)$$

where  $\rho_i$  is the density of component  $i$ , often given as a linear relation

$$\rho = \rho_L + \rho_T(T - T_L), \quad (2.88)$$

where  $T_L$  is the liquidus temperature, and  $\rho_L$  then the density at the liquidus temperature, and  $\rho_T$  the change of density per kelvin [66].

The choice of activation energy is something that the original authors had not decided on at publication time, searching for a representation for an ‘energy of activation for molecular motion [...] [needed] to move the molecule from an equilibrium position to the activated state’ [128]. In later works [23], they settled for the activation energy of viscous flow,  $E^{\text{vis}}$ , which is the fitting parameter from the Arrhenius equation for dynamic viscosity  $\eta$ , given by

$$\eta(T) = \eta_0 e^{\frac{E^{\text{vis}}}{RT}}. \quad (2.89)$$

The model in eq. (2.86) arises from a theory of modelling the energy required to detaching the molecules in the liquid from their neighbours, and the energy released when molecules fill the resulting holes [43, 128]. Except for the chemical potential, all the material specific parameters in eq. (2.86) are for the pure components of the mixture, where the index  $i$  denotes the parameter for component  $i$ . This is often practical, as measurements on specific mixtures are by the nature of the sheer amount of possible compound combinations much less common than measurements for the pure elements. But it is also a theoretical stretch, as there are often excess terms to mixture parameters relative to the weighted average from the concentration of each component [66].

After the initial publishing of the model in eq. (2.86), Winter and Drickamer soon performed experiments in equimolar ( $c_0 = c_1 = 0.5$ ) binary liquid alloys (Sn–Bi, Sn–Cd, Sn–Zn, Sn–Pb, Sn–Ga, Sn–Hg, and Bi–Pb) [23]. They got agreeing sign between predictions and measurements for six out of the seven systems, and predicted magnitudes ranging from within 1 % off the measurement to a factor two off. According to them, the results were ‘totally consistent with [the] previously presented theory’ [23]. This excitement has to be taken into context that they are celebrating the apparent understanding of a very little understood phenomena for its time, and the fact that the temperature dependence for two measurements of Sn–Pb at different temperatures was correctly predicted, was

a significant part of the result. For three of the systems, the authors didn't have any measured chemical potential for the mixtures, so they had to resort to the chemical potential for an ideal mixture, which can be a very imprecise assumption. In a more recent publication by Eslamian et al. from 2010, the calculations for the Dougherty and Drickamer model on the systems measured by Winter and Drickamer were redone with more newly assessed component parameters, and with the newer parameters they got predicted coefficients that differed by a factor of up to 128 from the same predictions by Winter and Drickamer, with agreeing sign compared to the measurements now for five out of the seven measured systems [129].

### Shukla and Firoozabadi

In 1998, Shukla and Firoozabadi published a model based on irreversible thermodynamics, the same framework as used by Dougherty and Drickamer. This newer model is given as [130, eq. (24)]

$$S_T = \frac{\frac{\bar{U}_1}{\tau_1} - \frac{\bar{U}_0}{\tau_0}}{c_0 T \frac{\partial \mu_0}{\partial c_0}} + \frac{(\bar{V}_0 - \bar{V}_1) \left( c_0 \frac{\bar{U}_0}{\tau_0} + c_1 \frac{\bar{U}_1}{\tau_1} \right)}{(c_0 \bar{V}_0 + c_1 \bar{V}_1) c_0 T \frac{\partial \mu_0}{\partial c_0}}, \quad (2.90)$$

where the new parameters are the partial molar internal energy  $\bar{U}_i$  and the ratio  $\tau_i = E_i^{\text{vap}}/E_i^{\text{vis}}$ , where  $E_i^{\text{vap}}$  is the energy of vaporization of component  $i$ . For fluids,  $\bar{U}_i$  is close to the partial molar enthalpy (see eq. (2.3)). One can then use the fact that the partial molar enthalpy  $\Delta H_i$  is related to the activity coefficient through [99]

$$\Delta H_i = -RT^2 \left( \frac{\partial \ln \gamma_i}{\partial T} \right). \quad (2.91)$$

A recent article by Hoang and Galliero where they simulated thermodiffusion in a Lennard-Jones (LJ) fluid using non-equilibrium molecular dynamics (NEMD) found that the predictive model by Shukla and Firoozabadi was 'the most reasonable' model available for liquids, but still 'could [not] be considered as able to provide reliable predictions' in the general case with liquids with different sizes and masses [122].

The dimensionless value  $\tau$ , being the ratio between the energy of vaporisation  $E^{\text{vap}}$  and activation energy of viscous flow  $E^{\text{vis}}$ , is often set to a constant value ranging from 3.0 to 4.0 [95, 122, 129, 130]. This is an accurate estimation for organic liquids, for which the model by Shukla and Firoozabadi was originally developed,<sup>12</sup> where the ratio is indeed in this range [131, 132]. But for liquid metals, the ratio is much higher, in the range 8 to 25 [131, 132]. So for liquid alloys, we must calculate this value, and can not simply use a constant for all mixtures. For that calculation,  $E^{\text{vis}}$  is found as described in eq. (2.89), while  $E^{\text{vap}}$ , due to the assumption in eq. (2.3) that the enthalpy and internal energy is similar in fluids, can be taken to be equal to the enthalpy of vaporisation, which is readily available in tables [133].

<sup>12</sup>Their publication is titled 'A new model of thermal diffusion coefficients in binary hydrocarbon mixtures'.



**Artola et al.**

A quite different model, based on kinetic theory, was published by Artola et al. in 2008, given as [134, eq. (5)]

$$S_T = \frac{E_1^{\text{self}} - E_0^{\text{self}}}{RT^2} + \frac{M_1 - M_0}{M_0 + M_1} \frac{E_0^{\text{self}} + E_1^{\text{self}}}{RT^2}, \quad (2.92)$$

where the new parameter is the activation energy of self-diffusion  $E_i^{\text{self}}$  for component  $i$ . Self-diffusion is the diffusion for a single molecule of component  $i$  diffusing in the mixture, whereas interdiffusion is the collective mixing, driven by differences in the chemical potential, a relation between the two being approximated by the Darken equation [72]

$$D \approx \phi(c_1 D_{\text{self},0} + c_0 D_{\text{self},1}), \quad (2.93)$$

where  $\phi$  again is the TDF. Thus, for a dilute system, the interdiffusion coefficient approaches the coefficient of self-diffusion of the minority component [63]. The activation energy of self-diffusion is defined as the fitting parameter from the Arrhenius equation for the self-diffusion  $D_{\text{self}}$ , given by

$$D_{\text{self}}(T) = D_0^{\text{self}} e^{-\frac{E^{\text{self}}}{RT}}. \quad (2.94)$$

Equation (2.92) is much like the other models presented here, but with the term  $c_0 T \frac{\partial \mu_0}{\partial c_0} = \phi RT^2$  replaced by simply  $RT^2$ , i.e., assuming an ideal mixture where  $\phi \approx 1$  [43]. With this, the concentration dependence of the resulting Soret coefficient arises only from the concentration dependence of the activation energy of self-diffusion.

**Eslamian et al.**

Developed especially for thermodiffusion in binary liquid alloys, Eslamian et al. published a model in 2010, given as [129, eq. (21)]

$$S_T = \frac{E_0^{\text{vis}} - E_1^{\text{vis}} - (z_1 \mathcal{E}_0 - z_0 \mathcal{E}_1) c_1 F T}{c_0 T \frac{\partial \mu_0}{\partial c_0}}, \quad (2.95)$$

where the new parameters are for component  $i$ :  $z_i$  the valency of the ions and  $\mathcal{E}_i$  the thermoelectric power, and where  $F$  is Faraday's constant.

It models the electronic contribution that arises from the metallic bonding in the liquid alloy, delocalising the electrons, giving high electronic conductivity in the fluid.

A curious thing about the proposed model is that it is not symmetrical, thus breaking with the very fundamental relationship of the definition of the Soret coefficient in eq. (2.45), where for a binary mixture, the Soret coefficient for component 0 is equal with the opposite sign of the Soret coefficient for component 1, as  $\nabla c_0 = \nabla(1 - c_1) = -\nabla c_1$ .

**Jafar-Salehi et al.**

Jafar-Salehi et al. in 2014 published a revised version of the model of Eslamian et al., given as [135, eq. (12)]

$$S_T = \frac{E_0^{\text{vis}} - E_1^{\text{vis}} - (z_1 \mathcal{E}_0 - z_0 \mathcal{E}_1) c_1 F T}{RT^2} \times \left( c_0^2 \left[ \frac{\rho_1}{\rho_0} - 1 \right] + c_0 \right), \quad (2.96)$$

where the new parameter is the density  $\rho_i$  for component  $i$ . The only difference from the model of Eslamian et al. is that the derivative of the chemical potential is replaced by the expression

$$\frac{\partial \mu_0}{\partial c_0} = \frac{RT}{c_0^2 \left( \frac{\rho_1}{\rho_0} - 1 \right) + c_0}. \quad (2.97)$$

This approximation is taken from a publication which assumes dilute mixtures [136].<sup>13</sup> The benefit from the approximation in eq. (2.97) is that the model in eq. (2.96) thus only depends on material parameters for the pure components, while not needing any measured chemical potential for the mixture, which can be very prone to error in its derivatives.<sup>14</sup>

A curious thing about the model in eq. (2.96) is that the concentration  $c$  here is explicitly stated to be the *mass fraction*, while it is based on the model by Eslamian et al., which explicitly uses the *mole fraction*. While the Soret coefficient is invariant to whether using mole fraction or mass fraction,<sup>15</sup> the parameters used for the predictive models for thermodiffusion are *not* invariant.

Similarly to the model by Eslamian et al., the model by Jafar-Salehi et al. is not symmetric, which again breaks with the definition of the Soret coefficient.

### Summarising thoughts to the models

Now, summarising the knowledge from the presented models for thermodiffusion in binary liquids, it is clear that the factor  $1/\frac{\partial \mu}{\partial c}$  plays a significant role in the behaviour of the thermodiffusive process. A result from this is that when  $\frac{\partial \mu}{\partial c}$  approaches 0, the Soret coefficient diverges. This is also clear from the definition of the interdiffusion and thermodiffusion coefficients from irreversible thermodynamics, which we recall from eqs. (2.57) and (2.58) as

$$D = \frac{L_{00}}{\rho c_1 T} \frac{\partial \mu_0}{\partial c_0} \quad \text{and} \quad D_T = \frac{L_{0q}}{\rho c_0 c_1 T^2}. \quad (2.98)$$

When  $\frac{\partial \mu}{\partial c} \rightarrow 0$ , it leads to  $D \rightarrow 0$ , while  $D_T$  is independent of  $\frac{\partial \mu}{\partial c}$ . Thus, with a non-zero thermodiffusion coefficient and an interdiffusion coefficient approaching zero, the Soret coefficient  $S_T \equiv \frac{D_T}{D}$  increases rapidly. Physically, the interdiffusion stops up as the gradient in chemical potential goes down, while the thermodiffusion continues, and the resulting concentration gradient is not as strongly inhibited by the interdiffusion as usual, leading to higher ability for concentration separation, and therefore a higher Soret coefficient. This has already been observed for organic binary mixtures with miscibility gaps, such as nitrobenzene–hexane, cyclohexane–methanol, cyclohexane–aniline, and poly(dimethyl siloxane)–poly(ethyl-methyl siloxane) (PDMS–PEMS) [26, 34–37]. This has not yet been investigated for liquid alloys, although there are several alloys which observe liquid miscibility gaps [71]. Williams and Philbrook measured the Soret coefficient for Ag–Te, which has a liquid miscibility gap, but

<sup>13</sup>Jafar-Salehi et al. acknowledges the dilute limit, while still applying their model on equimolar mixtures, which clearly is not a valid assumption. Also, note that Maier et al., the authors of the publication from where eq. (2.97) is from, don't give any motivation, origin, or derivation for the equation [136].

<sup>14</sup>See section 5.3.

<sup>15</sup>See appendix A.2.

they measured Soret coefficients only for mixtures with silver concentrations from 17.5 at.% to 69 at.%, whereas the liquid miscibility gap is from 69.7 at.% to 88.1 at.%, so they did not observe nor investigate any critical behaviour [53, 137].

Many of the parameters in the models presented in this chapter are difficult to measure precisely. This is especially the case for the activation energy for viscosity  $E^{\text{vis}}$ , the activation energy of self-diffusion  $E^{\text{self}}$ , and the derivative of the chemical potential with respect to concentration  $\frac{\partial \mu}{\partial c}$ . The problems arise from the activation energies being fitted parameters to the exponential change in measured viscosity and self-diffusion respectively as functions of temperature. For liquid alloys, with high melting points, measurements are often uncertain due to the need of thermal protection. With this, the exponential change is often weak, so the activation energy is often ill-fitted or has large uncertainty. For the derivative of the chemical potential, it is expressed from the second derivative of the Gibbs energy, and therefore any measurement errors in the Gibbs energy are amplified in the process.<sup>16</sup> With such uncertain parameters, precise quantitative predictions for the Soret coefficient can hardly be expected. For the testing of the models, measuring close to a point where the Soret coefficient is sensitive may be more indicative of their performance, so measuring the Soret coefficient at and around a liquid miscibility gap can be of high value for the investigation of the qualitative accuracy of a model.

---

<sup>16</sup>See section 5.3.



# Chapter 3

## Methods

### 3.1 Selection of concentrations for alloys

#### 3.1.1 Ag–Al

The phase diagram of Ag–Al is calculated using the Gibbs energies reported by Witusiewicz et al. [67], and is shown in fig. 3.1. The annotated point is the eutectic point.

For investigating the Soret effect in X-ray, due to the weakness of thermodiffusion relative to interdiffusion, an as high concentration separation as possible is wanted. With the expression for concentration separation from eq. (2.46), the separation is expected to be at a maximum when the concentration is approximately  $c_{\text{Ag}} \approx 50 \text{ at.}\%$ , due to the factor  $c_0(1 - c_0)$  having its peak at  $c_0 = 0.5$ . While the Soret coefficient itself is not a constant for the system across the concentration range, it tends to be weakly dependent on concentration, especially for non-dilute mixtures [80]. It has also been found in experiments by Engelhardt et al. that the interdiffusion coefficient of Ag–Al is close to constant over the concentration range 20.4 at.% to 42.5 at.% [81]. Thus for these experiments, measuring the Soret coefficient for low concentrations of one component is expected to be difficult, as the low value of  $c_0(1 - c_0)$  will generally give a low steady-state concentration separation  $\Delta c_\infty$ , and thus a low contrast in the X-ray radiography (XRR) images. Furthermore, at higher concentrations of silver in X-ray, the dark silver across the sample is drowning out the signal from the lighter aluminium, making it important that the relative concentration of silver between the cold and the hot ends is maximised. Therefore, for these experiments, the alloys  $\text{Ag}_{20}\text{Al}_{80}$ ,  $\text{Ag}_{25}\text{Al}_{75}$ ,  $\text{Ag}_{30}\text{Al}_{70}$ ,  $\text{Ag}_{45}\text{Al}_{55}$ ,  $\text{Ag}_{50}\text{Al}_{50}$ , and  $\text{Ag}_{55}\text{Al}_{45}$  were selected to be investigated.

For the investigated concentration range, the liquidus temperature is the highest for  $\text{Ag}_{55}\text{Al}_{45}$ , where it is 964 K. It was decided to keep the isothermal temperature at 1023 K for the experiments, so that the temperature was well above the liquidus points of the investigated alloys along the entire sample. The interdiffusion coefficient measurements of Engelhardt et al. were conducted at 983 K. A slight increase of the interdiffusion coefficient is expected with increasing temperature, following eq. (2.40).

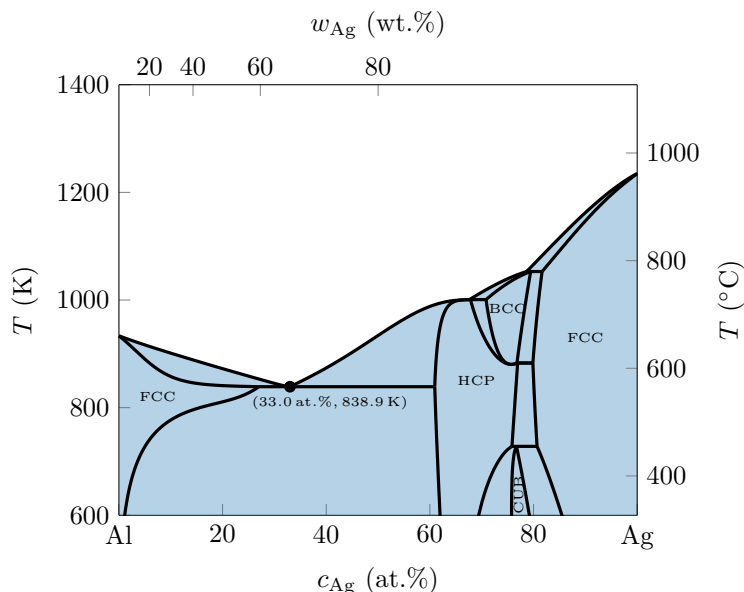


FIGURE 3.1: Calculated phase diagram of Ag–Al.

### 3.1.2 Ag–Cu

The phase diagram of Ag–Cu is calculated using the Gibbs energies reported by Witusiewicz et al. [67], and is shown in fig. 3.2. The annotated point in the figure is the eutectic point. Its phase diagram is quite simple, having only liquid and face-centred cubic (FCC) phases, or mixtures thereof.

The eutectic point of Ag–Cu being at 1053 K made it impossible to use the same temperature as for Ag–Al (1023 K), as there simply is no Ag–Cu alloy with such a low liquidus temperature. Also, with the use of a temperature gradient over the samples, the entire sample needed to be liquid, and the operating temperature needed to be even higher than the eutectic temperature. With the eutectic temperature in mind, it was decided to measure Ag–Cu at 1123 K. This operating temperature essentially only made it possible to investigate the eutectic concentration ( $\text{Ag}_{60.2}\text{Cu}_{39.8}$ ), as other alloy compositions have liquidus points at higher temperatures, which would have required even higher operating temperatures.

As mentioned in section 1.2.2, the density of liquid silver is  $9.3 \text{ g cm}^{-3}$ , while the density of liquid copper is  $8.0 \text{ g cm}^{-3}$  [75, 84]. This makes the Ag–Cu mixture much denser than Ag–Al, and thus darker under X-ray irradiation. These similar densities also contribute to the disadvantage of having a lower contrast between the two components in the X-ray spectrum.

With the low X-ray contrast, no concentration data is expected to be obtained from XRR, and the experiment should be conducted in a shear cell to allow ex situ determination of the steady-state concentration separation.

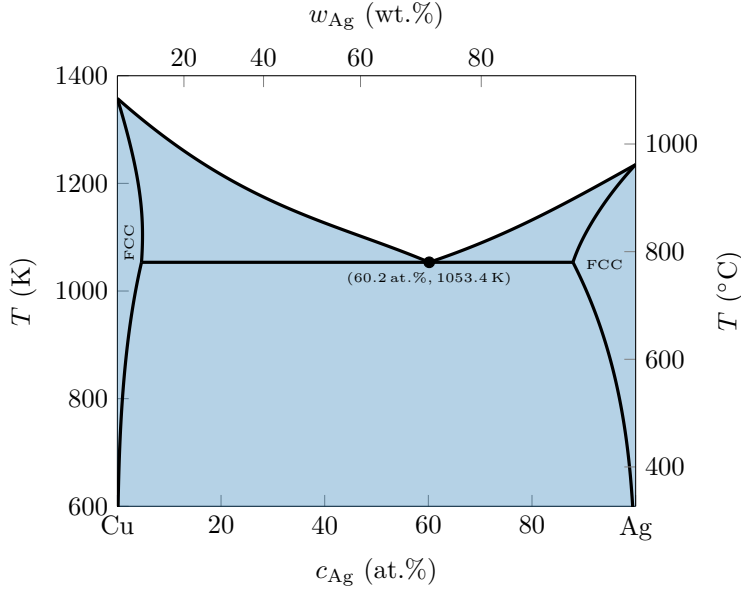


FIGURE 3.2: Calculated phase diagram of Ag–Cu.

### 3.1.3 Ag–Al–Cu

The phase diagram of the ternary Ag–Al–Cu system is shown in fig. 3.3, calculated using the Gibbs energies reported by Witusiewicz et al. [68].<sup>1</sup> The liquidus surface is shown in a Gibbs triangle, where the corners represent the pure elements, the triangle sides the different binaries, and a line parallel to a triangle side indicates constant concentration of the third component [94]. The eutectic point of the Ag–Al–Cu system is annotated in fig. 3.3, which is for the composition  $\text{Ag}_{18.1}\text{Al}_{69.1}\text{Cu}_{12.8}$ , with a melting temperature of 773.6 K [68]. This is lower than any liquidus temperature of the three constituent binaries.

Note that the atomic mass ratio of the eutectic point at  $\text{Ag}_{18.1}\text{Al}_{69.1}\text{Cu}_{12.8}$  is similar to that of the eutectic point of binary Ag–Cu, which as earlier stated was for the alloy  $\text{Ag}_{60.2}\text{Cu}_{39.8}$ . With that, the relative ratio of silver and copper in the ternary eutectic of  $\frac{c_{\text{Ag}}}{c_{\text{Cu}}} = \frac{18.1 \text{ at.}\%}{12.8 \text{ at.}\%} \approx 1.41$  is quite similar to the ratio in the binary eutectic of  $\frac{c_{\text{Ag}}}{c_{\text{Cu}}} = \frac{60.2 \text{ at.}\%}{39.8 \text{ at.}\%} \approx 1.51$ .

As Ag–Al–Cu is a ternary system, with two free component concentrations, the full concentration profile can not be deduced from XRR imagery, which only gives scalar grey value for each pixel in the image. Therefore, a thermodiffusion experiment has to be conducted with a shear cell.<sup>2</sup> This means that the interdiffusion coefficient can not be measured during the experiment. The interdiffusion

<sup>1</sup>The Redlich-Kister parameter for the hexagonal close-packed (HCP) phase of Al–Cu used in the evaluation by Witusiewicz et al. [68] is, along with most other binary Al–Cu phases in that work, from the COST 507 database compiled by Ansara et al. [138]. Note that in the printed database, while the HCP for Al–Cu is listed in the index, it is not reported anywhere in the text itself. In the database file accompanying the report, however, the value is included as  $L = A_0 = 38107$  [139]. Using this value for the Al–Cu HCP excess Gibbs energy faithfully reproduces the values and figures in the publication of Witusiewicz et al., and was thus used for the phase diagram calculations here.

<sup>2</sup>See section 3.2.2.

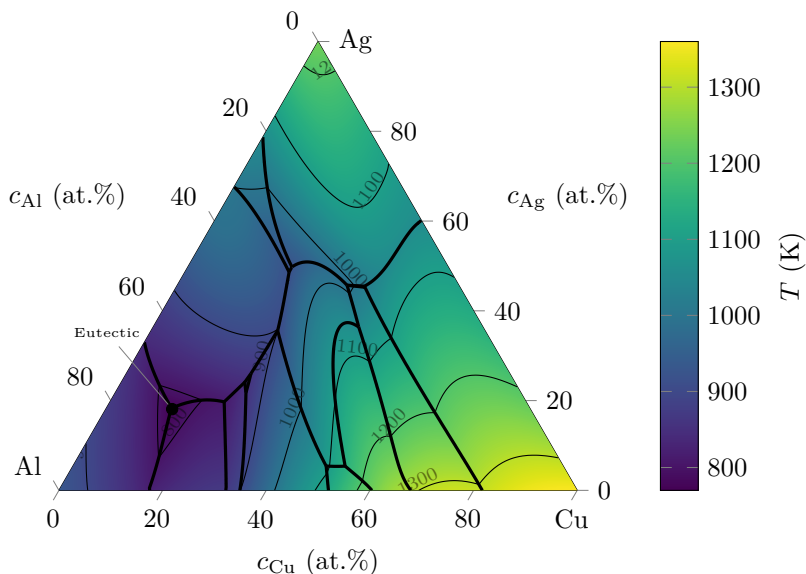


FIGURE 3.3: Calculated liquidus surface of ternary Ag–Al–Cu. The thick lines are phase boundaries for the solidus, while the thin lines are contours of constant temperature for the liquidus.

in the ternary system has however already been thoroughly investigated by Engelhardt by using XRR, by using the trick of keeping one of the components at constant concentration for both diffusion couples, a so-called quasi-binary measurement [62].

Note that Engelhardt used a eutectic composition of  $\text{Ag}_{17.6}\text{Al}_{68.6}\text{Cu}_{13.8}$ , as determined by Cooksey and Hellawell in a publication from 1967, contrary to the newer evaluation of  $\text{Ag}_{18.1}\text{Al}_{69.1}\text{Cu}_{12.8}$  by Witusiewicz et al. from 2005 [62, 68, 140].

For this thesis, the thermodiffusion of the eutectic Ag–Al–Cu as measured by Sonderrmann et al. was used [141]. Sonderrmann et al. followed Engelhardt, and used the eutectic of Cooksey and Hellawell instead of Witusiewicz et al. [62, 68, 140]. For this thesis, an additional composition was measured, with the concentration of equimolar Ag–Al, with the addition of Cu, so that its concentration was equal to that of the eutectic. To keep it consistent with the earlier thermodiffusion measurement of Sonderrmann et al., the copper concentration was thus kept at  $c_{\text{Cu}} = 13.8 \text{ at.}\%$ , with the ternary composition then at  $\text{Ag}_{43.1}\text{Al}_{43.1}\text{Cu}_{13.8}$ . Using the Gibbs energies of Witusiewicz et al. makes it possible to calculate the liquidus temperature at this composition [68], calculated to a temperature of 936.7 K.<sup>3</sup>

As can be seen in the publication of Witusiewicz et al., there is much greater uncertainty to the liquidus curves for a ternary system than for a binary system [68], as the equations for the Gibbs energy not only describes the

<sup>3</sup>For comparison, the liquidus temperature of the alloy with copper concentration from the eutectic evaluated by Witusiewicz et al. of  $\text{Ag}_{43.6}\text{Al}_{43.6}\text{Cu}_{12.8}$  is calculated to be 938.7 K. The two compositions and liquidus temperatures are so close that no big difference in the Soret coefficient between the two compositions is expected.



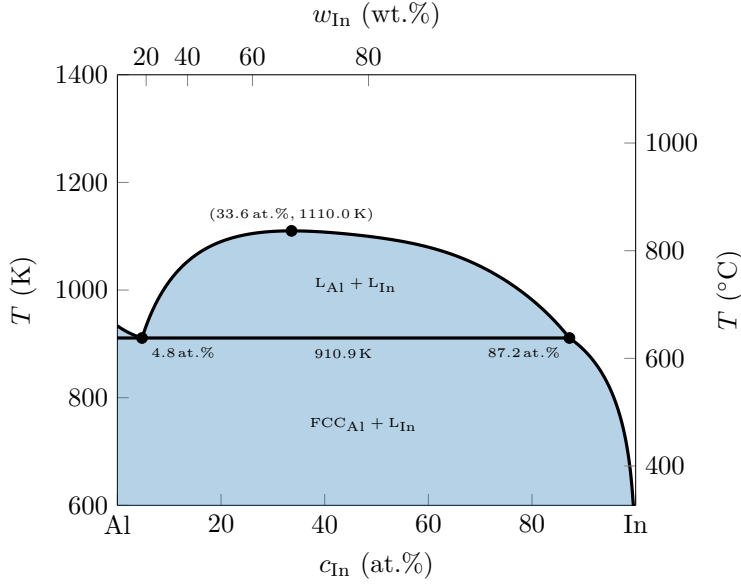


FIGURE 3.4: Calculated phase diagram of Al–In.

dependency on a scalar component, but over an entire surface of possible coupled concentrations. With this, extra caution was taken in selecting a temperature for the thermodiffusion experiment that was well above the liquidus temperature. With the selected composition and its liquidus temperature in mind, the same temperature as for the binary  $\text{Ag}_{60.2}\text{Cu}_{39.8}$  was thus selected for the experiment, i.e., 1123 K.

### 3.1.4 Al–In

The phase diagram of Al–In is calculated using the excess Gibbs energy reported by Singh and Sommer [71], and is shown in fig. 3.4.<sup>4</sup> The annotated points are the monotectic points and the critical point. The melting point of pure indium of 429.75 K (156.60 °C) is not shown within the plotted temperature range, as it is very much lower than the rest of the liquidus points.

For this thesis, only a few experiments were performed on the Al–In system, with successful results being obtained for  $\text{Al}_{85}\text{In}_{15}$  and  $\text{Al}_{78}\text{In}_{22}$ , with the coldest (bottom) temperature of the sample being at 1100 K, which according to the phase diagram in fig. 3.4 should be just above the miscibility gap. The binodal temperature (where it is thermodynamically favourable for the phases to separate) for the investigated concentrations is from the thermodynamic evaluation of Singh and Sommer given to be at 1064 K and 1097 K respectively, while the spinodal temperature (where the mixed liquid is no longer stable at all, and the thermodynamic factor (TDF) is zero) is given to be at 986 K and 1072 K respectively [71].

<sup>4</sup>Note that one of the Redlich-Kister parameters in the publication by Singh and Sommer has an error in it. The  $B_2$  term in its Table 4 should have a minus sign, i.e., should read  $-7.47862$ . The correct values are reported in an earlier conference proceeding by Sommer et al., from where the later publication bases its values [142].

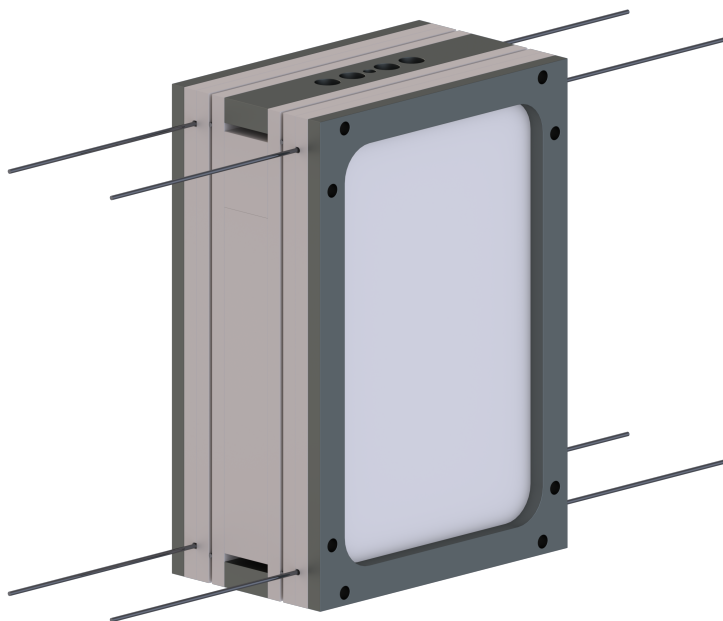


FIGURE 3.5: Digital render of the compact sample cell.

To the best of my knowledge, there is no full investigation on whether the excess volume of liquid Al–In is positive, negative, or negligible. Kaban et al. found good agreement between measurements of density of a segregating liquid  $\text{Al}_{64}\text{In}_{36}$  alloy and the predicted values from ideal mixing ( $V_E = 0$ ) [143]. This was however only measured below the critical temperature, i.e., in the demixed state. It has been postulated that demixing systems generally have positive excess volumes, although there are exceptions to this rule [144, 145]. With this in mind, due to the lack of full investigation of the real behaviour of the density in liquid Al–In, ideal mixing for calculating the density of the alloy is still used in this thesis.

## 3.2 Sample cell

### 3.2.1 Furnace cell

The sample cell is based on a setup which has been developed for interdiffusion measurements in liquid alloys [63, 146, 147]. To use the sample cell for thermodiffusion experiments a heater design was developed that allows for a temperature difference along the sample. The updated sample cell developed for this project can be seen in fig. 3.5.

In addition to the new heater layout, the main new feature for this iteration was the addition of pistons, which are shown in the exploded view in fig. 3.6.<sup>5</sup> The annotations indicate (A) the boron nitride (BN) crucible with (B) samples and (C) pistons, as well as (D) the heat plates, where (E) the heating wire is

<sup>5</sup>The pre-existing sample cells also have pistons, but their form is different, being cylinders of equal width to the bigger reservoirs.

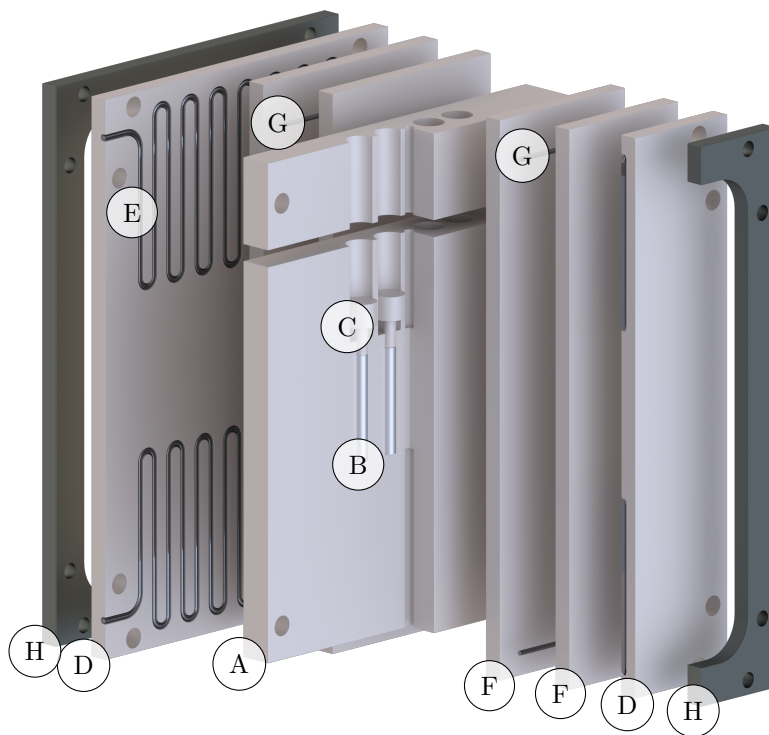


FIGURE 3.6: Digital render of the sample cell in an exploded and cut view.

placed. Between the heating wire and crucible are (F) two extra BN plates with (G) molybdenum wire as separator. The sample cell is held together by (H) the niobium frame. The plates, wires and frame in front of the crucible, as well as the crucible parts themselves, are cut in the figure to reveal the pistons and samples. The BN plates between the crucible and the heating wires are also cut in the figure to reveal the meandering course of the heating wire. The space between the BN plates makes a larger temperature gradient possible.

The outer dimensions of the sample cell is  $58\text{ mm} \times 40\text{ mm} \times 24\text{ mm}$ , while the sample borings are  $12.5\text{ mm}$  deep and  $1.3\text{ mm}$  wide. The thermocouples reach in to each of the ends of the sample boring, and the two thermocouples are thus  $12.5\text{ mm}$  apart when fully inserted. The heaters don't reach over the samples, always having a buffer zone of at least  $1.5\text{ mm}$  until each of the ends of the sample, so that there is enough room for the temperature distribution to linearise. The samples were also slightly compressed by the pistons from above, giving even more distance to the top heater.

The borings for the sample cells containing Al-In were slightly wider, at  $1.6\text{ mm}$ , to fit the wires of the pure components,<sup>6</sup> which were not possible to purchase in  $1.2\text{ mm}$  width, and thus the next possible width of  $1.5\text{ mm}$  was purchased.

The furnace, being  $40\text{ mm}$  wide, housed four samples, all at the same depth, with one pair of samples on each side of the thermocouples in the centre. The samples in the pair were  $4.0\text{ mm}$  apart centre-to-centre, no matter the sample thickness. The outer samples from each pair had a total distance between themselves of  $13.6\text{ mm}$  centre-to-centre. The heaters had 16 turns spanning over  $30\text{ mm}$ , so it was assumed that all the four samples had negligibly different mean temperatures between themselves. For the temperature distribution along the samples in the cell, see section 3.2.3.

### 3.2.2 Shear cell

In addition to the furnace cell, an additional version that could shear the samples was developed, based on the interdiffusion shear cell. This way, the sample concentrations could be measured *ex situ* as well as *in situ*, through methods such as energy-dispersive X-ray spectroscopy (EDXS) together with the use of XRR imagery. In this shear cell, the samples are placed in stacked shear plates, with the plates having opposite fixed and movable holes, such that a rod could pass through the plates. At any wanted point, which in this case was at the steady-state at the end point of the thermodiffusive process, the plates were sheared, as shown in fig. 3.7. The samples are at different depths in the cell, so they do not cross each other during the shearing. Due to this layering, the shear cell could only host two samples, compared to four in the furnace cell from section 3.2.1. After cooling down, the individual samples could be extracted from the sheared plates, embedded in epoxy, and analysed in the scanning electron microscope (SEM) with EDXS.

The benefits of the shear cell are for once that for systems where the two components have too low contrast between themselves, the shear cell setup allows experiments to be performed where the exclusively *in situ* regular furnace would have given too low contrast to accurately determine the concentration along the

---

<sup>6</sup>See section 3.3.

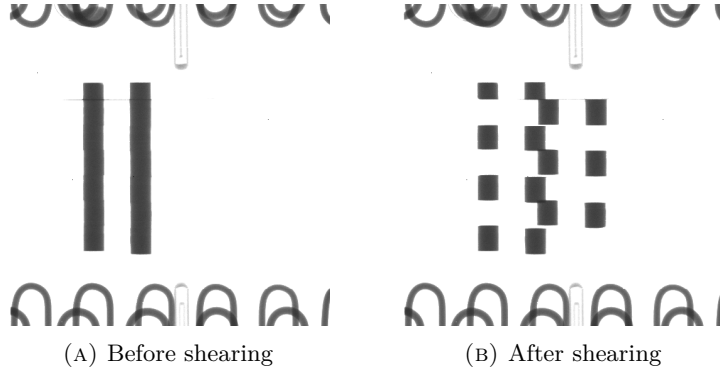


FIGURE 3.7: XRR images from a shear cell experiment.

sample. Secondly, for ternary or higher order systems, where the number of independent concentrations are higher than one, the individual concentrations can not be determined using XRR any more, as the black-and-white image has only one degree of freedom (scalar grey values from black to white). Thirdly, the use of a shear cell allows for calibration of the method of determining the concentration from the grey values in the XRR image.

A drawback with the shear cell and EDXS is however that the concentration separation is only known for the moment of shearing, and thus no transient concentration separation information is available. Also, as already mentioned, the shear cell could only fit two samples. Thanks to the XRR images captured during the shear cell experiments, the steady-state could still be indicated by the apparent stop in change of grey value.<sup>7</sup> Also, the images could ensure the lack of bubbles and cavities, the presence of which may induce Marangoni convection, disturbing the measurements [56, 57].

### 3.2.3 Temperature distribution

As previously mentioned, the validity of eqs. (2.46) and (2.74) depend in part on the temperature gradient along the samples being linear. One could assume that in the case of a steady temperature difference along the samples, with a constant heat conductivity all over the sample cell, the temperature gradient would indeed be linear, as it is the solution to the heat equation

$$\frac{\partial T}{\partial t} = \lambda \frac{\partial^2 T}{\partial z^2} \quad (3.1)$$

with heat conductivity  $\lambda$  and temperature  $T(z)$  as a function of position  $z$ . Thus, if  $\frac{\partial T}{\partial t} = 0$ , i.e., steady temperature distribution, it leads to a description for  $T$  having to be at most linearly dependent on  $z$  for the double-derivative to be zero.

To check that this was the case, the temperature distribution over the sample cell was investigated, by using a deepened boring for the top thermocouple, and then using three sheathed thermocouples with a diameter of 0.5 mm at

<sup>7</sup>There is a possibility that even with a constant grey value, there is a mass flux if the three components move such that the resulting grey value from the local composition is constant along the cell. This is deemed very unlikely.

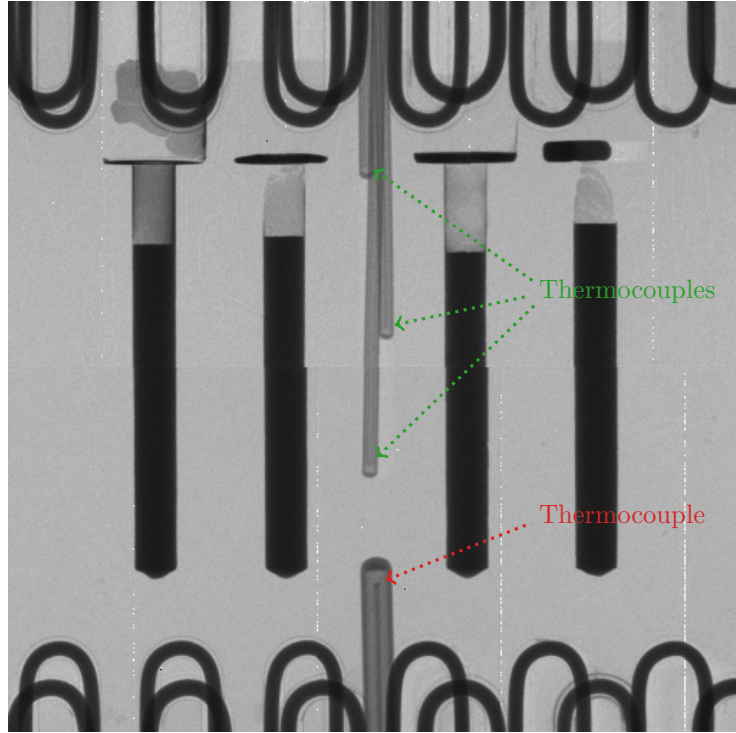


FIGURE 3.8: X-ray image of the sample cell used for measuring the temperature distribution.

different depths, instead of the standard 1.0 mm thermocouple at the top of the samples, as seen in for example fig. 3.7. An X-ray image of the sample cell with the extra deep boring for the thermocouples, and three thinner thermocouples (green arrows) inserted instead for one at the top, in addition to the regular thermocouple at the bottom (red arrow), is shown in fig. 3.8. It was ensured that the thermocouple positions were fixed during the entire test.

The temperatures from all four thermocouples (three at the top and one normal at the base) were recorded first in a close to isothermal case, and once with a temperature gradient where the bottom heating wires were turned off, while the top temperature was maintained constant.

The recorded temperature distributions are displayed in fig. 3.9. The figure shows plots of the temperature distributions in the case of an isothermal setup (left) and temperature gradient setup (right), measured from the test imaged in fig. 3.8. From the data it is apparent that the temperature gradient indeed is close to linear in the sample cell. The Pearson correlation coefficient in the gradient setting is  $r = -0.987$ , indicating a very likely linear relationship. In the isothermal case some spread in the temperatures is apparent, but it has to be remembered that the thermocouples themselves have some measurement error, even at room temperature. The thermocouples used conform to the DIN 60584-1 standard, meaning a measurement error of the absolute temperature of at most  $\pm 0.004 \times (T - 273.15 \text{ K})$  above 648 K, and a constant maximum error of  $\pm 1.5 \text{ K}$  under 648 K, giving a maximum measurement error at  $T = 1073 \text{ K}$  of 3.2 K [148].

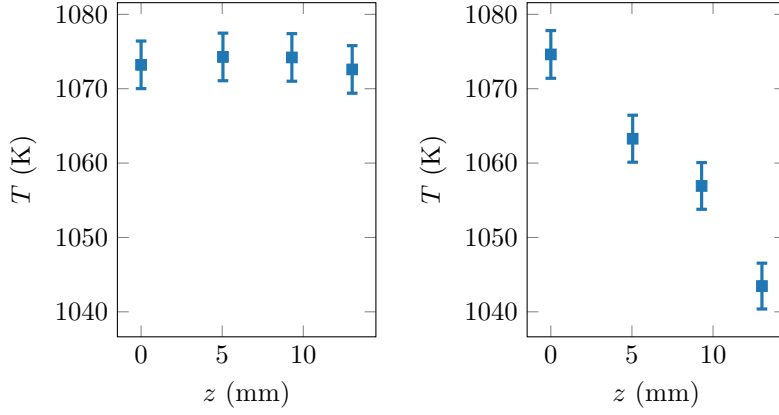


FIGURE 3.9: Plots of the temperature distribution in the sample cell. The uncertainty in temperature is from the measurement error as given by the thermocouple supplier [148].

TABLE 3.1: List of metals used.

Element	Description	Purity	Supplier
Ag	Silver shot, 1 mm to 5 mm	99.99 %	Alfa Aesar
Al	Aluminium shot, 4 mm to 8 mm	99.999 %	abcr GmbH
Al	Aluminium shot, 4 mm to 8 mm	99.999 %	Alfa Aesar
Al	Aluminium wire, 1.50 mm diameter	99.999 %	chemPUR
Cu	Copper rod, 3.18 mm diameter	99.999 %	Alfa Aesar
In	Indium wire, 1.5 mm diameter	99.99 %	chemPUR

### 3.3 Sample preparation

The samples used for the work presented here were weighed on a scale with a precision of 0.01 mg. Metals of high purity were used, and are listed in table 3.1. The three different aluminium sources were used for the Ag–Al, Ag–Al–Cu, and Al–In measurements, respectively. Fragments of the pure metals were weighed on the scale to achieve the wanted concentration, and subsequently alloyed.

All samples used for the experiments presented in this work were alloyed in an arc-melting furnace (MAM 1 Type H180T, Edmund Bühler GmbH, Germany), unless otherwise is written. The metals were placed inside the chamber together with a piece of pure titanium. After applying a high vacuum of  $1 \times 10^{-5}$  mbar or better, a high purity argon atmosphere was introduced. The titanium piece was melted before the other metals to react with the remaining oxygen, so that the amount of oxides in the samples were further reduced.

Due to the miscibility gap in the liquid phase of the Al–In system (see the phase diagram for Al–In in fig. 3.4), a good alloying of Al–In samples in the concentration range from 4.8 at.% to 87.2 at.% can not be easily performed like for alloys like Ag–Al. When the sample is heated to above the miscibility gap and a homogenous liquid mix is achieved, the subsequent cooling to room temperature will leave the sample enough time to demix during the cooling

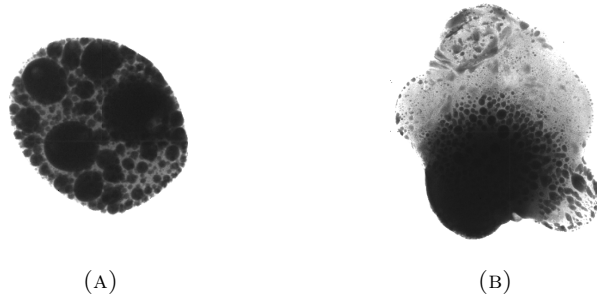


FIGURE 3.10: Two poorly annealed Al–In due to the liquid miscibility gap.

down to room temperature. The alloying was attempted in the arc melting furnace, but the solid samples would not form uniform phases after alloying (see an attempt with  $\text{Al}_{75}\text{In}_{25}$  in fig. 3.10a), and sometimes even have troubles with forming a spherical sample due to the multiple phases in the liquid state (see an attempt with  $\text{Al}_{80}\text{In}_{20}$  in fig. 3.10b).

For this system, wires of the pure metals were acquired (see table 3.1), and cut down and polished to lengths so that the combined metals when mixed would form alloys of wanted concentration and total volume. For this, it showed to be very important that the metal was kept away from water and oxygen, as layers of oxidation would form in the interface between the aluminium and indium wires, leading to problems of filling the cavity in that region. In the first tested sample cells, the samples always got bubbles at the interface, as the metal would rather leak past the pistons (or not be pushed in at all), than clear away the oxidation layer. Therefore, all results presented here were from sample cells where the aluminium and indium wires were carefully washed and kept in isopropanol from they were being cut and polished until they were inserted into the sample cell.

As the wires didn't have an even width, and especially the extreme softness of indium, targeting a precise concentration was not as feasible as when using the arc melting furnace for the other alloys. Still, the masses of the wire components were known, so the concentration itself was precisely known, albeit difficult to target to a specific round number.

A problem of the wire-alloying method was that the metal wire in the crucible would melt before mixing, so that the melt that was squished out of the piston was not homogeneous, as shown in fig. 3.11b. Therefore, if, e.g., the aluminium was placed at the top of the sample cell, as in fig. 3.11, aluminium would pour more out from the piston than indium, so that the initially known concentration was offset by the non-isotropic expulsion of ejected metal. If possible, the concentration in a sample with a lot of ejecta was calculated using the two samples with minimal ejecta as references. If all samples had similar amounts of ejecta, it was assumed that the end concentration was not significantly different from the initial concentration, although that can not be known for certain.



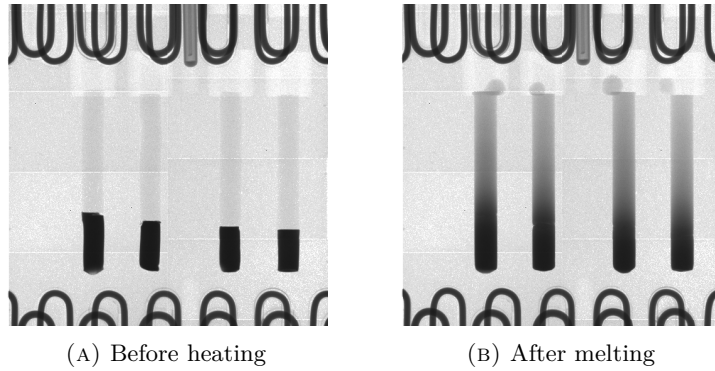


FIGURE 3.11: Before heating and shortly after melting of a new Al-In sample cell.

### 3.4 X-ray imagery

To get the time dependent concentration separation and interdiffusion coefficient, as described by eq. (2.74), a knowledge of the development of the concentration separation is needed.

In optically transparent fluids, methods like optical digital interferometry (ODI) is common, where lasers of different wavelengths are used, and the angles of refraction are measured over the sample [149]. This way, the refractive index can be determined and, linked with the previous knowledge of the dependence of the refractive index on the concentration of the mixture, the concentration across the sample cell can be computed.

In previous experimental works on binary alloys, closed containers with columns of the liquid where used which were submitted to a thermal gradient for a certain amount of time, then quickly cooled and finally analysed in the solid state [51–53]. To avoid changes of the concentration gradient during solidification, some experiments instead used a shear cell technique, where the sample is split up in segments after the annealing while still in the liquid state [54, 55]. A drawback of both these methods is that possible bubbles in the melt cannot be detected. As mentioned earlier, these bubbles can disturb diffusion measurements [56, 57].

To measure the interdiffusion coefficient, the concentration separation over time is needed, but without any in situ method, samples have to be analysed at different times, also making it time-consuming to analyse for several times.

As has been shown by Sondermann et al., using in situ XRR allows time- and space-resolved measurements of thermodiffusion in liquid alloys, where bubbles or free surfaces can be directly detected during the experiment [60]. This allows measurements to be made thousands of times during the thermodiffusive process, compared to a handful of times for an ex situ method [53, 60, 150].

For X-ray imaging we used a micro-focus X-ray source (XT9160-TED, Viscom AG, Hannover, Germany) which was operated at 100 kV and 120  $\mu$ A, and a CdTe detector with a 100  $\mu$ m pixel size (XC-Thor series, Direct Conversion AB, Danderyd, Sweden). With the sample cell located between the source and detector, the resulting images have a resolution of 20 pixels per millimetre across the sample, due to the magnification of a factor  $\frac{d_{SD}}{d_{SS}}$ , with the distances source–detector (SD) and source–sample (SS) indicated in fig. 3.12, a figure

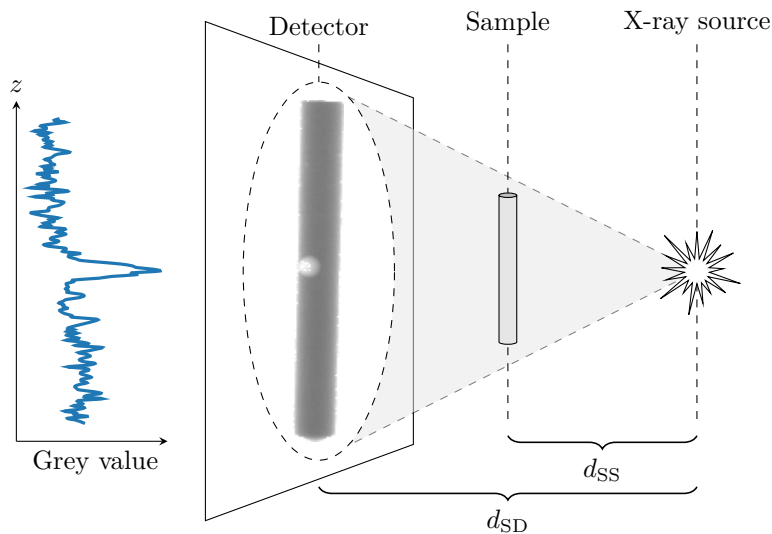


FIGURE 3.12: Schematic of the X-ray setup.

adapted from a previous PhD thesis of the group [63].

### 3.4.1 Image noise

The captured X-ray images were noisy, as can be seen in fig. 3.13, where an XRR image was taken of a sample cell. A high degree of noise is visible all over the image, and especially stripes over the different segments of the X-ray detector are visible both horizontally and vertically.

The raw images were all filtered by flat-field correction with reference grey images, the reference images being featureless images, as shown in fig. 3.14. The noise from the detector is especially apparent if a histogram of the grey values in fig. 3.14 is calculated, as is shown in the top plot of fig. 3.15. A wide range of grey values is registered, with a wide peak with a standard deviation of  $\sigma_{\text{unfiltered}} \sim 240$ . If one takes several reference images, and filters one with the others, the noise is greatly reduced, as indicated by the much sharper peak in the bottom plot of fig. 3.15 (bins of 16 in both plots). There is still some deviation in the filtered reference image, though, showing that not only is there a static noise constant in all images, but also a random fluctuating noise between each image, amounting to a standard deviation of  $\sigma_{\text{filtered}} \sim 25$ . Due to this deviation, it was important to not use only one reference image, but a series of reference images to attempt to average out the random fluctuations as best as possible. The average of around 200 reference images captured in sequence were used for the flat-field correction. From this series, it was also observed that the first  $\sim 5$  reference images had uneven slope of grey values across the image, while the first  $\sim 100$  reference images had slightly increasing average grey value, probably due to cold starting of the X-ray source and detector. Therefore, those first images were discarded in the flat-field correction, and only the stable reference images were used.

For flat-field correction, one takes a featureless image  $B^*$ , where the deviation

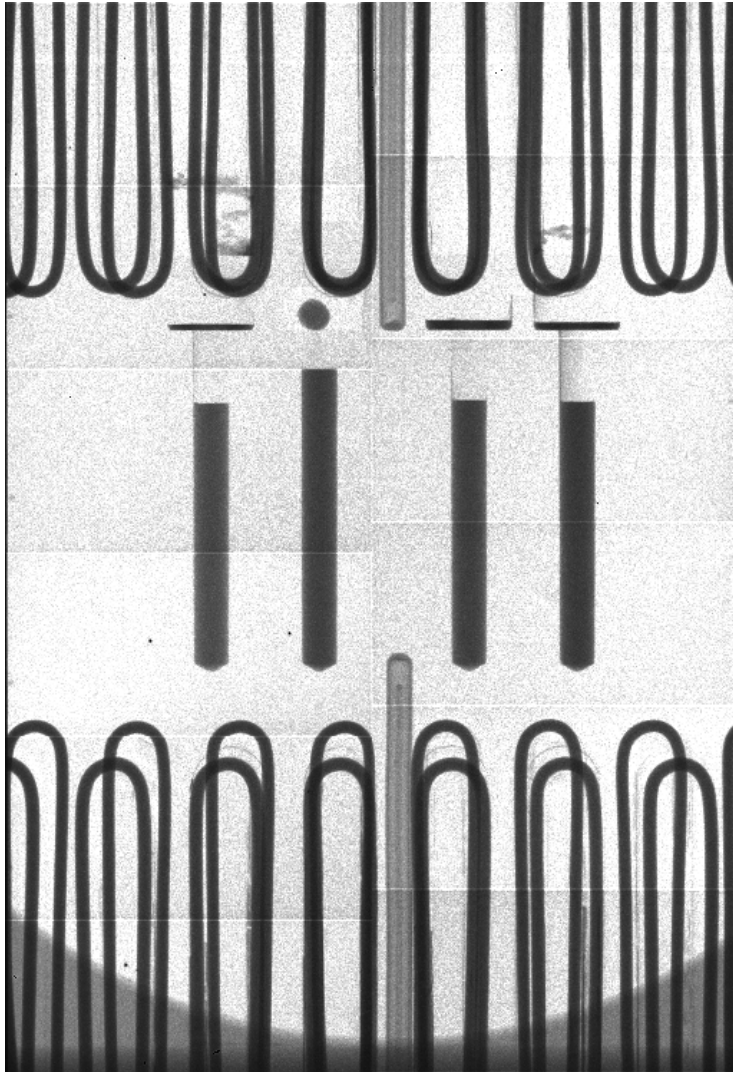


FIGURE 3.13: Raw XRR image straight from the detector.

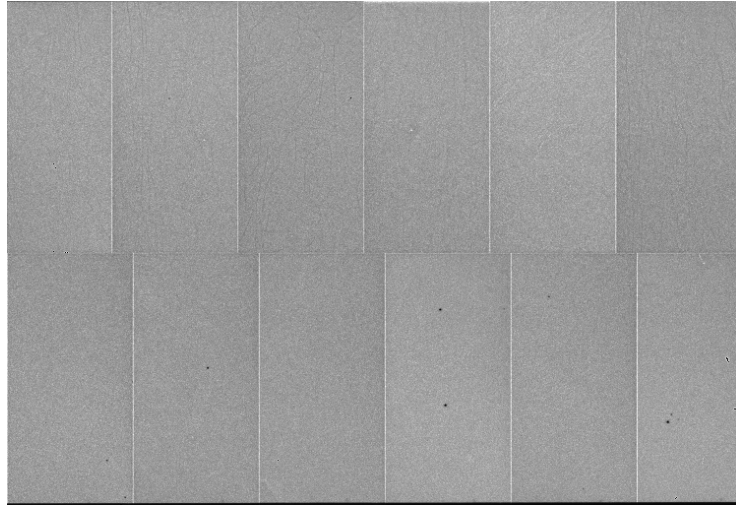


FIGURE 3.14: Reference image used for flat-field correction.

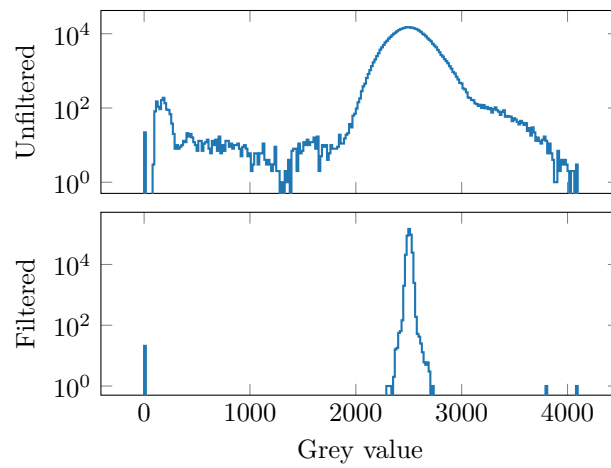


FIGURE 3.15: Histograms of grey values in fig. 3.14.

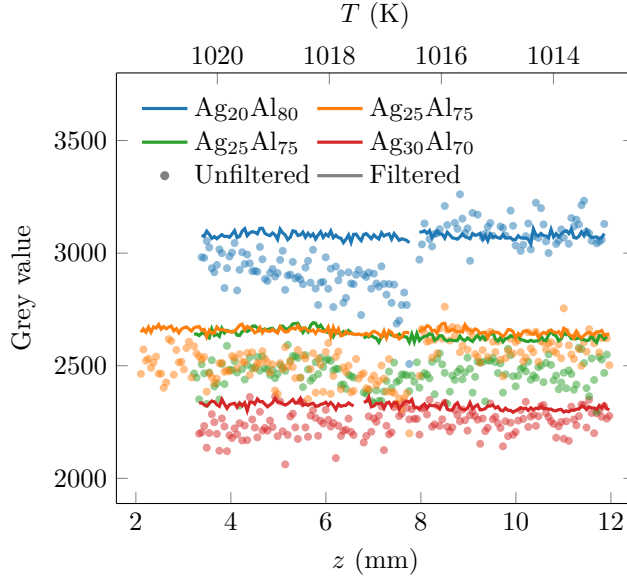


FIGURE 3.16: Grey value along the samples in fig. 3.20 with and without filtering.

from the mean grey value  $B$  for each pixel is read as the static noise. It is assumed that this static noise is scaling with the brightness of the image. Then, as the image of the experiment  $A^*$  has the same static noise as the reference image, the wanted image without the noise  $A$  is then given by

$$A = A^* \times \frac{B}{B^*}. \quad (3.2)$$

$A$  is the filtered image.

With this, the noise of the recorded images is reduced, as already shown in fig. 3.15.

The grey value along the samples in the above case is shown in fig. 3.16. A great reduction of the noise in the data is shown.<sup>8</sup>

### 3.5 Energy-dispersive X-ray spectroscopy

For the investigation of ternary alloys, or alloys that did not have sufficient contrast using XRR, EDXS was utilised. With EDXS, the energy of X-rays generated by a focused electron beam is measured and analysed to identify the energy levels from a database of indexed elements [151]. The relative intensity of the different energy levels are then measured to identify the relative concentration of the different elements. For the EDXS performed for this thesis, a X-MaxN50 detector operated under AZtec software, both by Oxford Instruments, were used in tandem with a Merlin SEM from Carl Zeiss AG.

<sup>8</sup>Note that as the image noise is randomly distributed, even unfiltered concentration data will give similar coefficients to the filtered concentration data when fitted to a time series. Therefore this step is mainly for aesthetic purposes.

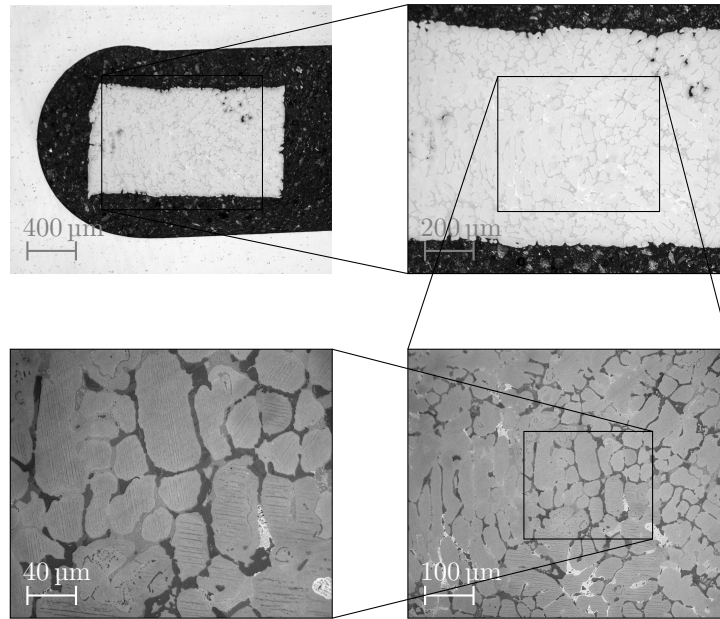


FIGURE 3.17: Light microscopy imaging of a sample of  $\text{Ag}_{43.1}\text{Al}_{43.1}\text{Cu}_{13.8}$  later analysed with EDXS.

After shearing, and subsequent cooling and solidification of the liquid alloy, the sheared samples were extracted from the BN plates, placed in an aluminium frame embedded in Struers PolyFast epoxy resin. After curing and subsequent sanding and polishing, the samples were analysed in the SEM. Such a polished and sheared sample piece of Ag–Al–Cu is shown in fig. 3.17 at 5x, 10x, 20x and 50x zoom. Using EDXS, the composition of the three constituting elements was measured over the entire sheared section. This procedure was performed for each sheared piece of the samples, and repeated three times at different depths into the sheared sample.

### 3.6 Temperature measurement and control

The temperature in the sample was measured at the top and the bottom of the samples, 12.5 mm apart, with two sheathed thermocouples of type K with a diameter of 1.0 mm. Delivered by THERMOEXPERT Deutschland GmbH, the thermocouples have an Inconel coating, rated for temperatures of up to 1373 K. The thermocouples were held in their position only by the friction to the surrounding graphite foam and casing, and therefore sometimes fell out from their intended position during the experiment, especially the bottom thermocouple, due to gravity and/or shaking. This is sometimes visible in the photos in this thesis, like for example in fig. 3.11.

The point where the temperature is measured is the tip of the inner wires, isolated inside the inconel sheathing [148]. This has to be taken into consideration when the temperature gradient is calculated, as the precise distance between the two measurement points must be known for an accurate determination of the

temperature gradient. The measurement point was roughly 0.9 mm deep inside the sheathing.

As mentioned in section 3.2.3, the thermocouples are subject to an measurement error of  $\Delta T = 0.004 \times (T - 273.15 \text{ K})$ , according to the manufacturer [148]. It follows then that for the experiments presented here, the measurement error is within 2.8 K to 3.6 K. The temperature readout itself, read with a Eurotherm model 2704, was stable to within  $\pm 0.1 \text{ K}$  after reaching the target temperature.

The precision of the temperature measurement itself could be ascertained during the liquefying and solidification of the samples. This is shown in fig. 3.18, where on the left, the melting of samples of  $\text{Ag}_{20}\text{Al}_{80}$  (blue),  $\text{Ag}_{25}\text{Al}_{75}$  (orange and green), and  $\text{Ag}_{30}\text{Al}_{70}$  (red) are illustrated by the deformation of the originally 1.2 mm wide solid samples into the 1.3 mm wide sample cell borings, the sample length  $L$  thus getting reduced. The vertical lines show the Ag–Al liquidus temperatures for the relevant concentrations, as calculated from the Gibbs energies evaluated by Witusiewicz et al. [67], with the calculated liquidus temperature annotated at the times when the temperature crossed the liquidus for each concentration. On the right, the solidification of samples of Al–In is indicated by the temperature measurement of the sample cell. The cooling rate is slightly reduced as the temperature passes the monotectic temperature (the vertical line), where the aluminium-rich phase in the Al–In mixture solidifies, releasing the latent heat during the phase transition. The monotectic temperature is calculated from the Gibbs energies evaluated by Sommer et al. [142].<sup>9</sup> As it can be seen in the plots, the phase transitions occurred close to the predicted temperatures, meaning that the temperature measurement error reported from the supplier is credible, while also further certifying the quality of the alloys and their components.

### Controlling the temperature

The heat to the sample cell was delivered through the molybdenum heating wires, driven by two power supplies, one for each side of the samples. To sustain temperatures of 1000 K inside the sample cell, a total combined power of roughly 200 W was needed.

The electrical powers for each side were controlled by separate proportional–integral–derivative (PID) controllers, basing the output of a system on the measured error (proportional term), history of error (integral term) and step-change of error (derivative term) from a control signal. The PID for the electrical power was controlled by the Eurotherm 2704 multichannel controller and LabVIEW software. The LabVIEW program was previously developed for earlier conducted interdiffusion measurements in the laboratory used. It was quite old and outdated, and difficult to maintain due to the use of older sub-packages and lack of documentation. The PID coefficients initially used for the interdiffusion experiments were adequate for maintaining a constant temperature across the samples during the entire experiment, but not great for a thermodiffusion experiment, with separate acting heaters, where the temperature first should be isothermal, and then as quickly as possible changed to a stable temperature gradient, by having the top heater have constant temperature, while the bottom heater were to drop its temperature as far down as possible.

<sup>9</sup>See footnote 4 in section 3.1.4.



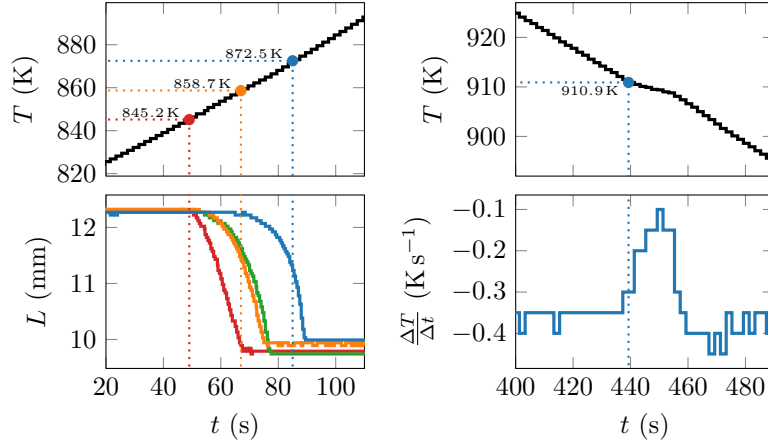


FIGURE 3.18: Indirect measurements of phase transitions during melting and solidification. The onset of the melting process is indicated by a change in the sample length as can be seen for Ag–Al alloys in the graph in the left. The onset of solidification can be seen as change in the cooling rate for the example of Al–In.

Alternatively, a setting could have been used, so that the top and bottom temperatures could have been increased and decreased equally, so that the mean temperature is kept constant. But the maximum temperature difference was different between each experiment, depending on the water cooling of the sample chamber, vacuum quality, heating wire wear, graphite foam wear, etc. So setting the top and bottom heaters to say 1010 K and 990 K, respectively, after having the isothermal phase at 1000 K, would either have been impossible to achieve, resulting in the bottom heater unable to fall down to the target temperature, giving mean temperature not equal to 1000 K anyway, or, if it was possible to achieve the target temperatures, having given a temperature difference that was less than the full potential of the setup. As the Soret effect is so weak, and the uncertainty for the experimental setup so high, it was preferred to achieve a maximum temperature difference, to maximise the concentration difference and thus the image signal, with the cost of having to change the mean temperature during the experiment.

An attempt was done to find better-fitting PID coefficients, during which it was discovered that the actual PID control function was<sup>10</sup>

$$f(t) = \frac{32}{K_P} e(t) + \frac{1}{4K_I} \sum_{\tau}^t e(\tau) \Delta\tau + \frac{K_D}{4} \frac{\Delta e(t)}{\Delta t}, \quad (3.3)$$

<sup>10</sup>The derivative term  $\frac{\Delta e(t)}{\Delta t}$  appeared to be based on filtered data for the temperature control. The temperature measurements are discrete data in increments of 0.1 K, and therefore the derivative term is integer amounts of  $\frac{0.1 \text{ K}}{2 \text{ s}}$  (the data recording interval being 2 s). When the temperature changes slowly close to the target, the discreteness of the data would have made the PID controller exaggerate the error term if there was simply a 0.1 K noise or flip in temperature. What filter the algorithm is using is difficult to say, but applying a Savitzky–Golay filter of bin size 51 and polynomial order 3 as implemented by the Python SciPy package to the temperature data returned voltages very similar to the ones supplied by the hidden control function [152, 153].



with the error signal

$$e(t) = T_t(t) - T_m(t), \quad (3.4)$$

where  $T_t(t)$  and  $T_m(t)$  are the target and measured temperatures, respectively, at time  $t$ .  $K_P$ ,  $K_I$  and  $K_D$  are the PID coefficients. Note that the PID control in eq. (3.3) is different from the textbook PID control function [154]

$$f(t) = K_P e(t) + K_I \sum_{\tau}^t e(\tau) \Delta\tau + K_D \frac{\Delta e(t)}{\Delta t}. \quad (3.5)$$

After trial and error, the PID coefficients for eq. (3.3) were improved from the original set of

$$\begin{aligned} K_{P,1} &= 143.7, & K_{I,1} &= 227, & K_{D,1} &= 38, \\ K_{P,2} &= 72.2, & K_{I,2} &= 105, & K_{D,2} &= 17, \end{aligned} \quad (3.6)$$

to the new set

$$\begin{aligned} K_{P,1} &= 130, & K_{I,1} &= 100, & K_{D,1} &= 100, \\ K_{P,2} &= 130, & K_{I,2} &= 100, & K_{D,2} &= 100, \end{aligned} \quad (3.7)$$

where subscript 1 indicates the top heater being controlled by thermocouple 1 (TC1), and 2 indicates the bottom heater being controlled by thermocouple 2 (TC2).

The effectiveness of the two coefficient sets in eqs. (3.6) and (3.7) are shown in fig. 3.19 for both the mode of keeping the top temperature constant and the mode of keeping the mean temperature constant. As can be seen in the figure, the mode of keeping the top temperature constant (left side of the figure) was much more rapid than the mode of setting a temperature difference so that the mean temperature was constant (right side of the figure). In the case of the constant mean temperature, a total temperature difference of  $\Delta T = -20$  K was set, which the PID control slowly was able to attain. But due to the PID control slowly decreasing the heater to attain the bottom temperature close to the previously set temperature, the PID control only carefully decreases the power, and thus the temperature, at the cold side. In this slow mode of constant mean temperature, the old coefficient set spent almost 50 min to attain a stable temperature difference of  $\Delta T = -20$  K, while the new coefficient set spent 35 min, in addition to reducing the oscillation in TC1 and TC2. Still, the mode of keeping the top temperature constant was much quicker, by targeting an unattainably low bottom temperature, so that the bottom heater simply turned off, reaching the maximum possible temperature difference in less than ten minutes for both coefficient sets.

As can be seen on the left side of fig. 3.19, when it comes to arriving at the target absolute temperature, the old PID coefficient set from eq. (3.6) and the newer set from eq. (3.7) perform more similarly than the case of constant mean temperature on the right of the figure, although the newer PID coefficient set favours overshooting over the more dampened older PID coefficient set. This makes a system controlled with the newer set not cool down as much as one controlled with the older set, which can be a benefit if working with samples close to solidification or close to a critical temperature, under which where the samples would get demixed. As can be seen on the lower left of the figure, the build-up time of the temperate difference itself is somewhat quicker for the new

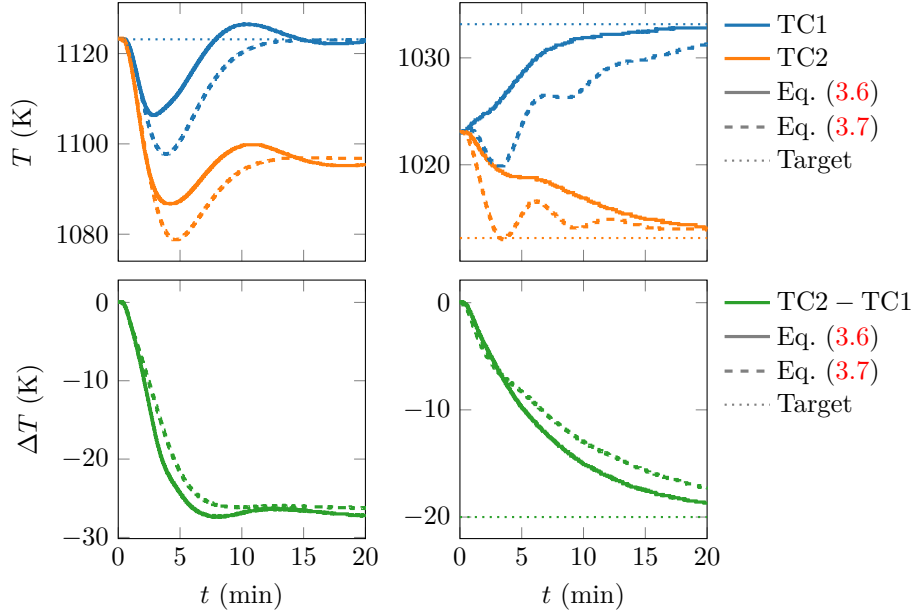


FIGURE 3.19: Comparison between the sets of PID coefficients in eqs. (3.6) and (3.7).

set than the old set, with 50 % of the final temperature difference  $\Delta T$  being reached within 2.5 min for the new set, compared to 3.1 min for the old set. The time to reach 90 % of the final temperature difference was 5.0 min for the new set, compared to 5.9 min for the old set.

Still, changing the temperature by manually setting the power is even quicker if the power needed is already known, due to the PID controller carefully treading closer to the target value. It would be beneficial to use a temperature controller which was custom made for thermodiffusion experiments, i.e., first isothermal, then a quickly applied stable temperature gradient. An option would be to combine the two, manual and PID control, by first setting the stable isothermal temperature with the PID, and then, when the temperature difference is to be initiated, use the stable isothermal power to predict the power needed for the top heater to heat the cell alone. Assuming that the total power  $P = P_1 + P_2$  supplied at the isothermal state (summed from the powers supplied to each side of the sample cell) is similar to the power needed at the top heater for the gradient state would be approximately the same (assuming similar heat loss), the current for the top heater for the gradient state is

$$I_{\text{top}} = \sqrt{\frac{P_{\text{top}}}{R_{\text{top}}}} = \sqrt{\frac{R_1 I_1^2 + R_2 I_2^2}{R_{\text{top}}}}, \quad (3.8)$$

with  $R$  being the electrical resistance. The resistance over the circuits were changing with temperature, so an exact resulting current can not be accurately predicted, but at least guessed. So a possibly better way to control the temperature could have been to use the estimate from eq. (3.8) during the initial phase

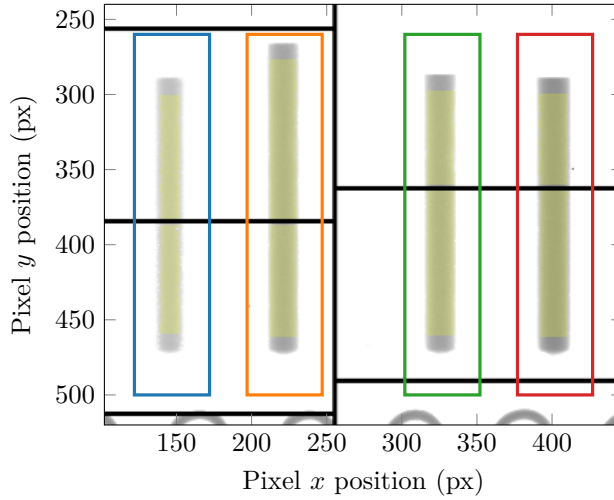


FIGURE 3.20: Tracking of the samples in an XRR image.

of the temperature gradient, assuming for example the resistance to be equal, and then gradually re-inserting the PID control to stabilise the temperature, after the initial gradient is quickly, while unstably, applied. This was planned, and initially attempted using a Python script and the PyQt toolkit for creating a graphical user interface (GUI), but it turned out to be difficult, and was abandoned due to lack of time.

Ultimately, using the LabVIEW program for temperature control with its PID controller, the stable temperature gradient was achieved within 15 min, as seen in fig. 3.19. As previously mentioned, the temperature difference itself attained 90 % of the to-be difference after only 5 min, which is much less than the characteristic time for the systems analysed in this thesis (see eq. (2.75)), which was at least 30 min, and up to several hours for the Al-In system when close to the miscibility gap.

## 3.7 Data analysis

### 3.7.1 Digitally tracking the sample

The sample cell had a tendency to move around in the image, mostly due to changes in the power in the heating wire, expanding or contracting the wires, moving the sample cell position by up to 0.4 mm, which in the image amounted to 7 px. Therefore, the tracking of the sample had to be dynamic.

To track the sample in the data analysis software, the grey value in the image was analysed. Tracking the grey values within a preselected area (the blue, orange, green, and red boxes in fig. 3.20), the sample was defined as being where the grey value was below a set limit for the exposure in the image. Then, the data analysis could locate the sample in each preselected area, also when they moved, as shown by the yellow overlay in fig. 3.20, indicating where the algorithm “sees” the sample. The algorithm cuts off 10 pixels on each side of the sample, as the physical sample ends were slightly rounded, and therefore had

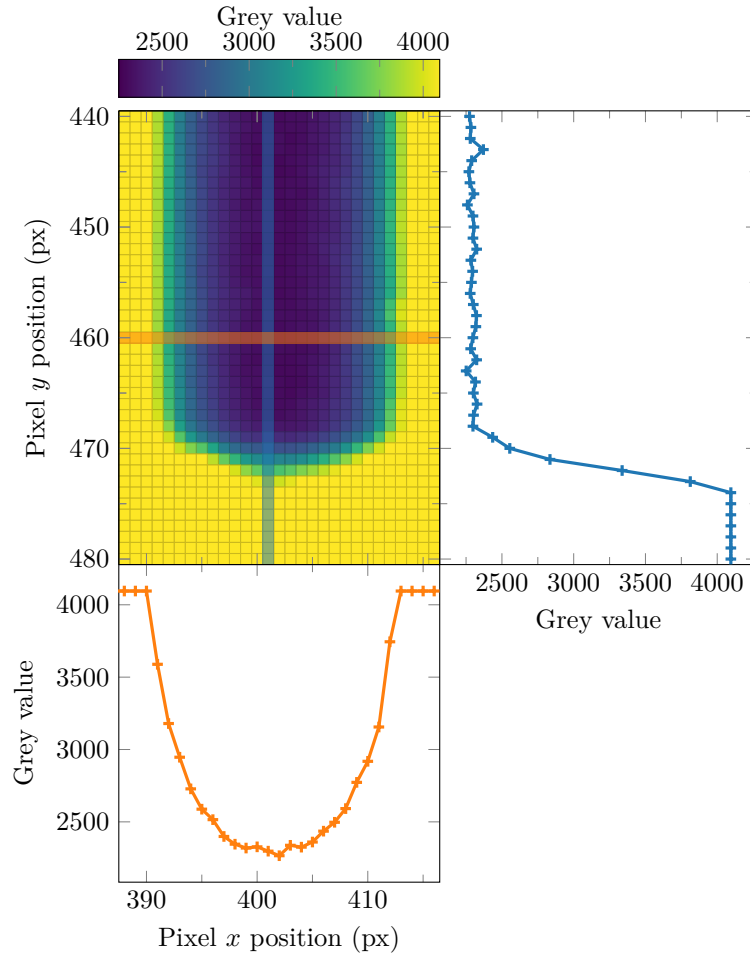


FIGURE 3.21: Grey values at one of the sample ends in fig. 3.20.

increasing grey value at the end, as shown in fig. 3.21, showing a cut-out from fig. 3.20 with increased contrast, and a plot of the grey value along  $x = 401$  px, which is highlighted in blue on the image.

### 3.7.2 Assigning grey values along the samples

As the alloy sample is cylindrical, the grey value changes across the sample, as shown in fig. 3.21, where the grey value across a slice of the sample is shown in orange. To find the concentration along the sample itself (along the blue line in the figure), a grey value has to be assigned to each slice (along the orange line), and the concentration calculated from it. Taking the minimum grey value of each slice is a reasonable method, but due to some noise in even the filtered images, the minimum grey value is not necessarily representative of the actual sample thickness. It was attempted to perform a curve fit of each slice with the

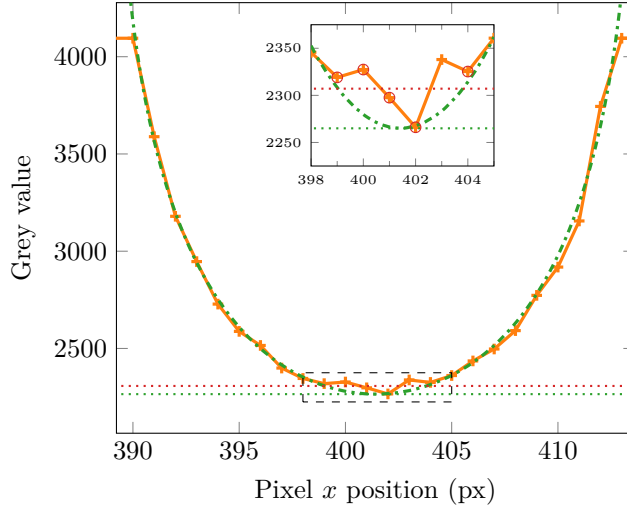


FIGURE 3.22: Fit of eq. (3.9) onto the orange line in fig. 3.21.

grey value  $g$  from a cylinder of radius  $R$ , given from Beer's law by [155]

$$g(x) = \begin{cases} g_0, & |x - x_0| > R \\ g_0 e^{-2aR\sqrt{1 - \frac{(x-x_0)^2}{R^2}}}, & |x - x_0| \leq R \end{cases}, \quad (3.9)$$

where  $g_0$  is the background grey value,  $x_0$  is the centre of the sample, and  $a$  is the absorption parameter. Then, the minimum grey value of the sample is simply

$$g_{\min} = g_0 e^{-2aR}. \quad (3.10)$$

The fit of the function in eq. (3.9) onto the orange slice in fig. 3.21 is shown in fig. 3.22 in green, where the fitted absorption parameter is 0.944 825, and thus with a sample diameter of 1.3 mm,  $g_{\min} = 2265.01$  grey values. The background grey value is fitted to be  $g_0 = 5826.43$ , but it is capped for the imaged data by the 12-bit detector to a grey value of  $2^{12} - 1 = 4095$ . This process is however very computationally expensive, as each experiment records thousands of X-ray images, every image contains four samples, and each sample is almost 200 pixels wide, resulting in over a million curve fits.

It was therefore decided to perform a much simpler arithmetic mean of the five lowest grey values of the slice, reducing the computational time for the analysis with two orders of magnitude, from  $\sim 1000$  s to  $\sim 10$  s. In the case of the slice shown in fig. 3.22, the grey value was then found to be  $g_{\min} = 2307.10$ , shown in red, with the bottom five data points encircled.

As only the relation between the grey values of the different samples is needed, and not the absolute value, the mean of the five lowest values method gives material coefficients equal to the curve fit method, within the experimental uncertainties.

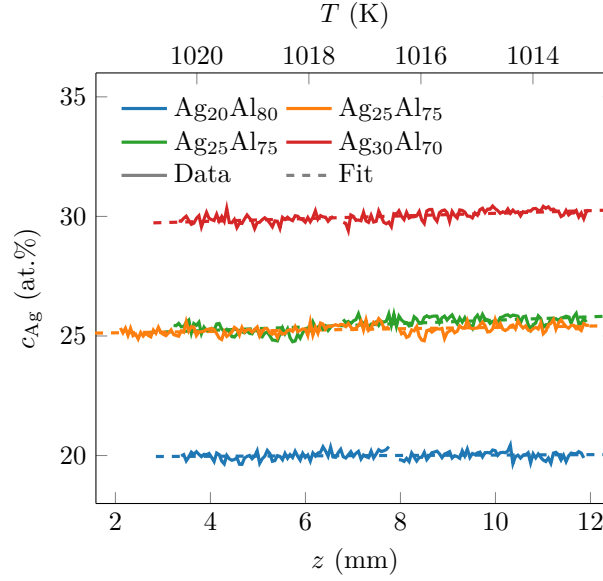


FIGURE 3.23: Calculated concentrations along the samples in fig. 3.20.

### 3.7.3 Calculating concentration from grey value

When the grey value is known along all samples, like the lines in fig. 3.16, and for all images, they are ready to be translated into concentration. Using two of the samples in the image as references, the concentration is calculated for each grey value in each sample in each image, using the equation [156]

$$c_s(I_s) = c_A + \frac{\ln \frac{I_A}{I_s}}{\ln \frac{I_A}{I_B}} (c_B - c_A), \quad (3.11)$$

where  $c_s$  is the concentration of the investigated sample,  $c_A$  and  $c_B$  are the concentrations for the two references, which are set to the concentration that is known from the sample preparation.  $I_A$  and  $I_B$  are the mean intensities, and thus the mean grey values of the two references, due to the proportionality in gain for the XRR detector. Finally,  $I_s$  is the intensity for the investigated sample, and thus grey value of the investigated sample.<sup>11</sup>

From a sample that is 200 px long in the image, it gives 200 grey values along it, and therefore 200 concentration values along it. As mentioned in section 3.7.1, 10 pixels from each end of the sample were masked out, as the changing grey value there from a thinning sample would be falsely interpreted as changing concentration. The concentration data for the samples in fig. 3.20 is shown in fig. 3.23. Compare this with the grey values used for the calculation, which was shown in fig. 3.16.

<sup>11</sup>For the derivation of eq. (3.11), see appendix A.3.

### Adjusting for density change

During the thermodiffusion experiment, the temperature varies along the sample due to the temperature gradient applied to the sample, and also due to the mean temperature over the sample changing when the bottom temperature is lowered while the top temperature is kept constant (see section 3.6). This variation of temperature leads to a variation in density, which results in the grey value changing along the sample. This grey value change comes in addition to the grey value changing due to the mass transport from the Soret effect, and has to be subtracted from the XRR image data to not be falsely interpreted as mass transport.

From Beer's law [155],

$$I = I_0 e^{-\mu d}, \quad (3.12)$$

where the intensity  $I$  transmitted through a medium of thickness  $d$  with a constant absorption coefficient  $\mu$  is related to the intensity  $I_0$  of the incident beam, the absorption coefficient can be related proportionally to the density  $\rho$  of the medium, i.e.,  $\mu = \tilde{\mu}\rho$  [157]. The relation between the intensity transmitted at one temperature compared to another temperature can then, due to the fundamental absorption coefficient  $\tilde{\mu}$  and thickness of the sample  $d$  being equal for both situations, be related as

$$\frac{\ln \frac{I_A}{I_0}}{\rho_A} = \frac{\ln \frac{I_B}{I_0}}{\rho_B}, \quad (3.13)$$

where the subscripts  $A$  and  $B$  denote the parameters describing the conditions at the different temperatures. The density of the alloy at a temperature  $T$  is given by the linear relation

$$\rho(T) = \rho_L + \rho_T(T - T_L), \quad (3.14)$$

where  $T_L$  is the liquidus temperature of the alloy,  $\rho_L$  is the density at the liquidus temperature, and  $\rho_T$  is the change of density per kelvin [66].<sup>12</sup> The density of the alloy is assumed to be from ideal mixing of the pure components, as given by [66]

$$\rho_{\text{tot}} = \frac{\sum_i c_i M_i}{\sum_i c_i V_i + V_E}, \quad (3.15)$$

where then the excess volume  $V_E = 0$  and the partial molar volume  $V_i = \frac{M_i}{\rho_i}$  for a binary system  $A$ - $B$  gives

$$\rho_{AB} = \frac{c_A M_A + c_B M_B}{c_A \frac{M_A}{\rho_A} + c_B \frac{M_B}{\rho_B}}. \quad (3.16)$$

For some alloys, for example Ag-Al, data for non-ideal mixing were available [70], but the implementation thereof did not change the data noticeably, so an ideal mixing was preferred for ease of implementation across all possible alloys.

The X-ray detector proportionally transforms beam intensity into grey value. Then, from eq. (3.13), the same expression can be used for the change in grey

<sup>12</sup>Note that with the definition of the volumetric coefficient of thermal expansion as  $\beta = \frac{1}{V} \frac{\partial V}{\partial T}$ , with  $V$  being volume, it follows that the thermal expansion coefficient is  $\beta = -\frac{\rho_T}{\rho}$ , or, thanks to the fact that  $\rho_T \ll \rho_L$ :  $\beta = -\frac{\rho_T}{\rho_L}$ .

value due to changing temperature, with the grey value  $g$  replacing all instances of the intensity  $I$ , with the same subscripts. The extra grey value due to the changing temperature in the sample can then be given as

$$\Delta g = g_B - g_A = g_A \left( \left[ \frac{g_A}{g_0} \right]^{\frac{\rho(T_B)}{\rho(T_A)} - 1} - 1 \right). \quad (3.17)$$

As the change in density is very small,<sup>13</sup>  $g_A$ , or the grey value at the reference temperature, is approximated by taking the average grey value along the sample. In the majority of the experiments detailed in this thesis, the background grey value  $g_0$  was clipped to the detector's maximum grey value, driven by the detector's limited dynamic range and the intent to enhance contrast between the darker samples. Consequently,  $g_0$  could not be directly extracted from the XRR image data. It was therefore instead estimated by another relation from Beer's law: the absorption coefficient can be described as being proportional to the concentration, through  $\mu = \hat{\mu}c$  [156]. Then, using the two references in the image with known differing concentrations and measurable grey values,<sup>14</sup> the background grey value  $g_0$  was found by the relation

$$g_0 = \left( \frac{g_A^{c_B}}{g_B^{c_A}} \right)^{\frac{1}{c_B - c_A}}, \quad (3.18)$$

with the two references being denoted by the indices  $A$  and  $B$  (the resulting background grey value  $g_0$  is independent on which reference is being used for either of the indices). This relies on the thicknesses of the two reference samples being equal, which it may not be due to small differences in the production of the sample cell, but again due to the small order of changing density in the samples, this was deemed good enough.

The subtraction of the extra grey values from eq. (3.17) was then applied twice: once for the temperature changing along the sample with the mean temperature in the sample used as the reference temperature, and once for the mean temperature in the sample itself changing during the experiment, with the stable isothermal temperature used as the reference. For a typical thermodiffusion experiment as performed in this thesis, the grey value change from thermal expansion is expected to be around 20% of the one from thermodiffusion itself, so it is crucial to take this grey value change into consideration so that the density change is not falsely interpreted as atom migration. The ratio between the grey value change from thermal expansion and the concentration separation from the Soret effect is shown for an alloy with the same thermal expansion as aluminium in fig. 3.24,<sup>15</sup> where the ratio is shown in a contour plot for the initial concentration  $c_0$  and the Soret coefficient  $S_T$ . The area where the ratio is larger than one (i.e., where the grey value change from the thermal expansion is greater than the grey value change from the concentration separation from the Soret effect itself) is shown as a hatched yellow area.

<sup>13</sup>The biggest temperature difference along the samples in the experiments described here were less than 50 K, and with a thermal expansion coefficient typically on the order of  $\beta \sim 10^{-4} \text{ K}^{-1}$ , the change in density is smaller than 0.5%.

<sup>14</sup>See section 3.7.3.

<sup>15</sup>All liquid metals and alloys typically have thermal expansion coefficients on the order of  $\beta \sim 10^{-4} \text{ K}^{-1}$ , where the four pure elements used in this thesis (Ag, Al, Cu, and In) have thermal expansion factors ranging from  $0.9 \times 10^{-4} \text{ K}^{-1}$  for Ag to  $1.3 \times 10^{-4} \text{ K}^{-1}$  for Al.



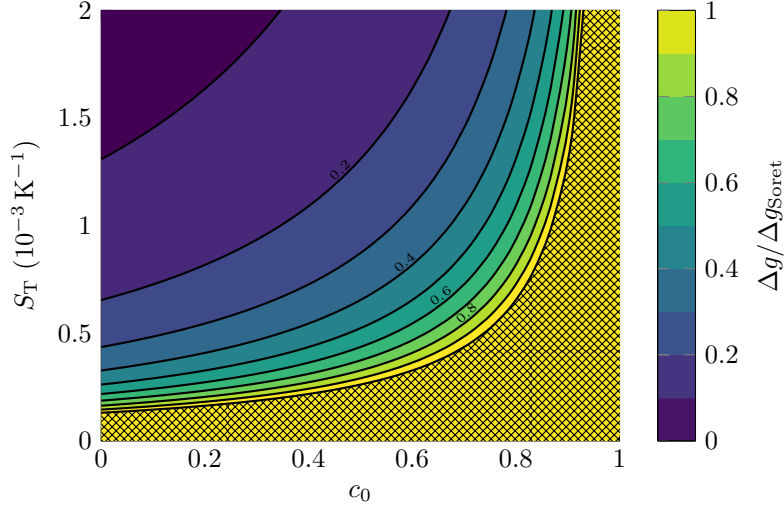


FIGURE 3.24: Ratio between grey value change from thermal expansion and Soret effect.

As for the grey value adjustment due to the changing mean temperature, as each image contains the reference samples, and the mean temperature along the different samples is the same (ignoring slight length differences among the samples), an adjustment for the changing mean temperature is not necessary for the Soret coefficient and interdiffusion coefficient measurements, but purely aesthetic, as it keeps the sample grey value in the images consistent during the experiment. Both these corrections are done in all data presented in this work unless otherwise noted.

### 3.7.4 XRR image scale calibration

For measuring the temperature difference  $\Delta T$  along the sample, it is crucial to have the length of the samples. The length of the sample is also needed to calculate the interdiffusion coefficient, which is given as  $D = \frac{L^2}{\pi^2 \theta}$  from eq. (2.75). With even a five percent error in sample length, that error propagates to ten percent in the calculation of the interdiffusion coefficient.

Due to the repeated experimenting with a single furnace sample cell, thanks to the non-intrusive usage of in situ XRR, the sample length can change between each new experiment during the repeated melting and solidification of the sample between each experiment. Therefore, the sample length had to be determined for each sample for each experiment.

While the sample length may change for each experiment, the span between the samples does not. Therefore, to get a fixed reference on the scale in the images, the centre axis of each sample was tracked through the automatic identification of the samples as described in section 3.7.1. The total pixel span between the outer samples could thus be counted, and the pixels per millimetre be calculated from the known span of the samples of 13.6 mm, as previously described in section 3.2.1.

To check the preciseness of this method, the lengths of four newly prepared

TABLE 3.2: Sample lengths measured with different methods.

	Sample 1	Sample 2	Sample 3	Sample 4
Before embedding	12.28 mm	12.28 mm	12.30 mm	12.28 mm
Measured with XRR	12.27 mm	12.27 mm	12.32 mm	12.32 mm

samples were measured with a calliper before embedding into the furnace sample cell, and then again during an experiment, before the melting of the samples, with XRR together with the method described above. With these two methods, the lengths of the four samples were very similar, as shown in table 3.2. The resolution of the methods is 0.01 mm with the calliper and 0.05 mm using the XRR image. The biggest difference is for the 4<sup>th</sup> sample, with a 0.3 % difference, amounting to a 0.7 % difference in the calculated interdiffusion. This length discrepancy is smaller than the minimal length measured by one pixel, and well within the total uncertainty of the interdiffusion coefficient measurement.

This method only works for the furnace cell, where all the samples are in the same plane in the sample cell. For the shear cell, the two samples are at different depths in the sample cell, and the apparent size of the samples will therefore be different. For the shear cells, the length can be calibrated to the thickness of the shear plates, which have a known thickness of 1.5 mm per piece.

### 3.7.5 Calculating the Soret coefficient

For the calculation of the Soret coefficient, only the concentrations at the two sample ends are of interest, as the Soret coefficient is calculated from the steady-state total concentration difference between the cold and hot side.<sup>16</sup> As mentioned in section 3.7.1, the concentration at the sample ends was not accessible. Therefore, a simple line was fitted to the array of concentrations along the sample with the method of least squares, and the concentrations at the ends were calculated with the function for that line. This line fit then also acted as a filter, taking the trend from all the concentration values along the sample into consideration, giving a simple linear description for this trend. This line fit is a simplification, as the theoretical concentration distribution over the sample during the experiment follows a more complicated function, namely the one given in eq. (2.74). The derivative of eq. (2.74) with respect to  $z$  can be evaluated to be

$$\frac{\partial}{\partial z}c(z, t) = \frac{\Delta c_{\infty}}{L} \left( 1 - \frac{4}{\pi} \sum_{n=0}^{\infty} \frac{1}{2n+1} \sin \left[ \frac{\{2n+1\}\pi z}{L} \right] e^{-[2n+1]^2 t / \theta} \right), \quad (3.19)$$

which is constant (and thus eq. (2.74) is linear) for all  $z \in [0, L]$  only when  $t \rightarrow \infty$ . This then means that the previously mentioned line fit is only valid at the steady-state. But only the concentration distribution at the steady-state is necessary for the calculation of the Soret coefficient from eq. (2.46), so  $t \rightarrow \infty$  is a good approximation, and taking the linear fit is thus valid.

The samples were mixed by heating up in a horizontal state, and rotating to a

---

<sup>16</sup>See eq. (2.46).

vertical state after the samples had fully melted.<sup>17</sup> The calculated concentrations along the samples were observed to have a slope already during this isothermal phase, before the initiation of the temperature gradient, while the sample should have been homogenous. During the isothermal phase, this slope was found to be stable over several characteristic times of the system, where any real concentration gradient would have been changing due to interdiffusion or potential sedimentation. It was therefore concluded that if the concentration was non-changing in the isothermal phase, the sample had to be homogenous, and the apparent slope in concentration had to be from small changes in thickness in the sample cavity of the furnace, presumably from the furnace manufacturing. This then will give an apparent darkening in the thicker end of the sample, and thus a calculated higher concentration of the denser component in that end. This apparent concentration trend was therefore subtracted from the concentration data of each sample, and a perfectly homogenous sample was assumed before the initiation of the temperature gradient,  $\Delta c(t < 0) = 0$ . For the basis of the average slope in the sample concentrations, the concentration data from the images captured the last 20 minutes (approximately 100 images) before the initiation of the temperature gradient were used.

With this slope-adjusted concentration, the Soret coefficient for each sample in an experiment was calculated by using eq. (2.46), so that the concentration difference  $\Delta c$  along the sample was taken from the endpoint concentrations calculated from the linear fit, where again the last 20 minutes of the available concentration data were used for the average steady-state slope. All experiments had a duration of at least three hours after the initiation of the temperature gradient. This duration was assumed to be long enough to have attained the steady-state concentration distribution, as previous interdiffusion coefficient measurements of the Ag–Al and Ag–Cu systems give characteristic times for the sample lengths in this thesis to be around  $2.5 \times 10^3$  s, which means that a sample at three hours of temperature gradient has reached approximately  $1 - e^{-3 \times 3600 / 2500} \approx 98.5\%$  of the steady-state concentration separation [62]. This is well within the uncertainty of these experiments.

As the samples were shorter than the distance between the thermocouples, the effective temperature difference along the sample was calculated to be  $\Delta T = (T_c - T_h) \times \frac{L}{L_T}$ , where  $T_c$  and  $T_h$  are the temperatures measured on each side of the samples, with  $L_T$  being the distance between the thermocouples, which could be measured from the XRR images, and  $L$  the sample length, also measured from the images. This assumes a linear temperature dependency, which was already established in section 3.2.3. With the knowledge of the initial sample concentration  $c_0$  from the alloying process of the samples, the Soret coefficient is given by

$$S_T = -\frac{\Delta c}{\Delta T} \frac{1}{c_0(1 - c_0)}. \quad (3.20)$$

---

<sup>17</sup>When this was not performed, and the samples were melted also in the vertical state, it was observed that the concentration separation changed over time while in the isothermal state, indicating that the different components of the alloy had melted at different points, and therefore had ordered themselves by density by the time the entire sample was liquid. A mixing of the samples after melting was therefore crucial.

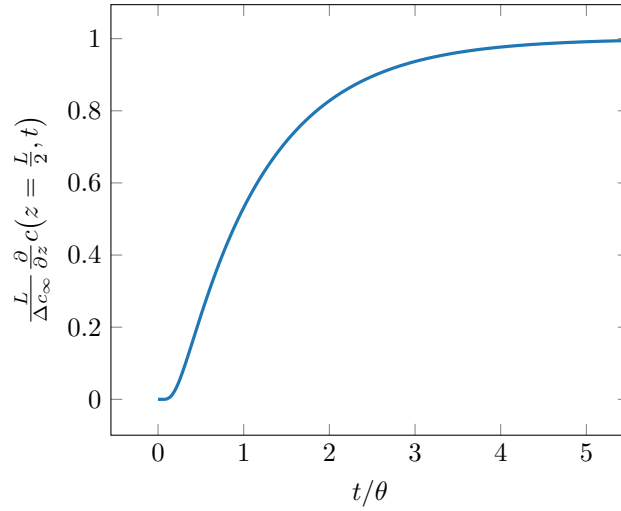


FIGURE 3.25: Plot of eq. (3.21).

### 3.7.6 Calculating the interdiffusion coefficient

#### From the full description of the concentration

The interdiffusion coefficient is possible to obtain from the knowledge about the transient behaviour of the concentration in the sample, as mentioned in section 2.2.2. If the concentration is determined along the sample at different time steps, eq. (2.74) can be fitted to that concentration data, and the interdiffusion coefficient be calculated from the fitted characteristic time.

For experiments where either the Soret coefficient is too small, the temperature gradient too small, or the component contrast too low, the concentration data may be too noisy to fit the full eq. (2.74) to it without large uncertainties.

#### From the derivative of the centre concentrations

Another option is to measure the slope of the spatial concentration gradient at the centre of the sample, and fit this slope from each time step to the expression of the derivative of the concentration with respect to  $z$  calculated at  $z = \frac{L}{2}$ . From eq. (3.19), the  $z$ -derivative at the centre is given as

$$\frac{\partial}{\partial z}c\left(\frac{L}{2}, t\right) = \frac{\Delta c_{\infty}}{L} \left( 1 - \frac{4}{\pi} \sum_{n=0}^{\infty} \frac{[-1]^n}{2n+1} e^{-[2n+1]^2 t/\theta} \right), \quad (3.21)$$

a plot of which is shown in fig. 3.25. Again, the interdiffusion coefficient is calculated from the fitted characteristic time. The benefit of this method is that the change in behaviour of the derivative initially is slow, identified by the twist at the beginning of the curve in fig. 3.25. This is practical, as it means the fitting procedure is less sensitive to the data at the beginning of the temperature gradient, when the equation expects an instantaneously applied temperature gradient, which is not possible in practice. The fitting method of least squares is the most sensitive to data where the derivative of the fitting function is

the greatest, where the error for the respective data point grows quicker than where the rate of change is slow. This time period of the experiment where the temperature gradient goes from zero to a stable gradient is thus affecting the value of the fitted coefficients less than the comparative fitting of eq. (2.74). In addition to this, using the slope of only the centre of the samples thus ignores the sample ends, where the concentration values can not be accurately described due to the brightening of the sample ends, as mentioned in section 3.7.1.

A drawback with using the slope at the centre of the samples, however, is that the total change in grey value along the samples is low, due to the Soret effect generally being so weak. With the discretization of the grey values, this means that the potential slope of the centre is heavily discretized. Furthermore, with the random noise in the image, and therefore in the concentration data, fitting over only a subset of the sample length requires a strong concentration signal for an accurate fit of the concentration slope only at the centre of the sample, which again requires that the Soret coefficient is not too small, the temperature gradient not too small, or the component contrast not too low.

### From the edge concentrations

As earlier shown, due to the weak effect of thermodiffusion, fitting with eqs. (2.74) and (3.21) is dependent on clear data with high signal-to-noise ratio. When this is not the case, another option may be to simply use the concentrations from the endpoints of the sample for each time step, and obtain the interdiffusion coefficient from the fit to the transient total concentration difference  $\Delta c(t) = c(L, t) - c(0, t)$ .<sup>18</sup> In the case of this experimental setup, where there are heavily discretised grey values, and thus discretised concentration values, taking the concentrations at the endpoints of the samples gives the best possible range of the concentration, and the best signal-to-noise ratio. The total concentration difference  $\Delta c(t) = c(L, t) - c(0, t)$  is from eq. (2.74)

$$\Delta c(t) = \Delta c_{\infty} \left( 1 - \frac{8}{\pi^2} \sum_{n=0}^{\infty} \frac{e^{-[2n+1]^2 t / \theta}}{[2n+1]^2} \right). \quad (3.22)$$

Note that the characteristic time  $\theta$  typically is used to denote the time for a system to reach  $1 - e^{-1} = 1 - \frac{1}{e} \approx 0.632$  of its end value. As not a simple exponential term is used, but rather infinite series in eqs. (2.74), (3.21) and (3.22), the speed of the development towards the steady-state value varies along the sample. In eq. (3.22), for example, the characteristic time used for thermodiffusion instead indicates the time for the system to reach  $1 - \frac{8}{\pi^2} \sum_{n=0}^{\infty} \frac{e^{-(2n+1)^2}}{(2n+1)^2} \approx 0.702$  of the steady-state total concentration difference.

Something that should not be forgotten while using eq. (3.22) on the concentration data from the experiments discussed in this thesis, is that the equation describes the endpoint concentrations, which as discussed in section 3.7.1 are not available. As mentioned in section 3.7.5, a linear fit is taken of the concentrations along the sample. With the behaviour of the concentration dependency

<sup>18</sup>As mentioned earlier, the end point concentrations were not available due to the thinning of the samples. An option could have been to fit the concentration 5% from each end to  $c(0.95L, t) - c(0.05L, t)$ , but the random noise in the data from a specific pixel for each image would have been higher than any grey value change from thermodiffusion. Therefore the filtering from the linear fit was preferred over reading concentration from just two pixels of the entire sample.

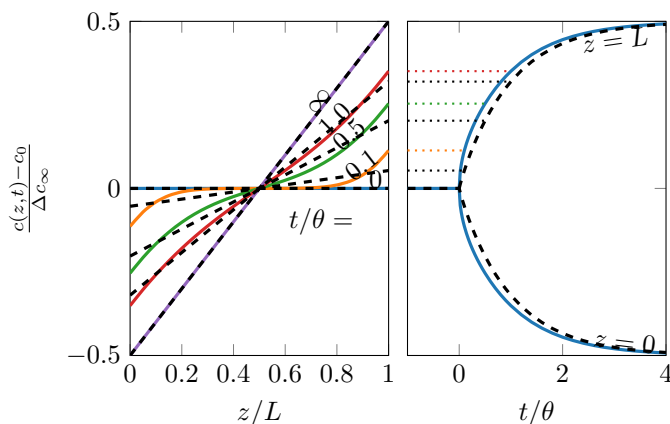


FIGURE 3.26: Concentration for different times with result from linear fit of eq. (2.74).

of position  $z$ , this fit underestimates the endpoint concentration, as shown in fig. 3.26, where on the left hand side the concentration from eq. (2.74) is shown for different times, with corresponding linear fits over the entire sample  $z \in [0, L]$ . On the right hand side, the concentration at the two ends is shown in blue, while the concentration at the endpoints as given by the linear fits at different times is shown with the black dashed line. As is clear from the figure, the concentration separation as described by the linear fit is far from representative of the actual endpoint concentration, especially during the initial phase after the application of the temperature gradient. The more of the sample ends that are ignored (as mentioned in section 3.7.1, 10 px on each side of the sample were cut off), the worse this discrepancy between expectation and reality is.<sup>19</sup>

Another potential issue with using eqs. (2.74), (3.21) and (3.22) for computational fitting is that only a finite amount of terms  $N$  can be used for the series in the equations. The series converge quickly for a high amount of terms, as is shown in fig. 3.27, where on the left eq. (3.22) is shown for different amounts of terms in the sum, and on the right the error relative to using infinite terms is shown.<sup>20</sup> Already at  $N = 100$  terms, the convergence is so quick that the relative error to the idealised infinite terms on the time range  $\frac{t}{\theta} \in [10^{-3}, 10^1]$ , equivalent to from one second to several hours in these experiments, is smaller than the decimal floating point error of a modern computer of around  $10^{-16}$ . Therefore, 100 terms is used for the calculations with the infinite series in this thesis, unless otherwise noted. The problem with using a finite number of terms is that the value of  $\Delta c(t)$  at  $t = 0$  from eq. (3.22) becomes non-zero, as can be seen the left side of fig. 3.27. Using only one term results in  $\frac{\Delta c(t=0)}{\Delta c_\infty} = 0.1894$ , which is far from the correct value of exactly 0 for the infinite sum. Using 100 results in 0.0020, which at least is significantly smaller than the uncertainty of the fitting method itself. To ensure that eq. (3.22) returns  $\Delta c = 0$  at the initiation of the temperature gradient ( $t = 0$ ), the prefactor  $\frac{8}{\pi^2}$ , which is the reciprocal of the

<sup>19</sup>And in the edge case, where all but the centre pixels are cut away, we get the linear fit as used in the centre slope calculation of eq. (3.21).

<sup>20</sup> $10^6$  terms were used for “infinite”. A calculation using  $10^7$  terms as “infinite” was also performed, with the same results, showing that the result is converging.

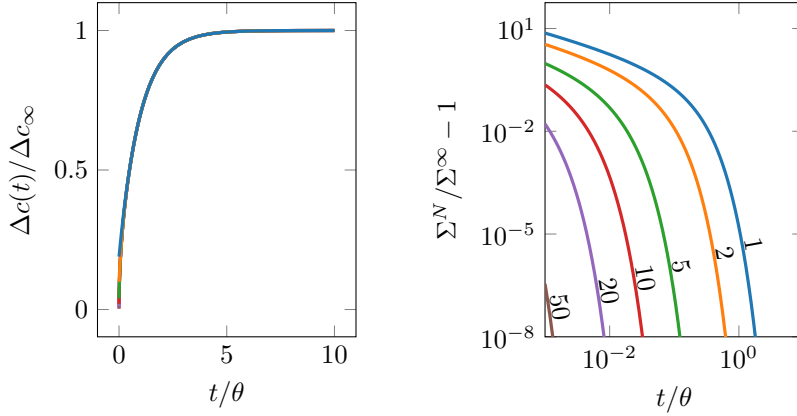


FIGURE 3.27: Relative error for different amounts of terms in eq. (3.24).

infinite sum

$$\sum_{n=0}^{\infty} \frac{1}{(2n+1)^2}, \quad (3.23)$$

must be adjusted to the finite sum of the series. Therefore, to fix this problem when fitting to the measured time-dependent concentration separation using  $N$  terms, the actually fitted equation must be

$$\Delta c(t) = \Delta c_{\infty} \left( 1 - \frac{1}{\sum_{n=0}^N \frac{1}{[2n+1]^2}} \sum_{n=0}^N \frac{e^{-[2n+1]^2 t/\theta}}{[2n+1]^2} \right). \quad (3.24)$$

However, using eq. (3.24) gives worse convergence all over the range of  $t$  than using the constant prefactor of  $\frac{8}{\pi^2}$ , with the same amount of terms, except for at  $t = 0$  itself.

The two issues presented in the previous two paragraphs inhibit the ability to retrieve the accurate interdiffusion coefficient for the imaged system. To test the ability to retrieve the accurate interdiffusion coefficient, noiseless concentration data was simulated with eq. (2.74), which was calculated for an array of 200 equally spaced positions in  $z \in [0, L]$ , for 1000 equally spaced time steps from 0 to a range of end times  $t_{\max}$  ranging from  $10^{-1}$  to  $10^2$  characteristic times, representative of 1000 images of roughly 200 px long samples with the varying characteristic times encountered in the experiments. Calculating the time-dependent concentration for a known interdiffusion coefficient  $D$ , the linear fit was performed in each image to the concentration array with the 10 edge pixels being removed on each side, just like for the real experimental data. For this time series of concentration separations, eq. (3.22) was fitted to the data with varying terms of sums, both with a the constant  $\frac{8}{\pi^2}$  prefactor, and the adjusted prefactor as presented in eq. (3.24). The resulting fitted interdiffusion coefficient  $D_{\text{fit}}$  is shown for the different lengths of time arrays in fig. 3.28. The black dotted line indicates where  $D_{\text{fit}} = D$ . The lighter-coloured area around the lines is the uncertainty of the fit, shown as one standard deviation of the error for the fitted interdiffusion coefficient, as returned by the fitting procedure, which in

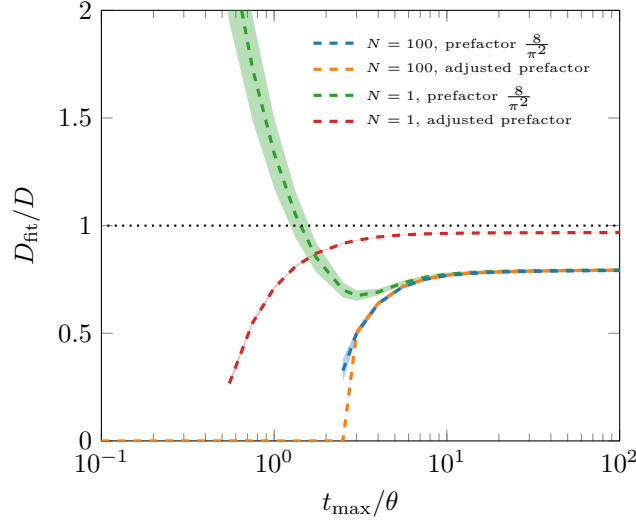


FIGURE 3.28: Fitting the interdiffusion coefficient to calculated data from eq. (2.74).

this case was the `curve_fit` function of the Python SciPy package [153]. Only the coefficients where the returned uncertainty is below 100 % are shown. In the rest of the fitted interdiffusion coefficients, the uncertainty was often so small that it is not visible.

Neither using 100 terms of eq. (3.22), nor eq. (3.24), gives an accurate fit, as demonstrated by the blue and orange dashed lines, respectively. For 100 terms of eq. (3.22) (blue dashed line), the fitting function is unable to determine a fit with less than 100 % uncertainty until an experiment lasts for at least 2.5 times the characteristic time of the system, from where the interdiffusion coefficient starts converging onto a value of  $D_{\text{fit}} \approx 0.8D$ . For 100 terms of eq. (3.24) (orange dashed line), the fitting function “hallucinates” a fit, finding an interdiffusion coefficient four orders of magnitude lower than the actual coefficient fed into eq. (2.74), until it finally converges for experiment durations  $t_{\text{max}}$  of 3.0 times the characteristic time and higher, but still only to  $D_{\text{fit}} \approx 0.8D$ .

The interesting result comes when only one term is used of the series. While the function with the *unadjusted* prefactor of  $\frac{8}{\pi^2}$  (green dashed line) behaves similar to using 100 terms, if one term with the *adjusted* prefactor is used (red dashed line), i.e., eq. (3.24) with  $N = 1$ , the fitted interdiffusion coefficient returns a remarkably close-to-correct value; within 10 % of the correct value when the experiment duration  $t_{\text{max}}$  is longer than 2 times the characteristic time, and within 5 % when the duration is 4.5 times the characteristic time or longer. The fitting algorithm fails to optimise the parameters of this fit if the experiment duration  $t_{\text{max}}$  is less than 0.5 times the characteristic time, though.<sup>21</sup>

In other words, the error from using the linear fit and the error from using

<sup>21</sup>To get an indication of the correctness of the fitting algorithm itself, 100 terms of eq. (3.22) with the unadjusted prefactor of  $\frac{8}{\pi^2}$  was fitted to the end concentrations from eq. (2.74) directly, which perfectly returned the input interdiffusion coefficient, except for simulation durations of less than 0.25 times the characteristic time, where it failed to optimise the parameters of the fit.



only one term of the prefactor-adjusted concentration separation seem to cancel each other out when the experiment duration is long enough, giving the most accurate rendition of the interdiffusion coefficient when the edge concentrations are not available.

### Summary of the observations

To summarise, there are three possible fitting procedures for the characteristic time, and therefore the interdiffusion coefficient of the system: eqs. (2.74), (3.21) and (3.22), where the first utilises all the concentration data points in both time and space of the sample, the second favours the concentrations at the centre of the sample, and the third favours the concentrations at the endpoints of the sample [158]. From the analysis of the influence of different terms in fig. 3.28, it is clear that using only one term of eq. (3.24) returns the most accurate interdiffusion coefficient when the concentration at the sample ends is deduced from a linear fit of the concentrations along the sample. It should be noted that especially when the signal-to-noise ratio is low, when using the end-point concentration description of eqs. (3.22) and (3.24) is the only viable way to retrieve the interdiffusion coefficient, efforts should be made to record the concentration data at least until 3 times the characteristic time of the system has passed, and preferably significantly longer.

Note that from the fits of eqs. (2.74), (3.21) and (3.22), also a fitted Soret coefficient is returned through the fitted steady-state concentration separation  $\Delta c_\infty = -S_T c_0 (1 - c_0) \Delta T$ , where the initial concentration  $c_0$  is known already before the experiment is initiated, and the temperature separation  $\Delta T$  is known from the temperature measurement. This fitted Soret coefficient is more prone to image noise than the one obtained from the definition of the Soret coefficient discussed in section 3.7.5, as there are two variables  $\Delta c_\infty$  and  $\theta$ , compared to only one variable  $\Delta c$  for the method discussed in section 3.7.5. It is still useful for comparison purposes, though, and can corroborate the validity of the interdiffusion coefficient calculated from the fit.



# Chapter 4

## Results

### 4.1 Ag–Al<sup>1</sup>

Several experiments were performed with liquid Ag–Al, with sample cells of either the alloys Ag<sub>20</sub>Al<sub>80</sub>, Ag<sub>25</sub>Al<sub>75</sub>, and Ag<sub>30</sub>Al<sub>70</sub>, or with the alloys Ag<sub>45</sub>Al<sub>55</sub>, Ag<sub>50</sub>Al<sub>50</sub>, and Ag<sub>55</sub>Al<sub>45</sub>. The middle concentration was represented by two samples, making it four samples per sample cell. The same sample cells could be used several times, as the experiment starts in the isothermal state with being homogenous, and the concentration gradient first appears due to thermodiffusion. On the onset of the next day of experimenting, the samples were melted, stirred in the liquid state by rotating of the samples, and thus again homogenous, ready for subsequent experimenting.

For calculating the Soret coefficient, as laid out in section 3.7.5, the average concentration distribution at the end of the experiment was extracted from the X-ray radiography (XRR) image data, shown for an Ag<sub>25</sub>Al<sub>75</sub> sample in fig. 4.1. The solid black line is the linear fit to the concentrations, with the dashed blue line indicating the isothermal state. The concentration distribution is close to linear at the steady state, as one would expect from eq. (2.74) after several characteristic times, as shown in e.g. fig. 2.5. The data shows that silver migrates to the cold side, which is to the right in the figure, as the silver concentration  $c_{\text{Ag}}$  is increased in that region. From the linear fit, the concentration separation is found to be  $\Delta c = c_c - c_h = 0.16 \text{ at.}\%$ , which together with the temperature difference along the sample  $\Delta T$  being  $-7.2 \text{ K}$  for the shown sample, and the knowledge of the initial concentration of the sample  $c_0 = 25 \text{ at.}\%$ , this for this specific sample in this specific experiment thus gives a Soret coefficient of  $S_T = 1.2 \times 10^{-3} \text{ K}^{-1}$  from eq. (2.46).

With the method described in the previous chapter, the transient concentration separation in liquid Ag–Al samples subject to a temperature gradient was successfully measured [150]. The concentration difference for an Ag<sub>25</sub>Al<sub>75</sub> sample over time with the hot end fixed at  $1023 \text{ K}$  is shown in fig. 4.2. The temperature measurement is shown in fig. 4.2a, while the concentration difference is in fig. 4.2b. The coloured line within the data is the same concentration

---

<sup>1</sup>The results for Ag–Al presented here have also been published in a peer-reviewed journal [150]. Due to a revised method of analysis, the coefficients reported in this section are slightly different to the ones published in that article.

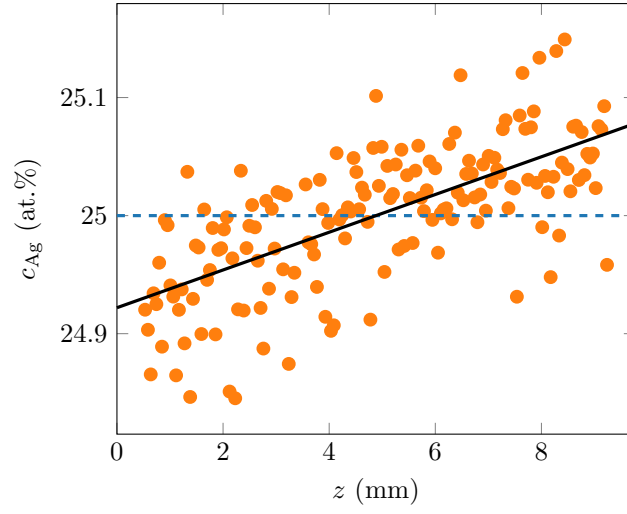


FIGURE 4.1: Concentration along a sample of  $\text{Ag}_{25}\text{Al}_{75}$  at the steady state.

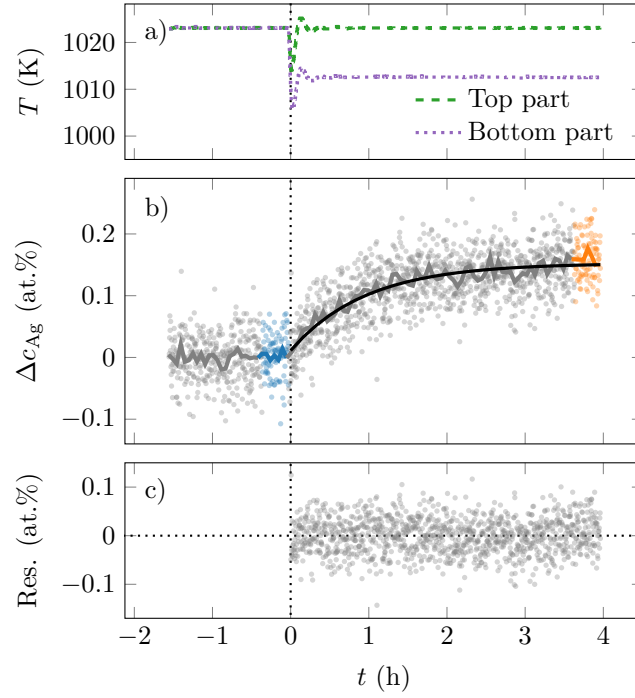


FIGURE 4.2: Temperature along a sample of liquid  $\text{Ag}_{25}\text{Al}_{75}$  (a), with the induced concentration difference  $\Delta c(t)$  along the sample (b), and the residuals to the fit of eq. (3.24) (c).

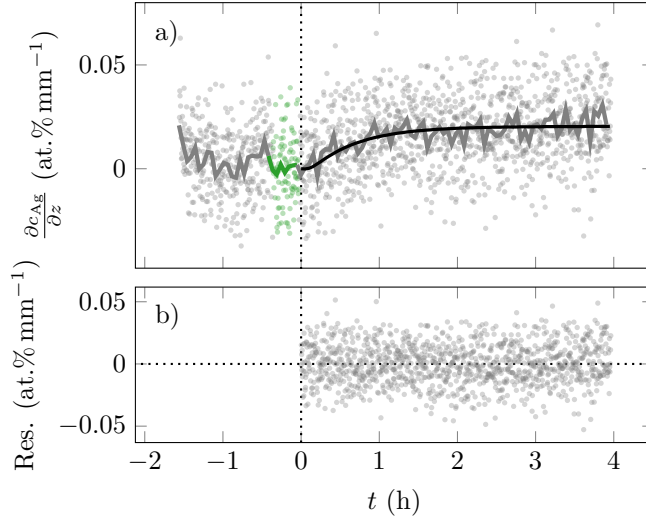


FIGURE 4.3: The slope of the concentration fit from the centre of a  $\text{Ag}_{25}\text{Al}_{75}$  sample.

data, but binned together with a bin size of 15, i.e., averaging over every 15 data points. The noise is then much reduced, indicating that it is of stochastic origin. The blue and orange regions show the basis for the averaged data used in fig. 4.1. The vertical dotted line indicates when the temperature gradient was initiated, and the exponential curve is the fit of eq. (3.24) to the experimental data after the temperature gradient had stabilised. The fit for this specific  $\text{Ag}_{25}\text{Al}_{75}$  sample in this specific experiment gave a interdiffusion coefficient of  $D = 2.8 \times 10^{-9} \text{ m}^2 \text{ s}^{-1}$ , or a characteristic time of  $\theta = 3.5 \times 10^3 \text{ s}$ . That indicates that the experiment ran for a duration of approximately 4.1 characteristic times, or achieving approximately 98% of the concentration separation at a steady state after an infinite time. The Soret coefficient from the fit of eq. (3.24) was returned as  $1.1 \times 10^{-3} \text{ K}^{-1}$ .

The residuals between the concentration data and the fit thereof with eq. (3.24) are shown in fig. 4.2c. The residuals are evenly distributed around 0, with a Pearson correlation coefficient of  $r = -0.017$ , indicating that the fit indeed is properly describing the concentration gradient, without the need for any additional mathematical functions to correct for hypothetical deviations of the data from the zero-line.

Using the method of tracking the slope of the centre of the sample, the coefficients can be independently determined, as described in section 3.7.6. Fitting a linear slope to the concentrations in the middle 60 px of the sample, normalising it to be a zero slope at the isothermal phase, the slopes are shown in fig. 4.3a. The sample shown is the same as in figs. 4.1 and 4.2, and the black solid line is the fit of eq. (3.21) to the slope data. The green region indicates the data which was used for the normalising. The residuals between the slope data and the fit thereof is shown in fig. 4.3b. The residuals are again evenly distributed around 0, with a Pearson correlation coefficient of  $r = 0.022$ . The noise is very strong, however, having the same strength as the signal itself. The fitted Soret coefficient of this method for this specific sample and experiment was

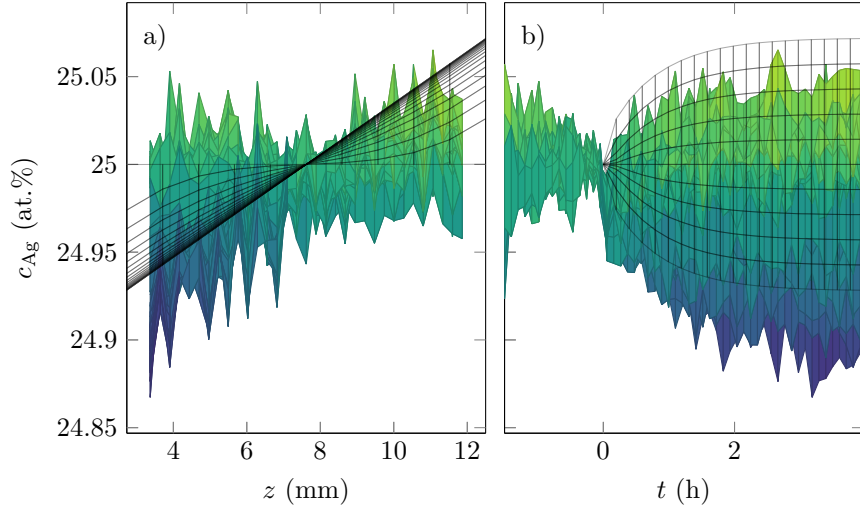


FIGURE 4.4: Concentration data for a sample of  $\text{Ag}_{25}\text{Al}_{75}$  with the fit of eq. (2.74).

$1.5 \times 10^{-3} \text{ K}^{-1}$ , while the interdiffusion coefficient was  $4.5 \times 10^{-9} \text{ m}^2 \text{ s}^{-1}$ , which gives a characteristic time of  $2.2 \times 10^3 \text{ s}$ . That indicates an experiment duration of 6.6 characteristic times, achieving 99.8% of the steady state concentration separation.

Finally, the full concentration equation for position  $z$  and time  $t$  from eq. (2.74) was fitted to the entire set of concentrations along the entire sample (along  $z$ ) for each image (each  $t$ ). This was a very computational expensive fit compared to the two previously mentioned methods, optimising the Soret coefficient  $S_T$  and interdiffusion coefficient  $D$  for the approximately  $200 \times 1500$  array of concentrations (a sample being approximately 200 px wide and imaged approximately 1500 times). The resulting fit for the same sample as before is shown in fig. 4.4, viewed perpendicular to the  $t$ -axis and the  $z$ -axis in figs. 4.4a and 4.4b respectively. The fitted Soret coefficient of this method for this specific sample and experiment was  $1.1 \times 10^{-3} \text{ K}^{-1}$ , while the interdiffusion coefficient was  $3.4 \times 10^{-9} \text{ m}^2 \text{ s}^{-1}$ , which gives a characteristic time of  $2.8 \times 10^3 \text{ s}$ . That indicates an experiment duration of 5.0 characteristic times, achieving 99% of the steady state concentration separation.

These experiments were repeated a minimum of five times with each sample cell, allowed by the noninvasiveness of XRR. The averaged Soret coefficient for each composition from the method described in section 3.7.5 is presented in fig. 4.5. The error bars show one standard deviation for the Soret coefficient for each concentration. The temperature difference was  $\sim 10 \text{ K}$  in all experiments. Note that due to the darkness from the high silver concentration and low contrast,  $\text{Ag}_{55}\text{Al}_{45}$  failed to deliver consistent coefficients, and has therefore been omitted from the results of this work.<sup>2</sup> The Soret coefficients show a slight increase for the lowest silver concentration ( $\text{Ag}_{20}\text{Al}_{80}$ ), but this increase is within the standard deviation of the measured Soret coefficients for all the  $\text{Ag}_{20}\text{Al}_{80}$  samples, and

<sup>2</sup>It was nevertheless still perfectly valid as a reference for correlating grey value to contrast together with the other samples in the image.

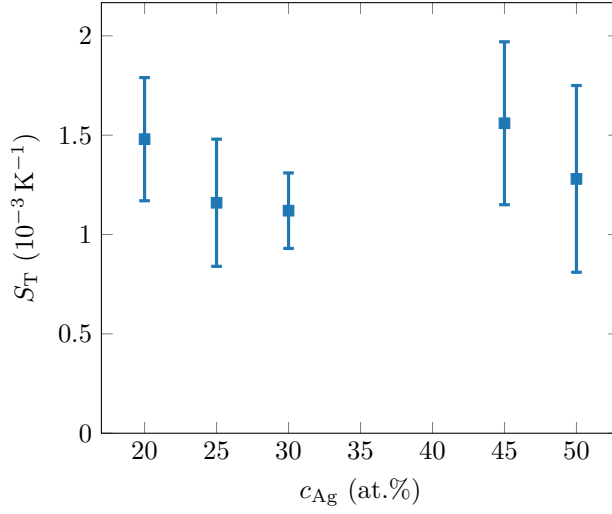


FIGURE 4.5: Soret coefficients for the measured concentrations of liquid Ag–Al at a mean temperature of 1017 K, accumulated from all experiments.

therefore not statistically significant. We thus conjecture that the Soret coefficient is independent of the concentration in the measured range from  $\text{Ag}_{20}\text{Al}_{80}$  to  $\text{Ag}_{50}\text{Al}_{50}$ . Weighting for the different uncertainties for each alloy, the averaged Soret coefficient over the entire measured concentration range is found to be  $(1.3 \pm 0.3) \times 10^{-3} \text{ K}^{-1}$ .

Similarly, the averaged interdiffusion coefficient for each composition from the fit of eq. (3.24) is presented in fig. 4.6, where they are compared with the measurements of Engelhardt et al., who measured the interdiffusion coefficients using the long capillary method in combination with XRR at a temperature of 983 K [81]. The error bars for the results of this thesis again show one standard deviation for the interdiffusion coefficient for each concentration. Due to lower contrast along the darker samples of  $\text{Ag}_{45}\text{Al}_{55}$  and  $\text{Ag}_{50}\text{Al}_{50}$ , the interdiffusion coefficient for these samples has greater uncertainty than for samples of lower silver concentrations. Weighting for the different uncertainties for each alloy, the averaged interdiffusion coefficient over the entire measured concentration range is found to be  $(4.1 \pm 1.1) \times 10^{-9} \text{ m}^2 \text{ s}^{-1}$ , again at a mean temperature of 1017 K.

The Soret and interdiffusion coefficients obtained from the different fitting methods are shown in fig. 4.7, with the definition of the Soret coefficient being eq. (2.46), the equation for the endpoint concentrations being eq. (3.24), the equation for the concentration slope at the centre of the sample being eq. (3.21), and the full equation for the concentrations along the sample being eq. (2.74). The dotted lines are drawn to more easily see the comparability between the different methods. It is evident that the methods give quite similar coefficients, building confidence for the experimental results themselves. For the Soret coefficient, the method of using the simple definition of the coefficient of eq. (2.46) is assumed to be the benchmark method, but especially the methods of the simple exponential for the endpoint concentrations of eq. (3.24) and the full fit of eq. (2.74) return very agreeing Soret coefficients. Meanwhile, the centre slope fit of eq. (3.21) is

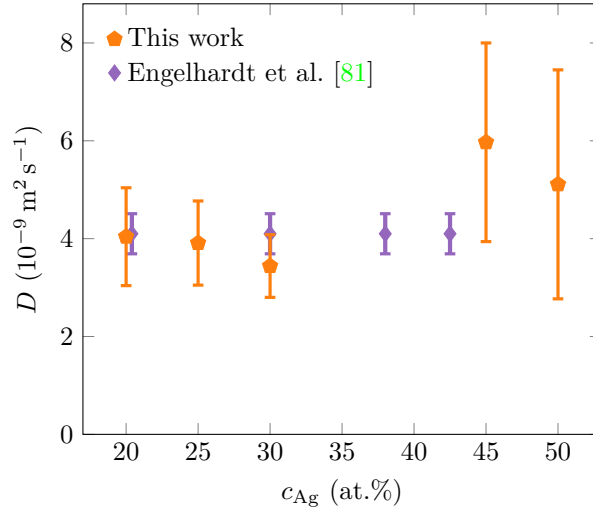


FIGURE 4.6: Interdiffusion coefficients for the measured concentrations of liquid Ag–Al at a mean temperature of 1017 K, accumulated from all experiments. The increased uncertainty for higher silver concentrations is due to worse contrast in the darker samples.

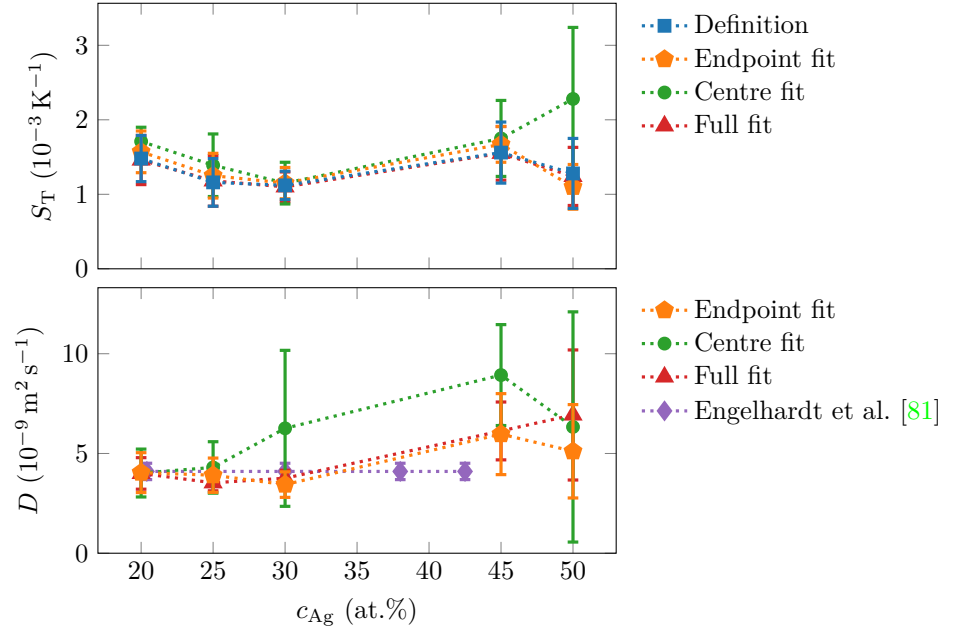


FIGURE 4.7: Soret and interdiffusion coefficients for liquid Ag–Al using different methods for analysing the measured data.



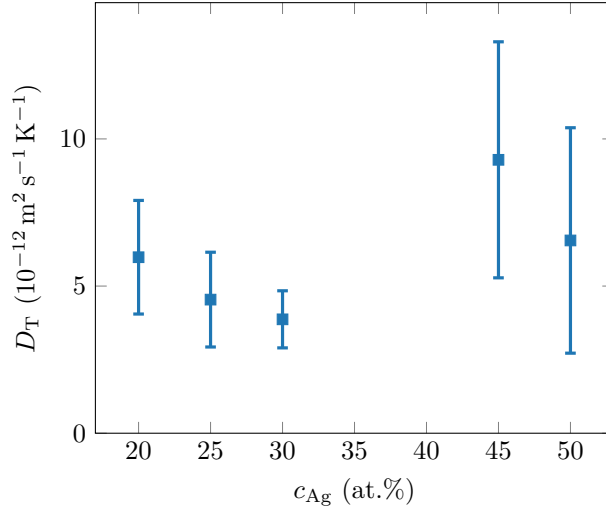


FIGURE 4.8: Thermodiffusion coefficients  $D_T$  for liquid Ag–Al at 1017 K.

more uncertain, especially for higher silver concentrations, where the dynamic range is lowered due to reduced contrast. For the interdiffusion coefficient, the fitting of eqs. (2.74) and (3.24) again give similar coefficients, while the fitting of eq. (3.21) again gives much more uncertain coefficients for the higher silver concentrations.

With the results for the Soret coefficients and interdiffusion coefficients for liquid Ag–Al, the thermodiffusion coefficient  $D_T$  can be calculated through the definition of the Soret coefficient  $S_T \equiv \frac{D_T}{D}$ . The resulting thermodiffusion coefficients are shown in fig. 4.8.

## 4.2 Ag–Cu

An experiment with two samples of  $\text{Ag}_{60}\text{Cu}_{40}$  was performed, with the isothermal temperature at 1123 K. The indicated concentration at the non-isothermal steady state is shown in fig. 4.9. As both samples had the same concentration, the relation from change in grey value to change in concentration was estimated from Beer’s law for the densities [155]. No significant change in concentration separation can be observed, and the same is confirmed from the transient concentration, shown in fig. 4.10. The temperature difference was quickly established, but no significant change in the concentration separation was observed, or at least drowned in the noise. This was expected, due to the darkness of Ag–Cu in X-ray. Therefore the experiment was performed in a shear cell, so that the sample could be divided into several parts at the end of the experiment, and the concentration be investigated ex situ by energy-dispersive X-ray spectroscopy (EDXS). It should be noted that the in situ XRR still is of value, as it identified a free surface in one of the samples, as can be seen in the X-ray image in fig. 4.11. The well-behaving sample (sample A) is the one used for the data analysis shown in the other figures. Also, the recorded X-ray data indicates

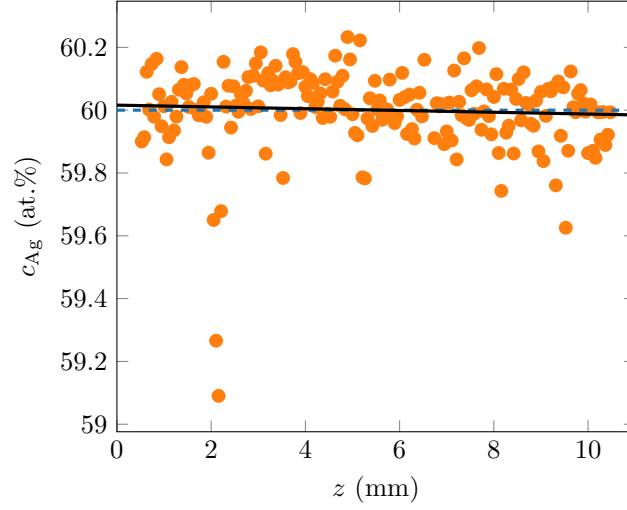


FIGURE 4.9: Indicated concentration along a sample of  $\text{Ag}_{60}\text{Cu}_{40}$  at the steady state.

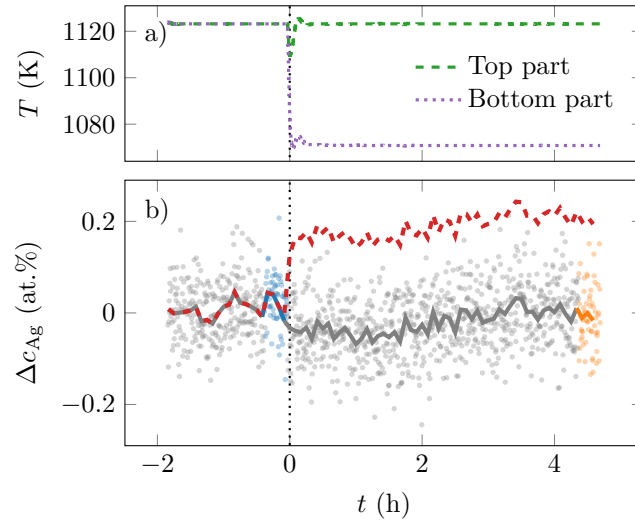


FIGURE 4.10: Indicated concentration difference  $\Delta c(t)$  along a sample of  $\text{Ag}_{60}\text{Cu}_{40}$ , showing no change, as expected due to the darkness of Ag–Cu in X-ray.

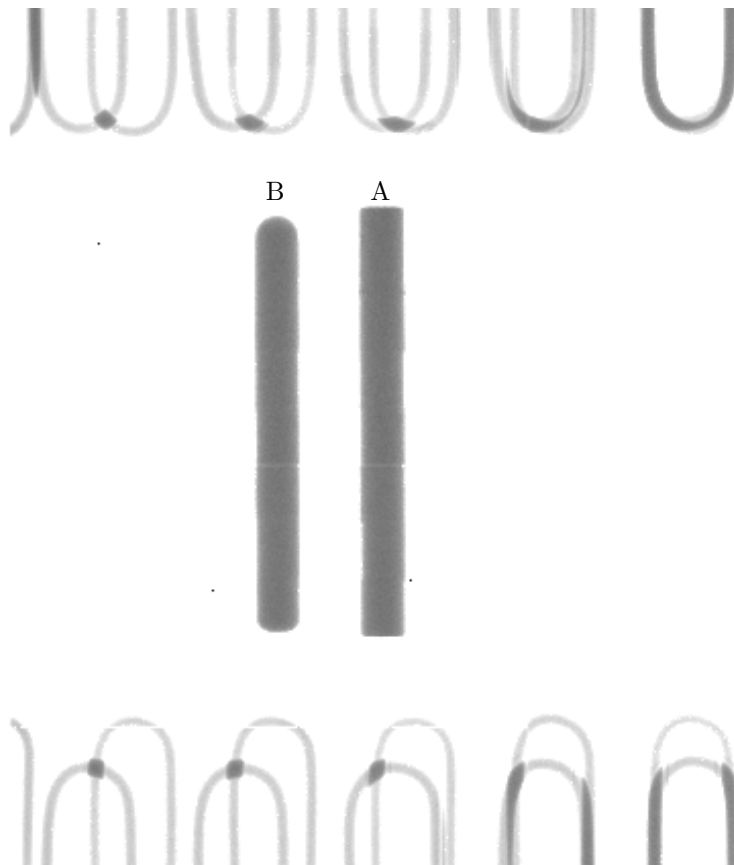


FIGURE 4.11: XRR image from the thermodiffusion experiment of liquid  $\text{Ag}_{60}\text{Cu}_{40}$ , revealing that sample B was not properly compressed.

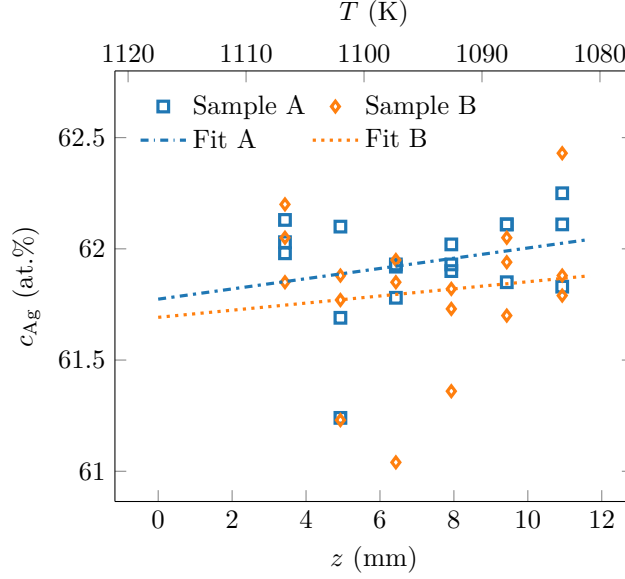


FIGURE 4.12: Concentration along two sheared samples of  $\text{Ag}_{60}\text{Cu}_{40}$ .

TABLE 4.1: Fitted concentration gradient  $\frac{\Delta c_{\text{Ag}}}{\Delta T}$  and Soret coefficient  $S_T$  to the concentration data from the thermodiffusion experiment on  $\text{Ag}_{60}\text{Cu}_{40}$ .

	Sample A	Sample B
$\frac{\Delta c_{\text{Ag}}}{\Delta T}$	$(-0.007 \pm 0.006) \text{ at.\% K}^{-1}$	$(-0.005 \pm 0.010) \text{ at.\% K}^{-1}$
$S_T$	$(0.30 \pm 0.27) \times 10^{-3} \text{ K}^{-1}$	$(0.21 \pm 0.40) \text{ K}^{-1}$

that the density adjustment as laid out in section 3.7.3 was properly performed. The dashed red line in fig. 4.10b shows the unadjusted concentration, with an indicated concentration separation jump of almost 0.2 at.% after the initiation of the temperature difference due to the density changing with temperature. Meanwhile, the adjusted data, in the usual grey, blue and orange colours show very little change in the indicated concentration separation  $\Delta c$ .

After 4.7 h with a temperature difference of  $\Delta T = -34.2 \text{ K}$ , the two liquid  $\text{Ag}_{60}\text{Cu}_{40}$  samples were sheared into six pieces each, cooled down, and extracted from the boron nitride (BN) plates. The sheared pieces were analysed in a scanning electron microscope (SEM). Using EDXS, the compositions of the different sections were calculated. The concentration of the different sheared sections is shown in fig. 4.12. There is a big spread in the concentration data, and only a slight increase of silver at the cold side, implying a small but positive Soret coefficient for the liquid  $\text{Ag}_{60}\text{Cu}_{40}$  alloy. The fitted  $\frac{\Delta c_{\text{Ag}}}{\Delta T}$  slopes for the two samples with the uncertainty as returned from the fitting function [153], as well as the resulting Soret coefficient  $S_T$  for the two samples, are shown in table 4.1.

As already mentioned, sample B was not properly compressed by the pistons

in the sample cell, leading to free surfaces on the top and bottom of that sample, as seen in fig. 4.11, possibly generating Marangoni convection disturbing the thermodiffusion process. It can be noted that sample B has higher uncertainty in the fitted concentration gradient and Soret coefficient than sample A, indicating that this convection played a role in sample B. Sample A had no visible free surfaces, and slightly less uncertainty, but still a very small Soret coefficient. If there is any thermodiffusion in liquid  $\text{Ag}_{60}\text{Cu}_{40}$ , it is at least on a much smaller order than other similar liquid alloys, like Ag-Al and Al-Cu [51, 77].

There is a noticeable difference in the concentration from weighing up the  $\text{Ag}_{60}\text{Cu}_{40}$  sample ( $c_{\text{Ag}} = 60.0 \text{ at.}\%$ ), compared to the average concentration from the readout from EDXS ( $c_{\text{Ag}} = 61.9 \text{ at.}\%$  for sample A and  $c_{\text{Ag}} = 61.8 \text{ at.}\%$  for sample B). It is unclear whether this is from inhomogeneities in the sample from the arc melting furnace, copper migrating to the end that was not covered by the shear plates, or a bias in the EDXS device/software in the SEM used. The fact that both samples have roughly the same higher silver concentration and the low measured Soret coefficient indicates the last option.

### 4.3 Ag-Al-Cu

An experiment with two samples of liquid  $\text{Ag}_{43.1}\text{Al}_{43.1}\text{Cu}_{13.8}$  was performed, with the mean isothermal temperature at 1123 K. Due to having three components in the melt, the migration of the three components inside the melt can not be determined from the XRR imagery, which only gives greyscale images, i.e., one variable for two unknowns (two free concentrations), as already discussed in section 3.2.2. Therefore, the shear cell was utilised for this experiment.

Also for the interdiffusion coefficients (in plural, as the interdiffusion coefficient is described as a matrix with elements for the different interacting components, as laid out in section 2.2.1) the determination can not be made, as the transient concentration behaviour for each component is not known. A general characteristic time for the system *can* be determined, however, as the change in grey value along the sample could be determined, and from this, the time to reach a steady grey value, and presumable a steady state, can be determined. From this characteristic time, with the knowledge of the sample length and using eq. (2.75), a quasi-interdiffusion coefficient can be determined. Due to a problem with the temperature control at the beginning of the non-isothermal phase, the concentration behaviour of that phase was disturbed. Therefore a fitting of eq. (3.24) to the data could not be performed, but because the description of the slope of the concentration gradient in the centre has a flat part in the beginning, it mostly filtered out these problematic concentration values, making it possible to fit eq. (3.21) to these data. This is shown in fig. 4.13, with the fitted characteristic time of  $1.56 \times 10^3 \text{ s}$ , indicating that the samples were sheared after 10.8 characteristic times, or having reached more than 99.99 % of the steady state concentration separation, so ex situ measurements of the concentration should be highly representative of the steady state. The resulting quasi-interdiffusion coefficient of  $6.5 \times 10^{-9} \text{ m}^2 \text{ s}^{-1}$  is calculated from eq. (2.75) with a sample length of 10.0 mm. Note that the fit of eq. (3.21) here has been applied a shift, as there was not sufficient isothermal data to ascertain a stable isothermal slope to use as a normalising reference.

At the shearing of the samples, the mean temperature along the samples was

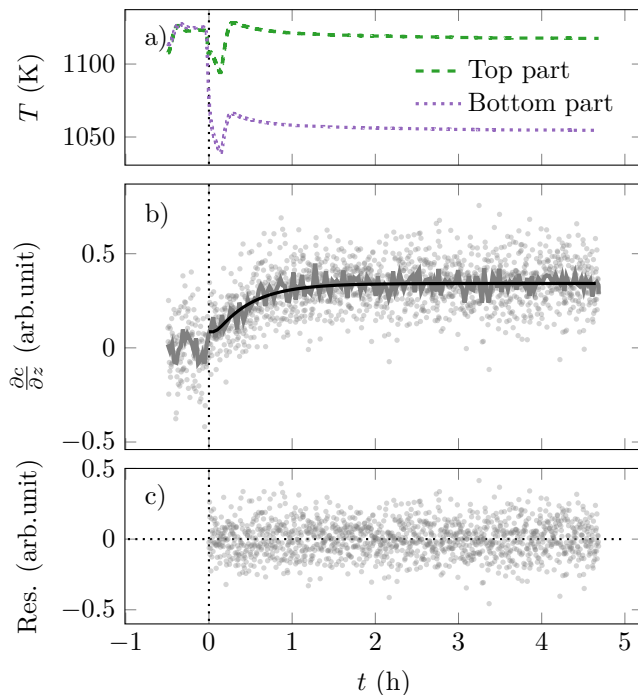


FIGURE 4.13: The slope of the concentration fit from the centre of a sample of liquid  $\text{Ag}_{43.1}\text{Al}_{43.1}\text{Cu}_{13.8}$ .

TABLE 4.2: Fitted  $\frac{\Delta c_i}{\Delta T}$  to the concentration data from the thermodiffusion experiment on  $\text{Ag}_{43.1}\text{Al}_{43.1}\text{Cu}_{13.8}$ .

	Sample A	Sample B
$\frac{\Delta c_{\text{Ag}}}{\Delta T}$	$(-0.041 \pm 0.008) \text{ at.\% K}^{-1}$	$(-0.037 \pm 0.011) \text{ at.\% K}^{-1}$
$\frac{\Delta c_{\text{Al}}}{\Delta T}$	$(0.039 \pm 0.009) \text{ at.\% K}^{-1}$	$(0.041 \pm 0.010) \text{ at.\% K}^{-1}$
$\frac{\Delta c_{\text{Cu}}}{\Delta T}$	$(0.002 \pm 0.006) \text{ at.\% K}^{-1}$	$(-0.003 \pm 0.009) \text{ at.\% K}^{-1}$

1089 K, with a temperature difference of  $\Delta T = -43.7 \text{ K}$  between the hot and cold ends.

After the thermodiffusion experiment of  $\text{Ag}_{43.1}\text{Al}_{43.1}\text{Cu}_{13.8}$ , the sheared sections of the two samples were analysed with EDXS in a SEM. The concentration of the different sheared sections is shown in fig. 4.14. There is a clear migration of silver to the cold side, aluminium to the hot side, and no significant migration of copper to either side. The fitted  $\frac{\Delta c_i}{\Delta T}$  slopes for all components  $i = \{\text{Ag}, \text{Al}, \text{Cu}\}$  of the two samples are shown in table 4.2, with the uncertainty as returned from the fitting function [153].<sup>3</sup> Using the definition for the two ternary Soret coefficients from eq. (2.68), the resulting Soret coefficients are given in table 4.3. Note that the frame-invariant Soret coefficients due to their mathematical description can not be assigned to a specific component, and therefore have been given the

<sup>3</sup>Recall that  $c_{\text{Ag}} + c_{\text{Al}} + c_{\text{Cu}} = 100 \text{ at.\%}$ , so that  $\nabla c_{\text{Ag}} + \nabla c_{\text{Al}} + \nabla c_{\text{Cu}} = 0$ . The deviation from this for sample B in table 4.2 is due to rounding errors from the EDXS software.

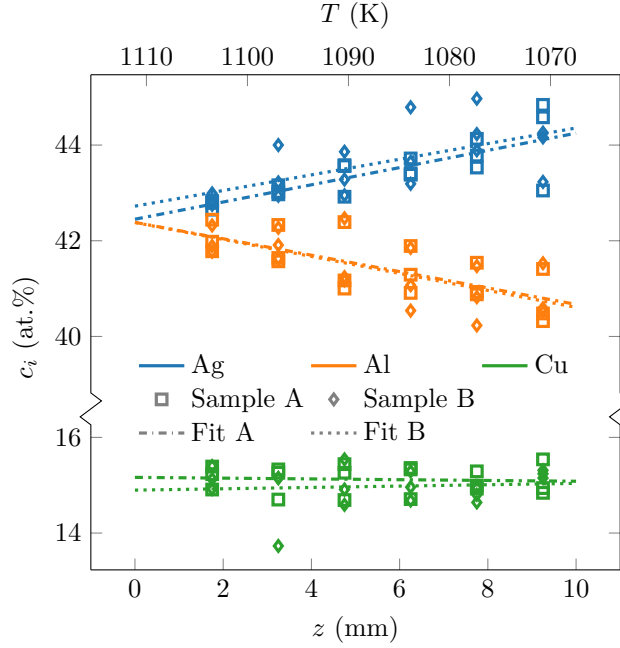


FIGURE 4.14: Concentration along two sheared samples of  $\text{Ag}_{43.1}\text{Al}_{43.1}\text{Cu}_{13.8}$ .

TABLE 4.3: Frame-invariant ternary Soret coefficients for  $\text{Ag}_{43.1}\text{Al}_{43.1}\text{Cu}_{13.8}$  as calculated with eq. (2.68) with the concentration gradients from table 4.2.

	Sample A	Sample B
$S_{T,0}$	$(1.1 \pm 1.0) \times 10^{-3} \text{ K}^{-1}$	$(0.6 \pm 1.3) \times 10^{-3} \text{ K}^{-1}$
$S_{T,1}$	$(-0.8 \pm 1.1) \times 10^{-3} \text{ K}^{-1}$	$(-1.2 \pm 1.3) \times 10^{-3} \text{ K}^{-1}$

generic indices 0 and 1.

## 4.4 Al-In

For Al-In, the immiscibility of the liquid alloy made it unfeasible to target a specific initial concentration, as described in section 3.3. The initial concentration could however be estimated by comparing with the samples that had the least spillage, and thus the closest to the initial concentration. Using this method, the concentration could be estimated within an accuracy of  $\pm 1$  at.%. With this, an experiment was conducted where one sample of  $\text{Al}_{85}\text{In}_{15}$  and one of  $\text{Al}_{78}\text{In}_{22}$  were successfully investigated at a mean temperature of 1110 K and a temperature difference of  $\Delta T = -20.0$  K. After homogenisation and an initial isothermal phase of 2.3 h, the samples were left in the temperature gradient for 4.2 h, where the concentration for the  $\text{Al}_{85}\text{In}_{15}$  sample at the isothermal and at the end of non-isothermal state is shown in fig. 4.15. The signal-to-noise ratio

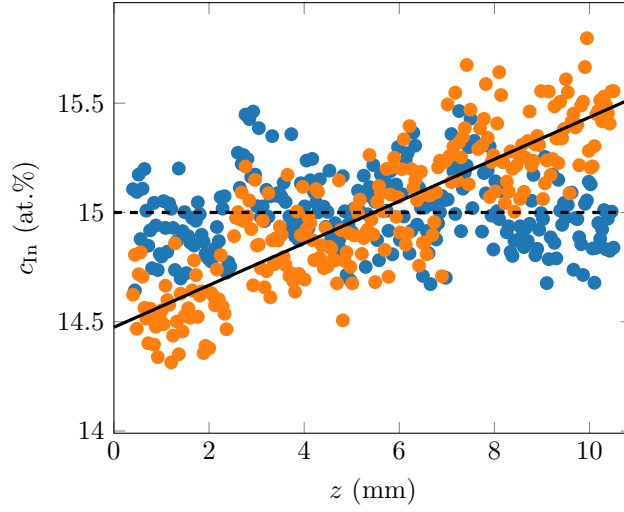


FIGURE 4.15: Concentration along a sample of  $\text{Al}_{85}\text{In}_{15}$  at the isothermal and at the end of the experiment.

for the sample in fig. 4.15 is in this case so much larger than for e.g. Ag–Al in fig. 4.1 that the subtraction of the shape of the isothermal concentrations is not necessary to clearly see the migration of the heavier indium towards the cold side to the right in the figure.

The transient concentration separation for the same  $\text{Al}_{85}\text{In}_{15}$  sample is shown in fig. 4.16. From that figure, it is evident that the sample was actually not near the steady state by the time the experiment was ended. The fit of eq. (3.24) (the black exponential curve) returned a Soret coefficient of  $S_T = 5.2 \times 10^{-3} \text{ K}^{-1}$  and an interdiffusion coefficient of  $D = 1.1 \times 10^{-9} \text{ m}^2 \text{ s}^{-1}$ , indicating that the experiment ended after only 1.4 characteristic times, having achieved roughly 75 % of the steady state concentration separation. Therefore, calculating the Soret coefficient from the concentration separation in fig. 4.15 and using eq. (2.46) would give a severely understated coefficient. This is further corroborated from the coefficients from fitting eq. (3.21) to the centre slopes and the fitting of eq. (2.74) to the full concentration data, as shown in figs. 4.17 and 4.18 respectively. The fitted Soret coefficient for the centre slope method is  $S_T = 4.3 \times 10^{-3} \text{ K}^{-1}$ , while the fitted interdiffusion coefficient is  $D = 1.4 \times 10^{-9} \text{ m}^2 \text{ s}^{-1}$ , indicating the termination of the experiment after 1.7 characteristic times, or 80 % of the steady state separation. For the full concentration fit method, the same coefficients are fitted to  $S_T = 4.5 \times 10^{-3} \text{ K}^{-1}$  and  $D = 1.8 \times 10^{-9} \text{ m}^2 \text{ s}^{-1}$ , indicating the termination of the experiment after 2.3 characteristic times, or almost 90 % of the steady state separation.

No matter which fitting method is used for the interdiffusion coefficient, it is clear that the steady state concentration was not reached at the end of the experiment, and a Soret coefficient can not be extracted from eq. (2.46), but has to come from the fitting of either eq. (3.24), eq. (3.21), or eq. (2.74). The coefficients from the three methods are compared in fig. 4.19. The horizontal error bars reflect the uncertainty in the precise concentration of the liquid Al–In alloy, while the vertical error bars show the uncertainty of the fit, as returned



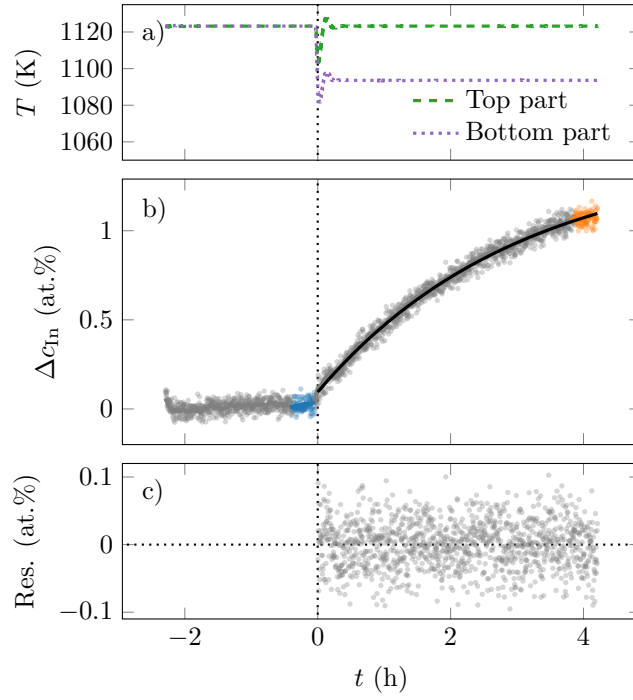


FIGURE 4.16: Concentration difference  $\Delta c(t)$  along a sample of liquid  $\text{Al}_{85}\text{In}_{15}$ .

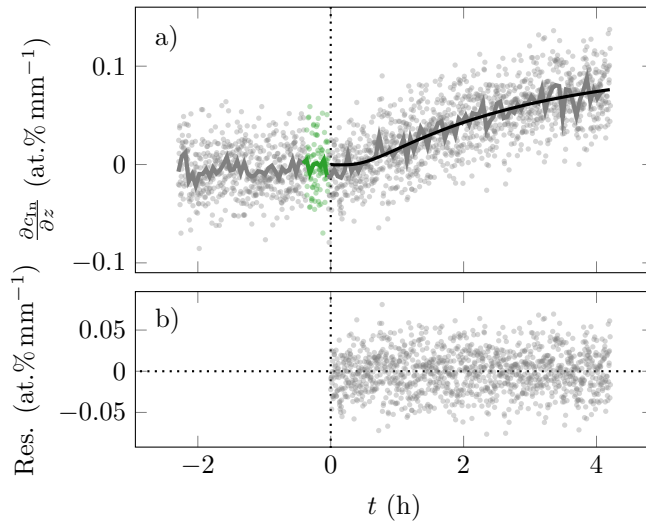


FIGURE 4.17: The slope of the concentration fit from the centre of a sample of  $\text{Al}_{85}\text{In}_{15}$ .

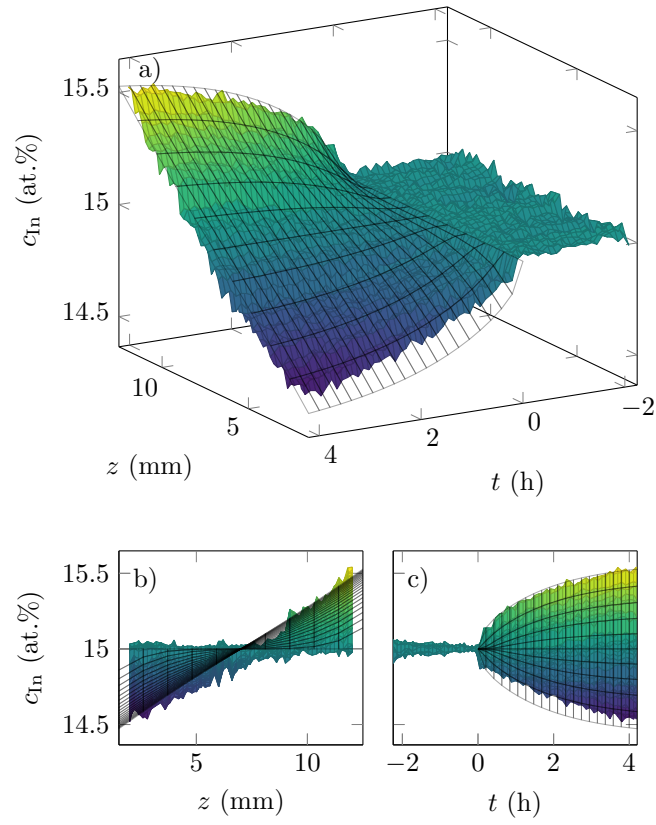


FIGURE 4.18: Concentration data for a sample of  $\text{Al}_{85}\text{In}_{15}$  with the fit of eq. (2.74).

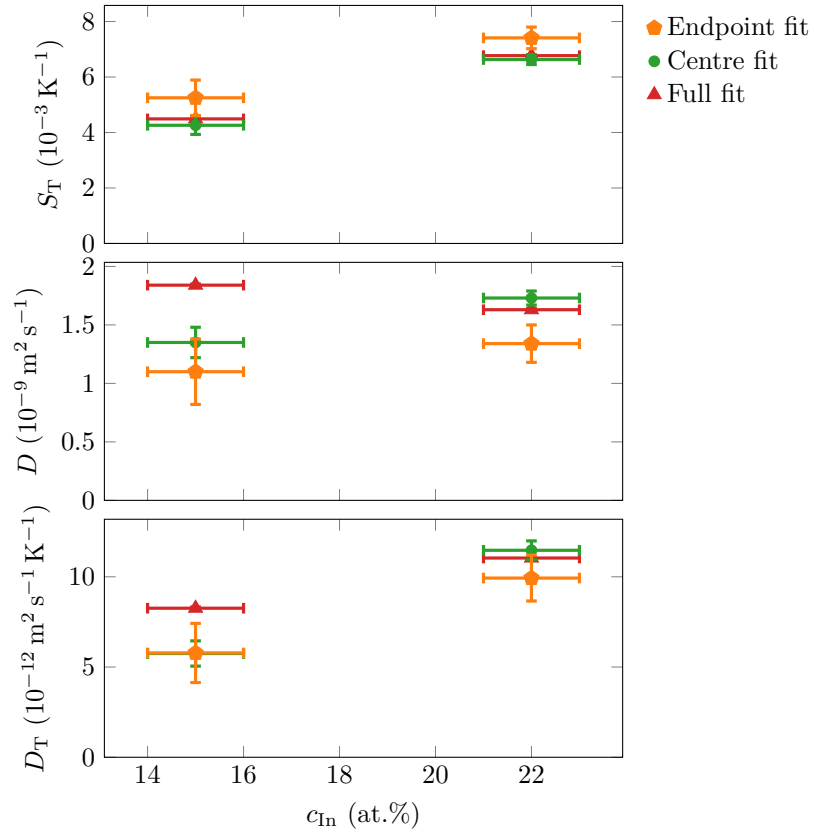


FIGURE 4.19: Soret, interdiffusion and thermodiffusion coefficients for liquid Al-In at a mean temperature of 1110 K using different methods for analysing the measurement data.

from the fitting function when taking the uncertainty in the concentration measurement into account [153]. For the method of fitting eq. (2.74) with the full concentration data, the number of data points is so high that the algorithm is very confident about the optimality of the coefficient, and thus returns a very low uncertainty. This is surely an underestimate of the real uncertainty in the measurement, as the fitted coefficients themselves can shift around up to 10 % in value, depending on when the start of the temperature difference  $t = 0$  is set. Still, it is clear that with the significant deviation for the Ag–Al experiments which were conducted several times, more experiments of the Al–In system are needed to make conclusive remarks on the Soret, interdiffusion and thermodiffusion coefficients of this system this close to the miscibility gap. This was however not possible within the time and scope of this thesis, and has to remain an objective for future work.

# Chapter 5

## Discussion

### 5.1 Comparison to previous measurements

#### 5.1.1 Ag–Al

While there to the best of my knowledge is no previous measurement of the thermodiffusion in *liquid* Ag–Al, there is a publication on thermomigration in *solid* Ag–Al, where McKee and Stark performed experiments in a temperature gradient with concentrations of  $\text{Ag}_{0.1}\text{Al}_{99.9}$  and  $\text{Ag}_2\text{Al}_{98}$  [121]. The measurements were on  $2\text{ mm} \times 6\text{ mm} \times 10\text{ mm}$  slabs of the alloys, where they varied the grain sizes between the samples. For a single crystal of  $\text{Ag}_2\text{Al}_{98}$  with the hot end at 923 K and a temperature gradient of  $450\text{ K cm}^{-1}$ , they measured a Soret coefficient of  $-2.0 \times 10^{-3}\text{ K}^{-1}$ , while they for a polycrystal (they reported having grain diameters of approximately 2 mm) sample measured a Soret coefficient of  $-0.9 \times 10^{-3}\text{ K}^{-1}$ , with silver migrating to the hot end in both cases.<sup>1</sup> Thus, the Soret coefficient measured here in liquid Ag–Al has the opposite sign and the same absolute value of the measurements in the polycrystal, and half the absolute value compared to the measurements in the single crystal. By comparison, previously published measurements on trace amounts of antimony in silver yielded a Soret coefficient five times higher in the solid state than in the liquid state, with antimony going to the hot side in both cases [79, 118]. The change in Soret coefficient with crystallinity of the solid sample is not atypical for these kinds of experiments; in the case of solid Al–Cu, the direction of the measured thermodiffusion even reverted with different grain sizes [160].

A curious thing about the experiments of McKee and Stark is that the temperature at the hot end of 923 K is between the liquidus and solidus temperature in the phase diagram. A small portion of the phase diagram,<sup>2</sup> plotted only for low concentrations of silver, is shown in fig. 5.1, with the vertical lines stretching over the temperatures across the sample. This means that for the samples in the experiments of McKee and Stark, the hot end was in a mixed liquid–face-centred

---

<sup>1</sup>The temperature at the hot and cold ends is not explicitly mentioned in the publication of the result (from 1974); only that the temperature gradient was  $450\text{ K cm}^{-1}$  [121]. In a succeeding publication from the same group in 1975, the temperature at the hot end was reported to be  $650^\circ\text{C}$ , i.e., 923 K, and the temperature at the cold end was that “determined by varying the temperature gradient across the crystal” [159]. Without further information available, I assume that this temperature setup was the same for the publication from 1974.

<sup>2</sup>For the full phase diagram, see fig. 3.1.

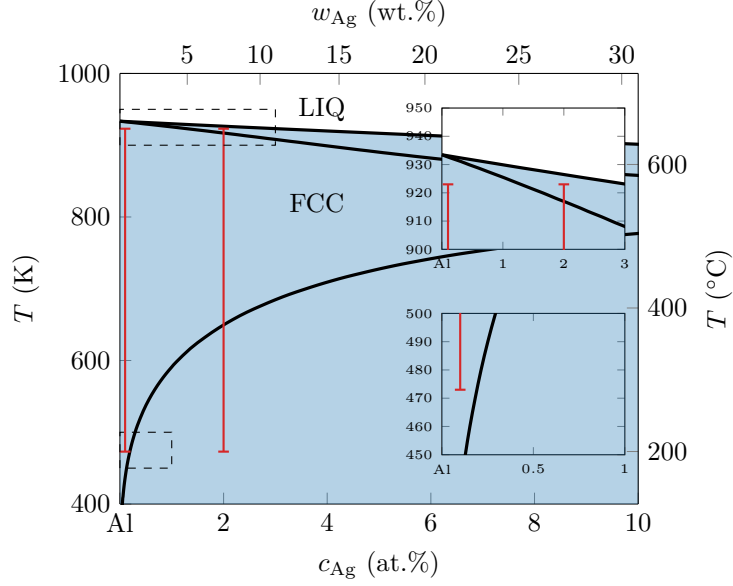


FIGURE 5.1: Cut-out of the phase diagram of Ag–Al, with temperatures from McKee and Stark indicated.

TABLE 5.1: Liquidus and solidus temperatures for  $\text{Ag}_2\text{Al}_{98}$  from different thermodynamic evaluations.

Evaluation	Liquidus	Solidus
Spencer and Kubaschewski (1987) [161]	923.9 K	905.6 K
Lim et al. (1995) [162]	924.1 K	906.3 K
Witusiewicz et al. (2004) [67]	926.5 K	917.0 K

cubic (FCC) phase, the middle was in the FCC state, and the cold end was in a mixed hexagonal close-packed (HCP)–FCC phase. The phase diagram in fig. 5.1 was calculated using parameters from Witusiewicz et al. from 2004, but using parameters from earlier published evaluations (Spencer and Kubaschewski from 1987, Lim et al. from 1995) indicate the same problem: the hot temperature used by McKee and Stark was between the liquidus and solidus temperatures [67, 161, 162]. The liquidus and solidus temperatures from all evaluations is shown in table 5.1. All the mentioned evaluations were published *after* the experiments of McKee and Stark, but also experimentally determined phase diagrams published *before* the experiments of McKee and Stark put the temperature of 923 K between the liquidus and solidus lines at 2 at.% silver [163]. It is from this clear that the sample was in a far from reproducible state, with possibly several different phases along it.

For the  $\text{Ag}_{0.1}\text{Al}_{99.9}$  sample, which *does* lie within a single phase of FCC in the phase diagrams of all evaluations, McKee and Stark could not measure any statistically significant thermomigration. Therefore, any conclusions on the relation between the Soret coefficient presented here for liquid Ag–Al alloy and the measurements of McKee and Stark in the (possibly) solid state of the same

alloy are not advisable.

The measured Soret coefficients for liquid Ag–Al as reported in this thesis are similar to previous investigations on liquid alloys of Ag–Te by Williams and Philbrook, on Al–Ni by Sondermann et al., and on Al–Cu by Bhat, where the denser element diffused towards the cold side in all cases [51, 53, 60, 77]. Of these alloys, Ag–Al has a much higher molar mass ratio than the other alloys (4.0 for Ag–Al, versus 1.2, 2.2, and 2.4, for Ag–Te, Al–Ni, and Al–Cu, respectively) [76], while no strong correlation between molar mass ratio and measured Soret coefficient for the different works is observed, although with high uncertainties and different methods of measurement, so any quantitative comparison should be made with caution. The Soret coefficient reported in this work is also within the same order of magnitude as systems of liquid alkali metal alloys, liquid salts, glass melts, and even several organic compounds [52, 80, 164, 165].

### Interdiffusion coefficient

The interdiffusion coefficient for liquid Ag–Al has earlier been measured by Engelhardt et al. [81], the results from which were shown for comparison in figs. 4.6 and 4.7. The interdiffusion coefficient reported in this thesis have the same value within the experimental error as the Ag–Al measurements of Engelhardt et al., who, using the long capillary method at a temperature of 983 K, reported a constant interdiffusion coefficient of  $(4.1 \pm 0.4) \times 10^{-9} \text{ m}^2 \text{ s}^{-1}$  for silver concentrations ranging from 20.4 at.% to 42.5 at.%. Especially for the lower concentrations, the agreement between the results in this thesis and the coefficients from Engelhardt et al. is very good, while the higher concentrations, where the samples get darker in X-ray, deviate. Engelhardt et al. did not measure for any silver concentrations higher than 42.5 at.%, so it's difficult to ascertain the precision of the results for the liquid  $\text{Ag}_{45}\text{Al}_{55}$  and  $\text{Ag}_{50}\text{Al}_{50}$  samples. But especially for the lower silver concentrations, the match with the previously published interdiffusion coefficient indicates that the convection, including the Marangoni convection due to gradients in interfacial tension, in these experiments was negligible.

The mean temperature used for liquid Ag–Al here (1017 K) was slightly higher than the one used by Engelhardt et al. (983 K), and therefore the interdiffusion coefficients for liquid Ag–Al measured in this work are expected to be slightly higher. It should also be remembered that the interdiffusion coefficients as returned by the fit of eq. (3.24) are expected to be slightly below the true value, as shown in fig. 3.28. These two aspects may explain the slightly lower interdiffusion coefficient compared to that reported by Engelhardt et al.

Another challenge with using the equation for the transient concentration (eq. (2.74)), or equations derived from it (eqs. (3.21), (3.22) and (3.24)), is that they base themselves on the assumption that the temperature gradient is achieved instantaneously. Though this in practice is impossible, the time required to reach 50 % of the targeted temperature gradient in the utilised setup is within 3 minutes, much shorter than the characteristic time for the thermodiffusive process, which is around 40 minutes, calculated from the interdiffusion coefficient and the sample length. Therefore it is assumed that the equation can be applied to describe the time dependence of the concentration gradient in this setup, which also seems to be supported by the agreement in interdiffusion between

these measurements and the literature (see fig. 4.6).

### Limiting resolution of X-ray radiography (XRR) imagery

While XRR allows for in situ measurements, which enables the measurement of interdiffusion coefficients, the small relative difference in concentration results in low contrast, and therefore is a limiting factor to the available precision of the measurements. For the experiments with  $\text{Ag}_{25}\text{Al}_{75}$ , the total grey value change across the sample is around 15 grey values, meaning a contrast resolution of around 0.01 at.%. This gives an uncertainty of  $\pm 0.1 \times 10^{-3} \text{ K}^{-1}$  in the measured Soret coefficient in the ideal case. This uncertainty is even larger for the  $\text{Ag}_{50}\text{Al}_{50}$  measurements, where the increased absorption of X-rays reduces the contrast by a factor of two, and therefore increases the minimum possible uncertainty in the Soret coefficient by the same factor. This limitation can be circumvented by increasing the temperature difference across the samples, which similarly increases the total concentration separation across the sample, and thus increases the grey value change across the sample. The temperature difference in the experiments with Ag–Al presented in this thesis, which was around 10 K, is much smaller than many previous works on thermodiffusion in liquid alloys, which use temperature differences often much larger than 100 K [54, 55, 77, 166]. This reduced temperature difference reduces the heat to be dissipated from the experimental setup, making it more suitable for situations where heat dissipation is a limiting factor, such as on orbital platforms. Additionally, a high temperature difference between the two ends of the sample gives significantly different interdiffusion coefficients along the sample, and therefore impedes the measurement and following comparison of the interdiffusion coefficient. This problem is therefore avoided with a smaller temperature difference.

#### 5.1.2 Ag–Cu

While there is no previously published measurement on thermodiffusion for liquid Ag–Cu, there are results on thermodiffusion for solid Ag–Cu by Jaffe and Shewmon, where they presented experiments on trace amounts of radioactive silver in solid copper, measuring a Soret coefficient of  $(-1.5 \pm 0.9) \times 10^{-3} \text{ K}^{-1}$ , with silver migrating to the hot side [167]. There have also been investigations on thermodiffusion in solid Sn–Ag–Cu (SAC) solder alloys, where Lin et al. investigated the migration of copper between layers of copper, silver and  $\text{Ag}_{3.2}\text{Sn}_{96.8}$ , where they found that the interface of silver and  $\text{Ag}_{3.2}\text{Sn}_{96.8}$  created a silver-rich interface which reduced the copper migration by a factor of three [168]. However, as mentioned for similar experiments on solid Ag–Al and other alloys in section 5.1.1, there is generally no correlation between the Soret coefficients measured in different phases of a system. Together with that the measurement in this thesis was with 60 at.% silver, compared to the trace amounts of silver in the experiment of Jaffe and Shewmon, and the high concentration of tin in the experiment of Lin et al., no conclusions on the relation between these findings can be made.

Due to the lack of information about transient concentration inside the sample cell, it can not directly be seen whether the sample actually reached the steady state, or if it was sheared during the thermodiffusive process, and therefore being terminated before the full concentration separation had been established. The



interdiffusion of liquid  $\text{Ag}_{60}\text{Cu}_{40}$  was however measured by Engelhardt, who at 1193 K measured an interdiffusion coefficient of  $(3.7 \pm 0.4) \times 10^{-9} \text{ m}^2 \text{ s}^{-1}$  with the shear cell technique [62]. With the expression for characteristic time in eq. (2.75) and a sample length  $L$  of 11.0 mm, this results in a characteristic time of  $\theta \approx 3.3 \times 10^3 \text{ s}$ , or achieving more than 99 % of the steady state concentration separation. The experiment in this thesis was performed with a mean temperature of 1099 K, i.e., slightly lower than Engelhardt, and therefore also a slightly lower interdiffusion coefficient is expected. The temperature difference is however so small that this can be assumed negligible for this experiment, and it can thus confidently be assumed that the thermodiffusive process had ample time to establish a concentration separation representative of the steady state.

The lack of a measurable concentration separation after the experiment for liquid  $\text{Ag}_{60}\text{Cu}_{40}$  could either be a indication of a general close-to-zero Soret coefficient, or imply a local minimum of the Soret coefficient, or even a point of reversal of sign of the Soret coefficient, which has been observed to exist for Na–K alloys [52], in addition to in several organic systems [80, 169]. It is also hypothetically possible that at the measured temperature, the Soret coefficient of the liquid  $\text{Ag}_{60}\text{Cu}_{40}$  alloy is negative, which would lead to the denser silver-rich alloy to accumulate at the hot side at the top of the sample column. If the absolute value of such a negative Soret coefficient was large enough, such a setup could overcome the critical Rayleigh number of the system, and become unstable, as described by Velarde and Schechter [170]. For an unstable density distribution to occur for liquid  $\text{Ag}_{60}\text{Cu}_{40}$ , i.e., a layer of higher density above a layer of lower density, the Soret coefficient would have to be greater than  $-5.1 \times 10^{-3} \text{ K}^{-1}$  at 1099 K, following from the description for ideal density in eq. (3.16) and a linear concentration from eq. (2.46). Basing on the available literature, such great Soret coefficients are rare in liquid alloys, and negative Soret coefficients even more rare, so this is deemed highly unlikely to be the case. Also, no significant copper migration was observed in any of the two ternary Ag–Al–Cu alloys investigated, while there was a significant migration of the two other components, where an unstable density layering would have disturbed the thermodiffusion for all components, not only for one of them (copper). It is thus the most likely explanation that the Soret coefficient is indeed negligible for the measured alloy.

The thermodiffusion in liquid Ag–Cu was modelled by Sarder et al., using molecular dynamics (MD) simulations [171]. They found the Soret coefficient to be ‘very small’, finding a Soret coefficient for liquid  $\text{Ag}_{62.5}\text{Cu}_{37.5}$  of approximately  $2 \times 10^{-3} \text{ K}^{-1}$  at a temperature of 1099 K, with silver migrating to the cold side. This is much larger than what was found in the experiment presented in this thesis (table 4.1). In an earlier publication, the previously mentioned group did similar simulations on liquid Al–Ni, finding a heat of transport ten times higher than that found for Ag–Cu [101]. But due to the thermodynamic factor (TDF) also being higher for liquid Al–Ni alloys than for liquid Ag–Cu alloys, the resulting Soret coefficient for Al–Ni based on their results was found to be  $2.6 \times 10^{-3} \text{ K}^{-1}$  (nickel to the cold side) at a concentration of  $c_{\text{Ni}} = 21.5 \text{ at.}\%$  and a mean temperature of 1398 K [101]. This specific liquid Al–Ni alloy was later measured experimentally at the same mean temperature by Sondermann et al., who found a Soret coefficient of  $(1.5 \pm 0.3) \times 10^{-3} \text{ K}^{-1}$ , i.e., significantly lower than the results from the MD simulations [60]. The publication of Sarder et al. also simulated other parameters for liquid Ag–Cu, which show similar

discrepancy to available experimental data. While the simulated self-diffusion coefficients for pure Ag and Cu are in good agreement with measurements [81, 172], the simulated interdiffusion coefficient is a factor three off a published experiment on the liquid alloy [62], and the TDF is off by 45 % from the value calculated from the Gibbs energy for  $\text{Ag}_{62.5}\text{Cu}_{37.5}$  at 1099 K as published by Witusiewicz et al. [67]. This good fit for the pure components and lack thereof for the mixed alloys arises from the construction of the model used by Sarder et al. for the simulations, where the Ag–Cu model, originally developed by Williams et al., was based on combining models fitted to the pure component properties, together with an extra cross-interaction function fitted to the interaction energies for the alloy at 0 K [173]. The model in use for example predicts the general shape of the phase diagram for Ag–Cu, but misses the eutectic temperature and concentration by 118 K and 14 at.%, respectively [67, 173]. To summarise, only a qualitative predictability can at best be expected of the Soret coefficient from the simulations of Sarder et al. Their results show silver to migrate towards the cold side, with a fairly constant Soret coefficient across the entire concentration range [171]. Silver was indeed found to migrate towards the cold side in the measurement presented in this thesis, although much weaker than what was found by Sarder et al., and barely significant compared to the determined error bars. The concentration dependency of the Soret coefficient was not experimentally investigated for this thesis, but the results from Sarder et al. indicate that the coefficient should not change significantly at other concentrations.

### Interdiffusion coefficient

Due to the lack of concentration separation and the low X-ray contrast, no interdiffusion coefficient could be ascertained from the experiment, and therefore no comparison with earlier reported values can be made [62]. Thanks to the in situ XRR imagery, it was still possible to monitor the development of free surfaces, which were present in one of the two investigated samples. There were however no free surfaces detected in the other sample, indicating that the process of thermodiffusion had proper conditions for occurring in that sample.

### 5.1.3 Ag–Al–Cu

A similar experiment to the one presented in section 4.3 has been performed on near-eutectic  $\text{Ag}_{17.6}\text{Al}_{68.6}\text{Cu}_{13.8}$  by Sondermann et al. at a mean temperature of 983 K [141]. The concentration along the samples from that experiment is shown in fig. 5.2. Again, there is a clear migration of silver to the cold side, aluminium to the hot side, and no significant migration of copper to either side, just as found in this work for  $\text{Ag}_{43.1}\text{Al}_{43.1}\text{Cu}_{13.8}$ . The fitted  $\frac{\Delta c_i}{\Delta T}$  slopes for all components of the two samples of  $\text{Ag}_{17.6}\text{Al}_{68.6}\text{Cu}_{13.8}$  are shown in table 5.2.

The migration of silver (the heaviest component of the alloy) to the cold side and aluminium (the lightest component of the alloy) to the hot side in both experiments conform to the general rule in binary mixtures: that the denser component tends to migrate to the cold side, and subsequently the lighter component to the hot side [174]. The intermediate component (copper) does not seem to have any net migration at all in the mixtures. In non-equilibrium molecular dynamics (NEMD) simulations on a ternary Lennard-Jones (LJ) mixture, Artola and Rousseau showed that in such a simple ternary mixture

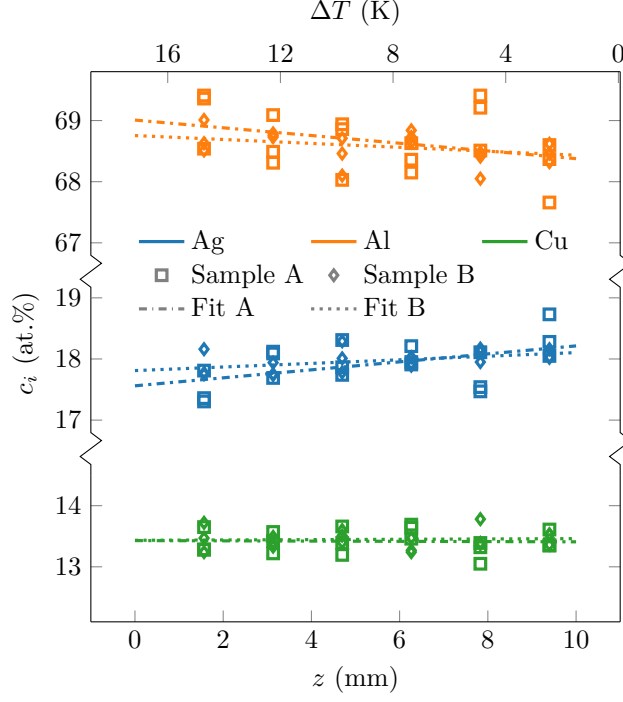


FIGURE 5.2: Concentration across the two sheared samples of  $\text{Ag}_{17.6}\text{Al}_{68.6}\text{Cu}_{13.8}$  from Sonderrmann et al. [141].

TABLE 5.2: Fitted  $\frac{\Delta c_i}{\Delta T}$  to the concentration data from the thermodiffusion experiment on near-eutectic  $\text{Ag}_{17.6}\text{Al}_{68.6}\text{Cu}_{13.8}$  as conducted by Sonderrmann et al. [141].

	Sample A	Sample B
$\frac{\Delta c_{\text{Ag}}}{\Delta T}$	$(-0.042 \pm 0.018) \text{ at.\% K}^{-1}$	$(-0.019 \pm 0.008) \text{ at.\% K}^{-1}$
$\frac{\Delta c_{\text{Al}}}{\Delta T}$	$(0.040 \pm 0.026) \text{ at.\% K}^{-1}$	$(0.021 \pm 0.013) \text{ at.\% K}^{-1}$
$\frac{\Delta c_{\text{Cu}}}{\Delta T}$	$(0.001 \pm 0.010) \text{ at.\% K}^{-1}$	$(-0.002 \pm 0.008) \text{ at.\% K}^{-1}$

TABLE 5.3: Frame-invariant ternary Soret coefficients for samples of near-eutectic  $\text{Ag}_{17.6}\text{Al}_{68.6}\text{Cu}_{13.8}$  as calculated with eq. (2.68) with the concentration gradients from table 5.2.

	Sample A	Sample B
$S_{T,0}$	$(2.5 \pm 3.0) \times 10^{-3} \text{ K}^{-1}$	$(0.9 \pm 1.4) \times 10^{-3} \text{ K}^{-1}$
$S_{T,1}$	$(-0.5 \pm 2.6) \times 10^{-3} \text{ K}^{-1}$	$(-0.4 \pm 1.3) \times 10^{-3} \text{ K}^{-1}$

the heaviest component always goes to the cold side and the lightest component always goes to the hot side, while the component of intermediate mass varied its direction of migration, depending on composition and mass ratios of the components [175]. For all their investigated compositions and mass ratios, when the concentration of the intermediate component was kept fixed, the separation ratio  $\frac{\Delta c_i}{\Delta T}$  for the intermediate component went linearly from being positive (migrating towards the hot side) to negative (migrating towards the cold side) when the two other components were varied in concentration, from the lighter component being dilute to the heavier component being dilute, respectively. This behaviour was thus not observed in the experiments for liquid  $\text{Ag}_{17.6}\text{Al}_{68.6}\text{Cu}_{13.8}$  and  $\text{Ag}_{43.1}\text{Al}_{43.1}\text{Cu}_{13.8}$ . Copper in the liquid binary Al–Cu has a clear thermodiffusive migration towards the cold side [51, 77], while no significant migration was observed for liquid  $\text{Ag}_{17.6}\text{Al}_{68.6}\text{Cu}_{13.8}$  and  $\text{Ag}_{43.1}\text{Al}_{43.1}\text{Cu}_{13.8}$ , and only a barely significant migration towards the hot side in liquid Ag–Cu, as found for this thesis, which decidedly is not a linear trend, and thus does not conform with the findings of Artola and Rousseau in a LJ mixture [175].

Using the definition for the frame-invariant ternary Soret coefficients from eq. (2.68), the resulting two Soret coefficients are given in table 5.3.

The uncertainty in the Soret coefficients in tables 4.3 and 5.3 is propagated from the uncertainty in the concentration gradients (tables 4.2 and 5.2 respectively). Due to the nature of propagation of uncertainty, while the uncertainties in the concentration gradients are relatively low, 20 % and 23 % for  $\frac{\Delta c_{\text{Ag}}}{\Delta T}$  and  $\frac{\Delta c_{\text{Al}}}{\Delta T}$ , respectively, the resulting uncertainty for the frame-invariant ternary Soret coefficient is much larger, 93 % for  $S_{T,0}$  and 137 % for  $S_{T,1}$ .

Outside of these liquid Ag–Al–Cu experiments, to the best of my knowledge, there has been only one investigation on the thermodiffusion in liquid ternary alloys, with the experiments of Winter and Drickamer on three compositions of liquid Bi–Pb–Sn, with fixed  $c_{\text{Sn}} = 50 \text{ at.}\%$ , and varying fractions of lead and bismuth [23]. Only a graphical description of a decreasing Soret coefficient by increasing bismuth concentration was shown, with no information about the temperature or duration of the experiment. Indeed, even the literature on investigations on interdiffusion in liquid ternary alloys is sparse [62, 63, 176, 177]. The liquid alloy Ag–Al–Cu is one of the few experimentally investigated ternary systems, in part being the reason why this alloy and its binary constituents were investigated in this thesis [62].

For investigations of thermodiffusion in organic liquids, the focus has earlier been on binary mixtures, and first with the establishment of benchmarking investigations in different labs on ground and in space, the focus has started to move onto ternary organic mixtures first in the last decade [158]. With

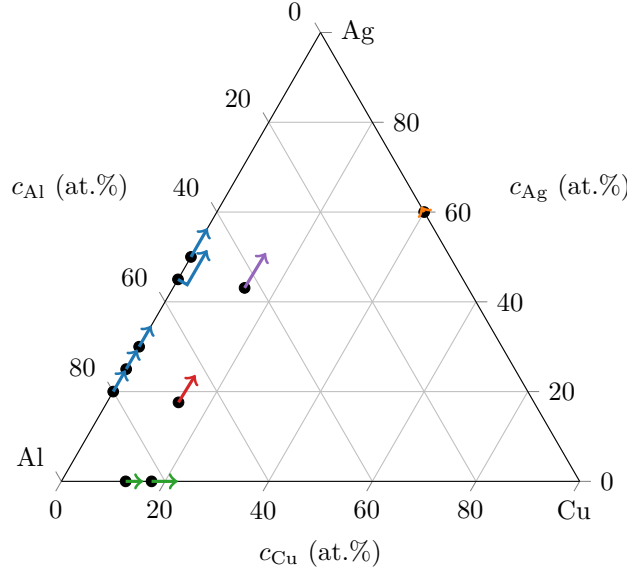


FIGURE 5.3: Measured  $\frac{\nabla c_i}{\nabla T}$  for Ag–Al–Cu and its binary constituents.

this shifting focus to ternary mixtures, first now in the last years have the community started to synchronise their efforts to report the Soret coefficients of three-component mixtures, as different reports have used different nomenclature and descriptions for the coefficients themselves [110]. It feels safe to state that there is a coming commitment to the investigation and reporting of ternary and higher-order systems in the years to come.

With the description laid out in section 2.2.1, originally published by Ortiz de Zárate, the Soret coefficient can be reported frame-invariant, i.e., independent on whether using atomic concentration or mass concentration [110]. A disadvantage of this conversion is that no single frame-invariant Soret coefficient can be assigned to fully represent the movement of one of the components, and a physical interpretation of the calculated frame-invariant Soret coefficients  $S_{T,i}$  is difficult. The description does however approach the binary Soret coefficient  $S_T$  when approaching the dilute limit of one of the three components [110].

A comparison of only the concentration gradient with respect to the temperature gradient (commonly denoted  $S'_{T,i} = \frac{\nabla c_i}{\nabla T}$  in the literature, as described in section 2.2.3) is possible to use, though, as  $\nabla c_0 + \nabla c_1 + \nabla c_2 = 0$ . This parameter is shown graphically for the results on Ag–Al–Cu (violet vector) and its binary constituents Ag–Al (blue) and Ag–Cu (orange) in fig. 5.3, with the results of Bhat for Al–Cu added (green) to complete the triangle [51, 77],<sup>3</sup> and the results for near-eutectic  $\text{Ag}_{17.6}\text{Al}_{68.6}\text{Cu}_{13.8}$  from Sondermann et al. (red) [141]. The arrows point towards the direction of concentration migration towards the cold side, with the length of the arrows being arbitrary, but with correct length relation between the different data points. It has for organic systems been shown that with the vectors as displayed in fig. 5.3, with the continuous behaviour of the

<sup>3</sup>Note that only the complete data of  $\text{Al}_{87.6}\text{Cu}_{12.4}$  and  $\text{Al}_{82.6}\text{Cu}_{17.4}$  is reported, although they did measure more compositions below  $c_{\text{Cu}} = 12.4$  at.%.

concentration gradients, a stagnation point can occur, where all concentration gradients vanish simultaneously [169, 178]. If for liquid Ag–Al–Cu this point is at or near the alloy  $\text{Ag}_{60}\text{Cu}_{40}$  is impossible to say without more data and knowledge of the thermodiffusive behaviour over a bigger range of the Gibbs triangle.

It appears that the thermodiffusive drift gains strength with minor additions of copper, as the vector lengths of the two ternary compositions  $\text{Ag}_{17.6}\text{Al}_{68.6}\text{Cu}_{13.8}$  and  $\text{Ag}_{43.1}\text{Al}_{43.1}\text{Cu}_{13.8}$  are longer than the similar silver-aluminium ratios for the binary Ag–Al alloys. If this is due to actual increased strength or due to the different methods of XRR and energy-dispersive X-ray spectroscopy (EDXS) for determining the concentration difference across the investigated samples is difficult to say.

The measurement of thermodiffusion from the direct measurements of concentrations in the sheared samples has the benefit over the popular method of optical digital interferometry (ODI) and other optical methods employed in the community of thermodiffusion measurements on ternary organic liquids, as the non-linear behaviour of the refractive index investigated with those methods leave measurements in several composition ranges either hugely uncertain or simply impossible to ascertain, as the change in refractive index is reduced at those concentration ranges, as recently laid out in detail by Köhler et al. [158].

### Interdiffusion coefficient

The only reported interdiffusion coefficients for the ternary liquid Ag–Al–Cu system are of quasi-binary diffusion couples (i.e., couples where one component is kept constant, while the two other components are varied, like for the couple  $\text{Ag}_{12.6}\text{Al}_{73.6}\text{Cu}_{13.8}$  vs.  $\text{Ag}_{22.6}\text{Al}_{63.6}\text{Cu}_{13.8}$ ) with average concentration of the close-to-eutectic  $\text{Ag}_{17.6}\text{Al}_{68.6}\text{Cu}_{13.8}$  at temperatures of 973 K to 993 K by Kargl et al. [177] and Engelhardt [62].<sup>4</sup> The experiment on liquid  $\text{Ag}_{43.1}\text{Al}_{43.1}\text{Cu}_{13.8}$  presented in section 4.3 has the same mean copper concentration as those experiments, but with more silver and subsequently less aluminium, and also at 100 K higher temperature. The measured quasi-binary interdiffusion coefficients from Kargl et al. and Engelhardt are all in the range  $3.0 \times 10^{-9} \text{ m}^2 \text{ s}^{-1}$  to  $9.7 \times 10^{-9} \text{ m}^2 \text{ s}^{-1}$ , a range which the measurement in this thesis lies within, indicating that the experiment of this thesis captured a proper thermodiffusive process. Also, the interdiffusion coefficient for silver against aluminium in Ag–Al–Cu with constant relatively low copper concentration measured by Kargl et al. was found to be comparable to the interdiffusion coefficient for binary Ag–Al measured by Engelhardt et al. at the same relative concentration [81, 177]. This fits with the quasi-interdiffusion coefficient for liquid  $\text{Ag}_{43.1}\text{Al}_{43.1}\text{Cu}_{13.8}$  with relatively low copper concentration as reported here being comparable to the interdiffusion coefficient measured for  $\text{Ag}_{50}\text{Al}_{50}$  as reported earlier in this work (fig. 4.6).

<sup>4</sup>There have been some viscosity measurements on liquid Ag–Al–Cu, from where the interdiffusion coefficient could have been estimated with the Stokes-Einstein relation [39, 40], but these measurements were for 10 at.% silver with varying aluminium/copper concentration [87], and therefore no closer to this experiment's  $\text{Ag}_{43.1}\text{Al}_{43.1}\text{Cu}_{13.8}$  composition than the actual interdiffusion measurements of Kargl et al. and Engelhardt [62, 177].

#### 5.1.4 Al–In

In a publication of Bräuer and Müller-Vogt, they in the appendix refer to a

thermodiffusive coefficient [...] in the system Al–In (determined in our group as [...]  $-3.5 \times 10^{-8} \text{ cm}^2 \text{ s}^{-1} \text{ K}^{-1}$ ) [179]

with no further reference to a separate publication, operating temperature, or concentration. Their publication itself, however, reported measurements on interdiffusion in Al–In, using a diffusion couple consisting of  $\text{Al}_0\text{In}_{100}$  (pure indium) and  $\text{Al}_5\text{In}_{95}$ , measured at two different temperatures, 893 K and 953 K [179]. As the experiments in this thesis involved aluminium-rich compositions contrary to the indium-rich interdiffusion measurements of Bräuer and Müller-Vogt of  $\text{Al}_{2.5}\text{In}_{97.5}$ , and without any further information about the process used for the mentioned thermodiffusion experiment, it is difficult to make any statements about the comparability of these two experiments. This experiment is thus to the best of my knowledge the only properly documented experiment on thermodiffusion in Al–In.

Williams and Philbrook analysed liquid Ag–Te, which has a miscibility gap in the liquid state [53]. Williams and Philbrook measured the Soret coefficient for silver concentrations from 17.5 at.% to 69.0 at.%, whereas the miscibility gap for the liquid Ag–Te alloy is for from 69.7 at.% to 88.1 at.% silver [137]. The majority of the measurements were performed far away from the miscibility gap, and for the few experiments performed close to the miscibility gap, the Soret coefficient was observed to *decrease* closer to the miscibility gap, which is surprising when comparing to other measurements in organic systems, where the Soret coefficient *increases* when approaching the miscibility gap [26, 34–36]. Such an increase is the expected behaviour, as the Darken equation leads to a generally lower interdiffusion coefficient  $D$  when approaching the miscibility gap [72, 92, 93, 180, 181], while the thermodiffusion coefficient  $D_T$  in organic liquids has been observed to remain remarkably constant [35, 36], leaving the Soret coefficient ( $S_T \equiv \frac{D_T}{D}$ ) to diverge when approaching the miscibility gap. This behaviour of a relatively high Soret coefficient and a relatively low interdiffusion coefficient is also what was observed in the Al–In experiment reported here.

#### Interdiffusion coefficient

The interdiffusion coefficient of liquid Al–In has earlier been measured at the indium-rich side with reported coefficients for  $\text{Al}_5\text{In}_{95}$  and  $\text{Al}_{2.5}\text{In}_{97.5}$  by Griesche and Froberg and Bräuer and Müller-Vogt, respectively [179, 182]. On the aluminium-rich side, where the experiments of this thesis were conducted, Schiller thoroughly investigated the interdiffusion in liquid Al–In alloys [63]. Using long capillary diffusion couples and XRR, Schiller investigated the interdiffusion coefficient in alloys with the mean concentrations ranging from 1.5 at.% to 10.5 at.% indium, for temperatures from 953 K to 1273 K. This is still quite far away from the lowest concentration measured in this work of 15 at.% indium. Schiller observed only a weak decrease in the interdiffusion coefficient closer to (and for some concentrations even within) the miscibility gap, leading Schiller to conclude that for at least the measurements inside the miscibility gap, there were fine dispersions of segregated fluid undetectable to the available experimental setup, and the experiment measured a collective movement of the dispersions rather than the atomic interdiffusion [63].



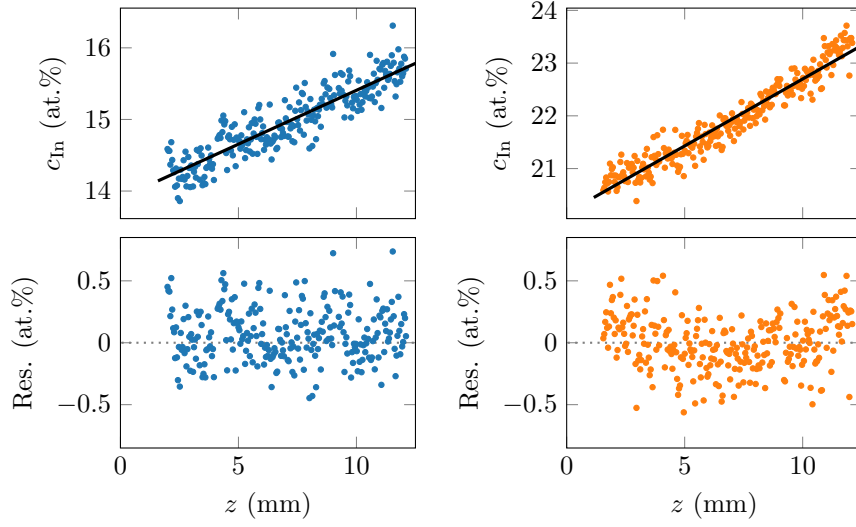


FIGURE 5.4: Concentration across the samples of  $\text{Al}_{85}\text{In}_{15}$  and  $\text{Al}_{78}\text{In}_{22}$  at the end of the experiment.

When comparing the interdiffusion coefficients in this work with those measured by Schiller further away from the miscibility gap, they behave as expected, where these experiments show a strong decline closer to the miscibility gap, as has also been found for other liquid alloys with miscibility gaps [92, 93, 181].

It can be noted that there appears to be an asymmetry in the concentration profile in fig. 4.18b, where the concentration distribution at the end of the experiment seems to be linearly distributed on the top/hot side, while there is a curved concentration distribution on the bottom/cold side. This is not the expected behaviour from the transient concentration as given by eq. (2.74) and shown in fig. 2.5, indicating that there is a significantly slower diffusion on the cold side than on the hot side, as the concentration distribution is linear when the system has reached the equilibrium, following eq. (2.74). This inequality in the interdiffusion coefficient along the alloy is further exposed in fig. 5.4, where the concentrations for both samples are shown from the last frame of the experiment, with linear fits and residuals to said fit. It is clear that while the linear fit is a valid representation of the concentrations at the end of the experiment for the sample of  $\text{Al}_{85}\text{In}_{15}$ , as the residuals are evenly distributed along the zero-line (left side of the figure in blue), the same is not the case for the sample of  $\text{Al}_{78}\text{In}_{22}$  (right side of the plot in orange). This indicates that the sample of  $\text{Al}_{85}\text{In}_{15}$  was closer to the equilibrium state than the sample of  $\text{Al}_{78}\text{In}_{22}$  at the end of the experiment. This can be explained by the sample of  $\text{Al}_{78}\text{In}_{22}$  being closer to the miscibility gap, as can be observed in fig. 5.5, where the temperature spanning over the two samples is shown in the phase diagram of the Al–In system. Closer to the miscibility gap, the TDF is closer to zero, and the interdiffusion therefore too, following the Darken equation (eq. (2.93)). This close to the miscibility gap, the change in interdiffusion along the sample is striking, leading to the deviation of the concentration distribution from the theoretical description in eq. (2.74), where a constant interdiffusion over the



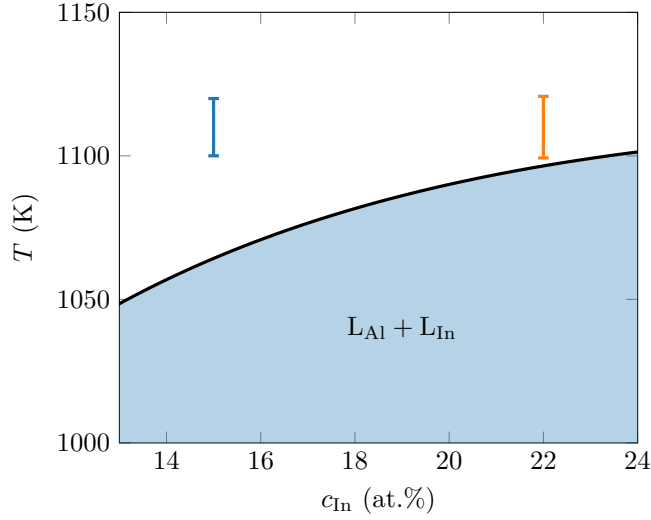


FIGURE 5.5: Concentrations of the investigated Al–In samples and the temperature subjected along them.

entire sample was assumed, which clearly no longer applies to the system this close to the miscibility gap.

## 5.2 Connecting the results with theory

### 5.2.1 Predictive models for thermodiffusion

There are several models for thermodiffusion in binary mixtures, both organic and alloys, as described in section 2.3, where a handful of models are presented. The selected models were chosen for different reasons: the models of Dougherty and Drickamer, Eslamian et al., and Jafar-Salehi et al. have been developed for and/or applied to liquid binary alloys in earlier works [23, 128, 129, 135]. The model of Artola et al. is based on kinetic theory, instead of the non-equilibrium thermodynamic approach of the previously mentioned models, especially interesting with the great amount of investigations into self-diffusion in liquid metals and alloys [81, 183, 184]. The model of Shukla and Firoozabadi, another non-equilibrium thermodynamic model, has been found to be the most reliable to predict thermodiffusion in LJ mixtures [122, 130, 185].

In the following, the predicted values will be calculated and discussed for each binary alloy investigated in this work, before a broader interpretation of the predictions will be made later.

#### Ag–Al

The density of the Ag–Al system was measured by Brillo et al. with concentrations increasing with steps of 20 at.%. Therefore, for the concentrations investigated here, only the  $\text{Ag}_{20}\text{Al}_{80}$  sample had its density profile measured. For the rest of the samples, an interpolation can be used. Brillo et al. found that Ag–Al has a negative excess volume at 1023 K, i.e., that the volume of the mixed alloy is less

than that of the separate pure components [70]. Due to the non-ideal behaviour of the excess volume in the Ag–Al system, a model would have to be decided for the excess volume, which for no existing model is widely accepted [66]. As the excess volume for the Ag–Al system is so low, the ratio between the excess volume and the total volume only being on the order of  $\frac{V_E}{V} \approx 2\%$  [70], the ideal mixing was assumed for the density anyway.

As for the other thermophysical properties of Ag–Al, the models introduced in section 2.3 make use of the activation energy of viscous flow, partial molar volume, energy of vaporisation, activation energy of self-diffusion, and the thermoelectric power, in addition to values derived from the Gibbs energy, which as previously stated was taken from the thermodynamic evaluation of Witusiewicz et al. [67]. None of these values, except for the properties derived from the Gibbs energy, are partial properties. Therefore, except for the partial properties, they are all calculated from the pure components in the binary mixture. While this ignores any non-ideal behaviour that often appears during mixing, this is very convenient, as finding a mixture where all these properties previously have been measured for the specific mixture and concentration would have been very challenging, if not impossible.

For the activation energy of viscous flow of aluminium and silver, the reference values reported by Assael et al. were used [74, 75]. For the molar volume, it is equal to the molar mass divided by the density, where the density values for the pure elements are taken from the aforementioned publications of Assael et al. as well. The atomic weights listed in the most recent IUPAC technical report are used for all elements in this thesis [76]. The energy of vaporisation for all pure elements in this thesis are taken from the book of Yaws and Satyro [133]. The activation energy of self-diffusion for aluminium as reported by Demmel et al. was utilised, along with the value for silver as reported by Engelhardt et al. [81, 186]. Finally, for the thermoelectric power of the pure elements, the value reported by Marwaha and Cusack was used for aluminium, and the value from Makradi et al. was used for silver [187, 188].

The Soret coefficients for Ag–Al as predicted by the models are shown in fig. 5.6, as calculated for the entire concentration range for a mean temperature of 1017 K, the same as for the experiments. The measurements as reported in section 4.1 are shown as black squares for comparison. The hatched pattern indicates where the alloy isn't fully liquid, and therefore where the model isn't valid. For the models in eqs. (2.95) and (2.96), the Soret coefficient for component  $A$  is not equal to the negative Soret coefficient for component  $B$ , as should follow from the definition of the Soret coefficient in eq. (2.45), and both calculations are therefore shown with the Soret coefficient for silver being a solid line and the negative Soret coefficient for aluminium being a dashed line. For the models in eqs. (2.86), (2.90) and (2.92), they correctly give  $S_{T,A} = -S_{T,B}$ , and the lines therefore overlap. None of the models accurately predict the behaviour of the Soret coefficient as measured in this thesis. They all to a varying degree predict a noticeable decrease in the Soret coefficient for the higher silver-concentrations measured, while this is not observed in the measurements. The deviation between the models and the measurements for a silver-concentration of  $c_{\text{Ag}} = 50 \text{ at.}\%$  is 273 % for the model of Dougherty and Drickamer, 28 % for the model of Jafar-Salehi et al. if the Soret coefficient for aluminium is used (416 % if the Soret coefficient for silver is used), and worse for every other model presented in this thesis. The model of Artola et al. even gives the incorrect sign, although it there

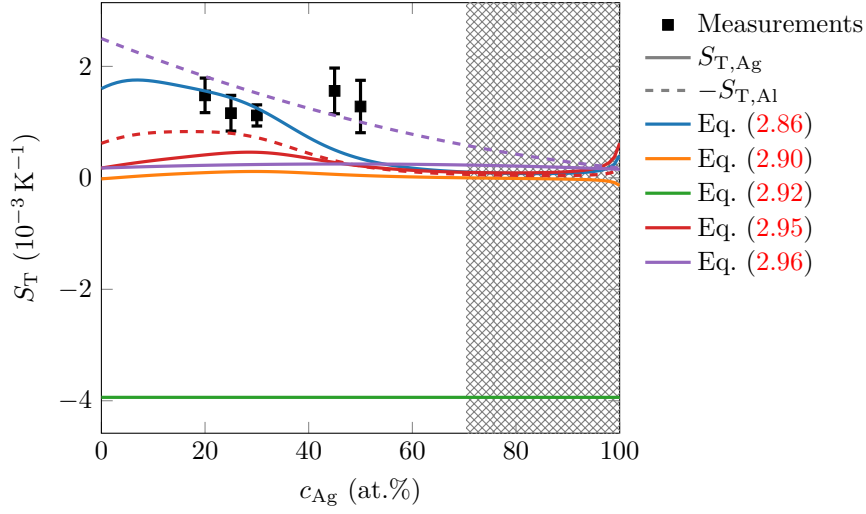


FIGURE 5.6: Calculated Soret coefficients for liquid Ag–Al with different models at a mean temperature of 1017 K.

should be noted that the model requires the activation energy of self-diffusion for each component of the mixture, which is not available in the literature for this alloy, except for the reported value by Engelhardt et al. for silver in liquid  $\text{Ag}_{20.4}\text{Al}_{79.6}$  [81]. Using the activation energy of self-diffusion for silver for this specific alloy, combined with the value for pure aluminium from Demmel et al. still predicts a negative Soret coefficient, though. This is consistent with other findings in the literature, where an incorrect sign has been predicted by the model when using NEMD simulations [185].

### Ag–Cu

For the models for thermodiffusion, the following sources were used for the thermophysical properties: for the Gibbs energy, the excess Gibbs energy parameters from Witusiewicz et al. were used [67]. For the component specific parameters, the same silver values as for Ag–Al were used. For copper, the density and activation energy of viscous flow by Assael et al. was used [84], the activation energy of self-diffusion as reported by Meyer was utilised [183], and the thermoelectric power from Chaïb et al. was used [189].

The Soret coefficients for Ag–Cu as predicted by the models are shown in fig. 5.7, as calculated for the entire concentration range for a mean temperature of 1099 K, the same as for the experiment. Just as in fig. 5.6, the hatched pattern indicates where the alloy isn't fully liquid, and therefore where the model isn't valid. With only one data point, it is difficult to say anything about the trend of the Soret coefficient, but it can be noted that the model of Shukla and Firoozabadi (eq. (2.90)) is within the uncertainty of the measurement itself. As the measured Soret coefficient is so close to zero, it can not be clearly established whether the models predict the incorrect sign, but it is at least clear that the absolute value of the Soret coefficient is grossly misrepresented by several of the models.

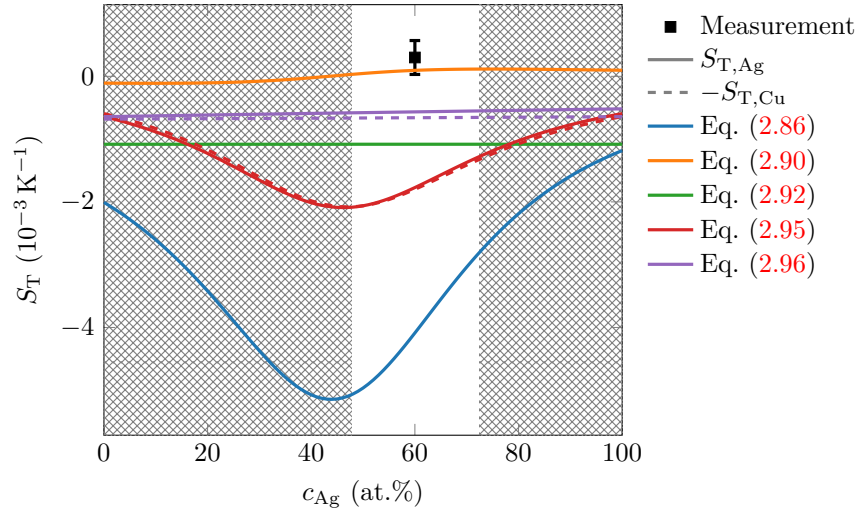


FIGURE 5.7: Calculated Soret coefficients for liquid Ag–Cu with different models at a mean temperature of 1099 K.

Note that due to the low contribution of the electronic part, as the absolute thermopower of Ag is nearly half that of Cu [188, 189], while the valency of Ag is double that of Cu [82], the model of Eslamian et al. (eq. (2.95)) has an almost zero discrepancy between the two directions of calculations of the Soret coefficient, as the discrepancy arises from the multiplication of  $c_{\text{Cu}}$  to the cross-multiplied thermopowers and valences ( $z_{\text{Cu}}\mathcal{E}_{\text{Ag}} - z_{\text{Ag}}\mathcal{E}_{\text{Cu}}$ ).

### Al–In

For the Gibbs energy of the Al–In system, the parameters from Singh and Sommer were used (see footnote 4 on page 39) [71]. For the component specific parameters, the aluminium values discussed earlier were used. For indium, the density and activation energy of viscous flow by Assael et al. was used [190], the activation energy of self-diffusion was calculated from the self-diffusion measurements by Careri et al. [191], and the thermoelectric power was taken from Marwaha and Cusack [187].

The Soret coefficients for Al–In as predicted by the models are shown in fig. 5.8, as calculated for the entire concentration range for a mean temperature of 1110 K, the same as for the experiment (the alloy is just above the critical point, and therefore a fully miscible liquid over the entire concentration range). All models are clearly misrepresenting the behaviour of the Soret coefficient close the miscibility gap. The models of Eslamian et al. and Dougherty and Drickamer predict the incorrect sign, and so does the model of Shukla and Firoozabadi, as it predicts a Soret coefficient of  $-0.12 \times 10^{-3} \text{ K}^{-1}$  and  $-0.11 \times 10^{-3} \text{ K}^{-1}$  for liquid  $\text{Al}_{85}\text{In}_{15}$  and  $\text{Al}_{78}\text{In}_{22}$  at 1110 K, respectively. First at  $c_{\text{In}} = 25 \text{ at.}\%$  does it change sign, and from there rapidly increase the absolute value of its predicted Soret coefficient.

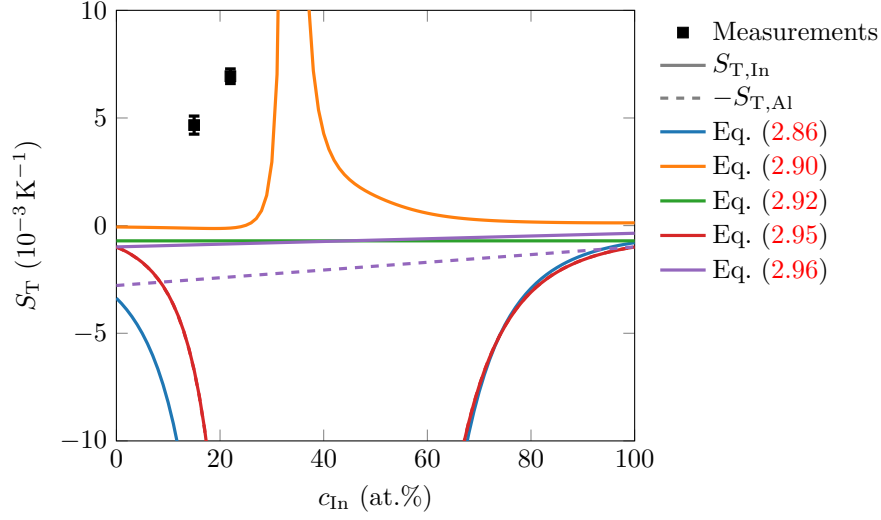


FIGURE 5.8: Calculated Soret coefficients for liquid Al–In with different models at a mean temperature of 1110 K.

### Summary of the predictability of the models

As can be seen in the predicted values for the Soret coefficients for the different alloys as shown in figs. 5.6 to 5.8, all models gravely fail to predict the behaviour of the measured alloy in at least one of the alloys.

While the model of Dougherty and Drickamer seems to predict Soret coefficients fairly close to the one measured for Ag–Al, the same model totally misses the measurements of Ag–Cu and Al–In.

The model of Shukla and Firoozabadi, which was the one best able to predict the simulations of Hoang and Galliero [122] and Gittus and Bresme [185], also fared among the best of the models presented in this work, but consistently predicted too low values, and even the incorrect sign for the measured concentrations of Al–In.

The model of Artola et al., like in the simulation results of Gittus and Bresme, failed to predict the correct sign in any of these experiments, although it should be noted that the activation energy of self-diffusion that is required for the calculation was not available for the specific alloys measured here, and therefore the pure component values were utilised instead. However, as the self-diffusion coefficient tends to be unchanging near a miscibility gap [192, 193], and with the lack of the TDF in the model of Artola et al., it seems unable to predict any critical behaviour.

The models of Eslamian et al. and Jafar-Salehi et al., which were explicitly developed for liquid alloys, break the fundamental relationship between the Soret coefficients in a binary mixture ( $S_{T,0} = -S_{T,1}$ ), and it is therefore advised to not use those models. Ignoring that fundamental flaw, they both fail to predict the sign of the measurements in Ag–Cu and Al–In, although they do both give fairly accurate predictions for Ag–Al, but only for one of the calculated directions, while the other direction is off by more than a factor of two.

As mentioned in section 2.3.2, the model of Jafar-Salehi et al. is based on the

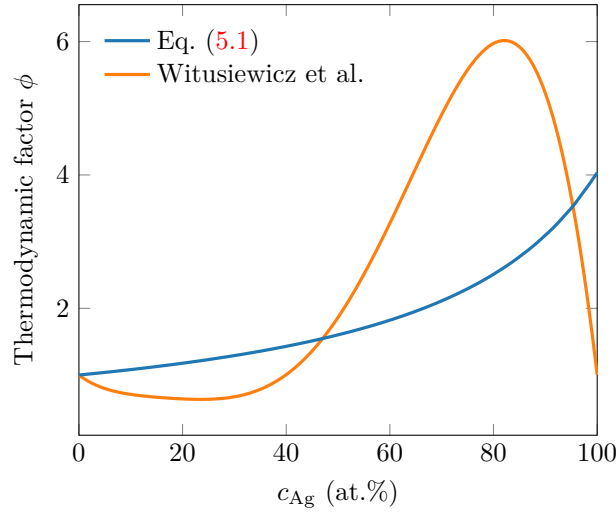


FIGURE 5.9: Calculated TDF from the approximation of eq. (2.97) and the actual eq. (2.31).

model of Eslamian et al., with the change being the replacement of the derivative of the chemical potential with an expression based on density (eq. (2.97)). This new expression through eq. (2.34) gives a TDF for liquid Ag–Al of

$$\phi_{JS} = \frac{1}{c_{Ag} \left( \frac{\rho_{Al}}{\rho_{Ag}} - 1 \right) + 1} \quad (5.1)$$

This expression is plotted in fig. 5.9 alongside the TDF as calculated with the Gibbs energy from the thermodynamic evaluation of Witusiewicz et al. [67], both plotted for a temperature of 1017 K. It is from this figure clear that the behaviour of the expression is nothing like the actual TDF. The approximation itself appears to stem from the work of Maier et al., developed for the dilute limit, which may explain why the expression for the TDF fails to give  $\phi_{JS} = 1$  for the ideal pure limit of  $c_{Ag} = 100$  at.%. The fit between the TDF from eq. (2.97) and the actual expression from eq. (2.31) is even worse for other alloys, so the fit of the model of Jafar-Salehi et al. with the measurements of the Soret coefficients in liquid Ag–Al in fig. 5.6 is therefore most likely a coincidence.

#### What if the experimental input parameters are wrong?

An argument could be made that at least one of the discussed models is correctly describing the effect of thermodiffusion in binary liquid alloys, but that one or several of the experimental input parameters (activation energy of viscous flow  $E^{vis}$ , density  $\rho$ , etc.) are incorrectly reported in the literature, and therefore that the inaccuracy of the predictions by such a model is due to those inaccurate measurements, and not the model itself.

To test this hypothesis, parameters with random deviations were generated, where the value was multiplied by a random factor of uncertainty, run through the models, and the result investigated to see whether any combination of such deviations gave predictions that aligned with the measurements reported here.

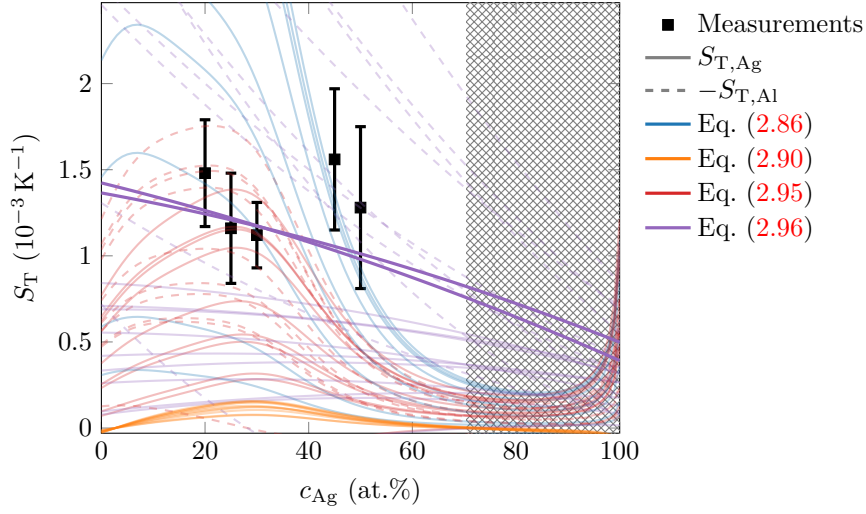


FIGURE 5.10: Calculated Soret coefficients for liquid Ag–Al with deviated parameters at a mean temperature of 1017 K.

This was tested with the measurements of the Ag–Al system, as it had the broadest band of investigated concentrations. For all models, and also for both “directions” of the models by Eslamian et al. and Jafar-Salehi et al., 200 sets of randomly deviated parameters were generated, where the deviation  $\delta$  was selected randomly from a uniform interval of  $\delta \in [0.75, 1.33]$ , and multiplied to the original parameter from the literature, e.g.,  $\hat{\rho}_{\text{Ag}} = \delta \times \rho_{\text{Ag}}$  for the deviated value  $\hat{\rho}_{\text{Ag}}$  for the density of liquid silver. In other words, the parameters reported in the literature were assumed to be a maximum of 33 % higher or 33 % lower than the “true” value. This was only done to the densities  $\rho_{\text{Ag}}$  and  $\rho_{\text{Al}}$ , activation energies of viscous flow  $E_{\text{Ag}}^{\text{vis}}$  and  $E_{\text{Al}}^{\text{vis}}$ , TDF  $\phi$ , energies of vaporisation  $E_{\text{Ag}}^{\text{vap}}$  and  $E_{\text{Al}}^{\text{vap}}$ , partial molar enthalpies  $\Delta H_{\text{Ag}}$  and  $\Delta H_{\text{Al}}$ , activation energies of self-diffusion  $E_{\text{Ag}}^{\text{self}}$  and  $E_{\text{Al}}^{\text{self}}$ , and thermoelectric powers  $\mathcal{E}_{\text{Ag}}$  and  $\mathcal{E}_{\text{Al}}$ . The valencies, physical constants ( $R$ ,  $F$ ), and molar masses were considered to have negligible uncertainty, as they are standard values [76, 82]. Also the temperature and concentration were assumed to be certain.

This estimated uncertainty of 33 % should encapsulate all measurement errors for all the parameters taken from the literature, based on the reported uncertainty for the thermoelectric power for aluminium, which had the highest reported uncertainty of all parameters used in the models, reported to be at most 10 % [187]. The uncertainty in the TDF is difficult to estimate, but in multicomponent (at least three component) systems is estimated to be around 20 % [97, 194, 195]. As binary systems are simpler, a reduced uncertainty is expected.<sup>5</sup>

Of the 200 sets of deviated parameters in this test, 10 concentration-dependent predictions are shown from each model in fig. 5.10. Of all the models, only the one by Jafar-Salehi et al. is able to predict a value of around  $(1.3 \pm 0.3) \times 10^{-3} \text{ K}^{-1}$  over the entire investigated concentration range, as was found in the experiments,

<sup>5</sup>The uncertainty from the TDF is further investigated in section 5.3

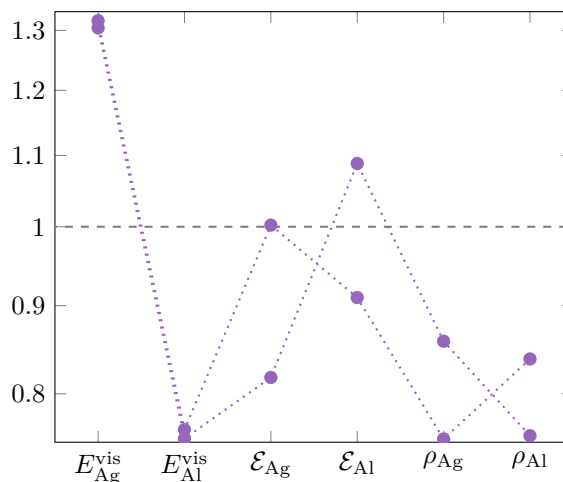


FIGURE 5.11: Deviations in parameters for the two accurate predictions in fig. 5.10.

with 2 of the 200 simulated parameter sets achieving coefficients within the error bars for that range. These two accurate predictions are shown in fig. 5.10 as thicker non-faded lines. The predictions from the model of Artola et al. are not included in the figure, as none of the parameter sets gave a Soret coefficient higher than  $-2.3 \times 10^{-3} \text{ K}^{-1}$ . Of all the other models that are close to at least one of the measured values, they either predict a much higher or a much lower value for the other concentrations.

The deviation to each individual parameter in the two sets that give predictions within the measured error bar is shown in fig. 5.11. From that figure, it is revealed that for the model of Jafar-Salehi et al. to predict accurate Soret coefficients, the “real” activation energy of viscosity for liquid silver  $E_{\text{Ag}}^{\text{vis}}$  has to be 30 % higher than the one reported in the literature, while the same parameter for aluminium has to be 30 % lower than the one reported in the literature, while the other parameters are allowed to deviate more freely.

The big question is then: is the model of Jafar-Salehi et al. correct, and thus the activation energy of viscosity incorrectly reported for silver and aluminium in the literature? The activation energies of viscosity used for these calculations were taken from systematic reviews by Assael et al. of all publications on temperature-dependent viscosity for the two liquid elements, where the different publications were critically examined, and the recommended reference values reported [74, 75]. For silver and aluminium, they reported standard deviations of 3.8 % and 13.7 % at the 95 % ( $2\sigma$ ) confidence level, respectively. Assuming the reported value of Assael et al. for silver follows a normal distribution, this means that such an error in reporting by Assael et al. would be outside of  $\frac{30}{3.8} \times 2\sigma \approx 16\sigma$ , which is extremely unlikely. This, combined with the use of an approximation for the derivative of the chemical potential that was developed for dilute mixtures and doesn’t give the correct ideal relationship for the case of  $c_{\text{Ag}} = 100 \text{ at.}\%$ , and the fact that the model of Jafar-Salehi et al. doesn’t even follow the fundamental relationship of the Soret coefficient ( $S_{\text{T},0} = -S_{\text{T},1}$ ), is extremely indicative (to put it lightly) to that the model of Jafar-Salehi et al. is incorrectly describing the



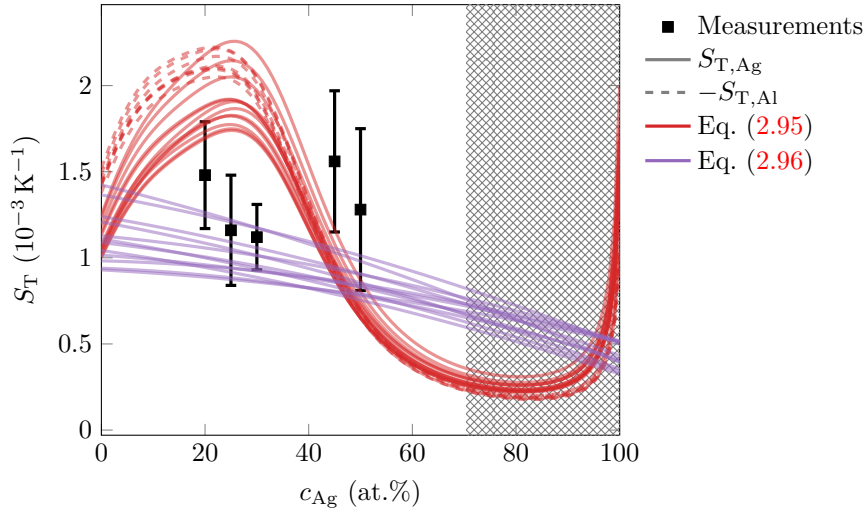


FIGURE 5.12: Calculated Soret coefficients for liquid Ag–Al with deviated parameters where within 100 % of the measurements at 1017 K.

Soret coefficient of the liquid Ag–Al system, and therefore binary liquid alloys in general, for which it was developed to be able to predict.

When increasing the uncertainty of the measured Soret coefficients up to 100 %, only the model of Eslamian et al., in addition to the model of Jafar-Salehi et al. (which is based on the model of Eslamian et al.), was able to predict values within that range for all investigated concentrations, with the Soret coefficient for silver being inside that range for 12 out of the 200 sets of deviated parameters, and the Soret coefficient for aluminium being inside that range for 7 out of 200, in addition to now 12 out of 200 for the model of Jafar-Salehi et al. calculated for silver (but none when calculated for aluminium). These are shown in fig. 5.12, where the predictions with the model of Eslamian et al. again show a strong concentration dependency for the predicted Soret coefficients, a trend that was at all not observed for the measured Soret coefficients.

For the deviated parameter sets in fig. 5.12, the deviation to each individual parameter is shown in fig. 5.13. The figure shows that again the predictions from the models of Eslamian et al. and Jafar-Salehi et al. both are only within 100 % of the measured Soret coefficients if the “real”  $E_{Ag}^{vis}$  is approximately 20 % higher than the one reported in the literature, while  $E_{Al}^{vis}$  is approximately 10 % lower than the one reported in the literature. Actually, assuming zero deviation for the other parameters ( $\mathcal{E}_{Ag}$ ,  $\mathcal{E}_{Al}$ ,  $\phi$ ,  $\rho_{Ag}$ ,  $\rho_{Al}$ ) still predicts values within 100 % of the measured Soret coefficients, showing how the selection of the activation energy of viscosity is the most crucial parameter for the models of Eslamian et al. and Jafar-Salehi et al. when applied to the liquid Ag–Al system.

Also, note how for the model of Eslamian et al. all the sets of deviated parameters for the calculation of the Soret coefficient for aluminium with the model of Eslamian et al. that are within 100 % of the measurements (centre plot of fig. 5.13) are among the same sets which predict the Soret coefficient for silver (leftmost plot of fig. 5.13). These points are shown in colours in the figure, while

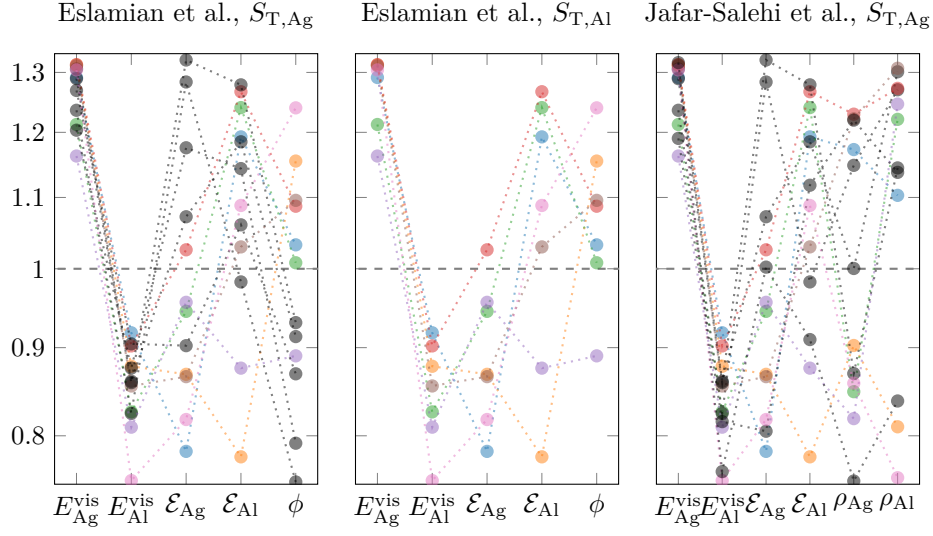


FIGURE 5.13: Deviations in parameters used for predictions in fig. 5.12.

the sets that predict correctly for silver but not aluminium are shown in black. This is due to the difference  $(E_{Ag}^{vis} - E_{Al}^{vis})$  appearing in the model of Eslamian et al. (see eq. (2.95)), which gets comparatively much larger than the other term in the numerator in that model,  $(z_{Al}\mathcal{E}_{Ag} - z_{Ag}\mathcal{E}_{Al})c_{Al}FT$ , drowning out the introduction of the term  $c_{Al}$ , the part of the model which makes it break with the fundamental relationship of the Soret coefficient  $S_{T,0} = -S_{T,1}$ . As the model of Jafar-Salehi et al. is based on the model of Eslamian et al., most of the parameter sets that predict Soret coefficients close to the measured ones are shared by both models. Due to the replacement of the TDF in the model of Jafar-Salehi et al. with a crude estimate that only vaguely holds for lower concentrations (eq. (5.1)), none of the predicted coefficients calculated for aluminium are close to the measurements, which were performed with aluminium-rich alloys.

Again, the likelihood of the activation energy of viscosity being incorrectly reported for silver and aluminium in the literature is extremely low, as an error in the reported activation energy of viscosity for silver of 20 at.% still implies the reported value being outside of  $10\sigma$ ; still extremely unlikely. Also the model of Eslamian et al. doesn't follow the fundamental relationship of the Soret coefficient, so both models are likely incorrectly describing the Soret coefficient of the liquid Ag–Al system.

This again supports the conclusion from works on simulated liquids that there is no current accurate predictive model for thermodiffusion in liquids [122, 185].

### 5.2.2 Possible theory behind thermodiffusion contributions

#### Morozov

With the lack of proper models describing thermodiffusion, as shown in the previous section, it is clear that the process is not yet fully understood. Ther-

modiffusion is a complex process, and in binary mixtures it has been found to be dependent on the mass differences, sizes, moment of inertia, and ionic properties of the different components, among other properties [197]. Attempts have been made to separate the Soret coefficient into different additive contributions in efforts to explain the change in the Soret coefficient when tuning one of the parameters listed above [80, 122, 198, 199].

An especially notable investigation is the work of Debuschewitz and Köhler, where they using different isotopes of the components in liquid benzene–cyclohexane found that the measured Soret coefficients could be split into an isotopic (molar mass dependent) part and a chemical (all other parameters) part, or [198]

$$S_T = S_{T,\text{iso}} + S_{T,\text{ch}}. \quad (5.2)$$

Based on that result, Morozov developed a theory for non-polar liquids where the Soret coefficient is split into a pure contribution (from pure component properties) and a mixing contribution from the mixing itself and the excess properties from that mixing process [196], or

$$S_T = S_{T,\text{pure}} + S_{T,\text{mix}}. \quad (5.3)$$

This mixing term  $S_{T,\text{mix}}$  was then described as being proportional to the derivative of the excess volume  $V_E$  of the mixture with respect to concentration,

$$S_{T,\text{mix}} \approx k \frac{\partial V_E}{\partial c_0}, \quad (5.4)$$

where  $k$  is a *negative* constant. This then means that if there is a significant change in excess volume  $V_E$  with respect to concentration, one should expect a significant change in the Soret coefficient as well. This relation was supported by the work of Hartmann et al., who observed a clear linear relation between the Soret coefficient and the derivative of the excess volume when investigating a large group of binary mixtures from a pool of organic solvents [80]. The ratio between the excess volume and the total volume is similar in liquid alloys to that of the organic solvents investigated by Hartmann et al. [66], but the applicability for the theory of Morozov has not yet been investigated for liquid alloy systems.

For the measurements of the liquid Ag–Al system in this work, the concentrations ranged from 20 at.% to 50 at.% silver, a range where the excess volume of the liquid alloy has by Brillo et al. has been found to vary significantly [70]. The negative derivative of the excess volume as described by Brillo et al. is plotted over the measured Soret coefficients in fig. 5.14, the negative sign to take the sign of the constant scale factor  $k$  into account. Brillo et al. gave parameters for two models for the excess volume, one conventional (solid blue line) on the same form as the Redlich-Kister (RK) polynomials shown in eq. (2.10), and one purely empirical (dashed blue line) that better followed the trend of their measurements [70]. In fig. 5.14, no clear relation between the measured Soret coefficients and the two excess volume models is clear. Neither a stable decay in the Soret coefficient, as for  $-\frac{\partial V_E}{\partial c_{\text{Ag}}}$  for the conventional model, nor an increase of the Soret coefficient towards approximately 35 at.% silver, as for the empirical model, is observed. Therefore, unless the mixing part of the theory of Morozov is small, or at least smaller than the noise in the experiments, the theory doesn't accurately capture the behaviour observed in these experiments.

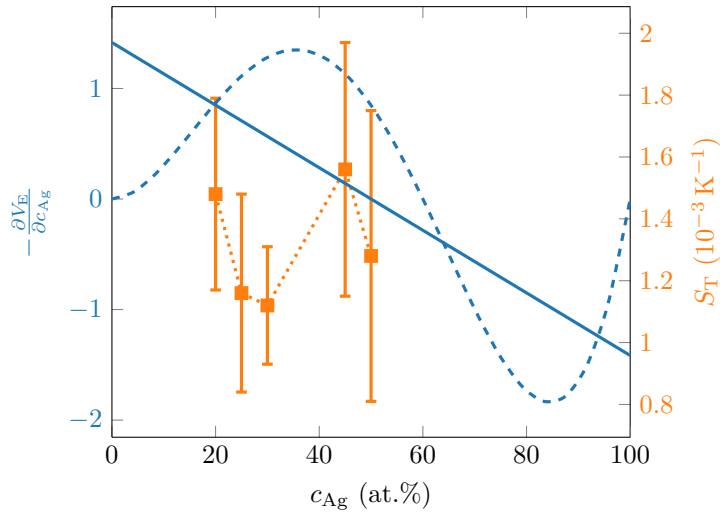


FIGURE 5.14: The derivative of the excess volume of the liquid Ag–Al system from Brillo et al., plotted over the Soret coefficients measured at 1017 K.

Notably, the excess volume of liquid Ag–Cu was by Brillo et al. found to be negligible, making the derivative of the excess volume much smaller for liquid Ag–Cu than for liquid Ag–Al [69]. According to the theory of Morozov, this then means that the measurement of a negligible Soret coefficient for liquid  $\text{Ag}_{60}\text{Cu}_{40}$  is due to the negligible excess volume of the system (and therefore a negligible  $S_{T,\text{mix}}$ ), and that the measured Soret coefficient comes from the pure part  $S_{T,\text{pure}}$  alone. This then again means that the pure part must be large for Ag–Al, and also Al–Cu (which has an even larger excess volume than Ag–Al and was found to have a Soret coefficient similar to Ag–Al by Bhat [51, 70]), while the pure part is negligible for Ag–Cu, possibly due to the pure contributions of Ag and Cu then cancelling out. More work is needed on measuring especially the alloys Ag–Cu and Al–Cu across their concentration ranges, to more firmly be able to either confirm or deny the theory of Morozov for liquid alloy systems.

### Gittus and Bresme

In a recent publication, Gittus and Bresme reported a potential correlation between the extrema of the Soret coefficient with respect to concentration and the extrema of the TDF with respect to concentration within the same mixture. This conclusion stems from their analysis of simulation results for the two parameters in LJ mixtures, where although they obtained interdiffusion coefficients  $D$  and thermodiffusion coefficients  $D_T$  with different trends with respect to concentration, the resulting Soret coefficient  $S_T$  had extrema in the same region as the obtained TDF with respect to concentration [185]. In general, for mixtures with weakly changing self-diffusion with respect to concentration, the Soret coefficient and TDF can be linked through the definition of  $S_T$  and the Darken equation (eqs. (2.45) and (2.93)). If  $D_T$  is weakly changing as well, the correlation is clear. In the results of Gittus and Bresme, however, although  $D_T$

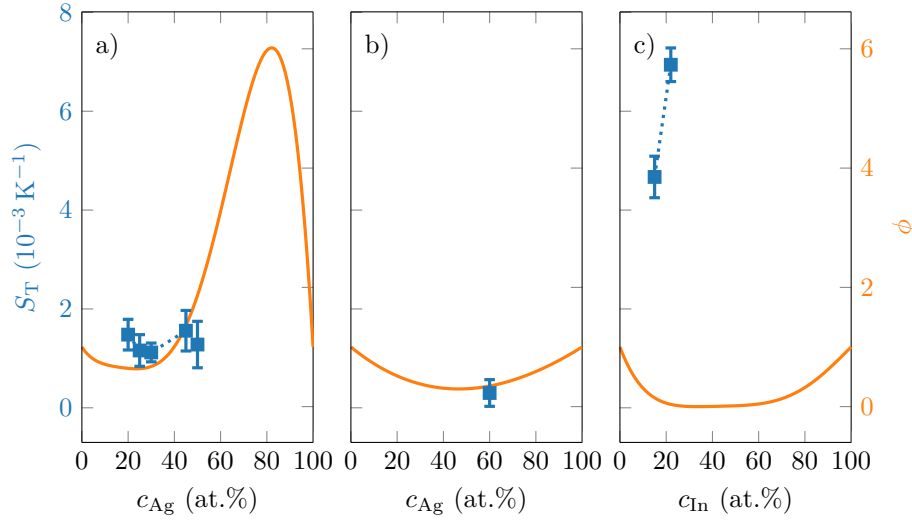


FIGURE 5.15: The measured Soret coefficients for Ag–Al, Ag–Cu, and Al–In plotted over their respective TDF.

varied greatly with concentration,  $D$  was behaving so that the link in extrema still appeared.

To test this for the systems investigated for this thesis, the Soret coefficients measured for Ag–Al, Ag–Cu, and Al–In are plotted over the TDF for each respective system in fig. 5.15, the TDF calculated from eq. (2.31) with the Gibbs energy from the thermodynamic evaluations of Witusiewicz et al. for Ag–Al and Ag–Cu, and Singh and Sommer for Al–In [67, 71].

For liquid Ag–Al at 1017 K (fig. 5.15a), the minimum of the TDF  $\phi$  is at  $c_{\text{Ag}} = 24 \text{ at.}\%$ , and it varies from  $\phi = 0.63$  to  $\phi = 1.86$  in the investigated composition range of 20 at.% to 50 at.% silver, i.e., beneficially for an observation of dependence of the Soret coefficient with the TDF [67]. Still, no clear correlation is visible between the Soret coefficient and the TDF. It should here be noted that also the interdiffusion coefficient itself does not vary significantly in this area of concentration, as reported by Engelhardt et al., albeit only measured in the range from 20.4 at.% to 42.5 at.% silver [81]. As seen in fig. 5.15a, for  $\text{Ag}_{25}\text{Al}_{75}$  the Soret coefficient is only slightly reduced relative to the coefficient for  $\text{Ag}_{20}\text{Al}_{80}$ , rather than increased, as the observation of Gittus and Bresme suggests. And finally, the strong increase of the TDF towards the higher silver concentrations does not result in any significant reduction for  $\text{Ag}_{45}\text{Al}_{55}$  and  $\text{Ag}_{50}\text{Al}_{50}$ .

For liquid Ag–Cu at 1099 K (fig. 5.15b), there's a minimum of the TDF near the equimolar composition, which then according to the findings of Gittus and Bresme should give a maximum of the absolute value of the Soret coefficient near that concentration [185]. As the Soret coefficient for  $\text{Ag}_{60}\text{Cu}_{40}$  was measured to be relatively small, according to both the Darken equation and the findings of Gittus and Bresme it then follows that the Soret coefficient is expected to decrease further near both the silver-rich and copper-rich ends. Further experiments at those ends would be able to elucidate whether this is a correct assumption. The

Darken equation has been shown to be invalid at the aluminium-rich side of Al–Ni [200], so it is not unthinkable that the same could be the case for Ag–Cu.

For liquid Al–In at 1110 K (fig. 5.15c), there is a strong concentration dependence of the TDF [71], as the temperature is just above the critical point of the alloy, where the TDF goes to zero. The Soret coefficient appears to have a strong concentration dependence as well, although it is difficult to assess the true uncertainty of the measurements with only two data points. The Soret coefficient for  $\text{Al}_{78}\text{In}_{22}$  was measured to increase by a factor of approximately 1.5 relative to  $\text{Al}_{85}\text{In}_{15}$ . For the same concentrations, the TDF as calculated from the thermodynamic evaluation of Singh and Sommer is given to be 0.148 and 0.038 [71], or a reduction by a factor 3.86. This mismatch in relative change indicates at least some change in either the self-diffusion coefficients for the alloy, the thermodiffusion coefficient, a strong deviation from the Darken equation, or a combination of these reasons. From the measured Soret and interdiffusion coefficients, the thermodiffusion coefficient  $D_T$  was calculated for both  $\text{Al}_{85}\text{In}_{15}$  and  $\text{Al}_{78}\text{In}_{22}$ , shown earlier in fig. 4.19, and they indicate some change in  $D_T$ , although with large uncertainty. The self-diffusion coefficient has been shown to exhibit only a weak temperature dependence in simulations of binary alloys with critical points [192, 193]. The concentration dependency of self-diffusion coefficients in non-critical liquid binary alloys tends to be low if the self-diffusion coefficients for the two pure components are similar at the investigated temperature [201–204], which is the case for Al–In at 1110 K [186, 191]. The non-linear scaling between the Soret coefficient and the calculated TDF may however also be from the choice of the thermodynamic evaluation for Al–In, as will be discussed further in section 5.3.2. In general, a closer investigation of the thermodiffusion in Al–In close to the miscibility gap would be of interest for elucidating the behaviour of this effect near the critical limit.

For liquid ternary Ag–Al–Cu, the description of the TDF is more complicated to interpret. For a ternary mixture, the TDF is a  $2 \times 2$  matrix, with matrix elements  $\phi_{i,j}$  defined in a similar fashion to the binary,<sup>6</sup> given as [97]

$$\phi_{i,j} = \frac{c_i}{RT} \frac{\partial \mu_i}{\partial c_j}. \quad (5.5)$$

The matrix description is analogous to the use of a matrix for the interdiffusion coefficients for a multicomponent system [62], as introduced in section 2.2.1, where for example the non-diagonal term  $\phi_{\text{Ag,Al}}$  describes the TDF for aluminium arising from the change in silver-composition, and vice versa for  $\phi_{\text{Al,Ag}}$ . This is shown in fig. 5.16, where the TDF is calculated for liquid Ag–Al–Cu at 1089 K using the thermodynamic parameters as reported for the ternary by Witusiewicz et al. [68]. In the pure limit (pure Ag, Al, or Cu, and thus in the corners in fig. 5.16) the diagonal entries  $\phi_{\text{Ag,Ag}}$  and  $\phi_{\text{Al,Al}}$  equal to 1, while the non-diagonal entries  $\phi_{\text{Ag,Al}}$  and  $\phi_{\text{Al,Ag}}$  equal to 0 [205]. The TDF matrix for the two measured systems is

$$\phi(\text{Ag}_{43.1}\text{Al}_{43.1}\text{Cu}_{13.8}, T = 1089 \text{ K}) = \begin{bmatrix} 0.07 & -2.10 \\ 1.27 & 4.53 \end{bmatrix} \quad (5.6)$$

---

<sup>6</sup>See section 2.1.3.

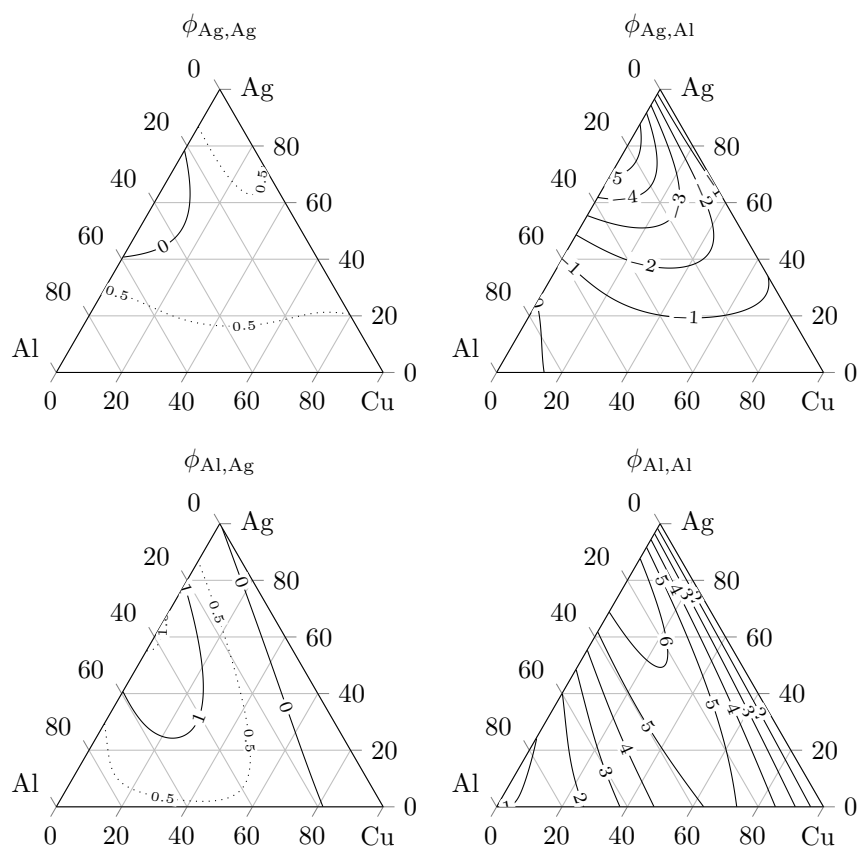


FIGURE 5.16: Ternary TDF  $\phi_{ij}$  for liquid Ag-Al-Cu at 1089 K. Half-integer contour lines are added to  $\phi_{\text{Ag,Ag}}$  and  $\phi_{\text{Al,Ag}}$  for better legibility.

and

$$\phi(\text{Ag}_{17.6}\text{Al}_{68.6}\text{Cu}_{13.8}, T = 983 \text{ K}) = \begin{bmatrix} 0.57 & -0.32 \\ 0.75 & 2.04 \end{bmatrix}. \quad (5.7)$$

The frame-invariant Soret coefficients as given in tables 4.3 and 5.3 are with high uncertainties, and no obvious correlation between the TDF and the frame-invariant Soret coefficients for the ternary alloy can be detected. Therefore, based on only the two ternary compositions measured of Ag–Al–Cu, there is no indication that there’s a correlation between the measured Soret coefficient and the TDF for the system. It should be noted that the publication by Gittus and Bresme investigates only the behaviour for a *binary* LJ mixture, and no higher order system is mentioned in the publication [185], so it is unclear whether the authors even considered a ternary system, and whether it followed the same correlating behaviour between thermodiffusion and the TDF or not.

With all this, it sums up to that there seems to be no strong link between the TDF and the Soret coefficient in the liquid alloys investigated here, as indicated in the results of Gittus and Bresme, although closer investigations of the self-diffusion, interdiffusion and thermodiffusion coefficients across the entire concentration range would be necessary to be able to determine conclusively whether there is a link at all, or if it is simply too weak to detect from the obtained results.

### 5.2.3 Hints to possible theory of thermodiffusion based on the results

Throughout this section of the thesis (section 5.2), several predictive models for thermodiffusion have been tested, but none were here found to accurately predict the concentration dependent behaviour of the Soret coefficient in the liquid binary alloys as observed in the experiments.

Meanwhile, the match of the interdiffusion coefficients found in the experimental results with the earlier published interdiffusion coefficients, together with the invariance of both Soret and interdiffusion coefficients with different fitting methods used, strongly suggest that the experimentally determined Soret coefficients were accurately measured.

Even when both the input parameters to the models and the experimental results were assumed very uncertain, only the model of Eslamian et al. was found to be within 100 % of the measurements. This involved assuming extremely unlikely systematic errors in published viscosity measurements, and also ignores the fact that the model by Eslamian et al. itself breaks with fundamental relationships for the Soret coefficient.

The proposed qualitative theory of Morozov was applied to the results, but no clear correlation between the derivative of the excess volume and the Soret coefficient could be found, meaning that for the theory to be correct in these alloys, only a weak dependency has to exist.

The correlation in extrema for the TDF and the Soret coefficient as proposed by Gittus and Bresme was not found in the experimental results presented in this thesis, outside of the general dependency of the Soret coefficient on the TDF as already described by irreversible thermodynamics theory.<sup>7</sup>

---

<sup>7</sup>See section 2.2.1.



Therefore it is concluded that neither the models nor the theories based on the contributions to thermodiffusion were able to accurately predict or explain the behaviour of the observed thermodiffusion or Soret coefficient. This is also the consensus in the literature, where new research is regularly published presenting new models, as well as debunking older models, and providing new hypotheses of the contributions to thermodiffusion [43, 95, 122, 128, 130, 185, 206–210].

Stepping back, some fundamental assertions on the origin of thermodiffusion can be made based on the results gathered for this thesis.

From the measurement of Al–In, the results support that the Soret coefficient is dependent on the TDF (although not with the strong correlation of extrema that was suggested by Gittus and Bresme), which as mentioned above already presents itself in the fundamental theory of Onsager,<sup>8</sup> where the chemical potential gradient, and thus the TDF, is introduced in the equations for thermodiffusion.

In all the measurements presented in this work, the Soret coefficients and the thermodiffusion coefficients have been shown to be within an order of magnitude, with the exception of the measurement of liquid Ag<sub>60</sub>Cu<sub>40</sub>, which gives a value around zero, making the uncertainty swallow any information on a possible coefficient of a smaller magnitude. As liquid Ag–Cu is the only system measured here with a known negligible excess volume, it may hint to the thermodiffusion being dependent on the excess volume  $V_E$ . The dependency could also be on a different excess property of the system, though, as it can be noted that of the systems investigated here, also the excess Gibbs energy itself is the smallest for the liquid Ag–Cu system [67, 71]. While the molar mass ratio of 1.7 for the Ag–Cu system is relative low compared to the other systems in this work (4.0 for Ag–Al and 4.3 for Al–In), it is similar to systems in other published works [51, 53, 60], systems with Soret coefficients similar to that for Ag–Al in this work, and is therefore likely not solely to blame for the reduced effect of thermodiffusion. The same goes for the density, which, while high in Ag–Cu, does not explain the lower Soret coefficient.

With all the possible parameters describing a liquid alloy system, like thermoelectric power, molar mass, enthalpy, density, and heat of vaporization, to name a few, there are many options for creating a new predictive model for the Soret coefficient. And as the Soret coefficient in the vast amount of reported experiments is on the order of  $S_T \sim 10^{-3} \text{ K}^{-1}$  (with the exception of systems where the TDF approaches zero), finding a combination of the various parameters which predicts a value in that range is no difficult task.

For future investigations on the background of thermodiffusion, the author of this thesis recommends to select systems which have critical properties (like a miscibility gap), zero excess volume, large difference in component molar masses, or similar interesting characteristics, which can help reveal dependency on or independence from these different parameters.

### 5.3 Selecting values for the excess Gibbs energy

As explained in section 2.3, most theoretical models for predicting the Soret coefficient in mixtures involve the derivative of the chemical potential with respect to the concentration  $c$  (or equivalently the TDF). As given by eq. (2.22),

---

<sup>8</sup>See section 2.2.1.

the chemical potential itself comes from the excess Gibbs energy, and the derivative thereof. This means that the thermodynamic evaluation from which the parameters are used to describe the excess Gibbs energy  $G_E$  is of importance in what value is returned from the model predicting the Soret coefficient. As mentioned in section 2.1.1, the parameters describing  $G_E$  are experimentally fitted, and in the case of the RK model (eq. (2.10)), higher order terms are added until the measured data are satisfactorily explained by the model. Any measurement error will then propagate to the equation for  $G_E$ , and then be magnified in the description for the derivative  $\frac{\partial G_E}{\partial c_i}$ . As the chemical potential  $\mu$  is dependent on the derivative of  $G_E$ , the derivative of  $\mu$  is therefore dependent on the double-derivative of  $G_E$ , or  $\frac{\partial^2 G_E}{\partial c_i^2}$ , meaning an even further magnification of the error in the description of  $G_E$ .

Here we will see how the selection of parameters for  $G_E$  may affect a model being dependent on the chemical potential. Only the cases for the systems Ag–Al and Al–In will be analysed, as they represent a fully miscible liquid and an immiscible liquid, respectively, and as they are the two most thoroughly investigated systems in this thesis.

### 5.3.1 The case of Ag–Al

There are three published thermodynamic evaluations on liquid Ag–Al [67, 161, 162], already listed in table 5.1. They all use the RK model for their description of the liquid alloy. The second evaluation is based on the data from the first evaluation, but was re-evaluated as the standard Gibbs energies for the pure components had been newly published, requiring a recalibration based on these new standard values, while also considering some newly published enthalpy data for the new evaluation [86, 162]. For the determination on parameters for the RK model, the authors for the second evaluation actively decided to reduce the highest order for the model, recognising that this would worsen the agreement between experiments and calculations, but pointing out the uncertainty in the concentrations for the experimental data used for the optimisation [162]. The third evaluation was motivated by the fact that the authors of it were not able to reproduce solid-liquid equilibria for phase diagram calculations using the already existing evaluations [67]. Using their own calorimetry measurements, in addition to the thermodynamic data published until then, they performed a new optimisation of the parameters for the RK model.

The  $G_E$ ,  $\frac{\partial G_E}{\partial c_{Ag}}$  and  $\frac{\partial^2 G_E}{\partial c_{Ag}^2}$  from these three evaluations are shown in fig. 5.17. The calculated TDF  $\phi$ , related to the second-derivative through eq. (2.33), is also shown. Especially from the shown disagreement in the second-derivative, it is clear that the selection of an evaluation is central to the calculated value of the TDF, and therefore most of the models used in section 5.2.1. Because the third evaluation was the most recent, from Witusiewicz et al. in 2004 (green in fig. 5.17) [67], it was selected to be used for this thesis.

It should be noted that the Wilson model, which was presented in eq. (2.12), has not been applied to describe the liquid Ag–Al system in the previous literature. Using that model would have led to problems with the predictive model of Shukla and Firoozabadi, as it relies on the enthalpy of the system [130]. As a first approximation, the Wilson model has a temperature-independent fitting parameter  $\lambda$ , which would give zero enthalpy, and thus zero Soret coefficient

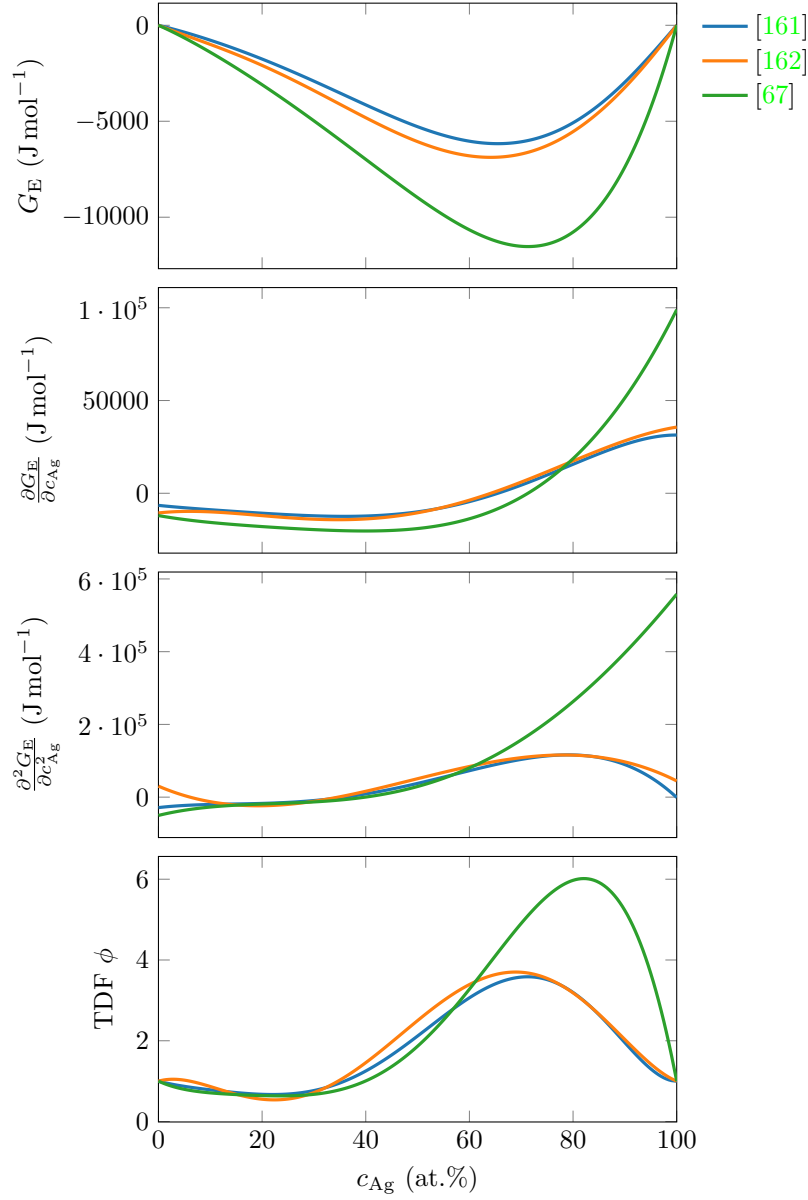


FIGURE 5.17: Excess Gibbs energy  $G_E$  for liquid Ag–Al, its two first concentration-derivatives, and TDF, all calculated for a temperature of 1017 K.

predicted for the thermodiffusion model of Shukla and Firoozabadi [98].

### 5.3.2 The case of Al–In

The Al–In system is interesting as there is no consensus on where the critical point lies, with critical temperatures between 1103 K and 1209 K being proposed the last four decades alone [71, 143, 211–213]. This disagreement also leads to very different thermodynamic evaluations of the liquid, as is shown in fig. 5.18. With these different thermodynamic evaluations, the different phase diagrams can be calculated in the concentration region where the thermodiffusion was investigated, i.e., Al<sub>85</sub>In<sub>15</sub> to Al<sub>78</sub>In<sub>22</sub>. The resulting phase diagrams are overlaid in fig. 5.19. From that figure, it is revealed that the certainty about the miscibility of the liquid alloy used for the thermodiffusion experiment can be questioned, although the lack of any observed demixing, with the behaviour of the concentration separation and the fitted interdiffusion coefficient, strongly suggests that the alloy was indeed not within the miscibility gap, and thus supports the use of the evaluations of either Murray, Singh and Sommer, or Kaban et al. [71, 143, 211], while discouraging the use of the evaluations of Ansara et al., and Kim and Sanders [212, 213]. Because the evaluation of Kaban et al. uses only two terms for their fitting of the RK model, which therefore gives a linear function for  $\frac{\partial^2 G_E}{\partial c_{In}^2}$ , and as the evaluation of Singh and Sommer is newer than the evaluation of Murray, the evaluation of Singh and Sommer was selected to be used for this thesis.

As the Soret effect is a very sensitive effect, the measured Soret coefficient near the miscibility gap can be used to verify or denounce a thermodynamic evaluation, if the calculated TDF decreases at a different rate than the Soret coefficient increases. As the Soret coefficient increased by a factor 1.5 while the TDF decreased by a factor 3.9 (see section 5.2.2) as calculated with the evaluation of Singh and Sommer, it may imply that the miscibility gap is calculated too high in that region, and that the evaluation of for example Kaban et al. may be the better one after all. The fact that the Soret coefficient is measured over a temperature range complicates this comparison, however, so a smaller temperature difference would be helpful for this investigation.

Note that there is another recent publication on a thermodynamic evaluation for liquid Al–In, where the authors have modelled the liquid using the non-random two-liquid (NRTL) model [214], which was presented in eq. (2.13). This was found by fitting the NRTL model to the results from the RK model given by the parameters of Ansara et al., and the two descriptions therefore give very similar results by design. It was therefore not further discussed here.

### 5.3.3 Summary

To summarise this section, it is clear that calculating the TDF for any system is highly dependent on the thermodynamic evaluation used. This should be kept in mind for any work where the TDF is applied or discussed. The sensitivity of the Soret effect, and its reciprocal dependency on the TDF makes it however an interesting potential way to verify or denounce a thermodynamic evaluation for systems where there is a big spread in possible evaluations.

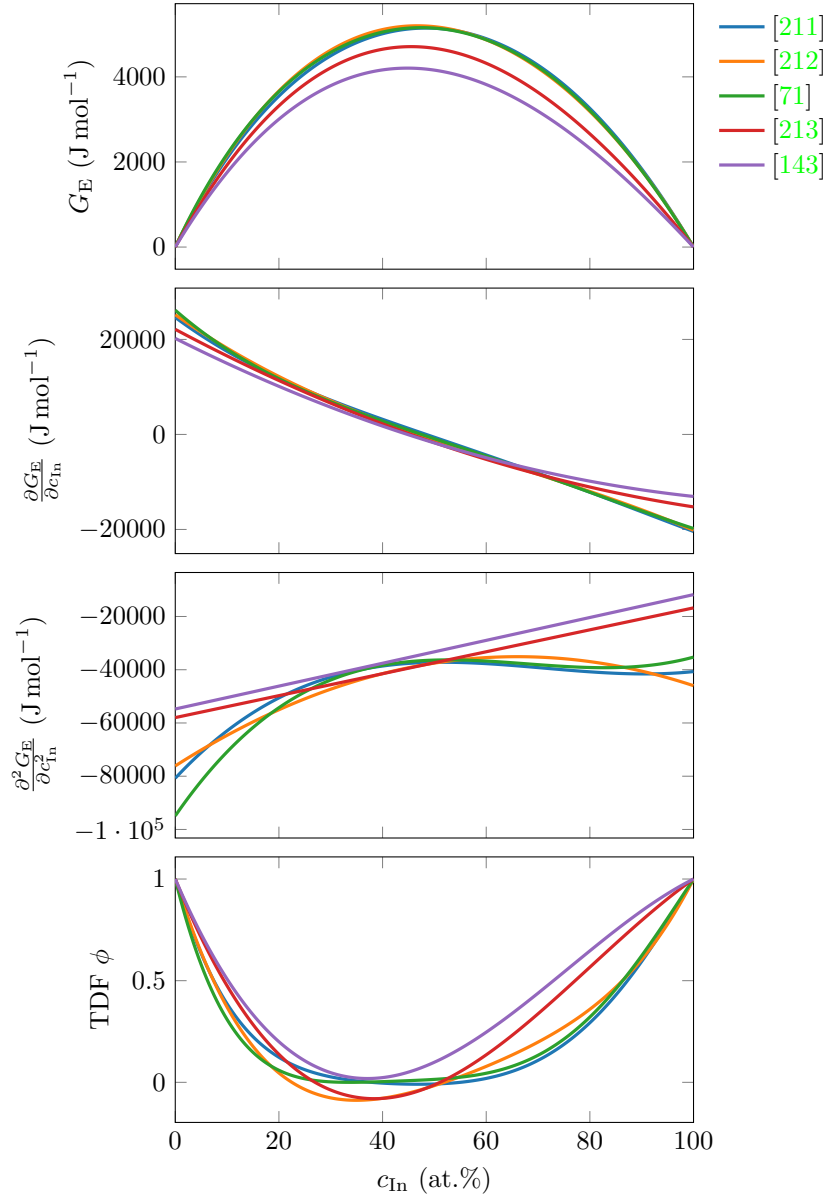


FIGURE 5.18: Excess Gibbs energy  $G_E$  for liquid Al-In, its two first concentration-derivatives, and TDF, all calculated for a temperature of 1110 K.

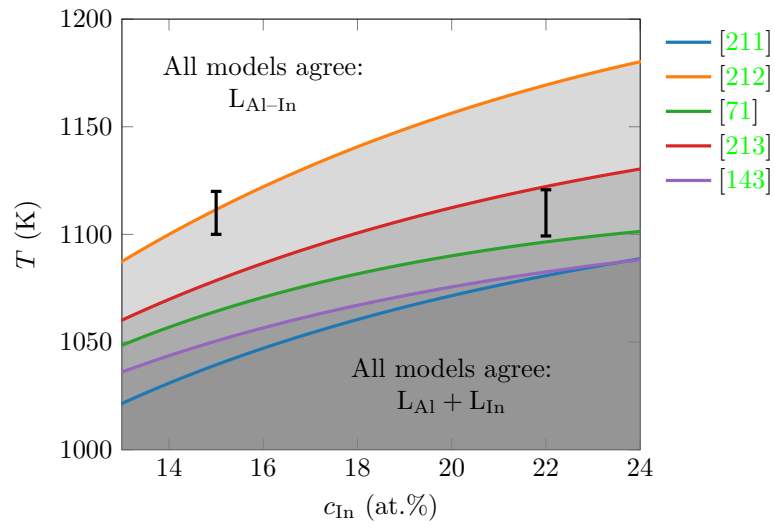


FIGURE 5.19: Different calculated phase diagrams for the Al-In system, shown in the region where the measurements on  $\text{Al}_{85}\text{In}_{15}$  and  $\text{Al}_{78}\text{In}_{22}$  were performed.

## Chapter 6

# Conclusions

Thermodiffusion in the liquid binary alloys Ag–Al, Ag–Cu, and Al–In, as well as in the liquid ternary alloy Ag–Al–Cu, has been experimentally investigated.

Thermodiffusion is especially relevant in liquid alloys, as their high melting points involve high temperatures and large temperature gradients. In metals, thermodiffusion can affect solders and the manufacturing of integrated circuits, it has been employed for crystal growth, and has recently been shown to be of use in creating metallic nanowires.

Earlier experimental efforts have focused on liquid organic systems, which often are too complex to be applicable to simulations, proposed theories and models for the effect. Precisely measuring the effect in liquid alloys grants the possibility to test these proposed hypotheses, while also giving the developers of such models new datasets with much higher credibility/certainty than those thus far available.

The few earlier measurements of thermodiffusion in liquid alloys have used methods that involve great uncertainties and inability to monitor impurities, transient behaviour (and thereby the interdiffusion coefficient), free surfaces, and bubbles that can greatly disturb the experiments. As recently shown by Sondermann et al., in situ X-ray radiography (XRR) allows a much better ability to monitor the conditions in the sample cell.

With this new method, much more precise measurements of the Soret coefficient  $S_T$  can be performed, and its dependence on several factors (such as component density, molar mass, and excess volume) can be properly elucidated.

A new sample cell was developed, using a boron nitride (BN) furnace with pistons to eliminate bubbles in the melt, heating wires on each side of the sample cell for temperature control. With the setup, thermodiffusion in liquid binary alloys could be investigated at temperatures of up to 1373 K, and with temperature gradients exceeding  $3 \text{ K mm}^{-1}$ . For liquid ternary alloys, or binary systems with inadequate X-ray contrast, a similar shear cell system was used, where the samples could be sheared into six pieces at the end of the experiment, and the concentrations for each piece determined ex situ through energy-dispersive X-ray spectroscopy (EDXS).

Through measurements and subsequent data analysis, the temperature gradient was shown to be linear, the thermocouples were shown to be accurately calibrated, the alloys to be properly weighed, and the proportional–integral–derivative (PID) control coefficients optimised.

Through investigation with simulated datasets, it was discovered that using only one term of the infinite-term description for the transient concentration difference gave the most accurate fit to the linearised transient description, a novel result that is useful for investigations on thermodiffusion in systems with high degrees of noise, while eradicating a possible source of systematic error in the reported interdiffusion coefficient from thermodiffusion experiments.

The pre-described method was applied to liquid Ag–Al, where the thermodiffusion could be successfully measured for concentrations from 20 at.% to 50 at.% silver. The Soret coefficient was found to be unchanging over the mentioned concentration range, and a value of  $S_T = (1.3 \pm 0.3) \times 10^{-3} \text{ K}^{-1}$  was determined, with silver (the heavier component) migrating to the cold side. This is the opposite direction of earlier measurements on thermodiffusion in the solid alloy, although it is argued that inconsistencies in those measurements may have been the reason for this disparity. The measured Soret coefficient in the liquid alloy is of the same order as earlier measurements in other liquid alloys, as well as in liquid organic systems. The interdiffusion coefficient could be measured from the transient behaviour of the concentration along the sample cell, and a coefficient in agreement with earlier direct measurements was found. This implies that the experiment was properly set up, and that impurities, as well as convection from sedimentation and free surfaces (Marangoni convection), were negligible. These results have been published in a peer-reviewed journal [150].

For liquid Ag–Cu, only a barely significant migration of silver towards the cold side was observed, using both XRR and EDXS. This is the same direction as found in earlier published molecular dynamics (MD) simulations, although much weaker than those simulated results. From the comparison of the other parameters of the simulations with earlier measurements on those parameters, it is argued that only a qualitative match in such a sensitive cross-effect as thermodiffusion can be expected. This weakness of the Soret coefficient can be seen in the view of a previously hypothesised theory on the dependency of thermodiffusion on the excess volume, as Ag–Cu possesses negligible excess volume, while the other measured systems in this work do not.

Using the earlier mentioned shear cell setup and EDXS, the thermodiffusion in liquid ternary Ag–Al–Cu was measured, where the heavier silver was found to migrate towards the cold side, the lighter aluminium towards the hot side, while the intermediate mass copper had no measurable net migration. This was the case for both liquid  $\text{Ag}_{17.6}\text{Al}_{68.6}\text{Cu}_{13.8}$  and  $\text{Ag}_{43.1}\text{Al}_{43.1}\text{Cu}_{13.8}$ , which together with the aforementioned results on binary Ag–Cu and earlier published measurements on Al–Cu break with earlier findings for simulations on simple Lennard-Jones (LJ) mixtures, where Artola and Rousseau observed that the direction of migration for the intermediate mass was linearly dependent on the concentrations of the other constituents. As for the migration of the silver and aluminium, the migration appears strengthened with the addition of copper, as compared to the aforementioned results on binary Ag–Al.

The liquid Al–In system has a miscibility gap, which according to theory and earlier measurements on organic systems with miscibility gaps implies that the Soret coefficient may diverge when closing into the miscibility gap. This has never before been observed in a liquid alloy. Using the experimental setup developed for this thesis on Al–In, the increase of the Soret coefficient near a miscibility gap could for the first time be measured in a liquid alloy, together with a observed strong decrease in the interdiffusion coefficient as compared to



earlier published measurements further away from the miscibility gap in the alloy. A Soret coefficient of up to  $7 \times 10^{-3} \text{ K}^{-1}$  was observed, with indium migrating towards the cold side, which is among the highest Soret coefficients ever measured in a liquid alloy. It is reasonable to assume that an even higher Soret coefficient could be measured when moving even closer to the miscibility gap.

From all these results,  $S_T$  is not found to be significantly dependent on the size of the ratio of molar masses or densities of the components. The measured coefficients are within the same order of magnitude of other measurements of similar liquid alloys, and even other types of liquid systems, such as organic systems and silicates, illustrating the remarkable universality of the Soret effect.

The coefficients measured for the binaries in this thesis could then be compared with the predictions from models for thermodiffusion, where no model was able to accurately predict the measured coefficient within its error bars for all systems when using the required parameters from the literature. Even when the input parameters were assumed uncertain, randomly varying the different parameters with  $\pm 33\%$  from their literature values, the only models able to predict within a factor two of the measured Soret coefficient for Ag–Al were ones which are the least physical (breaking with fundamental relationships for the Soret coefficient), while also assuming that published measurements on the viscosities of the pure components are outside of a  $10\sigma$  deviation from the reference values. It was therefore concluded that no predictive model published thus far is able to accurately predict the Soret coefficient for a liquid binary alloy system, a conclusion that is also supported by other publications on simulated LJ mixtures.

Furthermore, two qualitative theories for the Soret coefficient were tested, but for either model to be accurate, the proposed causalities have to be negligible to explain the behaviour of the concentration dependency of the Soret coefficient in the Ag–Al system.

These results highlight the current lack of understanding of the behaviour of the thermodiffusion in liquid alloys. Possible links between the excess volume and the Soret coefficient were proposed, and specific experiments for further investigations of confirmation or denunciation of theory were suggested.

Finally, using the measurements of the Soret coefficient around the miscibility gap is proposed as a method to facilitate the selection of a thermodynamic evaluation for such systems, where the critical limit may be difficult to properly ascertain, and where the divergence of the Soret coefficient is a sensitive measure of this limit.

With this, the thermodiffusion in liquid alloys has been better understood, inadequate models have been rejected, and possible new aspects of interesting research to thermodiffusion in liquid alloys have been highlighted.



# Appendix A

## Small calculations

### A.1 The derivation of the heat of transport $Q^*$

As stated in section 2.2.3, the definition of the heat of transport is *the heat needed to keep a specific system isothermal during mass diffusion* [120]. We will here show that this definition leads to the relation between the Soret coefficient and the heat of transport given in eq. (2.79).

We start with the mathematical definition of the heat of transport [104, p. 281]:

$$\mathbf{J}_q = \sum_{i=0}^{n-2} Q_i^* \mathbf{J}_i, \quad (\nabla T = 0), \quad (\text{A.1})$$

which for a binary mixture ( $n = 2$ ) becomes

$$\mathbf{J}_q = Q_0^* \mathbf{J}_0, \quad (\text{A.2})$$

or

$$Q^* \equiv Q_0^* = \frac{\mathbf{J}_q}{\mathbf{J}_0}. \quad (\text{A.3})$$

If we look back to the definition of the mass and heat flux from irreversible thermodynamics of (eq. (2.59))

$$\mathbf{J}_0 = -\rho D \nabla c_0 - \rho c_0 (1 - c_0) D_T \nabla T$$

and (eq. (2.62))

$$\mathbf{J}_q = -\lambda \nabla T - \rho c_0 D_F T \left( \frac{\partial \mu_0}{\partial c_0} \right) \nabla c_0,$$

we can model this system as being isothermal through setting  $\nabla T = 0$ , so that the equations turn into

$$\mathbf{J}_0 = -\rho D \nabla c_0 \quad (\text{A.4})$$

and

$$\mathbf{J}_q = -\rho c_0 D_F T \left( \frac{\partial \mu_0}{\partial c_0} \right) \nabla c_0, \quad (\text{A.5})$$

respectively.

Recall that the Dufour coefficient is equal to the thermodiffusion coefficient (eqs. (2.58) and (2.61), due to eq. (2.48)), and we then get the heat flux

$$\mathbf{J}_q = -\rho c_0 D_T T \left( \frac{\partial \mu_0}{\partial c_0} \right) \nabla c_0. \quad (\text{A.6})$$

If we put the expressions for the mass flux and heat flux in an isothermal system (eqs. (A.4) and (A.6)) into the definition of the heat of transport (eq. (A.3)), we get

$$Q^* = \frac{-\rho c_0 D_T T \left( \frac{\partial \mu_0}{\partial c_0} \right) \nabla c_0}{-\rho D \nabla c_0}, \quad (\text{A.7})$$

which through the well-known definition of the Soret coefficient  $S_T \equiv \frac{D_T}{D}$  quickly cancels down to

$$Q^* = c_0 S_T T \frac{\partial \mu_0}{\partial c_0}. \quad (\text{A.8})$$

Solving for the Soret coefficient, we get the expression

$$S_T = \frac{Q^*}{c_0 T \frac{\partial \mu_0}{\partial c_0}}. \quad (\text{A.9})$$

Inputting eq. (2.34), which was one of the many descriptions for the thermodynamic factor,  $\phi$ , we end up with our description from section 2.2.3 (eq. (2.79)):

$$S_T = \frac{Q^*}{\phi R T^2},$$

which is what we wanted to show.

## A.2 Soret coefficient calculation using mass ratio

The Soret coefficient in one dimension is defined as

$$S_T = -\frac{\partial c / \partial z}{\partial T / \partial z} \frac{1}{c_0(1 - c_0)}. \quad (\text{A.10})$$

We use mole fraction for  $c$ , but various literature often claim that the calculation of the Soret coefficient in *binary mixtures* is invariant on whether mole fraction or mass fraction is used. We will here show that this claim is correct.

The concentration defined from the mass fraction is given by

$$w_a = \frac{m_a}{m_a + m_b} \quad (\text{A.11})$$

for some binary mixture with components  $a$  and  $b$ . The concentration for atomic fraction is

$$c_a = \frac{n_a}{n_a + n_b}. \quad (\text{A.12})$$

We can now write mass concentration as a function of molar masses  $M_a$  and  $M_b$ , and the molar concentration:

$$w_a = \frac{n_a M_a}{n_a M_a + n_b M_b}, \quad (\text{A.13})$$

and thus, using  $n_i = c_i n$ ,

$$w_a = \frac{c_a M_a}{c_a M_a + c_b M_b} = \frac{c_a M_a}{c_a M_a + (1 - c_a) M_b}. \quad (\text{A.14})$$

We set  $c \equiv c_a$  and  $w \equiv w_a$ , and get

$$w = \frac{c M_a}{c M_a + (1 - c) M_b}. \quad (\text{A.15})$$

The temperature gradient is not dependent on the concentration, so we only need to look at the expression

$$\frac{\partial c / \partial z}{c_0(1 - c_0)}. \quad (\text{A.16})$$

We want to check whether the equivalent expression substituting  $c$  with  $w$  gives the same result. We start with the top part of the fraction in eq. (A.16), and input the weight fraction instead:

$$\frac{\partial w}{\partial z} = \frac{\partial}{\partial z} \left( \frac{c M_a}{c M_a + (1 - c) M_b} \right). \quad (\text{A.17})$$

From the quotient rule of derivation we get

$$\frac{\partial w}{\partial z} = \frac{\frac{\partial c}{\partial z} M_a (c M_a + (1 - c) M_b) - c M_a \left( \frac{\partial c}{\partial z} M_a - \frac{\partial c}{\partial z} M_b \right)}{(c M_a + (1 - c) M_b)^2}, \quad (\text{A.18})$$

which reduces to

$$\frac{\partial w}{\partial z} = \frac{c M_a^2 \frac{\partial c}{\partial z} + M_a M_b \frac{\partial c}{\partial z} - c M_a M_b \frac{\partial c}{\partial z} - c M_a^2 \frac{\partial c}{\partial z} + c M_a M_b \frac{\partial c}{\partial z}}{(c M_a + (1 - c) M_b)^2}, \quad (\text{A.19})$$

and further down to

$$\frac{\partial w}{\partial z} = \frac{M_a M_b \frac{\partial c}{\partial z}}{(c M_a + (1 - c) M_b)^2}, \quad (\text{A.20})$$

or written differently:

$$\frac{\partial w}{\partial z} = \frac{M_a M_b}{(c M_a + (1 - c) M_b)^2} \frac{\partial c}{\partial z}. \quad (\text{A.21})$$

Now, we want to check what the bottom part of eq. (A.16) evaluates to, and get

$$w_0(1 - w_0) = \frac{c_0 M_a}{c_0 M_a + (1 - c_0) M_b} \left( 1 - \frac{c_0 M_a}{c_0 M_a + (1 - c_0) M_b} \right), \quad (\text{A.22})$$

or written differently,

$$w_0(1 - w_0) = \frac{c_0 M_a}{c_0 M_a + (1 - c_0) M_b} \frac{(1 - c_0) M_b}{c_0 M_a + (1 - c_0) M_b}. \quad (\text{A.23})$$

Multiplying the two fractions with each other, we get

$$w_0(1 - w_0) = \frac{c_0 M_a (1 - c_0) M_b}{(c_0 M_a + (1 - c_0) M_b)^2}, \quad (\text{A.24})$$

or, after moving the terms around slightly,

$$w_0(1 - w_0) = \frac{M_a M_b}{(c_0 M_a + (1 - c_0) M_b)^2} c_0(1 - c_0). \quad (\text{A.25})$$

Now, since the Soret effect is so small, we have  $c \approx c_0$ , or in other words, the deviation in concentration due to thermodiffusion is very small. Therefore, from eq. (A.21) and eq. (A.25), we see that they get the same prefactors, so they cancel out in eq. (A.16):

$$\frac{\partial c / \partial z}{c_0(1 - c_0)} = \frac{\partial w / \partial z}{w_0(1 - w_0)}, \quad (\text{A.26})$$

and also in the definition of the Soret equation in eq. (A.10), for that matter:

$$S_T = -\frac{\partial c / \partial z}{\partial T / \partial z} \frac{1}{c_0(1 - c_0)} = -\frac{\partial w / \partial z}{\partial T / \partial z} \frac{1}{w_0(1 - w_0)}, \quad (\text{A.27})$$

which is what we wanted to show.

In other words, for a *two component* system, the Soret coefficient is invariant<sup>1</sup> to whether we use mass fraction or mole fraction.

Just to emphasise: this is *not* the case for ternary or higher-order mixtures, where the calculated Soret coefficient is different depending on the measure of concentration used.

### A.3 X-ray absorption related to concentration

In 2010, Griesche et al. published a short note on diffusion experiments using XRR [156]. They there gave an equation for the relation between the local concentration and transmitted intensity (which then becomes the imaged grey value) of a sample, based on Beer's law, but did not explicitly derive the final equation. I will here show all the steps needed to achieve the relation between concentration and grey value.

We have that the transmitted beam intensity is given by  $I = I_0 e^{-\mu d}$ , known as Beer's law [155],<sup>2</sup> with  $I_0$  being the incident beam intensity,  $\mu$  the linear absorption coefficient, and  $d$  the depth that the beam travels through the medium, i.e., the sample thickness. We here work with the known intensity  $I_s$  and the unknown concentration  $c_s$  of the sample, with two references where both intensity and concentration are known, with subscripts  $A$  and  $B$ .

As the sample thickness  $d$  and incident intensity  $I_0$  is equal for all samples, we get relations between all three samples (main sample and two references), with

$$\ln \frac{I_s}{I_A} = (\mu_A - \mu_s) d \quad (\text{A.28})$$

and

$$\ln \frac{I_A}{I_B} = (\mu_B - \mu_A) d, \quad (\text{A.29})$$

<sup>1</sup>When  $c \approx c_0$ . If the same holds true for extremely high concentration separation is not something I will concern myself with at the moment.

<sup>2</sup>Beer introduced the law as  $\lambda = \mu^d$  in their original publication from 1852. The relation between the old and the new notation is  $\lambda = I/I_0$  and  $\mu_{\text{old}} = e^{-\mu_{\text{new}}}$ .

which together becomes

$$\frac{\ln \frac{I_s}{I_A}}{\mu_A - \mu_s} = \frac{\ln \frac{I_A}{I_B}}{\mu_B - \mu_A}, \quad (\text{A.30})$$

or rearranged:

$$\frac{\ln \frac{I_s}{I_A}}{\ln \frac{I_A}{I_B}} = \frac{1 - \frac{\mu_s}{\mu_A}}{\frac{\mu_A}{\mu_B} - 1}. \quad (\text{A.31})$$

Now, Griesche et al. assumes that  $\mu$  is proportional to  $c$  for all samples, so we get the fractional relations  $\frac{\mu_s}{\mu_A} = \frac{c_s}{c_A}$  and  $\frac{\mu_B}{\mu_A} = \frac{c_B}{c_A}$ .

Putting in, rearranging, and using the fact that  $-\ln \frac{I_s}{I_A} = \ln \frac{I_A}{I_s}$ , we are left with the result

$$c_s = c_A + \frac{\ln \frac{I_A}{I_s}}{\ln \frac{I_A}{I_B}} (c_B - c_A). \quad (\text{A.32})$$

This is also the end equation of Griesche et al. in their paper.

## A.4 The link between results on time-dependence

Bierlein in 1955 published an equation for the time-dependent concentration across a sample cell [20]. Much later, in 2004, Costesèque et al. published another equation, which they claimed was

more tractable than the one proposed [...] by Bierlein. [113]

In 2008, Mialdun and Shevtsova published the same equation as Costesèque et al., and with the same derivation.

In equation 20 from Bierlein, they actually pass by the approximate end result from Costesèque et al. and Mialdun and Shevtsova, but in a very complicated form, given by<sup>3</sup>

$$\begin{aligned} c(z, t) = & \frac{1}{2} c_0 \left( \frac{S_T \Delta T [2 - 2c_0] e^{-S_T \Delta T [1 - 2c_0] \frac{z}{L}}}{1 - e^{-S_T \Delta T [1 - 2c_0]}} - \frac{2c_0}{1 - 2c_0} \right) \\ & \times 2\pi \Delta c_\infty \sum_{k=1}^{\infty} \left( k \left[ 1 - \{-1\}^k e^{\frac{1}{2} \left\{ \Delta T \frac{1}{\rho} \frac{\partial \rho}{\partial T} + S_T \Delta T (1 - 2c_0) \right\}} \right] \right. \\ & \times \left[ \frac{1}{2} \left\{ \Delta T \frac{1}{\rho} \frac{\partial \rho}{\partial T} - S_T \Delta T (1 - 2c_0) \right\} \sin \left\{ \frac{k\pi z}{L} \right\} \right. \\ & \left. \left. + k\pi \cos \left\{ \frac{k\pi z}{L} \right\} \right] \right. \\ & \times e^{-\left[ \left\{ \frac{1}{2} \left( \Delta T \frac{1}{\rho} \frac{\partial \rho}{\partial T} - S_T \Delta T (1 - 2c_0) \right) \right\}^2 + k^2 \pi^2 \right] t / \theta / \pi^2 - P \frac{z}{L}} \\ & \left/ \left[ \left\{ \frac{1}{2} \left( \Delta T \frac{1}{\rho} \frac{\partial \rho}{\partial T} - S_T \Delta T [1 - 2c_0] \right) \right\}^2 + k^2 \pi^2 \right] \right. \\ & \left. \left/ \left[ \left\{ \frac{1}{2} \left( \Delta T \frac{1}{\rho} \frac{\partial \rho}{\partial T} + S_T \Delta T [1 - 2c_0] \right) \right\}^2 + k^2 \pi^2 \right] \right] \right), \end{aligned} \quad (\text{A.33})$$

---

<sup>3</sup>Bierlein used different variable names for the different quantities. The equation has here been “translated” to the modern notation.

or in a more readable form:

$$c(z, t) = c^* + 2\pi\Delta c_\infty \sum_{k=1}^{\infty} \left( k[1 - \{-1\}^k e^P] \left[ B \sin \frac{k\pi z}{L} + k\pi \cos \frac{k\pi z}{L} \right] \right. \\ \left. \times \frac{e^{-[B^2 + k^2\pi^2]t/\theta/\pi^2 - Pz/L}}{[B^2 + k^2\pi^2][P^2 + k^2\pi^2]} \right) \quad (\text{A.34})$$

with

$$c^* = \frac{1}{2}c_0 \left( \frac{2S_T\Delta T[1 - c_0]e^{-S_T\Delta T[1 - 2c_0]z/L}}{1 - e^{-S_T\Delta T[1 - 2c_0]}} + \frac{-2c_0}{1 - 2c_0} \right), \quad (\text{A.35})$$

$$P = \frac{1}{2} \left( \Delta T \frac{1}{\rho} \frac{\partial \rho}{\partial T} + S_T\Delta T[1 - 2c_0] \right), \quad (\text{A.36})$$

and

$$B = \frac{1}{2} \left( \Delta T \frac{1}{\rho} \frac{\partial \rho}{\partial T} - S_T\Delta T[1 - 2c_0] \right). \quad (\text{A.37})$$

We use that the density  $\rho$  is linear with temperature, as described by Brillo in [66]

$$\rho = \rho_L + \rho_T(T - T_L), \quad (\text{A.38})$$

with, by using  $\text{Ag}_{20}\text{Al}_{80}$  as an example, the material parameters being  $\rho_L = 3.83 \times 10^3 \text{ kg m}^{-3}$ ,  $\rho_T = -4.2 \times 10^{-1} \text{ kg m}^{-3} \text{ K}^{-1}$  and  $T_L = 864 \text{ K}$  [70].

Then, with a relatively small temperature gradient of around 10 K and thus a small volume expansion, and a small Soret coefficient on the order of  $10^{-3} \text{ K}^{-1}$ , we get very small values for  $P$  and  $B$ , on the order of  $\sim 10^{-3}$ .

We can then simplify eq. (A.34) down to

$$c(z, t) = c^* + 2\pi\Delta c_\infty \sum_{k=1}^{\infty} \frac{k(1 - [-1]^k) \left( k\pi \cos \frac{k\pi z}{L} \right) e^{-(k^2\pi^2)t/\theta/\pi^2}}{(k^2\pi^2)(k^2\pi^2)}, \quad (\text{A.39})$$

and then further down to

$$c(z, t) = c^* + 2\Delta c_\infty \sum_{k=1}^{\infty} \frac{(1 - [-1]^k) \cos\left(\frac{k\pi z}{L}\right) e^{-k^2 t/\theta}}{k^2\pi^2}. \quad (\text{A.40})$$

From here, we see that every term with even  $k$  is 0, and therefore we only need to sum over the odd  $k$ , and thus get

$$c(z, t) = c^* + \frac{4}{\pi^2}\Delta c_\infty \sum_{k \text{ odd}} \frac{\cos\left(\frac{k\pi z}{L}\right) e^{-k^2 t/\theta}}{k^2}. \quad (\text{A.41})$$

Finally, from the definition of  $c^*$  in eq. (A.35), together with the approximation

$$\frac{e^{-ax}}{1 - e^{-x}} \approx \frac{1}{x} + \left( \frac{1}{2} - a \right) \quad (\text{A.42})$$

for small  $x$ , which is definitely the case here, with  $x = -S_T\Delta T(1 - 2c_0) \approx -10^{-2}$ , we get a representation for  $c^*$  of

$$c^* = \frac{c_0}{2} \left( 2[1 - c_0]S_T\Delta T \left[ \frac{1}{S_T\Delta T\{1 - 2c_0\}} + \frac{1}{2} - \frac{z}{L} \right] - \frac{2c_0}{1 - 2c_0} \right), \quad (\text{A.43})$$



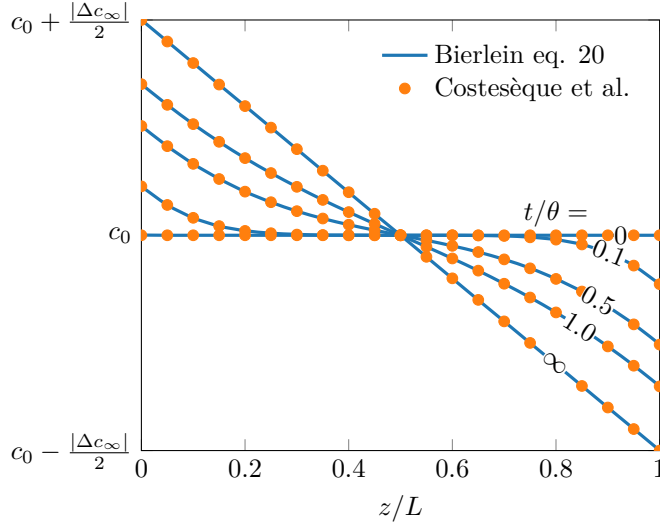


FIGURE A.1: Comparison between the equations for time-dependent concentration from Bierlein and Costesèque et al.

which simplifies to

$$c^* = \frac{c_0}{2} \left( \frac{2[1 - c_0]}{1 - 2c_0} - 2 \left[ \frac{1}{2} - \frac{z}{L} \right] \frac{\Delta c_\infty}{c_0} - \frac{2c_0}{1 - 2c_0} \right), \quad (\text{A.44})$$

and further down to

$$c^* = \frac{c_0}{2} \frac{2 - 2c_0 - 2c_0}{1 - 2c_0} - \Delta c_\infty \left( \frac{1}{2} - \frac{z}{L} \right), \quad (\text{A.45})$$

and straight down to

$$c^* = c_0 - \Delta c_\infty \left( \frac{1}{2} - \frac{z}{L} \right). \quad (\text{A.46})$$

So we then get the equation

$$c(z, t) = c_0 - \Delta c_\infty \left( \frac{1}{2} - \frac{z}{L} \right) + \frac{4}{\pi^2} \Delta c_\infty \sum_{k \text{ odd}} \frac{\cos\left(\frac{k\pi z}{L}\right) e^{-k^2 t/\theta}}{k^2}, \quad (\text{A.47})$$

or, rearranged:

$$c(z, t) = c_0 - \Delta c_\infty \left( \frac{1}{2} - \frac{z}{L} - \frac{4}{\pi^2} \sum_{k \text{ odd}} \frac{\cos\left[\frac{k\pi z}{L}\right] e^{-k^2 t/\theta}}{k^2} \right), \quad (\text{A.48})$$

which is just the same as what Costesèque et al. found in 2004 (and Mialdun and Shevtsova in 2008, for that matter).

This can also be illustrated by plotting the equation from Costesèque et al. over equation 20 from Bierlein, i.e., eq. (A.48) over eq. (A.33). This plot is shown in fig. A.1, and shows an excellent agreement all across the board.



# Appendix B

## Data tables

Here follows tables of various data from chapters 4 and 5, to help those who want to extract data from the figures.

### B.1 Ag–Al

#### B.1.1 Figure 4.5

TABLE B.1: Soret coefficients for the measured concentrations at a mean temperature of 1017 K.

Ag (at.%)	$S_T$ ( $10^{-3} \text{ K}^{-1}$ )	$\pm$ ( $10^{-3} \text{ K}^{-1}$ )
20	1.48	0.31
25	1.16	0.32
30	1.12	0.19
45	1.56	0.41
50	1.28	0.47

#### B.1.2 Figure 4.6

TABLE B.2: Interdiffusion coefficients for the measured concentrations at a mean temperature of 1017 K.

Ag (at.%)	$D$ ( $10^{-9} \text{ m}^2 \text{ s}^{-1}$ )	$\pm$ ( $10^{-9} \text{ m}^2 \text{ s}^{-1}$ )
20	4.04	1.00
25	3.91	0.86
30	3.44	0.64
45	5.97	2.03
50	5.11	2.34

## B.2 Ag–Cu

### B.2.1 Figure 4.12

TABLE B.3: Concentrations for Ag<sub>60</sub>Cu<sub>40</sub>.

(A) Sample A			(B) Sample B		
$z$ (mm)	Ag (at.%)	Cu (at.%)	$z$ (mm)	Ag (at.%)	Cu (at.%)
3.43	62.03	37.97	3.43	62.20	37.80
4.93	61.24	38.76	4.93	61.23	38.77
6.43	61.92	38.08	6.43	61.04	38.96
7.93	61.90	38.10	7.93	61.36	38.64
9.43	62.11	37.89	9.43	62.05	37.95
10.93	61.83	38.17	10.93	62.43	37.57
3.43	62.13	37.87	3.43	62.05	37.95
4.93	61.69	38.31	4.93	61.77	38.23
6.43	61.78	38.22	6.43	61.95	38.05
7.93	62.02	37.98	7.93	61.82	38.18
9.43	61.85	38.15	9.43	61.70	38.30
10.93	62.25	37.75	10.93	61.79	38.21
3.43	61.98	38.02	3.43	61.85	38.15
4.93	62.10	37.90	4.93	61.88	38.12
6.43	61.93	38.07	6.43	61.85	38.15
7.93	61.93	38.07	7.93	61.73	38.27
9.43	62.11	37.89	9.43	61.94	38.06
10.93	62.11	37.89	10.93	61.88	38.12

## B.3 Ag–Al–Cu

### B.3.1 Figure 4.14

Note that the sum of concentrations for each sheared piece of a sample may not add up to 100% exactly ( $c_{i\text{Ag}} + c_{i\text{Al}} + c_{i\text{Cu}} \neq 100 \text{ at.}\%$ ), but rather 99.99 at.% or 100.01 at.%. This is a rounding error from the EDXS software.

TABLE B.4: Concentrations in sample A of  $\text{Ag}_{43.1}\text{Al}_{43.1}\text{Cu}_{13.8}$ .

$z$ (mm)	Ag (at.%)	Al (at.%)	Cu (at.%)
1.75	42.65	42.44	14.91
3.25	42.97	42.33	14.70
4.75	42.92	42.39	14.69
6.25	43.41	41.89	14.71
7.75	43.53	41.54	14.93
9.25	43.05	41.41	15.54
1.75	42.79	41.98	15.23
3.25	43.16	41.57	15.26
4.75	43.56	41.00	15.44
6.25	43.38	41.29	15.33
7.75	44.13	40.88	14.99
9.25	44.84	40.32	14.84
1.75	42.83	41.78	15.39
3.25	43.02	41.64	15.33
4.75	43.58	41.17	15.26
6.25	43.72	40.91	15.36
7.75	43.78	40.93	15.29
9.25	44.58	40.48	14.94

TABLE B.5: Concentrations in sample B of  $\text{Ag}_{43.1}\text{Al}_{43.1}\text{Cu}_{13.8}$ .

$z$ (mm)	Ag (at.%)	Al (at.%)	Cu (at.%)
1.75	42.75	42.32	14.92
3.25	44.00	42.27	13.73
4.75	42.95	42.47	14.59
6.25	43.19	41.85	14.96
7.75	43.89	41.47	14.64
9.25	43.23	41.53	15.24
1.75	42.99	41.89	15.13
3.25	43.22	41.63	15.15
4.75	43.28	41.17	15.54
6.25	44.79	40.54	14.68
7.75	44.97	40.23	14.80
9.25	44.26	40.59	15.15
1.75	42.83	41.77	15.40
3.25	42.94	41.91	15.15
4.75	43.86	41.24	14.91
6.25	43.65	41.07	15.29
7.75	44.23	40.82	14.95
9.25	44.16	40.53	15.31

## B.4 Al–In

### B.4.1 Figure 4.19

TABLE B.6: Soret coefficients for the measured concentrations at a mean temperature of 1110 K.

(A) Fitted with eq. (3.24)		
In (at.%)	$S_T$ ( $10^{-3} \text{ K}^{-1}$ )	$\pm$ ( $10^{-3} \text{ K}^{-1}$ )
15	5.25	0.64
22	7.41	0.39

(B) Fitted with eq. (3.21)		
In (at.%)	$S_T$ ( $10^{-3} \text{ K}^{-1}$ )	$\pm$ ( $10^{-3} \text{ K}^{-1}$ )
15	4.26	0.33
22	6.63	0.18

(C) Fitted with eq. (2.74)		
In (at.%)	$S_T$ ( $10^{-3} \text{ K}^{-1}$ )	$\pm$ ( $10^{-3} \text{ K}^{-1}$ )
15	4.49	0.02
22	6.77	0.02

TABLE B.7: Interdiffusion coefficients for the measured concentrations at a mean temperature of 1110 K.

(A) Fitted with eq. (3.24)		
In (at.%)	$D$ ( $10^{-9} \text{ m}^2 \text{ s}^{-1}$ )	$\pm$ ( $10^{-9} \text{ m}^2 \text{ s}^{-1}$ )
15	1.10	0.28
22	1.34	0.16
(B) Fitted with eq. (3.21)		
In (at.%)	$D$ ( $10^{-9} \text{ m}^2 \text{ s}^{-1}$ )	$\pm$ ( $10^{-9} \text{ m}^2 \text{ s}^{-1}$ )
15	1.35	0.13
22	1.73	0.06
(C) Fitted with eq. (2.74)		
In (at.%)	$D$ ( $10^{-9} \text{ m}^2 \text{ s}^{-1}$ )	$\pm$ ( $10^{-9} \text{ m}^2 \text{ s}^{-1}$ )
15	1.84	0.01
22	1.63	0.01





# Bibliography

- [1] C. Ludwig, ‘Diffusion zwischen ungleich erwärmten Orten gleich zusammengesetzter Lösungen’, *Sitzungsber. Akad. Wiss. Wien Math.-Naturwiss. Kl.* **20**, 539 (1856).
- [2] C. Soret, ‘Sur l’état d’équilibre que prend au point de vue de sa concentration une dissolution saline primitivement homogène dont deux parties sont portées à des températures différentes’, *Arch. Sci. Phys. Nat.* **2**, 48–61 (1879).
- [3] J. K. Platten and P. Costesèque, ‘Charles Soret. A short biography’, *Eur. Phys. J. E* **15**, 235–239 (2004).
- [4] *Carl Friedrich Wilhelm Ludwig. Lithograph by R. Hoffmann, 1856, after F. Küss.* Wellcome Collection, <https://wellcomecollection.org/works/sp3s95a8> (visited on 19/12/2022).
- [5] *Portrait de Charles Soret*, Bibliothèque de Genève, (1880) <https://www.bge-geneve.ch/iconographie/oeuvre/icon-p-1912-107-857> (visited on 20/12/2022).
- [6] S. Srinivasan and M. Z. Saghir, *Thermodiffusion in multicomponent mixtures* (Springer, 2013).
- [7] J. H. van’t Hoff, ‘Lois de l’équilibre chimique dans l’état dilué, gazeux ou dissous’, *Kongl. Sv. Vet.-Akad. Handl.* **21**, 1–58 (1885).
- [8] P. van Berchem, ‘Sur l’état d’équilibre que prend, au point de vue de sa concentration, une dissolution gazeuse primitivement homogène, dont deux parties sont portées à des températures différentes’, *C. R. Hebd. Séances Acad. Sci.* **110**, 82–84 (1890).
- [9] S. Arrhenius, ‘Försök angående Sorets princip’, *Öfversigt af Kongl. Vetensk.-Akad. Förhandl.*, 61–66 (1894).
- [10] R. Gautier, ‘Prof. Charles Soret’, *Nature* **70**, 251–252 (1904).
- [11] D. Enskog, ‘Über eine Verallgemeinerung der zweiten Maxwellschen Theorie der Gase’, *Phys. Z.* **11**, 56–60 (1911).
- [12] S. Chapman, ‘V. On the kinetic theory of a gas. Part II.—A composite monatomic gas: diffusion, viscosity, and thermal conduction’, *Philos. Trans. A* **217**, 115–197 (1917).
- [13] R. C. Jones and W. H. Furry, ‘The separation of isotopes by thermal diffusion’, *Rev. Mod. Phys.* **18**, 151–224 (1946).
- [14] J. Tyndall, ‘On haze and dust’, in *Scientific addresses* (Charles C. Chatfield & Co., 1870), pp. 20–32.

- [15] K. Clusius and G. Dickel, 'Neues Verfahren zur Gasentmischung und Isotopentrennung', *Naturwiss.* **26**, 546–546 (1938).
- [16] K. Clusius and G. Dickel, 'Zur Trennung der Chlorisotope', *Naturwiss.* **27**, 148–148 (1939).
- [17] B. Cameron Reed, 'Liquid thermal diffusion during the Manhattan Project', *Phys. Perspect.* **13**, 161 (2011).
- [18] W. H. Furry, R. C. Jones and L. Onsager, 'On the theory of isotope separation by thermal diffusion', *Phys. Rev.* **55**, 1083–1095 (1939).
- [19] J. Bardeen, 'Concentration of isotopes by thermal diffusion: rate of approach to equilibrium', *Phys. Rev.* **57**, 35–41 (1940).
- [20] J. A. Bierlein, 'A phenomenological theory of the Soret diffusion', *J. Chem. Phys.* **23**, 10–14 (1955).
- [21] S. R. de Groot, 'Détermination des constantes de diffusion thermique et de diffusion ordinaire à partir des résultats expérimentaux de l'effet Soret pur', *J. Phys. Radium* **8**, 129–134 (1947).
- [22] C. C. Tanner, 'The Soret effect. Part 2', *Trans. Faraday Soc.* **49**, 611–619 (1953).
- [23] F. R. Winter and H. G. Drickamer, 'Thermal diffusion in liquid metals', *J. Phys. Chem.* **59**, 1229–1230 (1955).
- [24] B. R. Sundheim and J. D. Kellner, 'Thermoelectric properties of the molten silver nitrate-sodium nitrate system', *J. Phys. Chem.* **69**, 1204–1208 (1965).
- [25] S. Chapman and F. W. Dootson, 'XXII. A note on thermal diffusion', *Philos. Mag.* **33**, 248–253 (1917).
- [26] M. J. Story and J. C. R. Turner, 'Flow-cell studies of thermal diffusion in liquids. Part 5.—Binary mixtures of CH<sub>3</sub>OH with CCl<sub>4</sub>, benzene and cyclohexane at 25°C', *Trans. Faraday Soc.* **65**, 1523–1529 (1969).
- [27] P. Shewmon, 'The thermal diffusion of carbon in  $\alpha$  and  $\gamma$  iron', *Acta Metall.* **8**, 605–611 (1960).
- [28] J. Rauch and W. Köhler, 'Diffusion and thermal diffusion of semidilute to concentrated solutions of polystyrene in toluene in the vicinity of the glass transition', *Phys. Rev. Lett.* **88**, 185901 (2002).
- [29] S. Chapman, 'Thermal diffusion and the stars', *Mon. Not. R. Astron. Soc.* **77**, 539–540 (1917).
- [30] J. C. G. Walker, 'Thermal diffusion in the topside ionosphere', *Planet. Space Sci.* **15**, 1151–1156 (1967).
- [31] C. E. Leshner, J. Dannberg, G. H. Barfod, N. R. Bennett, J. J. G. Glessner, D. J. Lacks and J. M. Brennan, 'Iron isotope fractionation at the core-mantle boundary by thermodiffusion', *Nat. Geosci.* **13**, 382–386 (2020).
- [32] P. Baaske, F. M. Weinert, S. Duhr, K. H. Lemke, M. J. Russell and D. Braun, 'Extreme accumulation of nucleotides in simulated hydrothermal pore systems', *Proc. Natl. Acad. Sci.* **104**, 9346–9351 (2007).

- [33] M. Braibanti, P. A. Artola, P. Baaske, H. Bataller, J. P. Bazile, M. M. Bou-Ali, D. S. Cannell, M. Carpineti, R. Cerbino, F. Croccolo, J. Diaz, A. Donev, A. Errarte, J. M. Ezquerro, A. Frutos-Pastor, Q. Galand, G. Galliero, Y. Gaponenko, L. García-Fernández, J. Gavalda, F. Giavazzi, M. Giglio, C. Giraudet, H. Hoang, E. Kufner, W. Köhler, E. Lapeira, A. Laverón-Simavilla, J. C. Legros, I. Lizarraga, T. Lyubimova, S. Mazzoni, N. Melville, A. Mialdun, O. Minster, F. Montel, F. J. Molster, J. M. Ortiz de Zárate, J. Rodríguez, B. Rousseau, X. Ruiz, I. I. Ryzhkov, M. Schraml, V. Shevtsova, C. J. Takacs, T. Triller, S. Van Vaerenbergh, A. Vailati, A. Verga, R. Vermorel, V. Vesovic, V. Yasnou, S. Xu, D. Zapf and K. Zhang, ‘European Space Agency experiments on thermodiffusion of fluid mixtures in space’, *Eur. Phys. J. E* **42**, 86 (2019).
- [34] G. Thomaes, ‘Thermal diffusion near the critical solution point’, *J. Chem. Phys.* **25**, 32–33 (1956).
- [35] M. Giglio and A. Vendramini, ‘Thermal-diffusion measurements near a consolute critical point’, *Phys. Rev. Lett.* **34**, 561–564 (1975).
- [36] W. Enge and W. Köhler, ‘Thermal diffusion in a critical polymer blend’, *Phys. Chem. Chem. Phys.* **6**, 2373–2378 (2004).
- [37] A. Voit, A. Krekhov, W. Enge, L. Kramer and W. Köhler, ‘Thermal patterning of a critical polymer blend’, *Phys. Rev. Lett.* **94**, 214501 (2005).
- [38] A. Vailati, P. Baaske, H. Bataller, S. Bolis, M. Braibanti, M. Carpineti, R. Cerbino, F. Croccolo, J.-L. Dewandel, A. Donev, L. García-Fernández, F. Giavazzi, R. Haslinger, S. Hens, M. Knauer, W. Köhler, E. Kufner, J. M. Ortiz de Zárate, J. Peeters, C. J. Schwarz, I. Silkina, S. Xu and D. Zapf, ‘Giant fluctuations induced by thermal diffusion in complex liquids’, *Microgravity Sci. Technol.* **32**, 873–887 (2020).
- [39] W. Sutherland, ‘LXXV. A dynamical theory of diffusion for non-electrolytes and the molecular mass of albumin’, *Philos. Mag.* **9**, 781–785 (1905).
- [40] A. Einstein, ‘Über die von der molekularkinetischen Theorie der Wärme geforderte Bewegung von in ruhenden Flüssigkeiten suspendierten Teilchen’, *Ann. Phys.* **322**, 549–560 (1905).
- [41] S. Nell, F. Yang, Z. Evenson and A. Meyer, ‘Viscous flow and self-diffusion in densely and loosely packed metallic melts’, *Phys. Rev. B* **103**, 064206 (2021).
- [42] V. Vaibhav, J. Horbach and P. Chaudhuri, ‘Response of glassy liquids to thermal gradients’, *Phys. Rev. E* **101**, 022605 (2020).
- [43] M. Eslamian and M. Z. Saghir, ‘A critical review of thermodiffusion models: role and significance of the heat of transport and the activation energy of viscous flow’, *J. Non-Equilib. Thermodyn.* **34**, 97–131 (2009).
- [44] M. Zhang and F. Müller-Plathe, ‘Reverse nonequilibrium molecular-dynamics calculation of the Soret coefficient in liquid benzene/cyclohexane mixtures’, *J. Chem. Phys.* **123**, 124502 (2005).
- [45] W. G. Pfann, ‘Temperature gradient zone melting’, *JOM* **7**, 961–964 (1955).

- [46] H.-Y. Hsiao and C. Chen, ‘Thermomigration in Pb-free SnAg solder joint under alternating current stressing’, *Appl. Phys. Lett.* **94**, 092107 (2009).
- [47] C. Q. Ru, ‘Thermomigration as a driving force for instability of electromigration induced mass transport in interconnect lines’, *J. Mater. Sci.* **35**, 5575–5579 (2000).
- [48] M. Ben Sassi, S. Kaddeche, M. Lappa, S. Millet, D. Henry and H. Ben Hadid, ‘On the effect of thermodiffusion on solute segregation during the growth of semiconductor materials by the vertical Bridgman method’, *J. Cryst. Growth* **458**, 154–165 (2017).
- [49] J. Lewis and S. Huang, ‘High temperature furnace with a sharp temperature gradient’, *Rev. Sci. Instrum.* **34**, 271–273 (1963).
- [50] D.-G. Xie, Z.-Y. Nie, S. Shinzato, Y.-Q. Yang, F.-X. Liu, S. Ogata, J. Li, E. Ma and Z.-W. Shan, ‘Controlled growth of single-crystalline metal nanowires via thermomigration across a nanoscale junction’, *Nat. Commun.* **10**, 4478 (2019).
- [51] B. N. Bhat, ‘Thermotransport in liquid aluminum-copper alloys’, NASA TR R-415 (1973).
- [52] S. P. Murarka, T. Y. Kim, M. Y. Hsieh and R. A. Swalin, ‘Thermotransport studies in liquid alkali metal alloys’, *Acta Metall.* **22**, 185–189 (1974).
- [53] R. K. Williams and W. O. Philbrook, ‘The Soret effect in molten Ag-Te solutions’, *J. Electrochem. Soc.* **128**, 1034–1040 (1981).
- [54] J.-P. Praizey, ‘Benefits of microgravity for measuring thermotransport coefficients in liquid metallic alloys’, *Int. J. Heat Mass Tran.* **32**, 2385–2401 (1989).
- [55] J.-P. Praizey, S. Van Vaerenbergh and J.-P. Garandet, ‘Thermomigration experiment on board EURECA’, *Adv. Space Res.* **16**, 205–214 (1995).
- [56] M. Kassemi, S. Barsi, J. I. D. Alexander and M. Banish, ‘Contamination of microgravity liquid diffusivity measurements by void-generated thermocapillary convection’, *J. Cryst. Growth* **276**, 621–634 (2005).
- [57] R. Roşu-Pflumm, W. Wendl, G. Müller-Vogt, S. Suzuki, K.-H. Kraatz and G. Froberg, ‘Diffusion measurements using the shear cell technique: investigation of the role of Marangoni convection by pre-flight experiments on the ground and during the Foton M2 mission’, *Int. J. Heat Mass Tran.* **52**, 6042–6049 (2009).
- [58] F. Kargl, E. Sondermann, H. Weis and A. Meyer, ‘Impact of convective flow on long-capillary chemical diffusion studies of liquid binary alloys’, *High Temp. High Press.* **42**, 3–21 (2013).
- [59] J. K. Platten and J. C. Legros, *Convection in liquids* (Springer, 1984).
- [60] E. Sondermann, F. Kargl and A. Meyer, ‘In situ measurement of thermodiffusion in liquid alloys’, *Phys. Rev. Lett.* **123**, 255902 (2019).
- [61] E. Sondermann, ‘Einfluss von Kreuzkorrelationen auf die Interdiffusion in aluminiumreichen Al-Ni-Schmelzen’, PhD thesis (Ruhr-University Bochum, 2016).

- [62] M. Engelhardt, ‘Messung von Diffusionskoeffizienten in ternären AlCuAg-Legierungen und deren Subsystemen’, PhD thesis (RWTH Aachen University, 2014).
- [63] T. Schiller, ‘Further development of radiographic in situ interdiffusion experiments and investigation of (quasi-)binary Al-rich melts’, PhD thesis (Ruhr-University Bochum, 2022).
- [64] L. F. Mondolfo, *Aluminum alloys: structure and properties* (Elsevier, 1976).
- [65] T. Dursun and C. Soutis, ‘Recent developments in advanced aircraft aluminium alloys’, *Mater. Des.* **56**, 862–871 (2014).
- [66] J. Brillo, *Thermophysical properties of multicomponent liquid alloys* (De Gruyter Oldenbourg, 2016).
- [67] V. T. Witusiewicz, U. Hecht, S. G. Fries and S. Rex, ‘The Ag–Al–Cu system: part I: reassessment of the constituent binaries on the basis of new experimental data’, *J. Alloys Compd.* **385**, 133–143 (2004).
- [68] V. T. Witusiewicz, U. Hecht, S. G. Fries and S. Rex, ‘The Ag–Al–Cu system: II. A thermodynamic evaluation of the ternary system’, *J. Alloys Compd.* **387**, 217–227 (2005).
- [69] J. Brillo, I. Egry and I. Ho, ‘Density and thermal expansion of liquid Ag–Cu and Ag–Au alloys’, *Int. J. Thermophys.* **27**, 494–506 (2006).
- [70] J. Brillo, I. Egry and J. Westphal, ‘Density and thermal expansion of liquid binary Al–Ag and Al–Cu alloys’, *Int. J. Mater. Res.* **99**, 162–167 (2008).
- [71] R. N. Singh and F. Sommer, ‘Segregation and immiscibility in liquid binary alloys’, *Rep. Prog. Phys.* **60**, 57 (1997).
- [72] L. S. Darken, ‘Diffusion, mobility and their interrelation through free energy in binary metallic systems’, *Trans. TMS-AIME* **175**, 184–201 (1948).
- [73] W. C. Röntgen, ‘On a new kind of rays’, *Nature* **53**, 274–276 (1896).
- [74] M. J. Assael, K. Kakosimos, R. M. Banish, J. Brillo, I. Egry, R. Brooks, P. N. Qested, K. C. Mills, A. Nagashima, Y. Sato and W. A. Wakeham, ‘Reference data for the density and viscosity of liquid aluminum and liquid iron’, *J. Phys. Chem. Ref. Data* **35**, 285–300 (2006).
- [75] M. J. Assael, A. E. Kalyva, K. D. Antoniadis, R. M. Banish, I. Egry, J. Wu, E. Kaschnitz and W. A. Wakeham, ‘Reference data for the density and viscosity of liquid antimony, bismuth, lead, nickel and silver’, *High Temp. High Press.* **41**, 161–184 (2012).
- [76] T. Prohaska, J. Irrgeher, J. Benefield, J. K. Böhlke, L. A. Chesson, T. B. Coplen, T. Ding, P. J. H. Dunn, M. Gröning, N. E. Holden, H. A. J. Meijer, H. Moossen, A. Possolo, Y. Takahashi, J. Vogl, T. Walczyk, J. Wang, M. E. Wieser, S. Yoneda, X.-K. Zhu and J. Meija, ‘Standard atomic weights of the elements 2021 (IUPAC technical report)’, *Pure Appl. Chem.* **94**, 573–600 (2022).
- [77] B. N. Bhat, ‘Effect of thermotransport on directionally solidified aluminium-copper eutectic’, *J. Cryst. Growth* **28**, 68–76 (1975).

- [78] J. M. Brennan and N. Bennett, ‘Soret separation of highly siderophile elements in Fe–Ni–S melts: implications for solid metal–liquid metal partitioning’, *Earth Planet. Sci. Lett.* **298**, 299–305 (2010).
- [79] B. N. Bhat and R. A. Swalin, ‘Thermotransport of solutes in liquid silver’, *Z. Naturforsch.* **26 a**, 45–47 (1971).
- [80] S. Hartmann, G. Wittko, F. Schock, W. Groß, F. Lindner, W. Köhler and K. I. Morozov, ‘Thermophobicity of liquids: heats of transport in mixtures as pure component properties—the case of arbitrary concentration’, *J. Chem. Phys.* **141**, 134503 (2014).
- [81] M. Engelhardt, A. Meyer, F. Yang, G. G. Simeoni and F. Kargl, ‘Self and chemical diffusion in liquid Al–Ag’, *Defect Diffus. Forum* **367**, 157–166 (2016).
- [82] J. G. Speight, ed., *Lange’s handbook of chemistry* (McGraw-Hill Education, 2017).
- [83] S. Cheng, C.-M. Huang and M. Pecht, ‘A review of lead-free solders for electronics applications’, *Microelectron. Reliab.* **75**, 77–95 (2017).
- [84] M. J. Assael, A. E. Kalyva, K. D. Antoniadis, R. Michael Banish, I. Egry, J. Wu, E. Kaschnitz and W. A. Wakeham, ‘Reference data for the density and viscosity of liquid copper and liquid tin’, *J. Phys. Chem. Ref. Data* **39**, 033105 (2010).
- [85] S. P. Ringer, T. Sakurai and I. J. Polmear, ‘Origins of hardening in aged Al–Cu–Mg–(Ag) alloys’, *Acta Mater.* **45**, 3731–3744 (1997).
- [86] A. T. Dinsdale, ‘SGTE data for pure elements’, *Calphad* **15**, 317–425 (1991).
- [87] J. Brillo, R. Brooks, I. Egry and P. Quested, ‘Density and viscosity of liquid ternary Al–Cu–Ag alloys’, *High Temp. High Press.* **37**, 371–381 (2008).
- [88] L. Ratke and S. Diefenbach, ‘Liquid immiscible alloys’, *Mater. Sci. Eng. R Rep.* **15**, 263–347 (1995).
- [89] Y. I. Chang, ‘The integral fast reactor’, *Nucl. Technol.* **88**, 129–138 (1989).
- [90] X.-D. Zhang and J. Liu, ‘Perspective on liquid metal enabled space science and technology’, *Sci. China Technol. Sci.* **63**, 1127–1140 (2020).
- [91] G. L. Liu and J. Liu, ‘Convective cooling of compact electronic devices via liquid metals with low melting points’, *J. Heat Transf.* **143**, 050801 (2021).
- [92] R. A. Khairulin, S. V. Stankus and A. L. Sorokin, ‘Determination of the two-melt phase boundary and study of the binary diffusion in liquid Bi–Ga system with a miscibility gap’, *J. Non-Cryst. Solids* **297**, 120–130 (2002).
- [93] R. A. Khairulin, R. N. Abdullaev and S. V. Stankus, ‘Phase equilibria and mutual diffusion in liquid lithium–sodium alloys’, *J. Eng. Thermophys.* **28**, 472–483 (2019).
- [94] D. A. Porter, K. E. Easterling and M. Y. Sherif, ‘Thermodynamics and phase diagrams’, in *Phase transformations in metals and alloys* (CRC Press, Feb. 2009), pp. 1–63.

- [95] P.-A. Artola and B. Rousseau, ‘Microscopic interpretation of a pure chemical contribution to the Soret effect’, *Phys. Rev. Lett.* **98**, 125901 (2007).
- [96] O. Redlich and A. T. Kister, ‘Algebraic representation of thermodynamic properties and the classification of solutions’, *Ind. Eng. Chem.* **40**, 345–348 (1948).
- [97] R. Taylor and R. Krishna, *Multicomponent mass transfer*, Wiley series in chemical engineering (Wiley, New York, 1993).
- [98] G. M. Wilson, ‘A new expression for the excess free energy of mixing’, *J. Am. Chem. Soc.* **86**, 127–130 (1964).
- [99] S. M. Walas, ‘Activity coefficients’, in *Phase equilibria in chemical engineering* (Butterworth, 1985), pp. 165–244.
- [100] L. Ratke and P. W. Voorhees, ‘Thermodynamics of alloys’, in *Growth and coarsening: ripening in material processing* (Springer, 2002), pp. 7–41.
- [101] T. Ahmed, W. Y. Wang, R. Kozubski, Z.-K. Liu, I. V. Belova and G. E. Murch, ‘Interdiffusion and thermotransport in Ni-Al liquid alloys’, *Philos. Mag.* **98**, 2221–2246 (2018).
- [102] I. V. Belova, T. Ahmed, U. Sarder, W. Yi Wang, R. Kozubski, Z.-K. Liu, D. Holland-Moritz, A. Meyer and G. E. Murch, ‘Computer simulation of thermodynamic factors in Ni-Al and Cu-Ag liquid alloys’, *Comput. Mater. Sci.* **166**, 124–135 (2019).
- [103] R. Kita, S. Wiegand and J. Luettmmer-Strathmann, ‘Sign change of the Soret coefficient of poly(ethylene oxide) in water/ethanol mixtures observed by thermal diffusion forced Rayleigh scattering’, *J. Chem. Phys.* **121**, 3874–3885 (2004).
- [104] S. R. de Groot and P. Mazur, *Non-equilibrium thermodynamics* (Dover Publications, Inc., New York, 1962).
- [105] Z.-K. Liu, ‘Theory of cross phenomena and their coefficients beyond Onsager theorem’, *Mater. Res. Lett.* **10**, 393–439 (2022).
- [106] M. Hartung, ‘A detailed treatment of the measurement of transport coefficients in transient grating experiments’, PhD thesis (University of Bayreuth, 2007).
- [107] L. Onsager, ‘Reciprocal relations in irreversible processes. I.’, *Phys. Rev.* **37**, 405–426 (1931).
- [108] A. Vegh, J. Korošcs and G. Kaptay, ‘Extension of the Gibbs-Duhem equation to the partial molar surface thermodynamic properties of solutions’, *Langmuir* **38**, 4906–4912 (2022).
- [109] L. Dufour, ‘Changements de température lors de la diffusion des gaz’, *Arch. Sci. Phys. Nat.* **45**, 9–12 (1872).
- [110] J. M. Ortiz de Zárate, ‘Definition of frame-invariant thermodiffusion and Soret coefficients for ternary mixtures’, *Eur. Phys. J. E* **42**, 43 (2019).
- [111] E. Sondermann, N. Jakse, K. Binder, A. Mielke, D. Heuskin, F. Kargl and A. Meyer, ‘Concentration dependence of interdiffusion in aluminum-rich Al-Cu melts’, *Phys. Rev. B* **99**, 024204 (2019).



- [112] S. R. de Groot, ‘Théorie phénoménologique de l’effet Soret’, *Physica* **9**, 699–708 (1942).
- [113] P. Costesèque, T. Pollak, J. K. Platten and M. Marcoux, ‘Transient-state method for coupled evaluation of Soret and Fick coefficients, and related tortuosity factors, using free and porous packed thermodiffusion cells: application to CuSO<sub>4</sub> aqueous solution (0.25M)’, *Eur. Phys. J. E* **15**, 249–253 (2004).
- [114] A. Mialdun and V. M. Shevtsova, ‘Development of optical digital interferometry technique for measurement of thermodiffusion coefficients’, *Int. J. Heat Mass Tran.* **51**, 3164–3178 (2008).
- [115] A. Fick, ‘Ueber Diffusion’, *Ann. Phys.* **170**, 59–86 (1855).
- [116] J. S. Anderson and K. Saddington, ‘The use of radioactive isotopes in the study of the diffusion of ions in solution’, *J. Chem. Soc.*, S381–S386 (1949).
- [117] A. Mialdun and V. Shevtsova, ‘Measurement of the Soret and diffusion coefficients for benchmark binary mixtures by means of digital interferometry’, *J. Chem. Phys.* **134**, 044524 (2011).
- [118] W. Biermann, D. Heitkamp and T. S. Lundy, ‘Thermal diffusion of antimony and ruthenium in silver’, *Acta Metall.* **13**, 71–78 (1965).
- [119] A. B. Lidiard, ‘Mass transfer along a temperature gradient’, in *Thermodynamics: proceedings of the symposium held in Vienna from 22–27 July 1965*, Vol. 2 (1966), pp. 3–22.
- [120] R. A. Oriani, ‘Thermomigration in solid metals’, *J. Phys. Chem. Solids* **30**, 339–351 (1969).
- [121] R. A. McKee and J. P. Stark, ‘Concentration and grain size effects on thermal migration of silver in aluminum’, *Acta Metall.* **22**, 953–956 (1974).
- [122] H. Hoang and G. Galliero, ‘Predicting thermodiffusion in simple binary fluid mixtures’, *Eur. Phys. J. E* **45**, 42 (2022).
- [123] D. Enskog, ‘Zur Elektronentheorie der Dispersion und Absorption der Metalle’, *Ann. Phys.* **343**, 731–763 (1912).
- [124] S. Chapman and T. G. Cowling, *The mathematical theory of non-uniform gases* (Cambridge University Press, 1991).
- [125] E. R. S. Winter, ‘Diffusion properties of gases. Part III. The diffusion and thermal diffusion coefficients for isotopic gases and gas mixtures’, *Trans. Faraday Soc.* **46**, 81 (1950).
- [126] J. O. Hirshfelder, C. F. Curtiss and R. B. Bird, *Molecular theory of gases and liquids* (1964).
- [127] V. G. Jervell, ‘The kinetic gas theory of Mie fluids’, MA thesis (Norwegian University of Science and Technology, 2022).
- [128] E. L. Dougherty and H. G. Drickamer, ‘Thermal diffusion and molecular motion in liquids’, *J. Phys. Chem.* **59**, 443–449 (1955).
- [129] M. Eslamian, F. Sabzi and M. Z. Saghir, ‘Modeling of thermodiffusion in liquid metal alloys’, *Phys. Chem. Chem. Phys.* **12**, 13835 (2010).



- [130] K. Shukla and A. Firoozabadi, ‘A new model of thermal diffusion coefficients in binary hydrocarbon mixtures’, *Ind. Eng. Chem. Res.* **37**, 3331–3342 (1998).
- [131] R. H. Ewell and H. Eyring, ‘Theory of the viscosity of liquids as a function of temperature and pressure’, *J. Chem. Phys.* **5**, 726–736 (1937).
- [132] S. Glasstone, K. J. Laidler and H. Eyring, ‘Viscosity and diffusion’, in *The theory of rate processes* (McGraw-Hill Book Company, Inc., 1941), pp. 477–551.
- [133] C. L. Yaws and M. A. Satyro, ‘Enthalpy of vaporization – inorganic compounds’, in *Thermophysical properties of chemicals and hydrocarbons* (William Andrew, 2009), pp. 401–408.
- [134] P.-A. Artola, B. Rousseau and G. Galliéro, ‘A new model for thermal diffusion: kinetic approach’, *J. Am. Chem. Soc.* **130**, 10963–10969 (2008).
- [135] E. Jafar-Salehi, M. Eslamian and M. Z. Saghir, ‘Estimation of molecular and thermodiffusion coefficients for non-ideal molten metal alloys and its implication in solidification process’, *Can. J. Chem. Eng.* **92**, 1314–1324 (2014).
- [136] D. Maier, D. Klimm and R. Fornari, ‘Theoretical model for calculation of thermal diffusion factors in diluted binary melts’, *Chem. Phys. Lett.* **444**, 202–204 (2007).
- [137] I. Karakaya and W. T. Thompson, ‘The Ag-Te (silver-tellurium) system’, *J. Phase Equilib.* **12**, 56–63 (1991).
- [138] I. Ansara, A. T. Dinsdale and M. H. Rand, eds., *Thermochemical database for light metal alloys*, Vol. 2, COST 507: Definition of thermochemical and thermophysical properties to provide a database for the development of new light alloys (European Commission, Luxembourg, July 1998).
- [139] I. Ansara, A. T. Dinsdale and M. H. Rand, *Al-Mg COST 507 thermochemical database for light metal alloys*, (1998) <https://materialsdata.nist.gov/handle/11256/618> (visited on 16/05/2023).
- [140] D. J. S. Cooksey and A. Hellawell, ‘The microstructures of ternary eutectic alloys in the systems Cd–Sn–(Pb, In, Tl), Al–Cu–(Mg, Zn, Ag) and Zn–Sn–Pb’, *J. Inst. Met.* **95**, 183–187 (1967).
- [141] E. Sondermann, A. T. Krüger and A. Meyer, in preparation.
- [142] F. Sommer, H.-G. Krull and S. K. Yu, ‘Thermodynamics of immiscible systems’, in *Immiscible liquid metals and organics*, edited by L. Ratke (1993), pp. 79–90.
- [143] I. Kaban, S. Curiotto, D. Chatain and W. Hoyer, ‘Surfaces, interfaces and phase transitions in Al-In monotectic alloys’, *Acta Mater.* **58**, 3406–3414 (2010).
- [144] S. Amore, J. Horbach and I. Egry, ‘Is there a relation between excess volume and miscibility in binary liquid mixtures?’, *J. Chem. Phys.* **134**, 044515 (2011).
- [145] J. Brillo and I. Egry, ‘Density of multicomponent melts measured by electromagnetic levitation’, *Jpn. J. Appl. Phys.* **50**, 11RD02 (2011).

- [146] C. Neumann, E. Sondermann, F. Kargl and A. Meyer, ‘Compact high-temperature shear-cell furnace for in-situ diffusion measurements’, *J. Phys. Conf. Ser.* **327**, 012052 (2011).
- [147] E. Sondermann, C. Neumann, F. Kargl and A. Meyer, ‘Compact high-temperature shear-cell furnace for in-situ interdiffusion measurements’, *High Temp. High Press.* **42**, 23–30 (2013).
- [148] ThermoExpert° Deutschland GmbH, *Execution measuring points*, (2023) <https://thermoexpert.de/en/ausfuehrung-messstellen/> (visited on 03/08/2023).
- [149] V. Shevtsova, C. Santos, V. Sechenyh, J. C. Legros and A. Mialdun, ‘Diffusion and Soret in ternary mixtures. preparation of the DCMIX2 experiment on the ISS’, *Microgravity Sci. Technol.* **25**, 275–283 (2014).
- [150] A. T. Krüger, E. Sondermann and A. Meyer, ‘Measurement of the Soret coefficient in liquid Al-Ag alloys using x-ray radiography’, *Phys. Rev. B* **107**, 064301 (2023).
- [151] J. I. Goldstein, D. E. Newbury, P. Echlin, D. C. Joy, C. E. Lyman, E. Lifshin, L. Sawyer and J. R. Michael, *Scanning electron microscopy and x-ray microanalysis* (Springer, 2003).
- [152] A. Savitzky and M. J. E. Golay, ‘Smoothing and differentiation of data by simplified least squares procedures.’, *Anal. Chem.* **36**, 1627–1639 (1964).
- [153] P. Virtanen, R. Gommers, T. E. Oliphant, M. Haberland, T. Reddy, D. Cournapeau, E. Burovski, P. Peterson, W. Weckesser, J. Bright, S. J. van der Walt, M. Brett, J. Wilson, K. J. Millman, N. Mayorov, A. R. J. Nelson, E. Jones, R. Kern, E. Larson, C. J. Carey, Í. Polat, Y. Feng, E. W. Moore, J. VanderPlas, D. Laxalde, J. Perktold, R. Cimrman, I. Henriksen, E. A. Quintero, C. R. Harris, A. M. Archibald, A. H. Ribeiro, F. Pedregosa, P. van Mulbregt and SciPy 1.0 Contributors, ‘SciPy 1.0: fundamental algorithms for scientific computing in Python’, *Nat. Methods* **17**, 261–272 (2020).
- [154] ‘Control theory’, in *Process control and optimization*, edited by B. G. Lipták (CRC Press, 2006), pp. 89–455.
- [155] A. Beer, ‘Bestimmung der Absorption des rothen Lichts in farbigen Flüssigkeiten’, *Ann. Phys.* **162**, 78–88 (1852).
- [156] A. Griesche, B. Zhang, E. Solórzano and F. Garcia-Moreno, ‘Note: X-ray radiography for measuring chemical diffusion in metallic melts’, *Rev. Sci. Instrum.* **81**, 056104 (2010).
- [157] S. V. Stankus, R. A. Khairulin, A. G. Mozgovoi, V. V. Roshchupkin and M. A. Pokrasin, ‘An experimental investigation of the density of bismuth in the condensed state in a wide temperature range’, *High Temp.* **43**, 368–378 (2005).
- [158] W. Köhler, A. Mialdun, M. M. Bou-Ali and V. Shevtsova, ‘The measurement of Soret and thermodiffusion coefficients in binary and ternary liquid mixtures’, *Int. J. Thermophys.* **44**, 140 (2023).
- [159] R. A. McKee and J. P. Stark, ‘Violation of thermal equilibrium in a thermomigration experiment’, *Phys. Rev. B* **11**, 1374–1381 (1975).

- [160] R. E. Doerr and J. P. Stark, 'Effect of grain size on the thermal diffusion of copper in aluminum', *Metall. Trans.* **3**, 2461–2464 (1972).
- [161] P. J. Spencer and O. Kubaschewski, 'A thermodynamic evaluation of the Ag-Al system', *Monatsh. Chem.* **118**, 155–167 (1987).
- [162] S. S. Lim, P. L. Rossiter and J. E. Tibballs, 'Assessment of the Al-Ag binary phase diagram', *Calphad* **19**, 131–141 (1995).
- [163] M. Hansen and K. Anderko, *Constitution of binary alloys* (McGraw-Hill Book Company, Inc., 1958).
- [164] W. Fuchs and J. Richter, 'Soret coefficients and transported entropies of nonisothermal liquid alkali nitrate + silver nitrate mixtures', *Ber. Bunsenges. Phys. Chem.* **86**, 46–51 (1982).
- [165] M. Shimizu, S. Hosoya, T. Kato, J. Matsuoka, H. Kato, M. Nishi, K. Hirao, Y. Shimotsuma and K. Miura, 'Soret coefficient of a sodium borate melt: experiment with a vertical furnace and thermodynamic theory', *J. Ceram. Soc. Jpn.* **126**, 997–1004 (2018).
- [166] A. Ott, 'Isotope separation by thermal diffusion in liquid metal', *Science* **164**, 297–297 (1969).
- [167] D. Jaffe and P. G. Shewmon, 'Thermal diffusion of substitutional impurities in copper, gold and silver', *Acta Metall.* **12**, 515–527 (1964).
- [168] Y.-F. Lin, Y.-C. Hao and F.-Y. Ouyang, 'Improvement of thermomigration resistance in lead-free Sn3.5Ag alloys by Ag interlayer', *J. Alloys Compd.* **847**, 156429 (2020).
- [169] M. Schraml, H. Bataller, C. Bauer, M. M. Bou-Ali, F. Croccolo, E. Lapeira, A. Mialdun, P. Möckel, A. T. Ndjaka, V. Shevtsova and W. Köhler, 'The Soret coefficients of the ternary system water/ethanol/triethylene glycol and its corresponding binary mixtures', *Eur. Phys. J. E* **44**, 128 (2021).
- [170] M. G. Velarde and R. S. Schechter, 'Thermal diffusion and convective stability (III): a critical survey of Soret coefficient measurements', *Chem. Phys. Lett.* **12**, 312–315 (1971).
- [171] U. Sarder, T. Ahmed, W. Y. Wang, R. Kozubski, Z.-K. Liu, I. V. Belova and G. E. Murch, 'Mass and thermal transport in liquid Cu-Ag alloys', *Philos. Mag.* **99**, 468–491 (2019).
- [172] A. Meyer, S. Stüber, D. Holland-Moritz, O. Heinen and T. Unruh, 'Determination of self-diffusion coefficients by quasielastic neutron scattering measurements of levitated Ni droplets', *Phys. Rev. B* **77**, 092201 (2008).
- [173] P. L. Williams, Y. Mishin and J. C. Hamilton, 'An embedded-atom potential for the Cu-Ag system', *Model. Simul. Mater. Sc.* **14**, 817–833 (2006).
- [174] W. Köhler and K. I. Morozov, 'The Soret effect in liquid mixtures – a review', *J. Non-Equilib. Thermodyn.* **41**, 151–197 (2016).
- [175] P.-A. Artola and B. Rousseau, 'Isotopic Soret effect in ternary mixtures: theoretical predictions and molecular simulations', *J. Chem. Phys.* **143**, 174503 (2015).
- [176] C. Potard and P. Desre, 'Détermination des coefficients d'interdiffusion des alliages ternaires liquides Sn Ag Sb', *Mater. Res. Bull.* **9**, 1–11 (1974).

- [177] F. Kargl, M. Engelhardt, F. Yang, H. Weis, P. Schmakat, B. Schillinger, A. Griesche and A. Meyer, ‘In situ studies of mass transport in liquid alloys by means of neutron radiography’, *J. Phys.: Condens. Matter* **23**, 254201 (2011).
- [178] A. Mialdun, M. Bou-Ali and V. Shevtsova, ‘Soret vector for description of multicomponent mixtures’, *Sci. Rep.* **11**, 17735 (2021).
- [179] P. Bräuer and G. Müller-Vogt, ‘Measurements of aluminum diffusion in molten gallium and indium’, *J. Cryst. Growth* **186**, 520–527 (1998).
- [180] J. Klein, ‘The interdiffusion of polymers’, *Science* **250**, 640–646 (1990).
- [181] A. Ben Abdellah, J. G. Gasser, K. Bouziane, B. Grosdidier and M. Busaidi, ‘Experimental procedure to determine the interdiffusion coefficient of miscibility gap liquid alloys: case of GaPb system’, *Phys. Rev. B* **76**, 174203 (2007).
- [182] A. Griesche and G. Frohberg, ‘Determination of concentration profiles from diffusion experiments in liquid monotectic alloys by AAS’, *Fresen. J. Anal. Chem.* **352**, 607–608 (1995).
- [183] A. Meyer, ‘Self-diffusion in liquid copper as seen by quasielastic neutron scattering’, *Phys. Rev. B* **81**, 012102 (2010).
- [184] F. Kargl, H. Weis, T. Unruh and A. Meyer, ‘Self diffusion in liquid aluminium’, *J. Phys: Conf. Ser.* **340**, 012077 (2012).
- [185] O. R. Gittus and F. Bresme, ‘On the microscopic origin of Soret coefficient minima in liquid mixtures’, *Phys. Chem. Chem. Phys.* **25**, 1606–1611 (2023).
- [186] F. Demmel, D. Szubrin, W.-C. Pilgrim and C. Morkel, ‘Diffusion in liquid aluminium probed by quasielastic neutron scattering’, *Phys. Rev. B* **84**, 014307 (2011).
- [187] A. S. Marwaha and N. E. Cusack, ‘The absolute thermoelectric power of liquid metals’, *Phys. Lett.* **22**, 556 (1966).
- [188] A. Makradi, H. Chaaba and J. G. Gasser, ‘Experimental thermoelectric power of liquid silver-germanium alloys interpreted with an analytical energy-dependent calculation’, *Philos. Mag. B* **80**, 1727–1741 (2000).
- [189] C. Chaïb, J. G. Gasser, J. Hugel and L. Roubi, ‘Electrical resistivity and absolute thermoelectric power of liquid copper–lead alloys’, *Phys. B: Condens. Matter* **252**, 106–113 (1998).
- [190] M. J. Assael, I. J. Armyra, J. Brillo, S. V. Stankus, J. Wu and W. A. Wakeham, ‘Reference data for the density and viscosity of liquid cadmium, cobalt, gallium, indium, mercury, silicon, thallium, and zinc’, *J. Phys. Chem. Ref. Data* **41**, 033101 (2012).
- [191] G. Careri, A. Paoletti and M. Vicentini, ‘Further experiments on liquid indium and tin self-diffusion’, *Il Nuovo Cimento* **10**, 1088–1099 (1958).
- [192] S. K. Das, M. E. Fisher, J. V. Sengers, J. Horbach and K. Binder, ‘Critical dynamics in a binary fluid: simulations and finite-size scaling’, *Phys. Rev. Lett.* **97**, 025702 (2006).

- [193] S. K. Das, A. Kerrache, J. Horbach and K. Binder, ‘Phase behavior and microscopic transport processes in binary metallic alloys: computer simulation studies’, in *Phase transformations in multicomponent melts* (Wiley, Oct. 2008), pp. 141–156.
- [194] R. Taylor and H. A. Kooijman, ‘Composition derivatives of activity coefficient models (for the estimation of thermodynamic factors in diffusion)’, *Chem. Eng. Commun.* **102**, 87–106 (1991).
- [195] X. Liu, S. K. Schnell, J.-M. Simon, P. Krüger, D. Bedeaux, S. Kjelstrup, A. Bardow and T. J. H. Vlugt, ‘Diffusion coefficients from molecular dynamics simulations in binary and ternary mixtures’, *Int. J. Thermophys.* **34**, 1169–1196 (2013).
- [196] K. I. Morozov, ‘Soret effect in molecular mixtures’, *Phys. Rev. E* **79**, 031204 (2009).
- [197] S. Wiegand, ‘Thermal diffusion in liquid mixtures and polymer solutions’, *Journal of Physics: Condensed Matter* **16**, R357 (2004).
- [198] C. Debuschewitz and W. Köhler, ‘Molecular origin of thermal diffusion in benzene+cyclohexane mixtures’, *Phys. Rev. Lett.* **87**, 055901 (2001).
- [199] S. Hartmann, G. Wittko, W. Köhler, K. I. Morozov, K. Albers and G. Sadowski, ‘Thermophobicity of liquids: heats of transport in mixtures as pure component properties’, *Phys. Rev. Lett.* **109**, 065901 (2012).
- [200] E. Sondermann, F. Kargl and A. Meyer, ‘Influence of cross correlations on interdiffusion in Al-rich Al-Ni melts’, *Phys. Rev. B* **93**, 184201 (2016).
- [201] A. Paoletti and M. Vincentini-Missoni, ‘Diffusion in a liquid indium-tin alloy at several concentrations’, *J. Appl. Phys.* **32**, 559–561 (1961).
- [202] A. I. Pommrich, A. Meyer, D. Holland-Moritz and T. Unruh, ‘Nickel self-diffusion in silicon-rich Si-Ni melts’, *Appl. Phys. Lett.* **92**, 241922 (2008).
- [203] S. Szabó and Z. Evenson, ‘Self-diffusion in liquid Al-Ge investigated with quasi-elastic neutron scattering’, *Appl. Phys. Lett.* **110**, 161903 (2017).
- [204] F. Demmel, ‘Non-Arrhenius behaviour of nickel self-diffusion in liquid Ni<sub>77</sub>Si<sub>23</sub>’, *J. Phys. Condens. Matter* **34**, 395101 (2022).
- [205] R. Fingerhut, G. Herres and J. Vrabec, ‘Thermodynamic factor of quaternary mixtures from Kirkwood–Buff integration’, *Mol. Phys.* **118**, e1643046 (2019).
- [206] V. G. Jervell and Ø. Wilhelmsen, ‘Revised Enskog theory for Mie fluids: prediction of diffusion coefficients, thermal diffusion coefficients, viscosities, and thermal conductivities’, *J. Chem. Phys.* **158**, 224101 (2023).
- [207] V. Gallina and M. Omini, ‘On thermal diffusion in liquid metals’, *Il Nuovo Cimento B* **8**, 65–89 (1972).
- [208] L. J. T. M. Kempers, ‘A comprehensive thermodynamic theory of the Soret effect in a multicomponent gas, liquid, or solid’, *J. Chem. Phys.* **115**, 6330–6341 (2001).
- [209] S. Srinivasan and M. Z. Saghir, ‘Modeling of thermotransport phenomenon in metal alloys using artificial neural networks’, *Appl. Math. Model.* **37**, 2850–2869 (2013).

- [210] N. E. R. Zimmermann, G. Guevara-Carrion, J. Vrabec and N. Hansen, ‘Predicting and rationalizing the Soret coefficient of binary Lennard-Jones mixtures in the liquid state’, *Adv. Theory Simul.* **5**, 2200311 (2022).
- [211] J. L. Murray, ‘The Al-In (aluminum-indium) system’, *Bulletin of Alloy Phase Diagrams* **4**, 271–278 (1983).
- [212] I. Ansara, C. Chatillon, H. L. Lukas, T. Nishizawa, H. Ohtani, K. Ishida, M. Hillert, B. Sundman, B. B. Argent, A. Watson, T. G. Chart and T. Anderson, ‘A binary database for III-V compound semiconductor systems’, *Calphad* **18**, 177–222 (1994).
- [213] S. S. Kim and T. H. Sanders, ‘Thermodynamic assessment of the meta-stable liquidi in the Al-In, Al-Bi and Al-Pb systems’, *Model. Simul. Mater. Sci. Eng.* **14**, 1181 (2006).
- [214] Z. Zhang, H. Su, N. Chen and R. Peng, ‘Calculation of thermodynamic properties from two-liquid coexisting phase diagram of Al-In system by means of NRTL equation’, *J. Mater. Sci. Technol.* **15**, 35–38 (1999).

# Publications

Parts of this thesis have already been published in

- A. T. Krüger et al., ‘Measurement of the Soret coefficient in liquid Al-Ag alloys using x-ray radiography’, *Phys. Rev. B* **107**, 064301 (2023).

Parts of this work have been presented at

- 13<sup>th</sup> International Workshop on Subsecond Thermophysics (IWSSTP), 2022, Karlsruhe, Germany. Talk title: *Thermodiffusion in liquid alloys measured by X-ray radiography*.
- 18<sup>th</sup> International Conference on Diffusion in Solids and Liquids (DSL), 2022, Florence, Italy. Talk title: *Measurement of the Soret coefficient in liquid Al-Ag alloys using X-ray radiography*.
- DLR Doctoral Symposium, 2022, Hamburg, Germany. Poster title: *Measurement of thermodiffusion in liquid alloys using X-ray radiography*.
- 15<sup>th</sup> International Meeting on Thermodiffusion (IMT), 2023, Tarragona, Spain. Talk title: *Measurement of the Soret coefficient in liquid Al-Ag alloys using X-ray radiography*.





# Acknowledgements

And just like that, these three years as a PhD student at DLR are over, and here is the thesis to show it. I have very much enjoyed my time here, which has been very formative for me, both scientifically and privately.

I want to thank Herr Meyer for offering me this position here at the institute. For seeing my job application, for believing in me enough to be willing to hire me, when no one else had believed in me for over a year, I deeply thank you. Also a big thanks to Frau Zander for continuing that trust in me, giving me the prolongation so that I could finally finish this thesis.

Thank you to Prof. Daniel Hägele for agreeing to be the second assessor of this thesis, and for the great interest shown in this work.

To Elke Sondermann, I thank you very much for all the help, all the guidance, all the teaching, all the trust, and maybe most of all: all the patience. I have not a single day regretted having you as my supervisor.

To Matthias Kolbe, Fan Yang, Dirk Bräuer, Jürgen Brillo: thank you for your crucial help along the way, and for all the time you gave. Helping out with equipment, theory, IT systems, and in general for being great people to talk with, making me feel somewhat equally worthy.

Thank you to the DLR library for all the impossible-to-find publications you found and sent to me, and to the institute workshop for all the impossible-to-make parts you made for me. Also, thank you to everyone online who answer questions, publish code, and in general help out, all free of charge.

To all the PostDoc's who helped me with all kinds of small and big stuff: Toni, Masato, Gwen, Carolina, Nuria, Thomas, Will, etc., thank you for being cool people! And to all the PhD students: my fellow crowd, my friends, my colleagues, what would this time at DLR be without you? You are too many to all mention, and I'm sorry for that, because you all deserve the best. But especially the most heartfelt 'thank you' to Benni, Mélanie, and Ya-Chun.

As for outside-MP people, I especially want to thank Abbas, Christian, Giles, Lidia, and Tara for helping in making these years in Köln some great years. Just as in my previous thesis, I want to thank my family for asking, listening, supporting, and for being there for me during my entire life.

And finally, another thank you to Mélanie, for being the most epicest of friends, partner, mate, buddy, proof reader, construction-associate, therapist, travel-company, and now also parent to the epicest of kids.



# CV

---

Name:	Asbjørn Torsvik Krüger
Birthdate:	26.10.1995
Birthplace:	Tønsberg, Norway

---

2020–2024	PhD student, Institute of Material Physics in Space, German Aerospace Centre (DLR), Cologne, Germany
2018–2019	Lab and teaching assistant, Department of Physics, Norwegian University of Science and Technology (NTNU), Trondheim, Norway Measurement techniques (TFY4185), Instrumentation (TFY4190)
2017–2019	MSc student, Department of Physics, Norwegian University of Science and Technology (NTNU), Trondheim, Norway <i>Electrohydrodynamics and particle sintering as methods for production of microporous capsules</i>
2014–2017	BSc student, Department of Physics, Norwegian University of Science and Technology (NTNU), Trondheim, Norway

---



# Declaration of authorship

## **Affidavit according to § 9 (1) 4. of PromO 2023**

I declare in lieu of oath that I have written the submitted dissertation independently and without unauthorized external assistance, that I have not used any literature other than that specified in the dissertation and that I have identified all text passages that have been adopted in full or in part as well as all graphics, tables and evaluation programs used. I also confirm that the submitted electronic version of the dissertation is the same as the written version and that the dissertation has not been submitted and assessed elsewhere in this or a similar form.

I declare that digital images contain only the original data or clear documentation of the nature and extent of the image processing and that no commercial mediation or advice has been used.

Signed: \_\_\_\_\_  
Asbjørn Torsvik Krüger

Date: \_\_\_\_\_